

**Investigation of
Semiconductor-Metal
Heteronanostructured Assemblies
and Their Photoelectrochemical
Properties**

**Von der Naturwissenschaftlichen Fakultät der
Gottfried Wilhelm Leibniz Universität Hannover**

zur Erlangung des Grades
Doktor der Naturwissenschaften (Dr. rer. nat.)

genehmigte Dissertation
von
Jakob Cornelius Schlenkrich, M. Sc.

2024

Referentin: Prof. Dr. rer. nat. Nadja-Carola Bigall
Korreferent: Prof. Dr. rer. nat. habil. Armin Feldhoff
Weiterer Korreferentin: Prof. Dr. rer. nat. Maria Wächtler
Tag der Promotion: 14.03.2024

Kurzzusammenfassung

Um die CO₂ Emissionen zu verringern, besteht die Notwendigkeit, erneuerbare Energieträger ohne Treibhausgas Emissionen zu verwenden. Heterogene Katalysatoren können bei der Herstellung dieser Energieträger eine Schlüsselrolle spielen, da sie in der Lage sind, chemische Reaktionen zu beschleunigen oder zu ermöglichen. Ein geeigneter Energieträger ist Wasserstoff, dessen Herstellung einen hohen Energieaufwand erfordert. Die benötigte Energie kann unter anderem durch Sonnenenergie mittels eines Photokatalysators bereitgestellt werden. Ein Photokatalysator muss Licht absorbieren und die angeregten Elektronen und Löcher effizient trennen. Ein Halbleiter ist ein geeigneter Photokatalysator, da er aufgrund der elektronischen Bandlücke Licht absorbieren und Elektronen und Löcher trennen kann.

In dieser Arbeit geht es um die Synthese und Charakterisierung photokatalytischer Materialien, die auf Nanopartikeln basieren. Genutzt wurden halbleiter Nanopartikel, die mit einem metallischen Cokatalysator kombiniert und zu dreidimensionalen, porösen, gelartigen Netzwerken assembliert wurden. Um die Netzwerke aus den Nanopartikeldispersionen aufzubauen, wurden einerseits die Nanopartikel durch das Schockgefrieren einer wässrigen Dispersion, und damit einhergehendes Wachstum der Eiskristalle, zusammengepresst. Zum anderen wurden Nanopartikeldispersionen durch Oxidation der Liganden destabilisiert.

Photoelektrochemische Untersuchungen zeigten, dass der Kontakt zwischen dem Metall und dem Halbleiter, sowie die Verteilung der Metalldomänen, entscheidend für eine effiziente Ladungstrennung sind. Das Metall muss homogen in den Netzwerkstrukturen verteilt sein und der Abstand zwischen den Metalldomänen muss groß genug sein, um eine effiziente Ladungstrennung und Elektronenakkumulation zu gewährleisten. Diese Struktur-Eigenschafts-Korrelationen zeigen, dass eine hohe Kontrolle über die Verteilung der Metalldomänen notwendig ist, um die Eigenschaften für photokatalytische Anwendungen einzustellen.

Die Durchführung der photokatalytischen Wasserstoffproduktionsreaktion unter Verwendung der Netzwerkstrukturen hat gezeigt, dass Nanopartikel in Hydrogelen effizient für die Photokatalyse genutzt werden können. Die selbsttragende Netzwerkstruktur gewährleistet die Diffusion innerhalb des Netzwerks, und die hohe spezifische Oberfläche bleibt erhalten, während keine kolloidale Stabilität notwendig ist. Platin als Cokatalysator in den Hydrogelen führt zu hohen Wasserstoffproduktionsraten. Dabei zeigen die Experimente, dass der limitierende Schritt in diesen Systemen möglicherweise nicht die Elektronenübertragung vom Halbleiter auf das Metall ist, sondern eher die Diffusion innerhalb des Netzwerks oder die katalytische Reaktion selbst.

Stichworte: Halbleiter-Metal Hybrid, Nanopartikel-basierte Gele, Photoelektrochemie, Photokatalyse

Abstract

To reduce CO₂ emissions when using energy, there is the global need to use renewable energy carriers without a carbon footprint. Heterogeneous catalysts can play a key role in the production of these energy carriers due to their ability to fasten chemical reactions or even enable reactions which are energetically unfavored. A suitable energy carrier is hydrogen for which the production requires a high amount of energy. The needed energy can be provided by electric energy in an electrolyzer, but also by solar energy using a photocatalyst. A photocatalyst needs to absorb light and separate the excited electron and hole efficiently to use these charge carriers for further reactions. In example, a semiconductor can absorb light due to the electronic band gap between the valence and conduction band, and thus can act as a photocatalyst.

This work is about the synthesis and characterization of novel photocatalytic materials which are based on nanoparticles. As suitable semiconductors CdSe and CdS based materials have been used in form of quantum dots, nanorods, and nanoplatelets. Additionally, these semiconductors have been combined with a metal cocatalyst. These nanoparticles were synthesized and afterwards assembled into three dimensional porous gel-like networks. To build the networks out of the nanoparticle dispersions, two different methods have been used. On the one hand, by shock-freezing an aqueous dispersion the growing ice crystals press the nanoparticles together physically. On the other hand, nanoparticle dispersions were destabilized by chemical ligand oxidation. Photoelectrochemical investigations showed that the contact between the metal and the semiconductor as well as the metal domain distribution is crucial for an efficient charge carrier separation. The metal has to be distributed homogeneously in the network structures. However, the distance between the metal domains needs to be large enough to ensure an efficient charge carrier separation and electron accumulation in the metal domains. These structure property correlations indicate that a high control over the metal domain distribution is necessary to tune the properties for photocatalytic applications.

Performing the photocatalytic hydrogen production reaction using semiconductor and semiconductor metal hybrid gel structures revealed, nanoparticles in hydrogels can be used efficiently for photocatalysis. The self-supporting network structure ensures diffusion within the network and the high surface area is retained while colloidal stability is not needed. Platinum as cocatalyst in the hydrogels leads to high hydrogen production rates. The experiments indicate that the limiting reaction in these systems might not be the electron transfer from the semiconductor to the metal, but more probable the diffusion within the network or the catalytic reaction itself.

Keywords: semiconductor-metal hybrid, nanoparticle-based gel, photoelectrochemistry, photocatalysis

Preface

The research findings which are presented in this thesis have been elaborated from 2020 until the end of 2023 in the Institute of Physical Chemistry and Electrochemistry as well as partially in the Laboratory of Nano and Quantum Engineering. Both institutions are part of the Leibniz University Hannover. This work was accompanied by the supervision of Prof. Nadja C. Bigall and in the end of 2023 as well by Prof. Armin Feldhoff. Three projects of this thesis have been published in peer-reviewed journals and a manuscript of the fourth project has been submitted in a peer reviewed journal but is not published yet. Additionally, during that time I contributed as a coauthor to three more publications in peer reviewed journals. I furthermore presented my research on nine international conferences in form of either an oral presentation or a poster presentation.

The first article of this thesis was a shared first authorship of Anja Schlosser and me. Anja Schlosser conducted all syntheses and experiments related to nanoplatelets and wrote this section in the manuscript. I performed all syntheses and experiments of nanorod based samples and wrote this section in the manuscript. Additionally me and Dr. Dániel Zámbo revised the manuscript during the peer review process. Dr. Dániel Zámbo furthermore assembled the sections of Anja Schlosser and me in the manuscript and also designed the figures. Marina Rosebrock synthesized gold nanoparticles and gave comments on the manuscript. Rebecca T. Graf did TEM measurements and also commented on the manuscript. Giamper Escobar Cano did early experiments on combining nanoplatelets and metals. Prof. Nadja C. Bigall supervised to project and contributed to the interpretation of the results and gave important comments on the conceptualization and the final manuscript.

The second manuscript was written by me including all figures. The lab work was completely done by me except TEM measurements as mentioned in the following. Dr. Dániel Zámbo worked together with me on the conceptualization and contributed to the interpretation of the results. Furthermore, he gave comments to the manuscript and helped working on the revision during the peer review process. Anja Schlosser and Pascal Rusch did TEM measurements. They kindly measured much more samples than shown in the manuscript. Prof. Nadja Bigall had the supervision of the project and contributed to the interpretation of the results and gave useful comments on the manuscript.

The third manuscript has been written by me and most of the experiments were conducted by me as well. Dr. Franziska Lübke-Warwas helped performing photocatalytic measurements, synthesized CdS nanorods and worked with me on the conceptualization as well as gave many comments on the manuscript. Rebecca T. Graf and Christoph Wesemann measured TEM. Not all images were used in the manuscript for the publication. Rebecca T. Graf and Christoph Wesemann also gave comments to the manuscript. Larissa Schoske contributed with CdSe nanoparticle solutions and

reading the manuscript. Marina Rosebrock measured XPS, Karen D.J. Hindricks conducted BET measurements and Prof. Peter Behrens contributed as supervisor for the BET measurements. All as well read the manuscript and gave comments. Prof. Detlef W. Bahnemann and Prof. Dirk Dorfs gave useful comments on the manuscript. Prof. Nadja Bigall had the supervision of the work and contributed to the interpretation of the results and gave useful comments to the manuscript.

The manuscript in chapter 3.3 has been submitted to a peer reviewed journal. The manuscript was written by me and all experiments and syntheses were performed by me. Denis Pluta introduced me into the UV-Vis spectrometer and helped me evaluating the PLQY and fluorescence lifetime measurements. With this he contributed to some figures. Rebecca T. Graf and Christoph Wesemann measured TEM. Kindly, many more images have been taken than shown in the publication. Dr. Franziska-Lübke-Warwas gave important comments to the manuscript and improved it like this. Prof. Nadja Bigall had the supervision of the project and contributed to conceptualization and gave useful comments to the manuscript.

Acknowledgement

This thesis would not be as it is if there weren't many people supporting me during the time in the lab, evaluating the data, writing manuscripts and support me personally in my everyday life. I would like to thank Prof. Nadja Bigall for giving me the opportunity to work on my thesis in her group and the supervision over the last four years. Discussions and ideas lead to four great manuscripts I can be proud of. As second supervisor I have to thank Prof. Armin Feldhoff for advices and engagement during the last months.

Also I have to thank Prof. Nadja Bigall, Prof. Armin Feldhoff and Prof. Maria Wächtler for reviewing this thesis as referee and co-referees, respectively. Furthermore, I thank Prof. Denis Gebauer for being chair of the examination board and additional being examiner.

Dr. Dániel Zámbo introduced me into the topic of my doctoral thesis, how to write a paper, and helped to improve the way to work scientifically in the lab. I really enjoyed to discuss and plan experiments with him. That not only helped for the manuscripts where he directly contributed to, but also for the others. And of course having a buddy to tech-talk about cycling and bikes was always a motivation to come to work. Furthermore, I have to mention Dr. Franziska Lübke-Warwas. She build up the photocatalytic setup with help of Pascal Rusch and me. This opened up a new direction for investigating my materials. Many thanks to Franzi for all the discussions and the compensation my missing motivation to make figures for our manuscript.

For measuring and producing data, I would like to thank Pascal, Anja, Rebecca and Chris for all their time at the TEM. I thank Denis for his UV/Vis spectroscopy and SEM skills, Gerrit aswell for the SEM knowledge, Marina for expertise in XPS and Patrick for Cary related things. Beside helping to improve the scientific work, there was much more that kepted up motivation and brought fun during theses four years for which I am thankful. Therefore, I thank all members of the groups of Prof. Nadja Bigall, Prof. Dirk Dorfs and Prof. Jannika Lauth. Highlights were the regular breakfast, lunch breaks and definitely the meme channel on discord. I really enjoyed working with all.

I would like to thank the students who worked under my guidance on their thesis or research internships. Arlan Ospanow's and Ruben Denker's work contributed directly to this thesis. Maren Leuker and Fredrike von der Haar worked on slightly different topics. All did a good job and it was fun to work with them. All the best for their ongoing careers. I further need to thank collaboration partners from different institutes who contributed to this work. Karen D. J. Hindricks and Prof. Peter Behrens from the Institute of Inorganic Chemistry and Prof. Detlef W. Bahnemann from the Institute of Technical Chemistry.

There was much more beside the university during the last four years. Chris, Denis, Henning, André and Rebecca are colleagues and friends. We not only can talk about

chemistry, we also spend really good times having game nights, learn snowboarding, go cycling, making sushi or go climbing. I appreciate all this. My family is one more piece in the puzzle. Alexander, Jana, little Oscar, Burkhard, Maria, Angela and Michael. It is so nice that we have this strong family bond and I am always happy to have you around me. And Rebecca, you are my colleague, my friend and my partner. I don't know how you do this but you do so well. III

Contents

Kurzzusammenfassung	i
Abstract	iii
Preface	v
Acknowledgement	vii
1 Introduction	1
1.1 Motivation	1
1.2 Semiconductor Nanoparticles	2
1.2.1 Semiconductor Nanoparticle Synthesis	3
1.2.2 Quantum Size Effect	4
1.2.3 Optical Properties of Cadmium Chalcogenide Nanoparticles	6
1.2.4 Cadmium Chalcogenide Nanoplatelets	7
1.2.5 CdSe/CdS Core-Shell Nanorods	8
1.3 Semiconductor-Metal Hybrid Nanoparticles	10
1.3.1 Metal Domain Synthesis	11
1.3.2 Charge Carrier Properties	12
1.4 Nanoparticle-Based Gel Structures	14
1.4.1 Gel Structure Formation	14
1.4.2 Structure Property Correlation	16
1.5 Photocatalysis on Nanoparticle-Based Materials	17
1.6 Photoelectrochemistry of Nanoparticle-Based Systems	19
Bibliography	23
2 Photoelectrochemistry of Semiconductor-Metal Gel Structures	35
2.1 Summary	35
2.2 Interparticle Interaction Matters: Charge Carrier Dynamics in Hybrid Semiconductor-Metal Cryoaerogels	37
2.3 Revealing the Effect of Nanoscopic Design on the Charge Carrier Separation Processes in Semiconductor-Metal Nanoparticle Gel Networks	63
3 Hydrogen Evolution Reaction on Nanoparticle-Based Hydrogels	87
3.1 Summary	87
3.2 Investigation of the Photocatalytic Hydrogen Production of Semiconductor Nanocrystal-Based Hydrogels	89
3.3 Semiconductor-Metal Hybrid Nanoparticle-Based Hydrogels: Efficient Photocatalysts for Hydrogen Evolution Reaction	111

CONTENTS

4 Summary and Outlook	125
Curriculum Vitae	127
Publications and Conferences	129

Chapter 1

Introduction

1.1 Motivation

Nanotechnology gained high importance in industry and research in the last decades.^[1–3] Nanometer size structures in transistors for miniaturized devices^[4], ion trapping for quantum computation^[5], or quantum dots for bright emitting LED TVs.^[6] Reducing the size of materials may reduce the use of resources and open up new possibilities for manufacturing.^[7] Not only the manufacturing process or the size of the devices changes, but also the properties of the material. Nanomaterials have different properties compared to their respective bulk material.^[8] Reducing the size below 100 nm brings changes in the electronic band structure of the materials and new or improved properties evolve. With decreasing size, the surface to volume ratio increases, so that the surface reactivity increases and the surface properties become more prominent when having nanoparticles.

Heterogeneous catalysis reactions are surface reactions, where the reactants adsorb and desorb on the catalytically active surface. Due to the high surface area and high surface reactivity nanoparticles are predestinated catalysts.^[9] These catalysts, which change the activation barrier by introducing a different reaction pathway, do not change the overall thermodynamics of a reaction. To enable reactions which are not possible due to thermodynamic limitations, a photocatalyst can be used. A photocatalyst thereby, enables reactions with light irradiation which are not possible in the dark. The required energy for the reaction is given by photon absorption of the photocatalyst. Using energy coming from sunlight gives the possibility to catalyze reactions which can help to build up a sustainable industry. Reactions, which for example can reduce the need of fossil fuels or use CO₂ as resource to synthesize chemical raw materials, are the photocatalytic hydrogen production^[10] or CO₂ reduction.^[11]

Semiconducting materials can be used as photocatalysts. Due to the electronic band gap, electrons can be excited from the valence band into the conduction band by light absorption. The excited electron leaves a hole in the valence band and both the electron and the hole can be seen as charge carriers. These charge carriers can be used for further reactions like oxidation or reduction reactions. Thereby, titanium dioxide is the most studied semiconductor for photocatalytic applications^[12]. However, titanium dioxide has a comparably large band gap for which UV light is needed to be overcome. This implies, that most energy of the solar spectrum can not be used to

excite the photocatalyst. It is therefore desirable to have a photocatalyst material with a smaller band gap to use the solar light more efficiently.

The requirements for suitable photocatalysts are more comprehensive. Beside the band gap a high absorption coefficient, a catalytically active surface and a high photostability have to be mentioned. Furthermore, to make use of the advantages of nanomaterials an approach to synthesize nanoparticles is needed. A semiconducting material which fulfills the requirements to be a good nanoparticle-based photocatalyst is CdS.^[13] CdS has a smaller band gap than titanium dioxide, a high absorption coefficient and there is high control over the nanoparticle synthesis due to intensive research for decades.^[14] Thus, CdS nanoparticles can be synthesized with high precision and control over their shape, size and thus their properties. Furthermore, heterojunctions of two or more different materials are possible to tune the material characteristics further. Those factors result in a high motivation to use cadmium chalcogenide based nanoparticles or heterojunction for photocatalytic applications.

With the advantages of nanoparticles comes also a challenge. While the high reactivity of the surface is beneficial for catalytic reactions, it also leads to agglomeration to reduce the surface. This can be circumvented by stabilizing the nanoparticles with ligands. These ligands bind to the surface of the nanoparticles and introduce a repulsive force between the nanoparticles itself.^[15] However, having a ligand shell around the nanoparticles also reduces the accessibility of the surface. To overcome this, nanoparticle-based gel structures can be used. Nanoparticle-based gels have a self-supporting and highly porous network, in which the nanoscopic properties of the building blocks can be retained. A stabilization with ligands is not needed and a high surface area is maintained.^[16] With this the advantages of nanoparticles, meaning a high and reactive surface, can be retained but also the drawback of a limited surface accessibility can be overcome.

The goal of this work was to gain information about structure property correlations in semiconductor-metal hybrid nanoparticle based gel structures. The influence of the embedment of metal domains in the semiconductor network as well as the metal domain distributions were at the center of the investigations. Photoelectrochemical characterizations give insights in the charge carrier properties whereas photocatalytic experiments can prove the applicability of the synthesized materials. With this knowledge the aim was to optimize the semiconductor-metal interactions in nanoparticle based gel structures with regard to photocatalytic applications.

1.2 Semiconductor Nanoparticles

Beside fundamental research interests the broad range of possible applications of nanomaterials provides the driving force in nanotechnology. Finding new materials and new ways to synthesize these materials, as small as they need to be for a certain application, bring up the challenges of the current research.

In semiconductor nanomaterials the most prominent property change compared to the bulk material is the increasing band gap with decreasing particle size. This effect is called quantum size effect. It is correlated to the quantum confinement and influences the electronic band structure of the semiconductor which is visible in the photolumi-

nescence color change of CdSe quantum dots with their size.

Different semiconductor materials such as ZnO, ZnSe, ZnS, CdS, CdSe, PbS, PbSe etc. have a different exciton Bohr radius meaning the distance between the electron and the hole.^[17] This radius is mostly between 2 nm and 50 nm.^[18] A particle size smaller than the exciton Bohr radius of the material, leads to a confinement of the exciton. An exciton is an electron-hole pair which forms a quasi particle due to attractive coulomb forces. The control over the size of a material thus is desirable.

1.2.1 Semiconductor Nanoparticle Synthesis

To obtain uniform and precise properties of a nanoparticle dispersion, a monodisperse size of the nanoparticles is required. Due to the quantum size effect, which is introduced in section 1.1.2, small differences in size lead to slightly different electronic and with this optical properties.^[20] To have a nanoparticle dispersion with distinct properties, many crystallites with the same size need to be synthesized. The LaMer diagram can be used to explain the different phases of crystal growth in a colloidal synthesis, to understand the required parameters to ensure monodisperse nanoparticle growth (Figure 1.1).^[19] The theory of LaMer is based on the nucleation of sulfur, but is also applicable for the nucleation of different materials. Three phases have been defined. In the first phase, the concentration of the precursor increases. The concentration can reach three different benchmarks. Within the first regime, the precursors are soluble in the solvent. Further increasing the concentration leads to a supersaturation without

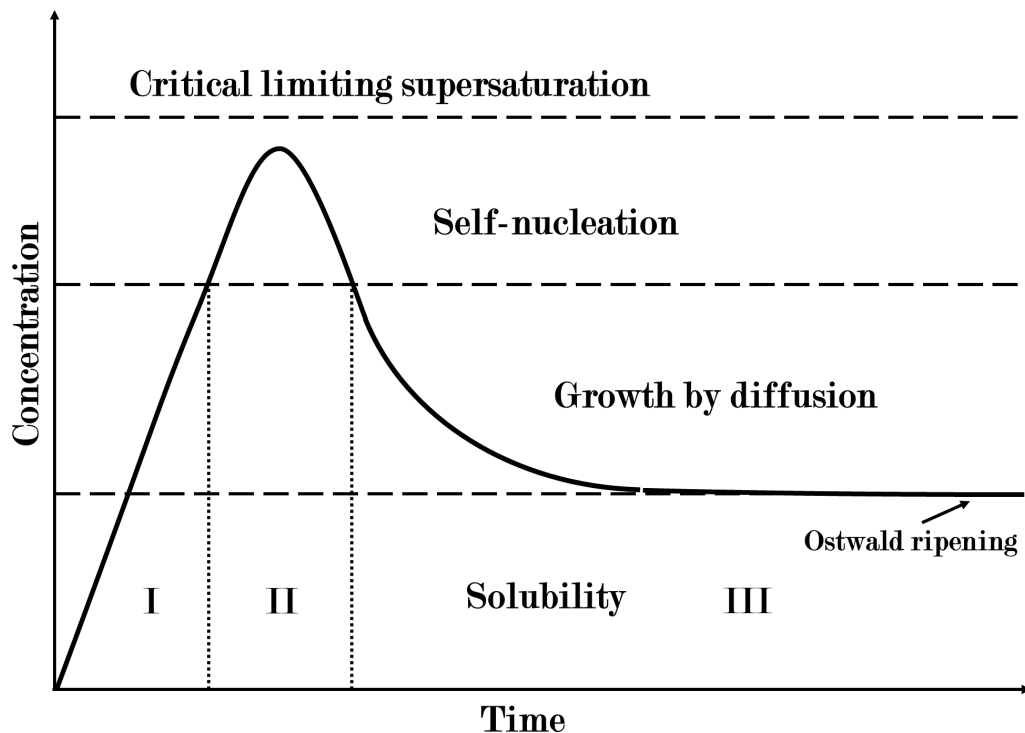


Figure 1.1: Schematic illustration of the precursor concentration over time. The three phases involve increasing concentration, self-nucleation and crystal growth. Self-nucleation occurs above a certain supersaturation of the precursors. This figure is adapted from LaMer et. al.^[19]

nucleation before with even higher concentration spontaneous self-nucleation occurs. Above the self-nucleation regime, a critical limiting supersaturation is reached. After the concentration is increased until the self-nucleation takes place, phase one ends and phase two starts which involves the nucleation. Due to the nucleation, the concentration decreases again until it falls off the regime of self-nucleation. With this, phase two and the nucleation ends. In phase three, the concentration is still supersaturated and the formed nuclei grow until the concentration decreases to the soluble regime. When the concentration is below the super saturation Ostwald ripening occurs where smaller particles dissolve and larger particles grow larger. To obtain a monodisperses nanoparticle dispersion, phase two, the self-nucleation, needs to be as short as possible, and the reaction has to be quenched before Ostwald ripening takes place. To shorten the time of self-nucleation hot-injection methods can be used. Here, a high boiling solvent is heated to temperatures between 200 °C and 400 °C and a precursor solution is injected rapidly into the hot solvent.^[21] With this, the concentration of the self-nucleation regime is reached instantaneously and many nuclei are formed at the same time. The high temperature promotes the nucleation and the following growth of the nanoparticles. In the lab, the rapid injection is mostly not ideal so that not all nuclei evolve simultaneously leading to imperfect monodisperse nanoparticle dispersion.^[21] The nucleation process in general is highly sensitive to the concentration of the precursor, impurities, ligands and others.^[22] The first semiconductor nanoparticle syntheses have been published by Bawendi^[23], Brus^[24], and Yekimov^[25] amongst others, who opened up a new research area and received the Noble Prize in Chemistry in 2023.^[26] To date, all kinds of nanoparticles can be synthesized. There are no restrictions to semiconductors, insulators, metallic or magnetic nanoparticles.^[27] Furthermore, various shapes like rods, cubes, wires, tetrapods and many more are possible by tuning the synthesis conditions with different solvents, temperatures, precursors or surfactants.^[28,29] Also heterojunctions with e.g. different semiconductors, semiconductors and metals or semiconductors and magnetic nanoparticles can be synthesized.^[30-32] For CdSe and CdS based materials this will be discussed in the in section 1.2.4.

1.2.2 Quantum Size Effect

The quantum size effect, meaning the increase of the band gap with decreasing particle size, can be quantified and described using two different approaches. Using the tight-binding model, which is correlated to the linear combination of atomic orbitals (LCAO), offers the possibility to describe crystallites with only a few nanometer in size.^[33] On the other hand for larger crystallites, which are still smaller than the exciton Bohr radius, a model based on the effective-mass approximation has been introduced by Brus.^{[8] [34] [35]}

In the tight-binding model, the electrons in the crystallite are assumed to be tightly bound to the respective atoms they belong to. This simplifies the Hamiltonian which makes the mathematical description less complicated. Another advantage of the tight-binding model compared to the effective-mass approximation is the consideration of the atomic structure of the crystallites. In sum, this model enables a precise determination of the band positions and the band gap of the considered crystallites.^[33] Beside the calculation of the energy values, the tight-binding model and the LCAO, respectively, visualize nicely the lower density of states in nanoparticles compared to

the bulk material. Combining n atomic orbitals leads to n molecular orbitals which are split in half being bonding and antibonding orbitals. The bonding orbitals are occupied and represent the highest occupied molecular orbital (HOMO) whereas, the antibonding orbitals are not occupied and represent the lowest unoccupied molecular orbital (LUMO). The energy difference between the HOMO and the LUMO gives the band gap in a semiconductor. In a bulk material there are several molecular orbitals that the sum can be seen as a continuous energy band. Since in a nanoparticle the amount of atomic orbitals and thus of molecular orbitals is limited, the number of states in the energy band is smaller compared to the bulk material.^[18]

In 1983 and 1984 Brus introduced the calculation of the band gap using the effective-mass approximation.^[8,34] Equation (1.1) gives the calculation of the band gap by adding other contributions to the band gap of a bulk material.^[36]

$$E_{nano} \simeq E_{bulk} + \frac{h^2\pi^2}{2R^2} \left[\frac{1}{m_e} + \frac{1}{m_h} \right] - \frac{1.8e^2}{\epsilon R} + \text{smaller terms} \quad (1.1)$$

Here E_{nano} is the band gap of the nanocrystal, E_{bulk} is the band gap of the bulk material, h is the Planck constant, R is the size of the crystallite, m_e and m_h are the effective mass of the electron and the hole, e is the elementary charge and ϵ is the permittivity of the material. The equation consists of three main terms. The second term describes the kinetic energy of the electron and the hole and the third term the

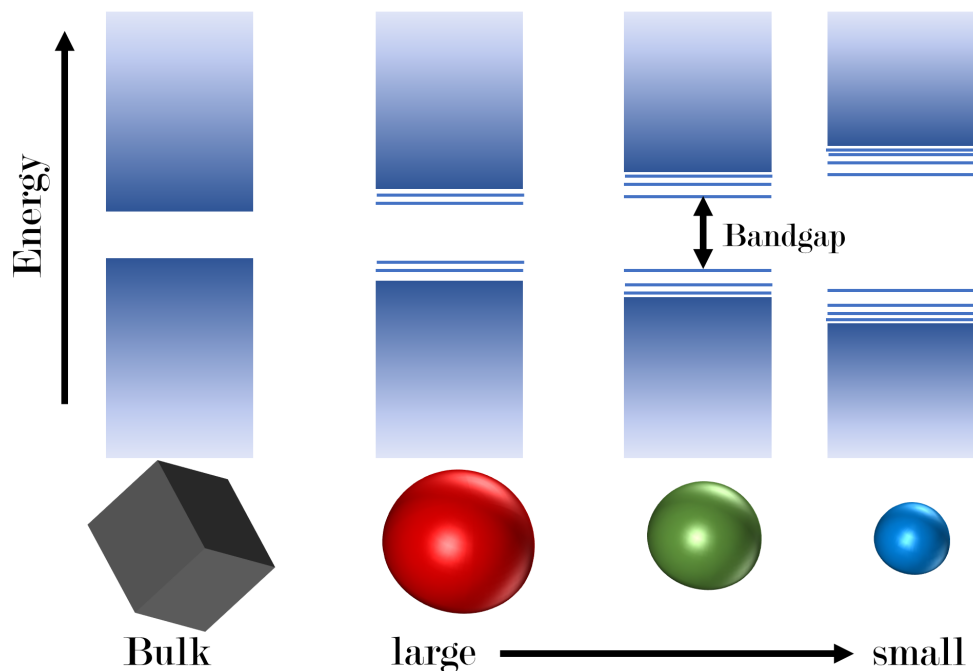


Figure 1.2: Schematic illustration of the quantum size effect of semiconductor materials. With decreasing size of the crystallites the band gap increases and the density of states is reduced. Visually, this can be observed by a color change of the nanoparticle solutions and their photoluminescence colors.

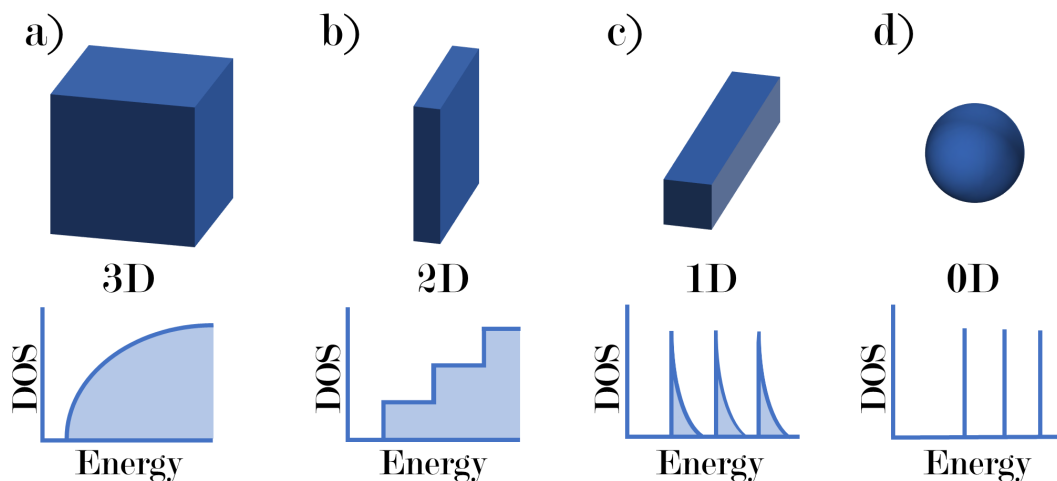


Figure 1.3: Ideal density of states of all four dimensions. Having continuous energy states in the 3D bulk material and discrete energy levels in the 0D quantum dot. From 3D to 0D, the directions of confinement increases from zero to three dimensions.

Coulomb attraction between the electron and the hole. Brus furthermore, introduced smaller terms which have just a low impact on the resulting value, and thus have not been described in detail here. In the approach of Brus, the electron and the hole in a nanoparticle (with a size smaller than the exciton Bohr radius) can be seen as individual particles whereas in the bulk materials the exciton can be seen as one particle. The quantum size effect is schematically shown in Figure 1.2.

Beside the size of nanoparticles the dimension has an impact on the optoelectronic properties. Quantum dots (0D) are confined in all three directions while quantum wires or quantum rods (1D) are confined in two directions. In quantum rods, the size of one direction is larger than the exciton Bohr radius. Furthermore, in a quantum well (2D) the confinement is only in one direction because the other two directions are larger than the exciton Bohr radius. The different confinements have a direct impact on the density of states (DOS) of the nanoparticles. The DOS of one electronic band of each mentioned dimension compared to the bulk material is shown in Figure 1.3

1.2.3 Optical Properties of Cadmium Chalcogenide Nanoparticles

The above described quantum size effect can have a direct influence on the optical properties of semiconductor nanoparticles. The common cadmium chalcogenide nanoparticles (CdS, CdSe, CdTe) absorb and emit light in the visible range. These cadmium chalcogenides have a direct bandgap which is essential for the photoluminescence. Both, absorption and emission spectra change depending on the size of the nanoparticle. As the band gap increases with decreasing particle size, the absorption onset and the emission wavelength shift to higher energies, and thus, smaller wavelengths.^[37–39]

Absorption spectra of nanoparticles show more distinct absorption maxima compared to the bulk material which as well is due to the quantum size effect. As described

above, the density of energy levels in the bulk material is continuously leading to a steady increase in the absorption with increasing energy. However, in the nanoparticles, due to the not continuous energy levels, absorption maxima occur at certain energies. The absorption spectra of single nanoparticles would show sharp maxima. In a nanoparticle solution an ensemble of many different nanoparticles is present, which have a size distribution and are imperfect regarding uniformity of the shape. This leads to slightly different band structures in each particle and thus to absorption maxima at different energies. In the spectra this leads to a broadening of the absorption at the maximum. A small size distribution in a nanoparticle solution is desirable and can be detected through distinct maxima in the absorption spectra.^[18]

Between the absorption and emission maxima a difference on the energy scale can be observed. This shift of the emission to lower energies is the so-called Stokes shift. Due to the Frank-Condon-principle an emitted photon has slightly more energy compared to the energy of the absorbed photon. This comes from differences in the vibrational modes. The excitation of an electron is more probable from the valance band into an excited vibrational mode in the conduction band due to a better overlap of the vibrational wave functions. The excited electron then undergoes a non radiative relaxation in the vibrational ground state which comes along with an energy loss of the excited electron.^[40,41] This energy loss results in a longer emission wavelength explaining the shift between the absorption and the emission maximum. The Stokes shift differs in different materials. CdS quantum dots for example have a larger Stokes shift than CdSe quantum dots of the same size.^[42] Additionally, the surrounding can have an influence on the Stokes shift as reported for CdSe/CdS dot-in-rod nanorods which is due to changes in the electronic fine structure.^[43,44]

1.2.4 Cadmium Chalcogenide Nanoplatelets

Cadmium chalcogenide 2D nanoplatelets differ from the OD and 1D cadmium chalcogenides regarding their optical and electronic properties.^[18] While in quantum dots and quantum rods the optical properties are influenced by the confinement in three and two directions, respectively, in nanoplatelets the confinement in only one direction is crucial for their properties. Synthetically a monolayer precise thickness control is possible.^[45] Regarding the thickness (the crucial dimension for their properties) this leads to highly monodispers nanoparticles.^[46] The precise synthetic control is due to the growth mechanism.^[47] Starting with a small nuclei the crystal grows selectively into a two dimensional nanoparticle. On the nuclei or a small two dimensional crystal a new island has to grow on one of the facets. Reaching a crucial size this island becomes thermodynamically stable and a full new layer on this facet can evolve. These islands grow faster on thin facets where the thickness is smaller than the critical size compared to the growth on the planar facet where the islands grow slower. In a synthesis not only two or only three monolayer nanoplatelets will grow but the thickness as well has an influence on the growth velocity. Two monolayer nanoplatelets grow faster than three monolayer nanoplatelets and these grow faster than four monolayer nanoplatelets etc. The different thicknesses than can be separated from each other by selective precipitation and centrifugation. The growth mechanism is visualized in Figure 1.4. After the synthesis of CdSe nanoplatelets semiconductor heterojunctions

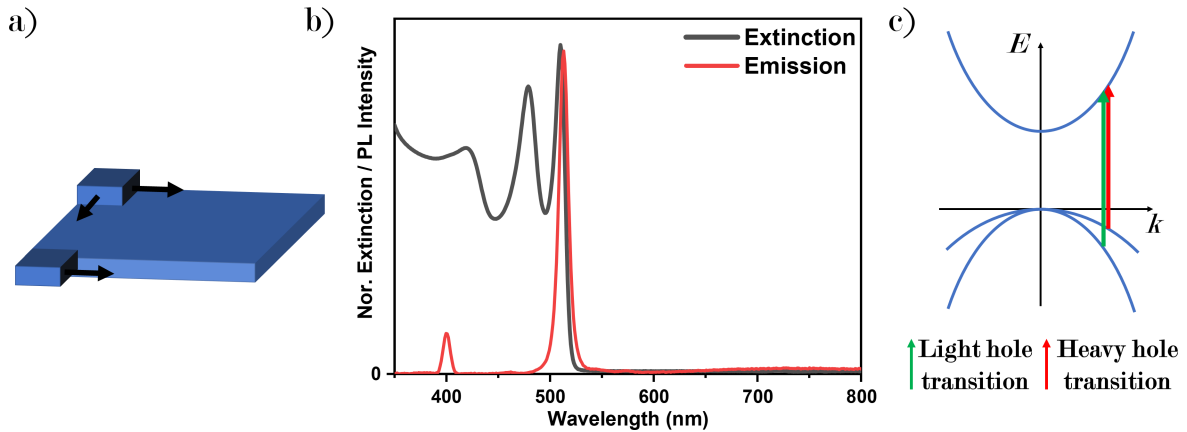


Figure 1.4: a) visualization of the growth mechanism of nanoplatelets. On top of the platelet the growth is slower compared to the growth on the edges. b) extinction and emission spectra of a CdSe nanoplatelet. The sharp absorption and emission features are characteristic for nanoplatelets. c) schematic representation of heavy hole and light hole-electron transitions.

can be synthesized by a second growth step. Core crown nanoplatelets are formed when the second material is grown only on the edges of the nanoplatelets but not on the top and bottom of the CdSe core nanoplatelets. This crown growth passivates the edges of the CdSe core and leads to improved photoluminescence properties.

The absorption and emission spectra of a nanoplatelet solution show really distinct absorption and emission peaks. In the absorption spectra two main peaks are present. The peak at lower energies represents the electron/heavy-hole transition and the peak at higher energies represent the electron/light-hole transition (Figure 1.4).^[46,48] This monodispersity and distinct peaks are hardly achievable with 0D and 1D nanoparticles which makes the nanoplatelets beside other properties interesting for optical applications.^[49–52] The absorption and emission spectra of CdSe nanoplatelets are shown in Figure 1.4.

1.2.5 CdSe/CdS Core-Shell Nanorods

The first synthesis of anisotropic, rod shaped nanoparticles made of a heterojunction based on CdSe and CdS has been reported by Talapin et al. 2003.^[44] Here, CdSe quantum dots serve as seeds for the nucleation of CdS. Hexagonal CdSe quantum dots are previously synthesized by means of a solution based hot injection method. Asymmetric growth of CdS arises from different growth rates on different CdSe facets.^[44] Hexagonal CdSe quantum dots are terminated by (100), (011) and (00 $\bar{1}$) facets. On the (00 $\bar{1}$) facet the growth rate is the highest leading to the rod shaped growth with the CdSe core being not centered in the CdS rod. The growth rates are influenced by lattice mismatches, interfacial strain or the amount of dangling bonds. To further enhance the selective growth surfactants can be used to bind on specific facets supporting the asymmetric growth. In this case, a phosphonic ligand binds on the (011) facet to hinder the growth in that direction and promote the rod shaped growth.^[53]

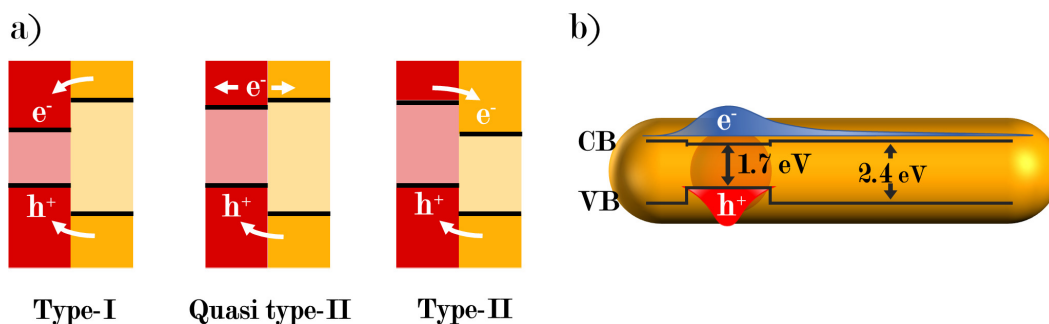


Figure 1.5: a) schematic illustration of the bandstructures in type-I, quasi-type-II and type-II semiconductor heterostructures. The arrows indicate the preferred charge carrier localization. b) band structure of CdSe/CdS nanorods with CdSe as the core in a CdS rod shaped shell. The quasi type-II band structure reduces the overlap of the electron and hole wave functions.

Shell growth in general is beneficial to passivate the surface of the core material using a material which has a larger bandgap than the core material. In CdSe/CdS core-shell structures CdSe has a smaller bandgap than CdS which implies radiative charge recombination takes place in the CdSe core. Surface passivation of the CdSe reduces midgap states within the bandgap, so called trap states. These trap states trap charge carriers which results in non-radiative recombination.^[54] Thus charge carrier properties change with shell growth which can indeed be observed for the CdSe/CdS nanorods. The type of the electronic band structure of semiconducting CdSe/CdS nanorods depends mainly on the size of the CdSe core.^[55,56] A large CdSe core results in a type-I band structure with the valence and conduction band of the CdSe laying in the bandgap of the CdS.^[57] With decreasing size of the CdSe the band gap increases according to the quantum size effect. With this the valence band of CdSe is still within the band gap of CdS but the conduction band of CdSe is very close to the conduction band of the CdS. The band structure thus changes from a type-I semiconductor to a quasi type-II semiconducting band structure.^[56] In a quasi type-II band structure, the electron and hole wavefunctions overlap less and the charge carriers are partially separated from each other. The different semiconductor heterostructure types and a schematic illustration of the band structure in CdSe/CdS nanorods is shown in Figure 1.5.^[58]

Charge separation within the semiconductor heterostructure has a major influence on the charge carrier lifetimes and further on photocatalytic properties.^[59] The localization of the hole in the CdSe core and the partial localization of the electron in the CdS rod shaped shell would lead to an efficient charge carrier separation within the semiconductor heterostructure. Electrons are only partially delocalized in the CdS shell. The location with highest probability still is in the CdSe core due to the coulomb attraction between the electron and the hole. This attraction is the so-called exciton binding energy and is a material specific property. Charge carrier separation thus can be further increased by full separation of the electron and hole. When exciting an electron in the CdS shell, the hole has to be transferred into the CdSe core for the charge separation. However, due to hole trap states in the CdS,

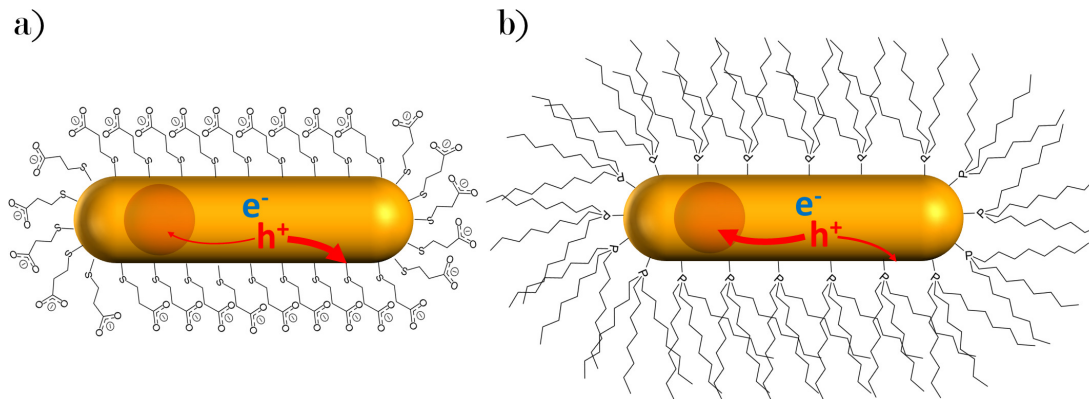


Figure 1.6: CdSe/CdS nanorods with different ligands and the schematic illustration of the influence on the hole trapping probability. a) mercaptopropionic acid with a thiol binding group produces more hole trap states compared to b) the trioctyl phosphine ligands with a phosphine as binding group. The hole trapping has an influence on the hole transfer efficiency from the CdS shell in the CdSe core.

hole trapping competes with the hole transfer to the CdSe core.^[59] In the CdSe/CdS nanorods, trap states are mainly located on the CdS surface. Ligands bind to the surface of the nanoparticle and thus influence surface states. Thiol ligands are known to form hole trap states within the thiol bond, so that ligands with different binding groups minimize trap states and can significantly improve the hole transfer into the CdSe core (Figure 1.6).^[59] The effect of the ligands on charge carrier trapping can be seen in the phase transfer of the nanoparticles from organic to aqueous solution. In organic solution a phosphine ligand binds on the surface of the nanorod whereas, in aqueous solution thiol ligands are used most often. Charge trapping introduces a non radiative charge carrier recombination pathway. Thus, the more charge carriers become trapped, the less excitons recombine radiatively and the ratio between absorbed and emitted photons decreases. The ligand exchange from phosphine ligands to thiol ligands increases the amount of trap states and leads to a significant decrease in photoluminescence quantum yield (PLQY). This shows the smaller ratio between absorbed and emitted photons.^[60] Micheel *et al.* investigated this using transient absorption measurements and found that especially thiol ligands tend to trap holes.^[59] The electrons in contrast are mainly trapped in unsaturated cadmium surface atoms which as well leads to a decrease in PLQY. For optical properties charge trapping in general is not beneficial. However, with regard to photocatalysis, charge separation is crucial but in CdSe/CdS nanorods electron trapping on the surface has less influence than the decreased charge carrier separation due to hole trapping.

1.3 Semiconductor-Metal Hybrid Nanoparticles

Combining semiconductors and metals in macroscopic materials is possible by various high precision top down approaches.^[61,62] The contact area of the metal and the semiconductor is mostly significantly smaller than the metals and semiconductors themselves. In semiconductor-metal hybrid nanoparticles the contact area, relative to

the crystallite sizes, becomes much larger, and thus becomes more important for the resulting material properties.^[63] Having the semiconductor and the metal nanocrystals in contact retains their characteristic properties as individual materials but enable new properties evolving due to the crystal contact. The semiconductor still absorbs light due to the excitation of electrons into the conduction band while the absorption of the metal due to localized surface plasmon resonance remains.^[30] Properties of the charge carriers are altered strongly due to the contact of the metal and the semiconductor. In example, the fluorescence and catalytic properties are influenced strongly.

1.3.1 Metal Domain Synthesis

The first nanoparticles that combined these two material classes consisted of ZnO or TiO₂ combined with gold, silver, copper or platinum.^[64,65] With the synthetic advances of the recent decades, more control over the uniformity of the semiconductor and with this the metal growth has been achieved. Through this the control of the size and location of the metal on the semiconductor is possible with high precision. Due to the high photoluminescence properties and high absorption coefficients of metal chalcogenides, the metal growth on CdSe and CdS has been studied intensively.^[66]

The synthesis of these hybrid materials is challenging due to lattice mismatches, different crystal structures, interfacial energy differences between semiconductor and metal, surface defects or surface reactivity.^[66] In general, the metal growth on a semiconductor is possible because the homogeneous nucleation has a higher energy barrier compared to heterogeneous nucleation on a seed.^[67] Typically, a homogeneous nucleation is not observed in nanocrystal synthesis without external forces like high temperature, supersaturation or an adequate reducing agent. This high energy barrier favors the heterogeneous nucleation, and thus, the synthesis of semiconductor-metal hybrid nanoparticles. However, a high control over the reaction conditions is needed to stay in the favored regime for heterogeneous nucleation.

The heterogeneous nucleation is influenced and can be controlled by different aspects. The chemical potential of a surface increases with decreasing nanoparticle size ac-

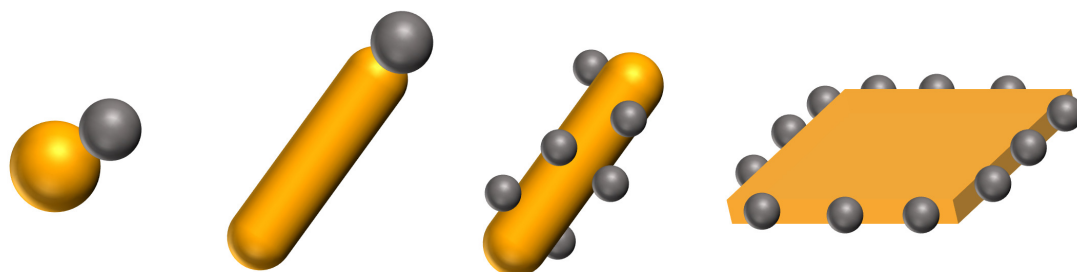


Figure 1.7: Different semiconductor metal hybrid nanoparticles with the semiconductor in orange and the metal in grey. Very different morphologies are possible with synthetic control. High surface energies have the main influence on the resulting morphology. High surface energies occur e. g. due to high curvatures or surface defects.

ording to the Gibbs-Thompsen effect.^[68] On the one hand, small nanoparticles with a high curvature would be more reactive.^[69] On the other hand, larger nanoparticles with an anisotropic shape with regional high curvatures have high chemical potential in these regions. Having a rod shaped nanoparticle as it is for CdSe/CdS nanorods, the tip region is more favored to serve for the nucleation of a metal domain.^[70] Beside the size and curvature, the facets can have a major impact. Having a facets of the semiconductor and the metal which have similar lattice constants would favor the nucleation on these facet of the semiconductor.^[71] Additionally, surface defects are surface sites with a high chemical potential. Gold growth on CdS nanorods show a preferred growth on the tips as discussed above, but also shows gold growth along the flat sites of the nanorods which can be correlated to surface defects.^[72] Ligand coverage is expected to further have an impact on the metal nucleation, but it is even more challenging to investigate and control this parameter. The combination of surface defects and ligand coverage can lead to different reaction kinetics regarding the metal growth from one nanoparticle batch to another. Figure 1.7 shows different morphologies of semiconductor-metal hybrid nanoparticles.

1.3.2 Charge Carrier Properties

CdSe/CdS semiconductor nanorods have a quasi type-II band structure.^[56] Metals such as gold or platinum have a Fermi level which is located energetically within the band gap of the CdS. As discussed above, in the CdSe/CdS semiconductor excited electrons are partially located in the CdS shell, and the hole is located in the CdSe core due to the higher valance band of the CdSe. The charge carriers recombine radiatively in the CdSe. However, the charge carriers can be trapped in mid gap states leading to non-radiative charge recombination. Typically, the metal has a continuous band of energy states and thus a band gap as in the semiconductor does not exist. Light absorption in the metal leads to the excitation of a localized surface plasmon resonance (LSPR), which is a cumulative oscillation of electrons due to the interaction of the electrons with the electric field of the light.^[73] With this oscillation the electrons are excited energetically.^[74] Additionally, inter band excitations can be observed mainly at higher energies close to the UV region which implies the absorption of additional light.^[75] Light absorption due to the LSPR leads to an absorption maximum which can be observed in absorption and extinction spectra. The location of the maximum depends on e. g. the amount of free charge carriers, refractive indexes of the material and the surrounding.^[76]

A crystal contact between the metal and the semiconductor opens up new pathways for charge carriers, mainly electrons (Figure 1.8). Excited electrons in the semiconductor can be transferred to the metal due to the Fermi level of the metal being below the conduction band of the semiconductor and the continuous energy states in the metal.^[77] The electron and hole from the semiconductor then are separated efficiently, leading to charge carrier lifetimes up to micro seconds.^[78,79] Due to the long lifetimes electrons can accumulate in a metal domain leading to a rise of the Fermi level.^[80,81] Charge recombination of electrons, which have been transferred to the metal, occurs only non-radiatively. Vice versa, excited electrons in the metal due to the LSPR are able to be transferred into the semiconductor. These electrons are so

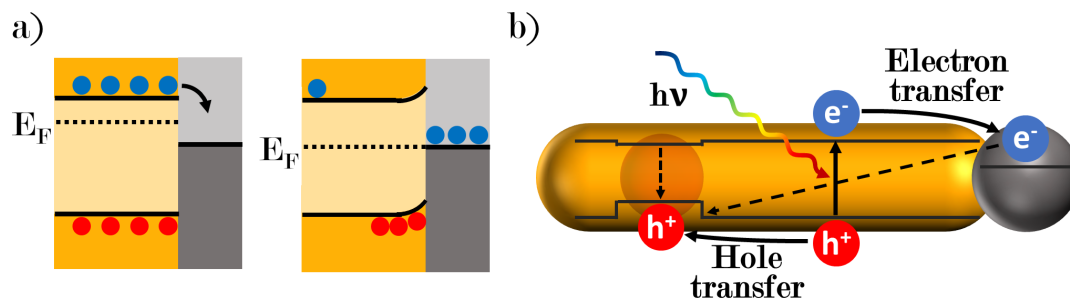


Figure 1.8: a) The formation of a Schottky barrier due to a semiconductor-metal contact. Electrons are transferred to the metal due to the differences in Fermi energy. A resulting electric field leads to band bending and barrier formation. b) The main electron and hole transfers (without charge trapping) in solid lines and the two different charge recombination pathways in dashed lines.

called hot-electrons.^[74] This transfer from the metal to the semiconductor occurs in the femto second range. The back reaction, the charge recombination, is in the pico second range and thus these charge carriers have a short lifetime. In general, both the electrons coming from the semiconductor and the hot-electrons can be used for further reactions. For both, several materials have been synthesized and the application in photocatalysis has been demonstrated.^[74,82–84]

Visualizing the band structure of semiconductor-metal hybrid nanoparticles often simplifies the contact by showing flat bands. This simplification has also been used in this work.^[85,86] However, having a semiconductor-metal contact in a sense of bulk materials, leads to a Schottky barrier at the interface. The Schottky barrier occurs due to the different work functions of the metal and the semiconductor.^[87] Electrons from the semiconductor flow to the metal since the work function of the metal is lower. With this, the Fermi level of the metal increases while the Fermi level of the semiconductor decreases. Reaching the equilibrium, a Helmholtz double layer is formed with negative charges in the metal and positive charges in the semiconductor.^[88] The resulting electric field leads to a band bending, building up a barrier near the interface (Figure 1.8). This region is called depletion region and can have a width of several hundreds of nanometers.^[89]

Since the size of the nanoparticles is much smaller than the width of a typical depletion layer, the semiconductor-metal interface cannot be described as a bulk contact.^[63] According to Smit et al., the Schottky barrier width and height of nanoscale interfaces depends on the size and shape of the contact.^[90] Different articles report a much lower Schottky barrier height (SBH) at nanoscale interfaces compared to bulk junctions, measured for example with conductive-probe atomic force microscopy.^[91–93] A smaller depletion layer and SBH can improve the charge injection from the semiconductor to the metal. Electron tunneling through the small Schottky barrier can be more probable and thermoionic transport increases with a lower SBH.^[94,95] Understanding the total characteristics of a nanosized Schottky barrier becomes even more complex when considering chemical surroundings as discussed by Tung.^[96] The discussion about a nano Schottky barrier shows the crucial role of the contact

between the semiconductor and metal for an efficient charge carrier transport. In a nanoparticle ensemble with not perfect size and shape uniformity it can be expected to observe small differences in the contacts, and thus in the SBH from one nanoparticle to the another. However, since the focus in this work was to investigate the resulting properties of a nanoparticle ensemble the interface has not been further studied.

1.4 Nanoparticle-Based Gel Structures

Gel structures in form of aerogels are self-supporting materials with low density, large specific surface area, and are famous for their low heat conductivity.^[97,98] Nanoparticle-based gel structures consist of nanoparticles and have materials specific features in the nanometer range while having a macroscopic monolithic size of micro- to centimeters. With this, these materials are the first to show quantum confined properties in a macroscopic material.^[99–101] Gels in general are known in the everyday life from applications in the kitchen, to hair styling or more medical applications like gel pads for ECG electrodes. The International Union of Pure and Applied Chemistry (IUPAC) defines a gel as „Non-fluid colloidal network or polymer network that is expanded throughout its whole volume by a fluid“.^[102] This in first case shows that a gel is not defined by the material itself rather than by the formation of a network.

First nanoparticle-based gels have been synthesized in 2004 by Brock *et al.*^[100] Starting with a nanoparticle dispersion a controlled destabilization is performed resulting in the formation of a network. Usually, a crystal contact is established during the gelation, but also ligand bridging techniques are possible to build up networks out of nanoparticles.^[103,104] In case of nanoparticle-based gels an inorganic network is formed which needs to be differentiated from classical sol-gel processed gels.^[16] In the sol-gel process, a liquid precursor undergoes a polymerization reaction with a continuous growth to a viscous sol and builds a gel afterwards.^[105] Metal oxide gels like SiO₂ and TiO₂ aerogels are well established materials synthesized by sol-gel methods.^[106,107] For the sol-gel process the resulting material has to have a precursor which is able to undergo a polymerization reaction. This restricts the list of materials being able to form gels with the sol-gel method.

1.4.1 Gel Structure Formation

Using nanocrystals as building block for the gel structure leads to nearly endless possibilities in the material choice. Nanoparticle-based gels have been synthesized from magnetic materials, metals, semiconductors, insulators, or even mixtures of these.^[108–112] Crucial for the gelation is the surface chemistry of the nanoparticles and the method to destabilize the colloidal dispersion. To date, various methods are known to have an impact on the colloidal stability.^[99,103,113–116] One method is the ligand removal by chemical oxidation of the ligands.^[99] In aqueous solutions hydrogen peroxide can oxidize for example thiol ligands on the nanoparticles surface. This leads to reduced electrostatic or steric repulsive forces and initiates the coagulation following flocculation and gelation. Controlling the concentration of the oxidizing agent

determines if a gel network or instead dense agglomerates are formed. Removing ligands from the surface is as well possible by introducing certain ions to the colloidal dispersion. Lanthanide ions like yttrium or ytterbium are known to form gels out of nanoparticles by removing ligands from the surface as well as by ligand bridging.^[103] Ligand bridging is possible if the chosen ion can coordinate to two ligands from different nanoparticles. Beside the controlled destabilization, porous gel structures can also be formed by shock freezing an aqueous colloidal dispersion.^[116] Here, nanoparticles are pressed into the grain boundaries of ice crystals. To ensure to have many small crystals and thus a porous network, shock freezing can be used. Like this a porous sheet like structure of the nanoparticles is formed. These described three methods have been used in this work, but there are more methods to trigger the gelation of a colloidal dispersion. Heating, high power illumination, or changing solvent polarity are further techniques.

After colloidal destabilization the gel is named solvogel, having a solvent (e.g. water) inside the pore system. Either the gel can be used for applications as a solvogel, or it can be dried to obtain so called aerogels. Due to the self-supporting and highly porous structure the most solvents can be used from organic to aqueous solutions. For nanoparticle dispersions a ligand exchange would be necessary to stabilize them

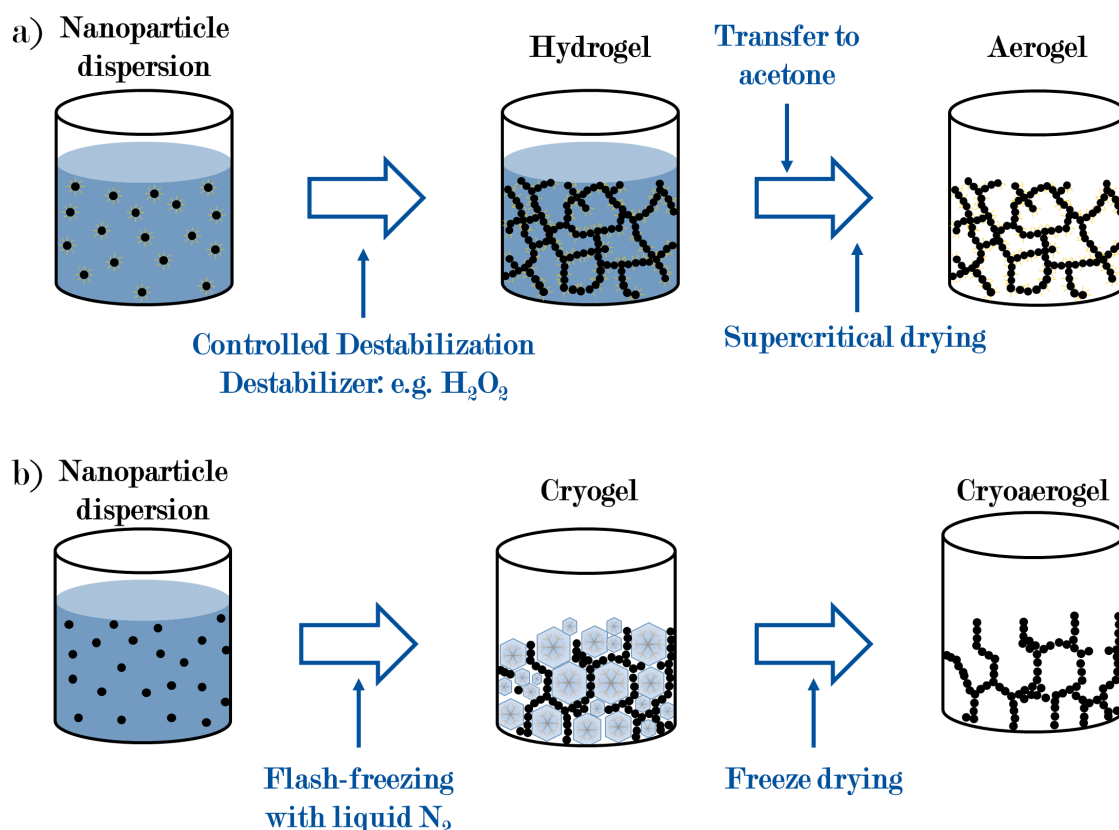


Figure 1.9: The pathway from a nanoparticle dispersion to a hydrogel and an aerogel. a) Using the approach of controlled destabilization of the colloidal solution and supercritical drying to obtain aerogels. b) Formation of cryogels and cryoaerogels starting with a colloidal solution which is gelled by flash-freezing and dried with freeze drying.

in a different solvent with different polarity (e.g. from low-polar hexane to polar aqueous solution). In contrast, for hydrogels the solvent can be exchanged through washing steps with the according solvent, making the applicability of solvogels very versatile. To dry solvogels ambient conditions can be used. However, then the gel network structure collapses partially due to the capillary forces of the evaporating water. This results in a less porous so-called xerogel. To overcome the capillary forces of colloiddally destabilized gels, supercritical drying can be used. For shock frozen gels freeze drying is suitable. For supercritical drying the solvent in the gel is first exchanged to acetone and then to liquid CO₂. Due to the supercritical point of CO₂ being at a processable pressure and temperature, a supercritical fluid in the gel can be removed without capillary forces. The solvent exchange in cryogels is not possible with washing steps due to the frozen state of the water. Therefore, freeze drying can remove the water by sublimation of ice under vacuum. Like this the cryogels can be dried without destructive capillary forces. The pathways from nanoparticle dispersions to cryoaerogels and aerogels is shown in Figure 1.9.

The great versatility of these methods to synthesize inorganic gels can be enhanced further when mixing different nanoparticles solutions before destabilization or shock freezing.^[112,117-119] For example, metal nanoparticles can be evenly distributed in a semiconductor nanoparticle-based gel. With the control over the amount of the different nanoparticles the properties of the resulting gel can be tuned with high precision. In example, for metals in a semiconductor gel the extend of fluorescence quenching and electron transfer to the metal nanoparticles can be controlled.^[120] As well, two different semiconductor nanoparticles can be mixed to get control over the resulting color of the gel.^[118] Thus, mixing and co-gelation can lead to promising properties in catalytic or optical applications. The former will also be shown and discussed in this work.

1.4.2 Structure Property Correlation

In general, assembling nanoparticles into network structures connects nanoparticles with each other. This leads to network properties which can differ those of the nanoparticle dispersion. Networks made of CdSe/CdS nanorods for example enable electron delocalization beyond one nanoparticle building block which leads to better charge carrier separation and longer charge carrier lifetimes.^[99] Noble metal based networks exhibit a conductivity through connected nanoparticles which can be used in electrocatalysis.^[121] By controlling the assembly using different gelation agents, or gelation methods, has an influence on the network properties of the same nanoparticle dispersion. Cryogelation for example, produces a different porosity and pore structure compared to the chemically destabilization.^[99,122] Cryoaerogels have a sheet like structure with pore sizes in the micro meter ranch. Destabilized aerogels instead, have a highly branched structure with smaller pores and a higher specific surface area compared to cryoaerogels. Not only the porosity of the macroscopic material but also the nanoparticle connection itself can be manipulated during the gelation process. Using an oxidative gelation agent, CdSe/CdS nanorods connect preferred tip-to-tip.^[99] However, with sulfide ions as destabilizing agent as well a more dense side-by-side arrangement can be achieved.^[113] The versatility and sensitivity of the gelation process shows the need to control the destabilization and to investigate the

influences of different gelation methods. In this work, the structure property correlation of semiconductor-metal hybrid nanoparticle-based networks has been investigated. Structural characterization has been connected to photoelectrochemical and photocatalytic characterizations.

1.5 Photocatalysis on Nanoparticle-Based Materials

A catalyst decreases the activation barrier of chemical reactions by allowing a different reaction pathway due to adsorption and desorption of reactants.^[123] With reversible ad- and desorption on the catalyst surface the catalyst is not changed during the reaction and can be recovered and used as a catalyst for other reactants. With this, a chemical reaction is accelerated and the selectivity of a reaction can also be improved.^[124] Because a catalyst only influences the kinetics of a reaction the thermodynamic requirements have to be given. If the reaction is thermodynamically not feasible a photocatalyst can be an opportunity to make these reactions possible.^[125] Here, the required energy can be provided by ultraviolet or visible light absorption. With this, a photocatalyst enables reactions which are not possible in the dark. A semiconductor as photocatalyst can absorb light by excitation of an electron from the valence band (VB) into the conduction band (CB) and leaving a hole in the VB. These charge carriers then can be used for further reactions. Nevertheless, the absorbed energy needs to fulfill the thermodynamic requirements of the photocatalytic reaction to enable the reaction. This implies a band gap of the semiconductor which is large enough to provide the energy needed for the reaction. Additionally, the band position of the VB and CB on the energy scale have to be suitable for the desired reaction so that even with a band gap which is large enough the reaction not necessarily can occur.^[126]

In case of water splitting a band gap of at least 1.3 eV is required to make the reaction thermodynamically possible. For full water splitting two half reactions occur. The oxygen evolution reaction (OER) and the hydrogen evolution reaction (HER).^[126] The focus mainly is on the HER to use hydrogen as an energy carrier. To circumvent the difficulties to build a photocatalyst which can catalyze both the OER and HER, a sacrificial agent can be used to substitute the OER to produce hydrogen while fulfilling a complete redox reaction.^[127,128] With a sacrificial agent, a photocatalyst which has not the requirements for the OER can be used for the HER. In case of CdS, which is known to be a good photocatalyst, the oxygen evolution reaction is not possible due to the energetic position of the valance band.^[129] However, for the hydrogen evolution reaction the band gap and band position of the conduction band of CdS are indeed suitable to be a photocatalyst for this reaction.^[130] Nevertheless, full water splitting would be of interest because hydrogen can be produced just with the catalyst, light and water as resources. Nonetheless, having a catalyst which is efficient for both half reactions is challenging so that focusing on one half reaction and adding a sacrificial agent can be more efficient than full water splitting. A renewable or earth abundant sacrificial agent could be an opportunity for the use of water as energy resource for photocatalytic HER. Polyethylene therephthalate (PET) or cellulose which have been investigated as sacrificial agents show potential.^[131–133] Here, different sacrificial agents were investigated but not with the focus on sustainability.

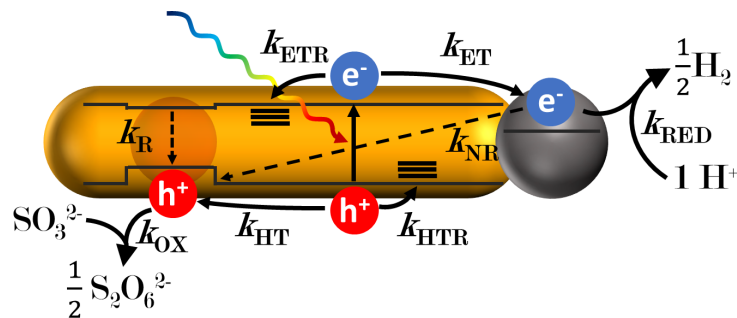


Figure 1.10: Illustration of the different competing processes in CdSe/CdS nanorods after photoexcitation. For the photocatalytic reaction charge trapping needs to be suppressed to guarantee an efficient charge carrier separation and an electron transfer to the co-catalyst.

For the HER the excited electron needs to be used for the reduction of protons to form hydrogen. Using the electron for this reaction is a multistep process with concurring side reactions (Figure 1.10). An ideal electron transfer consists of light absorption and electron excitation, electron transfer to the catalyst surface, proton adsorption on the catalyst surface, electron transfer to the proton and hydrogen desorption. As concurring side reactions the excited electron can recombine radiatively or non-radiatively in the semiconductor, or be trapped in mid band gap states. To favor the electron transfer to the reactant an efficient electron-hole separation and long charge carrier lifetimes are desirable. Introducing a co-catalyst can improve the charge carrier separation by an electron transfer to the co-catalyst. Furthermore, a co-catalyst can have a more catalytically active surface to further improve the catalytic reaction.^[83,134] As a co-catalyst e. g. a noble metal or a molecular co-catalyst can be used.^[78,135]

Platinum is known for the high catalytic activity in hydrogen related reactions. The high catalytic activity can be explained with the hydrogen binding energy being close to zero.^[136] Thus, protons and hydrogen can adsorb and desorb easily before and after the reaction. However, the catalytic mechanism is more complex and studies, focusing on electrocatalytic hydrogen production, show that not purely the low hydrogen binding energy is crucial, but also the type of hydrogen bond on the platinum surface.^[136] Furthermore, the catalytic mechanism varies depending on the pH. In acidic conditions H_3O^+ ions are the primary proton source while in alkaline conditions H_2O acts as proton donor. Due to the more difficult dissociation of H_2O compared to H_3O^+ the HER kinetics are higher in acidic conditions.^[137] This is described for electrocatalysis, but the dissociation and binding mechanism might be transferable to the photocatalytic HER. Despite the fact of better kinetics on the platinum surface in acidic conditions, alkaline conditions had to be applied for the photocatalytic reaction due to the use of OH^- as sacrificial agent as discussed in chapter 3.

Nanoparticles are designated for catalytic applications due to their high surface to volume ratio and the high control over the materials synthesis. Various materials were investigated for various reactions which can be catalyzed.^[78,138,139] Catalytic reactions have great potential to contribute to a transition towards a sustainable in-

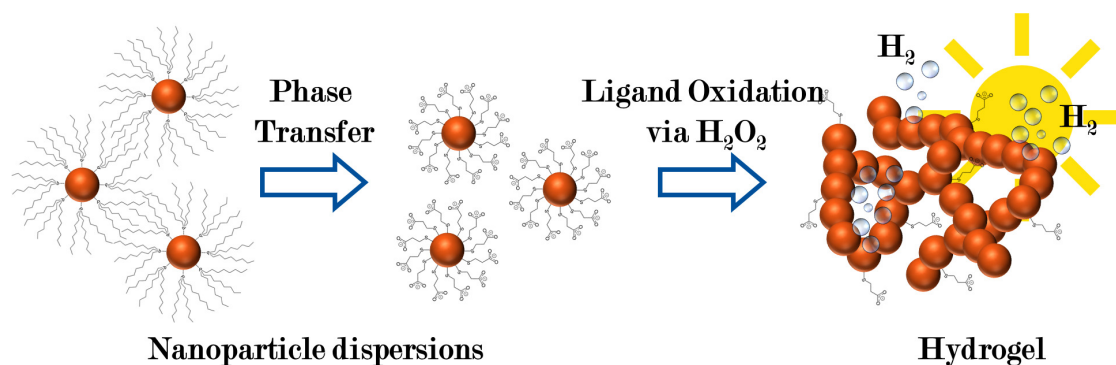


Figure 1.11: Way from synthesized nanoparticles in organic media to hydrogels which can be used for photocatalytic reactions. After a phase transfer with a thiol ligand the gelation is initiated with H_2O_2 . Ligand oxidation triggers the assembly and with solar irradiation a photocatalytic reaction can take place.

dustry, which gives the motivation to work in this research area. The applicability of nanoparticles in catalysis depends, among others, on the accessibility of the surface. The above introduced nanoparticle-based gel structures can retain a high surface area of the nanoparticles, while improving the applicability due to their self-supporting network structure. This approach has already been investigated to enable the use of nanoparticles efficiently for catalysis. Many investigations focused on electrocatalysis^[10,140,141] and some on photocatalysis^[142–144] using these gel structures. In studies of a photocatalytic gas phase reaction, the material of interest was titanium dioxide and titanium dioxide with noble metal nanoparticles.^[110,144] Beside titanium dioxide many more nanoparticle-based gels of various materials can be synthesized, but were not in the focus of the research yet. This work focused on other semiconducting materials than titanium dioxide for the use of hydrogels in photocatalysis namely cadmium chalcogenides. Figure 1.11 shows schematically how to use nanoparticle based hydrogels for photocatalysis when starting from nanoparticle dispersions.

1.6 Photoelectrochemistry of Nanoparticle-Based Systems

Electrochemical characterization of semiconducting materials can be a powerful method to get information for example about charge carrier mobilities in the material or about possible redox reactions on the semiconductor surface. Photoelectrochemistry can give further insights about the materials properties due to the investigation of the excited charge carriers. Especially, for semiconducting materials the amount of free charge carriers can be increased by light absorption. A photoelectrochemical cell consist of a working electrode, a reference electrode and a counter electrode. The working electrode (with the investigated material) either has to be placed in a transparent cell to allow illumination of the electrode or the working electrode itself can be a transparent conductive material so light can shine through the electrode. In this work a ITO coated glass slide has be used as working electrode, a Ag/AgCl electrode as reference electrode and a platinum wire as counter electrode.

In an electrochemical cell a semiconductor is in contact with an electrolyte which has a redox potential. Due to the contact, an electrochemical equilibrium is formed. The Fermi level of a n-type semiconductor is higher than the redox potential of the electrolyte. This leads to an electron transfer from the semiconductor to the electrolyte to balance the different potentials. Transferred electrons leave a positively charged hole in the semiconductor leading to a positive space charge layer near the surface of the semiconductor. Negatively charged electrolyte molecules accumulate on the surface of the semiconductor due to the positively charged layer.^[145] The resulting electric field leads to band bending and the formation of a barrier near the semiconductors surface. The arrangement of ions along the semiconductor-electrolyte interface is described by the Helmholtz double layer.^[88] This interface is similar to the above described semiconductor-metal interface. Since the theoretical explanation is mainly for bulk materials the extension of the double layer and the height of the resulting barrier at the interface in case of nanomaterials remains unclear. However, a barrier for electrons to be transferred into the solution has to be considered.

The two most important photoelectrochemical characterization methods for this work were the linear sweep voltammetry (LSV) and the intensity modulated photocurrent spectroscopy (IMPS). For both techniques the measurement cell was used as described above. In LSV measurements a bias potential is applied with gradual increase of the potential (usually from -0.6 V to 0.3 V). Additionally, alternating light pulses with 12.5 s of illumination and darkness periods illuminated the working electrode to investigate the differences between the dark- and the photocurrent. On the one hand, the photocurrent direction is of interest and on the other hand, the transitions from dark- to photocurrent and vice versa give useful information. The photocurrent can be positive or negative. Thereby, a positive photocurrent occurs when electrons from the semiconductor are transferred to the electrode and remaining holes are filled with electrons coming from the electrolyte redox system. Negative photocurrent results from electrons which are transferred into the electrolyte solution and holes are filled with electrons coming from the electrode (Figure 1.12). From the transition of dark- to photocurrent, information about the kinetics of collective electron movements can be gained.^[146,147] When one process namely the electron transfer or the hole filling process is faster than the other, the system has to reach an equilibrium. In a measurement, this can be seen by transients at the beginning of the illumination or after turning of the illumination. Either a higher positive photocurrent decreases until the equilibrium or vice versa with the negative photocurrent.

IMPS is a more complex measurement technique. The photocurrent of the material is measured frequency dependent. A different frequency dependent measurement which finds a broader application is the impedance spectroscopy (IS).^[148] In IS, a frequency modulated voltage is applied, whereas, in IMPS a frequency modulated illumination is applied.^[149] For illumination different light sources can be applied e. g. a LED, a laser or a xenon arc lamp. The easiest light source to control the frequency might be the LED, where the illumination of the LED can be controlled with a modulated current. Through illuminating the material in the electrochemical cell with a certain frequency, a modulated photocurrent response is obtained. This photocurrent response can be phase shifted and has a different amplitude compared to the incoming light

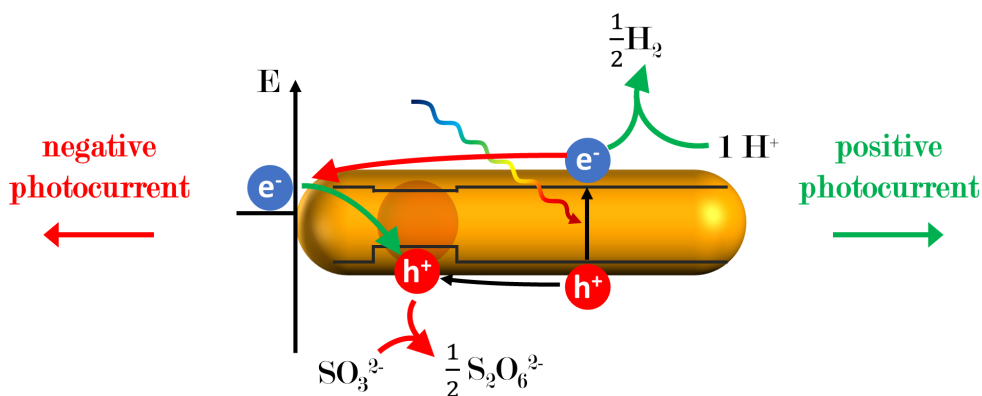


Figure 1.12: Charge carrier transfers leading to positive and negative photocurrent. Black arrows occurs for positive and negative photocurrent. Red arrows indicate electron and hole movements with resulting negative photocurrent. Green arrows indicate electron and hole transfers resulting in positive photocurrent.

(Figure 1.13). Varying, the modulated light frequency gives different photocurrent responses which than can be interpreted regarding the materials properties. However, to gain the data to interpret, the complexity of the resulting signals has to be handled. Briefly, a Lock-in amplifier extracts the phase shift and amplitude of the photocurrent response which then can be plotted in a so-called Nyquist plot.

Using IMPS for the characterization of semiconducting materials can give information about kinetics of collective charge carrier properties.^[150] A time component is introduced into the measurement due to the altered frequency of the modulated illumination. It needs to be said, that the time scale is way too long to investigate single charge carrier properties as for example the charge carrier live time of a single nanoparticle which is in the time scales from nanoseconds to microseconds. In contrast, the IMPS measurement investigates processes in the range of microseconds to seconds. Nevertheless, the results can be related to e. g. charge carrier recombination or charge trapping in a collective way and thus are a valuable method to gain insights

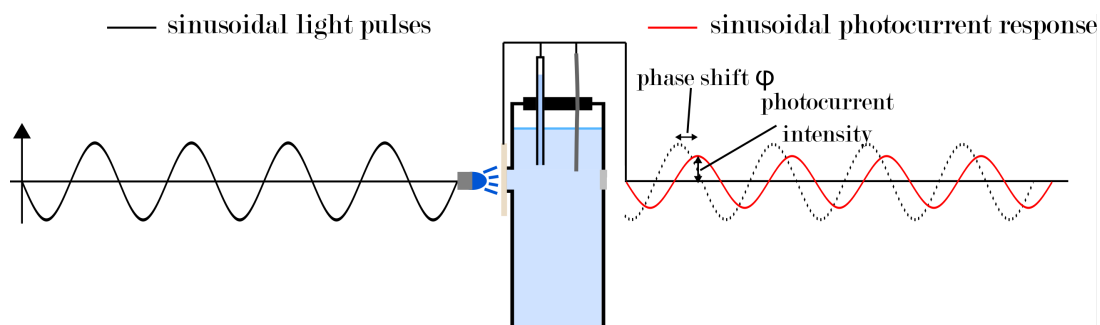


Figure 1.13: Schematic representation of the fundamentals of the intensity modulated photocurrent spectroscopy (IMPS). A sinusoidal light puls excites the working electrode with the sample. The electrochemical cell gives a photocurrent response which follows the light sinusoidally but with a certian phse shift and intensity. With the phase shift and the intensity the data can be plotted in a Nyquist plot.

about e.g. charge carrier transport mechanism in the materials. In semiconductor nanoparticle based gel structures the electron can travel through the network. This leads to different photocurrent contributions from electrons which are close to the electrode and electrons which first have to travel through the network to reach the electrode. In the IMPS spectra this gives two distinct semicircles. For nanoparticle mono and multilayers only one semicircle occurs since no electron transport takes place. This shows that IMPS is a suitable technique to investigate nanoparticle-based gel structures.

Bibliography

- [1] S. Malik, K. Muhammad, Y. Waheed, *Nanotechnology: A Revolution in Modern Industry*, *Molecules* **2023**, *28*, year.
- [2] M. J. Hanus, A. T. Harris, *Nanotechnology innovations for the construction industry*, *Progress in Materials Science* **2013**, *58*, 1056–1102.
- [3] N. Durán, P. D. Marcato, *Nanobiotechnology perspectives. Role of nanotechnology in the food industry: A review*, *International Journal of Food Science and Technology* **2013**, *48*, 1127–1134.
- [4] L. Li, Y. Yu, G. J. Ye, Q. Ge, X. Ou, H. Wu, D. Feng, X. H. Chen, Y. Zhang, *Black phosphorus field-effect transistors*, *Nature Nanotechnology* **2014**, *9*, 372–377.
- [5] A. Bautista-Salvador, G. Zarantonello, H. Hahn, A. Preciado-Grijalva, J. Morgner, M. Wahnschaffe, C. Ospelkaus, *Multilayer ion trap technology for scalable quantum computing and quantum simulation*, *New Journal of Physics* **2019**, *21*, year.
- [6] L. Protesescu, S. Yakunin, M. I. Bodnarchuk, F. Krieg, R. Caputo, C. H. Hendon, R. X. Yang, A. Walsh, M. V. Kovalenko, *Nanocrystals of Cesium Lead Halide Perovskites (CsPbX₃, X = Cl, Br, and I): Novel Optoelectronic Materials Showing Bright Emission with Wide Color Gamut*, *Nano Letters* **2015**, *15*, 3692–3696.
- [7] O. Ivanova, C. Williams, T. Campbell, *Additive manufacturing (AM) and nanotechnology: Promises and challenges*, *Rapid Prototyping Journal* **2013**, *19*, 353–364.
- [8] L. E. Brus, *A simple model for the ionization potential, electron affinity, and aqueous redox potentials of small semiconductor crystallites*, *The Journal of Chemical Physics* **1983**, *79*, 5566.
- [9] I. V. Zibareva, L. Y. Ilina, A. A. Vedyagin, *Catalysis by nanoparticles: the main features and trends*, *Reaction Kinetics Mechanisms and Catalysis* **2019**, *127*, 19–24.
- [10] R. Zhang, Y. Zhao, *Preparation and electrocatalysis application of pure metallic aerogel: A review*, *Catalysts* **2020**, *10*, 1–20.
- [11] K. Li, B. Peng, T. Peng, *Recent Advances in Heterogeneous Photocatalytic CO₂ Conversion to Solar Fuels*, *ACS Catalysis* **2016**, *6*, 7485–7527.

- [12] M. Nasr, C. Eid, R. Habchi, P. Miele, M. Bechelany, *Recent Progress on Titanium Dioxide Nanomaterials for Photocatalytic Applications*, *ChemSusChem* **2018**, *11*, 3023–3047.
- [13] X. Li, J. Yu, J. Low, Y. Fang, J. Xiao, X. Chen, *Engineering heterogeneous semiconductors for solar water splitting*, *Journal of Materials Chemistry A* **2015**, *3*, 2485–2534.
- [14] S. Ninomiya, S. Adachi, *Optical properties of wurtzite CdS*, *Journal of Applied Physics* **1995**, *78*, 1183–1190.
- [15] A. Heuer-Jungemann, N. Feliu, I. Bakaimi, M. Hamaly, A. Alkilany, I. Chakraborty, A. Masood, M. F. Casula, A. Kostopoulou, E. Oh, K. Susumu, M. H. Stewart, I. L. Medintz, E. Stratakis, W. J. Parak, A. G. Kanaras, *The role of ligands in the chemical synthesis and applications of inorganic nanoparticles*, *Chemical Reviews* **2019**, *119*, 4819–4880.
- [16] C. Ziegler, A. Wolf, W. Liu, A. K. Herrmann, N. Gaponik, A. Eychmüller, *Modern Inorganic Aerogels* **2017**, *56*, 13200–13221.
- [17] P. Mushonga, M. O. Onani, A. M. Madiehe, M. Meyer, *Indium phosphide-based semiconductor nanocrystals and their applications*, *Journal of Nanomaterials* **2012**, *2012*, year.
- [18] A. P. Alivisatos, *Perspectives on the physical chemistry of semiconductor nanocrystals*, *Journal of Physical Chemistry* **1996**, *100*, 13226–13239.
- [19] V. K. LaMer, R. H. Dinegar, *Theory, Production and Mechanism of Formation of Monodispersed Hydrosols*, *J. Am. Chem. Soc* **1950**, *72*, year.
- [20] H. Weller, *Kolloidale Halbleiter-Q-Teilchen : Chemie im Übergangsbereich zwischen Festkörper und Molekül*, *Angewandte Chemie* **1993**, 43–55.
- [21] C. De Mello Donegá, P. Liljeroth, D. Vanmaekelbergh, *Physicochemical evaluation of the hot-injection method, a synthesis route for monodisperse nanocrystals*, *Small* **2005**, *1*, 1152–1162.
- [22] C. de Mello Donegá, *Synthesis and properties of colloidal heteronanocrystals*, *Chemical Society Reviews* **2011**, *40*, 1512–1546.
- [23] C. B. Murray, D. J. Norris, M. G. Bawendi, *Synthesis and Characterization of Nearly Monodisperse CdE (E = S, Se, Te) Semiconductor Nanocrystallites*, *Journal of the American Chemical Society* **1993**, *115*, 8706–8715.
- [24] R. Rossetti, L. Brus, *Electron-hole recombination emission as a probe of surface chemistry in aqueous CdS colloids*, *Journal of Physical Chemistry* **1982**, *86*, 4470–4472.
- [25] E. A.A. Onushchenko, *Quantum size effect in three-dimensional microscopic semiconductor crystals*, *Jetp Letters* **1981**, *34*, 345–349.
- [26] Nobel Committee of Chemistry, *Quantum Dots - Seeds of Nanoscience*, **2023**.

-
- [27] D. V. Talapin, E. V. Shevchenko, *Introduction: Nanoparticle chemistry*, Chemical Reviews **2016**, *116*, 10343–10345.
- [28] I. Lisiecki, *Size, shape, and structural control of metallic nanocrystals*, Journal of Physical Chemistry B **2005**, *109*, 12231–12244.
- [29] S. Kumar, T. Nann, *Shape control of II-VI semiconductor nanomaterials*, Small **2006**, *2*, 316–329.
- [30] U. Banin, Y. Ben-Shahar, K. Vinokurov, *Hybrid semiconductor-metal nanoparticles: From architecture to function* **2014**, *26*, 97–110.
- [31] Y. Hu, S. Mignani, J. P. Majoral, M. Shen, X. Shi, *Construction of iron oxide nanoparticle-based hybrid platforms for tumor imaging and therapy*, Chemical Society Reviews **2018**, *47*, 1874–1900.
- [32] B. Mahler, B. Nadal, C. Bouet, G. Patriarche, B. Dubertret, *Core/shell colloidal semiconductor nanoplatelets*, Journal of the American Chemical Society **2012**, *134*, 18591–18598.
- [33] P. E. Lippens, M. Lannoo, *Calculation of the band gap for small CdS and ZnS crystallites*, Physical Review B **1989**, *39*, 10935.
- [34] L. E. Brus, *Electron-electron and electron-hole interactions in small semiconductor crystallites: The size dependence of the lowest excited electronic state*, The Journal of Chemical Physics **1984**, *80*, 4403.
- [35] Y. Kayanuma, *Wannier exciton in microcrystals*, Solid State Communications **1986**, *59*, 405–408.
- [36] L. Brus, *Electronic wave functions in semiconductor clusters: Experiment and theory*, Journal of Physical Chemistry **1986**, *90*, 2555–2560.
- [37] T. S. Kondratenko, M. S. Smirnov, O. V. Ovchinnikov, E. V. Shabunyaklyachkovskaya, A. S. Matsukovich, A. I. Zvyagin, Y. A. Vinokur, *Size-Dependent Optical Properties of Colloidal CdS Quantum Dots Passivated by Thioglycolic Acid*, Semiconductors **2018**, *52*, 1137–1144.
- [38] A. L. Rogach, *Nanocrystalline CdTe and CdTe(S) particles: wet chemical preparation, size-dependent optical properties and perspectives of optoelectronic applications*, Materials Science and Engineering: B **2000**, *69-70*, 435–440.
- [39] M. Kuno, J. K. Lee, B. O. Dabbousi, F. V. Mikulec, M. G. Bawendi, *The band edge luminescence of surface modified CdSe nanocrystallites: Probing the luminescing state*, The Journal of Chemical Physics **1998**, *106*, 9869.
- [40] J. Franck, E. G. Dymond, *Elementary processes of photochemical reactions*, Transactions of the Faraday Society **1926**, *21*, 536–542.
- [41] E. Condon, *A Theory of Intensity Distribution in Band Systems*, Physical Review **1926**, *28*, 1182.
-

- [42] Z. Yu, J. Li, D. B. O'Connor, L. W. Wang, P. F. Barbara, *Large resonant Stokes shift in CdS nanocrystals*, Journal of Physical Chemistry B **2003**, *107*, 5670–5674.
- [43] A. L. Efros, *Luminescence polarization of CdSe microcrystals*, Physical Review B **1992**, *46*, 7448–7458.
- [44] D. V. Talapin, R. Koeppe, S. Götzinger, A. Kornowski, J. M. Lupton, A. L. Rogach, O. Benson, J. Feldmann, H. Weller, *Highly Emissive Colloidal CdSe/CdS Heterostructures of Mixed Dimensionality*, Nano Letters **2003**, *3*, 1677–1681.
- [45] S. Ithurria, B. Dubertret, *Quasi 2D colloidal CdSe platelets with thicknesses controlled at the atomic level*, Journal of the American Chemical Society **2008**, *130*, 16504–16505.
- [46] S. Ithurria, G. Bousquet, B. Dubertret, *Continuous transition from 3D to 1D confinement observed during the formation of CdSe nanoplatelets*, Journal of the American Chemical Society **2011**, *133*, 3070–3077.
- [47] A. Riedinger, F. D. Ott, A. Mule, S. Mazzotti, P. N. Knüsel, S. J. Kress, F. Prins, S. C. Erwin, D. J. Norris, *An intrinsic growth instability in isotropic materials leads to quasi-two-dimensional nanoplatelets*, Nature Materials 2017 *16*:7 **2017**, *16*, 743–748.
- [48] C. R. Pidgeon, R. N. Brown, *Interband Magneto-Absorption and Faraday Rotation in InSb*, Physical Review **1966**, *146*, 575.
- [49] M. Lorenzon, S. Christodoulou, G. Vaccaro, J. Pedrini, F. Meinardi, I. Moreels, S. Brovelli, *Reversed oxygen sensing using colloidal quantum wells towards highly emissive photoresponsive varnishes*, Nature Communications 2015 *6*:1 **2015**, *6*, 1–9.
- [50] Z. Chen, B. Nadal, B. Mahler, H. Aubin, B. Dubertret, Z. Chen, B. Nadal, B. Mahler, H. Aubin, B. Dubertret, *Quasi-2D Colloidal Semiconductor Nanoplatelets for Narrow Electroluminescence*, Advanced Functional Materials **2014**, *24*, 295–302.
- [51] D. Dede, N. Taghipour, U. Quliyeva, M. Sak, Y. Kelestemur, K. Gungor, H. V. Demir, *Highly Stable Multicrown Heterostructures of Type-II Nanoplatelets for Ultralow Threshold Optical Gain*, Chemistry of Materials **2019**, *31*, 1818–1826.
- [52] F. Fan, P. Kanjanaboos, M. Saravanapavanantham, E. Beauregard, G. Ingram, E. Yassitepe, M. M. Adachi, O. Voznyy, A. K. Johnston, G. Walters, G. H. Kim, Z. H. Lu, E. H. Sargent, *Colloidal CdSe_{1-x}S_x Nanoplatelets with Narrow and Continuously-Tunable Electroluminescence*, Nano Letters **2015**, *15*, 4611–4615.
- [53] L. Carbone, C. Nobile, M. De Giorgi, F. D. Sala, G. Morello, P. Pompa, M. Hytch, E. Snoeck, A. Fiore, I. R. Franchini, M. Nadasan, A. F. Silvestre, L. Chiodo, S. Kudera, R. Cingolani, R. Krahne, L. Manna, *Synthesis and Micrometer-Scale Assembly of Colloidal CdSe/CdS Nanorods Prepared by a Seeded Growth Approach*, Nano Letters **2007**, *7*, 2942–2950.

-
- [54] A. J. Almeida, A. Sahu, A. Riedinger, D. J. Norris, M. S. Brandt, M. Stutzmann, R. N. Pereira, *Charge Trapping Defects in CdSe Nanocrystal Quantum Dots*, Journal of Physical Chemistry C **2016**, *120*, 13763–13770.
- [55] G. Rainò, T. Stöferle, I. Moreels, R. Gomes, J. S. Kamal, Z. Hens, R. F. Mahrt, *Probing the Wave Function Delocalization in CdSe/CdS Dot-in-Rod Nanocrystals by Time- and Temperature-Resolved Spectroscopy*, ACS Nano **2011**, *5*, 4031–4036.
- [56] H. Eshet, M. Grünwald, E. Rabani, *The Electronic Structure of CdSe/CdS Core/Shell Seeded Nanorods: Type-I or Quasi-Type-II?*, Nano Letters **2013**, *13*, 5880–5885.
- [57] D. Dorfs, T. Franzi, R. Osovsky, M. Brumer, E. Lifshitz, T. A. Klar, A. Eychmüller, *Type-I and type-II nanoscale heterostructures based on CdTe nanocrystals: A comparative study*, Small **2008**, *4*, 1148–1152.
- [58] F. Qiu, Z. Han, J. J. Peterson, M. Y. Odoi, K. L. Sowers, T. D. Krauss, *Photocatalytic Hydrogen Generation by CdSe/CdS Nanoparticles*, Nano Letters **2016**, *16*, 5347–5352.
- [59] M. Micheel, B. Liu, M. Wächtler, *Influence of Surface Ligands on Charge-Carrier Trapping and Relaxation in Water-Soluble CdSe@CdS Nanorods*, Catalysts 2020 Vol. 10 Page 1143 **2020**, *10*, 1143.
- [60] T. Kodanek, H. M. Banbela, S. Naskar, P. Adel, N. C. Bigall, D. Dorfs, *Phase transfer of 1- and 2-dimensional Cd-based nanocrystals*, Nanoscale **2015**, *7*, 19300–19309.
- [61] R. M. M. Hasan, X. Luo, *Promising Lithography Techniques for Next-Generation Logic Devices*, Nanomanufacturing and Metrology **2018**, *1*, 67–81.
- [62] X. Cheng, L. J. Guo, *A combined-nanoimprint-and-photolithography patterning technique*, Microelectronic Engineering **2004**, *71*, 277–282.
- [63] L. Amirav, M. Wächtler, *Nano Schottky?*, Nano Letters **2022**, *22*, 9783–9785.
- [64] A. Wood, M. Giersig, P. Mulvaney, *Fermi level equilibration in quantum dot-metal nanojunctions*, Journal of Physical Chemistry B **2001**, *105*, 8810–8815.
- [65] C. Wang, C. Liu, T. Shen, *Investigation on composite Au /TiO₂ nanoparticles (I)*, Chinese Science Bulletin **1998**, *43*, 210–213.
- [66] R. Costi, A. E. Saunders, U. Banin, *Colloidal hybrid nanostructures: A new type of functional materials*, Angewandte Chemie - International Edition **2010**, *49*, 4878–4897.
- [67] E. Ruckenstein, G. O. Berim, G. Narsimhan, *A novel approach to the theory of homogeneous and heterogeneous nucleation*, Advances in Colloid and Interface Science **2015**, *215*, 13–27.
- [68] N. Wu, X. Ji, R. An, C. Liu, X. Lu, *Generalized Gibbs free energy of confined nanoparticles*, AIChE Journal **2017**, *63*, 4595–4603.
-

- [69] B. O. Dabbousi, J. Rodriguez-Viejo, F. V. Mikulec, J. R. Heine, H. Mattoussi, R. Ober, K. F. Jensen, M. G. Bawendi, *(CdSe)ZnS core-shell quantum dots: Synthesis and characterization of a size series of highly luminescent nanocrystallites*, Journal of Physical Chemistry B **1997**, *101*, 9463–9475.
- [70] T. Mokari, E. Rothenberg, I. Popov, R. Costi, *onto Semiconductor Quantum Rods and Tetrapods*, Science **2004**, *304*, 1787–1790.
- [71] C. O’Sullivan, S. Ahmed, R. Gunning, C. Barrett, H. Geaney, A. Sanyal, A. Singh, K. Ryan, *Facet Specific Gold Tip Growth on Semiconductor Nanorod Assemblies*, ECS Meeting Abstracts **2009**, *MA2009-02*, 2322–2322.
- [72] G. Menagen, J. E. Macdonald, Y. Shemesh, I. Popov, U. Banin, *Au Growth on Semiconductor Nanorods: Photoinduced versus Thermal Growth Mechanisms*, Journal of the American Chemical Society **2009**, *131*, 17406–17411.
- [73] G. Baffou, R. Quidant, *Nanoplasmonics for chemistry*, Chemical Society Reviews **2014**, *43*, 3898–3907.
- [74] W. H. Lee, C. W. Lee, G. D. Cha, B. H. Lee, J. H. Jeong, H. Park, J. Heo, M. S. Bootharaju, S. H. Sunwoo, J. H. Kim, K. H. Ahn, D. H. Kim, T. Hyeon, *Floatable photocatalytic hydrogel nanocomposites for large-scale solar hydrogen production*, Nature Nanotechnology **2023**, *18*, 754–762.
- [75] P. Lyu, R. Espinoza, S. C. Nguyen, *Photocatalysis of Metallic Nanoparticles: Interband vs Intraband Induced Mechanisms*, Journal of Physical Chemistry C **2023**, *127*, 15685–15698.
- [76] G. Mie, *Beiträge zur Optik trüber Medien, speziell kolloidaler Metallösungen*, Annalen der Physik **1908**, *330*, 377–445.
- [77] F. V. Camargo, Y. Ben-Shahar, T. Nagahara, Y. E. Panfil, M. Russo, U. Banin, G. Cerullo, *Visualizing Ultrafast Electron Transfer Processes in Semiconductor-Metal Hybrid Nanoparticles: Toward Excitonic-Plasmonic Light Harvesting*, Nano Letters **2021**, *21*, 1461–1468.
- [78] M. Wächtler, P. Kalisman, L. Amirav, *Charge-Transfer Dynamics in Nanorod Photocatalysts with Bimetallic Metal Tips*, Journal of Physical Chemistry C **2016**, *120*, 24491–24497.
- [79] E. Khon, A. Mereshchenko, A. N. Tarnovsky, K. Acharya, A. Klinkova, N. N. Hewa-Kasakarage, I. Nemitz, M. Zamkov, *Suppression of the plasmon resonance in Au/CdS colloidal nanocomposites*, Nano Letters **2011**, *11*, 1792–1799.
- [80] R. C. Jeff, M. Yun, B. Ramalingam, B. Lee, V. Misra, G. Triplett, S. Ganapathyay, *Charge storage characteristics of ultra-small Pt nanoparticle embedded GaAs based non-volatile memory*, Applied Physics Letters **2011**, *99*, 2012–2015.
- [81] P. D. Cozzoli, M. L. Curri, A. Agostiano, *Efficient charge storage in photoexcited TiO₂ nanorod-noble metal nanoparticle composite systems*, Chemical Communications **2005**, 3186–3188.

-
- [82] J. J. Baumberg, *Hot electron science in plasmonics and catalysis: What we argue about*, Faraday Discussions **2019**, *214*, 501–511.
- [83] P. Kalisman, L. Houben, E. Aronovitch, Y. Kauffmann, M. Bar-Sadan, L. Amirav, *The golden gate to photocatalytic hydrogen production*, Journal of Materials Chemistry A **2015**, *3*, 19679–19682.
- [84] Y. Nakibli, L. Amirav, *Selective Growth of Ni Tips on Nanorod Photocatalysts*, Chemistry of Materials **2016**, *28*, 4524–4527.
- [85] J. Schlenkrich, D. Zámbo, A. Schlosser, P. Rusch, N. C. Bigall, J. Schlenkrich, D. Zámbo, A. Schlosser, P. Rusch, N. C. Bigall, *Revealing the Effect of Nanoscopic Design on the Charge Carrier Separation Processes in Semiconductor-Metal Nanoparticle Gel Networks*, Advanced Optical Materials **2022**, *10*, 2101712.
- [86] A. Schlosser, J. Schlenkrich, D. Zámbo, M. Rosebrock, R. T. Graf, N. C. Bigall, *Photoelectrochemical investigation of grown and mixed semiconductor-metal hybrid nanomaterials in Cryoaerogels*, under review **2021**.
- [87] E. H. Rhoderick, *The physics of Schottky barriers*, Journal of Physics D: Applied Physics **1970**, *3*, 1153–1167.
- [88] J. F. McClendon, *On the thickness of the helmholtz double layer*, Science **1927**, *66*, 200.
- [89] A. S. Grove, B. E. Deal, E. H. Snow, C. T. Sah, *Investigation of thermally oxidised silicon surfaces using metal-oxide-semiconductor structures*, Solid State Electronics **1965**, *8*, 145–163.
- [90] G. D. Smit, S. Rogge, T. M. Klapwijk, *Scaling of nano-Schottky-diodes*, Applied Physics Letters **2002**, *81*, 3852–3854.
- [91] F. Léonard, A. A. Talin, B. S. Swartzentruber, S. T. Picraux, *Diameter-dependent electronic transport properties of Au-Catalyst/Ge- nanowire Schottky diodes*, Physical Review Letters **2009**, *102*, 1–4.
- [92] M. T. Sheldon, P. E. Trudeau, T. Mokari, L. W. Wang, A. Paul Alivisatos, *Enhanced semiconductor nanocrystal conductance via solution grown contacts*, Nano Letters **2009**, *9*, 3676–3682.
- [93] F. Ruffino, M. G. Grimaldi, F. Giannazzo, F. Roccaforte, V. Raineri, *Size-dependent Schottky Barrier Height in self-assembled gold nanoparticles*, Applied Physics Letters **2006**, *89*, year.
- [94] F. Léonard, J. Tersoff, *Role of fermi-level pinning in nanotube schottky diodes*, Physical Review Letters **2000**, *84*, 4693–4696.
- [95] J. Guo, J. Wang, E. Polizzi, S. Datta, M. Lundstrom, *Electrostatics of nanowire transistors*, Proceedings of the IEEE Conference on Nanotechnology **2003**, *1*, 248–251.
-

- [96] R. T. Tung, *The physics and chemistry of the Schottky barrier height*, Applied Physics Reviews 1 **2014**, 011304, year.
- [97] S. S. Kistler, *The Relation between Heat Conductivity and Structure in Silica Aerogel*, J. Phys. Chem. **2002**, 39, 79–86.
- [98] L. L. Hench, J. O. N. K. West, *The Sol-Gel Process*, Chem. Rev. **1990**, 90, 33–72.
- [99] S. Sánchez-Paradinas, D. Dorfs, S. Friebe, A. Freytag, A. Wolf, N. C. Bigall, *Aerogels from CdSe/CdS Nanorods with Ultra-long Exciton Lifetimes and High Fluorescence Quantum Yields*, Advanced Materials **2015**, 27, 6152–6156.
- [100] J. L. Mohanan, S. L. Brock, *A new addition to the aerogel community: unsupported CdS aerogels with tunable optical properties*, Journal of Non-Crystalline Solids **2004**, 350, 1–8.
- [101] I. U. Arachchige, S. L. Brock, *Sol-gel methods for the assembly of metal chalcogenide quantum dots*, American Chemical Society **2007**, 40, 801–809.
- [102] J. Alemán, A. V. Chadwick, J. He, M. Hess, K. Horie, R. G. Jones, P. Kratochvíl, I. Meisel, I. Mita, G. Moad, S. Penczek, R. F. Stepto, *Definitions of terms relating to the structure and processing of sols, gels, networks, and inorganic-organic hybrid materials (IUPAC recommendations 2007)*, Pure and Applied Chemistry **2007**, 79, 1801–1829.
- [103] D. Zámbo, A. Schlosser, P. Rusch, F. Lübke, J. Koch, H. Pfnür, N. C. Bigall, *A Versatile Route to Assemble Semiconductor Nanoparticles into Functional Aerogels by Means of Trivalent Cations*, Small **2020**, 1906934.
- [104] S. Naskar, A. Freytag, J. Deutsch, N. Wendt, P. Behrens, A. Köckritz, N. C. Bigall, *Porous Aerogels from Shape-Controlled Metal Nanoparticles Directly from Nonpolar Colloidal Solution*, Chemistry of Materials **2017**, 29, 9208–9217.
- [105] L. L. Hench, W. Vasconcelos, *Gel-silica science*, Annu. Rev. Mater. Sci **1990**, 02, year.
- [106] G. Zu, J. Shen, W. Wang, L. Zou, Y. Lian, Z. Zhang, *Silica-titania composite aerogel photocatalysts by chemical liquid deposition of titania onto nanoporous silica scaffolds*, ACS Applied Materials and Interfaces **2015**, 7, 5400–5409.
- [107] J. Šubrt, E. Plížingrová, M. Palkovská, J. Boháček, M. Klementová, J. Kupčík, P. Bezdička, H. Sovová, *Titania aerogels with tailored nano and microstructure: Comparison of lyophilization and supercritical drying*, Pure and Applied Chemistry **2017**, 89, 501–509.
- [108] M. Georgi, B. Klemmed, A. Benad, A. Eychmüller, *A versatile ethanolic approach to metal aerogels (Pt, Pd, Au, Ag, Cu and Co)*, Materials Chemistry Frontiers **2019**, 3, 1586–1592.

-
- [109] L. Altenschmidt, S. Sánchez-Paradinas, F. Lübke, D. Zámbo, A. M. Abdelmonem, H. Bradtmüller, A. Masood, I. Morales, P. de la Presa, A. Knebel, M. A. G. García-Tuñón, B. Pelaz, K. D. Hindricks, P. Behrens, W. J. Parak, N. C. Bigall, *Aerogelation of Polymer-Coated Photoluminescent, Plasmonic, and Magnetic Nanoparticles for Biosensing Applications*, ACS Applied Nano Materials **2021**, *4*, 6678–6688.
- [110] A. L. Luna, F. Matter, M. Schreck, J. Wohlwend, E. Tervoort, C. Colbeau-Justin, M. Niederberger, *Monolithic metal-containing TiO₂ aerogels assembled from crystalline pre-formed nanoparticles as efficient photocatalysts for H₂ generation*, Applied Catalysis B: Environmental **2020**, *267*, 118660.
- [111] D. Pluta, H. Kuper, R. T. Graf, C. Wesemann, P. Rusch, J. A. Becker, N. C. Bigall, *Optical properties of NIR photoluminescent PbS nanocrystal-based three-dimensional networks*, Nanoscale Advances **2023**, 5005–5014.
- [112] T. Hendel, V. Lesnyak, L. Kühn, A. K. Herrmann, N. C. Bigall, L. Borchardt, S. Kaskel, N. Gaponik, A. Eychmüller, *Mixed aerogels from Au and CdTe nanoparticles*, Advanced Functional Materials **2013**, *23*, 1903–1911.
- [113] M. Rosebrock, D. Zámbo, P. Rusch, R. T. Graf, D. Pluta, H. Borg, D. Dorfs, N. C. Bigall, *Morphological Control Over Gel Structures of Mixed Semiconductor Metal Nanoparticle Gel Networks with Multivalent Cations*, Small **2023**, *19*, year.
- [114] V. Lesnyak, S. V. Voitekhovich, P. N. Gaponik, N. Gaponik, A. Eychmüller, *CdTe nanocrystals capped with a tetrazolyl analogue of thioglycolic acid: Aqueous synthesis, characterization, and metal-assisted assembly*, ACS Nano **2010**, *4*, 4090–4096.
- [115] C. C. Hewa-Rahinduwage, X. Geng, K. L. Silva, X. Niu, L. Zhang, S. L. Brock, L. Luo, *Reversible Electrochemical Gelation of Metal Chalcogenide Quantum Dots*, Journal of the American Chemical Society **2020**, *142*, 12207–12215.
- [116] A. Freytag, S. Sánchez-Paradinas, S. Naskar, N. Wendt, M. Colombo, G. Pugliese, J. Poppe, C. Demirci, I. Kretschmer, D. W. Bahnemann, P. Behrens, N. C. Bigall, *Versatile Aerogel Fabrication by Freezing and Subsequent Freeze-Drying of Colloidal Nanoparticle Solutions*, Angewandte Chemie International Edition **2016**, *55*, 1200–1203.
- [117] L. Nahar, R. J. Esteves, S. Hafiz, Ü. Özgür, I. U. Arachchige, *Metal Semiconductor Hybrid Aerogels: Evolution of Optoelectronic Properties in a Low-Dimensional CdSe/Ag Nanoparticle Assembly*, ACS Nano **2015**, *9*, 9810–9821.
- [118] A. Wolf, V. Lesnyak, N. Gaponik, A. Eychmüller, *Quantum-dot-based (Aero)gels: Control of the optical properties*, Journal of Physical Chemistry Letters **2012**, *3*, 2188–2193.
- [119] M. Rosebrock, D. Zámbo, P. Rusch, R. T. Graf, D. Pluta, H. Borg, D. Dorfs, N. C. Bigall, *Morphological Control Over Gel Structures of Mixed Semiconductor-Metal Nanoparticle Gel Networks with Multivalent Cations*, Small **2023**, *19*, year.
-

- [120] M. Rosebrock, D. Zámbo, P. Rusch, D. Pluta, F. Steinbach, P. Bessel, A. Schlosser, A. Feldhoff, K. D. Hindricks, P. Behrens, D. Dorfs, N. C. Bigall, *Spatial Extent of Fluorescence Quenching in Mixed Semiconductor-Metal Nanoparticle Gel Networks*, *Advanced Functional Materials* **2021**, *31*, year.
- [121] D. Müller, D. Zámbo, D. Dorfs, N. C. Bigall, *Cryoaerogels and Cryohydrogels as Efficient Electrocatalysts*, *Small* **2021**, *17*, year.
- [122] A. Schlosser, L. C. Meyer, F. Lübke, J. F. Miethe, N. C. Bigall, *Nanoplatelet cryoaerogels with potential application in photoelectrochemical sensing*, *Physical Chemistry Chemical Physics* **2019**, *21*, 9002–9012.
- [123] IUPAC, *Compendium of Chemical Terminology*, Blackwell Scientific Publications, Oxford, 2nd ed., **1997**.
- [124] I. Hermans, E. S. Spier, U. Neuenschwander, N. Turrà, A. Baiker, *Selective oxidation catalysis: Opportunities and challenges*, *Topics in Catalysis* **2009**, *52*, 1162–1174.
- [125] B. Liu, X. Zhao, C. Terashima, A. Fujishima, K. Nakata, *Thermodynamic and kinetic analysis of heterogeneous photocatalysis for semiconductor systems*, *Physical Chemistry Chemical Physics* **2014**, *16*, 8751–8760.
- [126] S. Chen, T. Takata, K. Domen, *Particulate photocatalysts for overall water splitting*, *Nature Reviews Materials* **2017**, *2*, 1–17.
- [127] F. Costantino, P. V. Kamat, *Do Sacrificial Donors Donate H_2 in Photocatalysis?*, *ACS Energy Letters* **2022**, *7*, 242–246.
- [128] J. Schneider, D. W. Bahnemann, *Undesired role of sacrificial reagents in photocatalysis*, *Journal of Physical Chemistry Letters* **2013**, *4*, 3479–3483.
- [129] D. Meissner, R. Memming, B. Kastening, D. Bahnemann, *Fundamental problems of water splitting at cadmium sulfide*, *Chemical Physics Letters* **1986**, *127*, 419–423.
- [130] Y. J. Yuan, D. Chen, Z. T. Yu, Z. G. Zou, *Cadmium sulfide-based nanomaterials for photocatalytic hydrogen production*, *Journal of Materials Chemistry A* **2018**, *6*, 11606–11630.
- [131] D. W. Wakerley, M. F. Kuehnle, K. L. Orchard, K. H. Ly, T. E. Rosser, E. Reisner, *Solar-driven reforming of lignocellulose to H_2 with a CdS/CdO_x photocatalyst*, *Nature Energy* **2017**, *2*, 1–9.
- [132] F. Eisenreich, *Photocatalysis as an Effective Tool for Upcycling Polymers into Value-Added Molecules*, *Angewandte Chemie - International Edition* **2023**, *62*, 1–11.
- [133] T. Uekert, H. Kasap, E. Reisner, *Photoreforming of Nonrecyclable Plastic Waste over a Carbon Nitride/Nickel Phosphide Catalyst*, *Journal of the American Chemical Society* **2019**, *141*, 15201–15210.

-
- [134] S. B. Potdar, C. M. Huang, B. V. Praveen, S. Manickam, S. H. Sonawane, *Highly Photoactive Titanium Dioxide Supported Platinum Catalyst: Synthesis Using Cleaner Ultrasound Approach*, *Catalysts* **2022**, *12*, year.
- [135] J. M. Lei, S. P. Luo, S. Z. Zhan, *Photocatalytic system with water soluble nickel complex of S,S-bis-(2-pyridylmethyl)-1,2-thioethane over CdS nanorods for hydrogen evolution from water under visible light*, *International Journal of Hydrogen Energy* **2018**, *43*, 19047–19056.
- [136] P. Lindgren, G. Kastlunger, A. A. Peterson, *A Challenge to the $G \sim 0$ Interpretation of Hydrogen Evolution*, *ACS Catalysis* **2020**, *10*, 121–128.
- [137] A. H. Shah, C. Wan, Y. Huang, X. Duan, *Toward Molecular Level Understandings of Hydrogen Evolution Reaction on Platinum Surface*, *Journal of Physical Chemistry C* **2023**, *127*, 12841–12848.
- [138] Y. Zhou, C. Jin, Y. Li, W. Shen, *Dynamic behavior of metal nanoparticles for catalysis*, *Nano Today* **2018**, *20*, 101–120.
- [139] A. Y. Shan, T. I. M. Ghazi, S. A. Rashid, *Immobilisation of titanium dioxide onto supporting materials in heterogeneous photocatalysis: A review*, *Applied Catalysis A: General* **2010**, *389*, 1–8.
- [140] S. Park, N. Utsch, M. Carmo, M. Shviro, D. Stolten, *Iridium-Nickel Nanoparticle-Based Aerogels for Oxygen Evolution Reaction*, *ACS Applied Nano Materials* **2022**, *5*, 18060–18069.
- [141] D. Wen, W. Liu, D. Haubold, C. Zhu, M. Oschatz, M. Holzschuh, A. Wolf, F. Simon, S. Kaskel, A. Eychmüller, *Gold Aerogels: Three-Dimensional Assembly of Nanoparticles and Their Use as Electrocatalytic Interfaces*, *ACS Nano* **2016**, *10*, 2559–2567.
- [142] J. Kwon, K. Choi, M. Schreck, T. Liu, E. Tervoort, M. Niederberger, *Gas-phase nitrogen doping of monolithic TiO_2 nanoparticle-based aerogels for efficient visible light-driven photocatalytic H_2 production*, *ACS Applied Materials and Interfaces* **2021**, *13*, 53691–53701.
- [143] F. Rechberger, M. Niederberger, *Translucent nanoparticle-based aerogel monoliths as 3-dimensional photocatalysts for the selective photoreduction of CO_2 to methanol in a continuous flow reactor*, *Materials Horizons* **2017**, *4*, 1115–1121.
- [144] A. L. Luna, S. Papadopoulos, T. Kyburz, E. Tervoort, L. Novotny, M. Niederberger, *Insights into light and mass transport in nanoparticle-based aerogels: The advantages of monolithic 3D photocatalysts*, *Journal of Materials Chemistry A* **2021**, *9*, 22380–22391.
- [145] J. Bisquert, P. Cendula, L. Bertoluzzi, S. Gimenez, *Energy diagram of semiconductor/electrolyte junctions*, *Journal of Physical Chemistry Letters* **2014**, *5*, 205–207.
- [146] S. G. Hickey, D. J. Riley, *Photoelectrochemical studies of CdS nanoparticle-modified electrodes*, *Journal of Physical Chemistry B* **1999**, *103*, 4599–4602.
-

- [147] S. G. Hickey, D. J. Riley, *Intensity modulated photocurrent spectroscopy studies of CdS nanoparticle modified electrodes*, *Electrochimica Acta* **2000**, *45*, 3277–3282.
- [148] B. Y. Chang, S. M. Park, *Electrochemical impedance spectroscopy*, *Annual Review of Analytical Chemistry* **2010**, *3*, 207–229.
- [149] K. Adhitya, *Intensity-Modulated Spectroscopy Instrument and Its Applications*, University of Sheffield **2016**.
- [150] S. G. Hickey, D. J. Riley, E. J. Tull, *Photoelectrochemical studies of CdS nanoparticle modified electrodes: Absorption and photocurrent investigations*, *Journal of Physical Chemistry B* **2000**, *104*, 7623–7626.

Chapter 2

Photoelectrochemistry of Semiconductor-Metal Gel Structures

2.1 Summary

In this chapter, semiconductor-metal hybrid gel structures were synthesized and investigated using optical, structural and photoelectrochemical characterization methods. In section 2.2, cryogelated hybrid network structures with either the metal and the semiconductor as mixed nanoparticles, or the metal as on-grown domains on the semiconductor were investigated. Additionally, two colloiddally destabilized hybrid gel structures were in the focus in section 2.3. It has been shown that the contact between the semiconductor and the metal as well as the metal domain distribution is crucial for an efficient charge carrier separation and a potential application in photocatalysis.

Having two different nanoparticle dispersions, which can be mixed while maintaining the colloidal stability, enables the synthesis of multicomponent cryoaerogels. This has been done by mixing semiconductor nanoparticles with metal nanoparticles to obtain a semiconductor-metal hybrid cryogel. CdSe/CdS core crown nanoplatelets and CdSe/CdS nanorods have been mixed with platinum and gold nanoparticles, respectively. To gain information about the contact between the semiconductor and the metal and the consequences for the charge carrier separation, these mixed cryoaerogels have been compared to hybrid nanoparticles. In hybrid nanoparticles, before the cryogelation platinum and gold is grown directly on the nanoplatelets and nanorods, respectively.

Optically no differences between the on-grown and mixed cryogels were observed. Only the pure semiconductor cryogels showed a clear difference. Here, no contribution to the extinction of the metal is present. Structurally, in scanning electron microscopy (SEM) only minor differences were visible. However, in transmission electron microscopy (TEM) images a slightly inhomogeneous metal distribution was observed having mixed cryogels. In contrast, when having on-grown metal domains the metal distribution is homogeneous.

The photoelectrochemical characterization revealed, that the charge transfer from the semiconductor to the metal is more efficient when the metal has been grown on the semiconductor before cryogelation. In pure semiconductor and mixed semiconductor-

metal cryogels, the photocurrent is mainly positive in the linear sweep voltammetry as well as intensity modulated photocurrent spectroscopy (IMPS) measurements. This indicates an efficient electron transfer from the semiconductor to the indium thin oxide (ITO) electrode. In contrast, in the cryogels from the on-grown hybrid particles the electron transfer from the semiconductor to metal is competing the transfer to the ITO electrode which is shown by more negative photocurrents especially in the IMPS. The differences are related to the more homogeneous distribution as well as a better contact between the semiconductor and the metal due to the epitaxial growth.

In colloiddally destabilized nanoparticle-based gels, a crystal contact between the nanoparticles is given when the gelation mechanism involves ligand removal from the particles surface. As indicated by the measurements with cryogels, this is beneficial for efficient charge carrier separation. To further investigate the influence of the metal domain distribution semiconductor-metal hybrid nanoparticles were gelated using hydrogen peroxide and ytterbium chloride as destabilization agents. CdSe/CdS nanorods with gold domains grown distributed over the whole nanorod were compared to nanorods with gold grown only on the tip of the nanorod. TEM images show that the nanoscopic morphology of the gold distribution has been transferred into the macroscopic gel structures. Photoelectrochemical investigations showed, that in gels with less metal domains and larger distances in between each other the charge carrier separation is more efficient. In IMPS measurements, a photocurrent maximum at a certain frequency evolves which is followed by a decrease of the negative photocurrent. This change in the photocurrent is correlated to an increase in charge recombination after a electron accumulation in the metal over time. In case of metal domains on the tips of the nanorods, the photocurrent decreased less compared to gels with metal domains all along the nanorods. This has been interpreted as a more efficient charge recombination due to electron tunneling from metal domain to metal domain and thus a less efficient charge separation.

2.2 Interparticle Interaction Matters: Charge Carrier Dynamics in Hybrid Semiconductor-Metal Cryoaerogels

Anja Schlosser, Jakob Schlenkrich, Dániel Zámbo, Marina Rosebrock, Rebecca T. Graf, Giamper Escobar Cano, and Nadja C. Bigall

Published in *Advanced Materials Interfaces* 2022, 9, 2200055
<https://doi.org/10.1002/admi.202200055>



RESEARCH ARTICLE

ADVANCED
MATERIALS
INTERFACES

www.advmatinterfaces.de

Interparticle Interaction Matters: Charge Carrier Dynamics in Hybrid Semiconductor–Metal Cryoaerogels

Anja Schlosser, Jakob Schlenkrich, Dániel Zámbo,* Marina Rosebrock, Rebecca T. Graf, Giamper Escobar Cano, and Nadja C. Bigall*

Integration of noble metals into semiconductor-based nanoparticle gel structures facilitates the extraction of photoexcited charge carriers upon illumination. While charge carrier generation takes place in the semiconductor component, noble metals in contact to the semiconductor act as electron sinks. Thus, the nature of the interface between the components is of essential importance, as it dictates the characteristics of the interparticle contact. Here, the influence of the nanoscale building block design on the charge carrier dynamics in cryoaerogels consisting of CdSe/CdS nanorods and nanoplatelets as well as of gold or platinum is reported. It is shown that direct growth of noble metal domains onto the semiconductor prior to the gelation significantly facilitates charge carrier separation in their cryoaerogel structures compared to gels from the colloidal mixtures of semiconductor and noble metal nanoparticles, the latter ones having less defined metal/semiconductor boundaries and much more arbitrary component distributions. Although the structure of the different cryoaerogel systems is similar at the micro- and macroscale, nanoscale differences caused by the two synthetic routes drive essentially different behavior regarding the charge carrier dynamics efficiency. These effects are observed spectroelectrochemically via intensity-modulated photocurrent spectroscopy emphasizing the importance of the semiconductor–metal connection in the hybrid structures.

1. Introduction

Assembling nanoparticles (NPs) of different material classes, namely, metals and semiconductors, into hybrid nanomaterials not only merges the advantages of the counterparts but leads to even altered physicochemical properties pointing toward advanced applications.^[1–3] While semiconductor NCs are able to produce charge carriers upon photoexcitation, noble metals have a high electron affinity due to the position of their Fermi level within the energy landscape. The Fermi level position of the metal in the bandgap of the semiconductor allows the separation of the photoexcited electrons in the ps range,^[4] leading to electrons in the metal domains with long lifetimes up to tens of μs .^[5,6] The efficiency of this charge carrier separation is governed by the nature of the interface between the components^[7] as well as the recombination kinetics inside the semiconductor heterostructures.^[8,9] This effective charge carrier separation has been discussed recently to be of high interest for, e.g., applications in photocatalysis.

When it comes to applications, nanoparticles frequently need to be assembled in a way that the physicochemical properties are either conserved or even extended in a most beneficial way. In this regard, hydrogels and aerogels of nanoparticles are highly interesting, as they are self-supporting networks only consisting of the nanoscopic building blocks, and since they are at the same time highly voluminous, monolithic, and have enhanced surface accessibility to their hierarchical nanoporous architectures.^[2,3,10–25] Nanocrystal hydrogels and aerogels can be prepared via chemical or physical methods.^[1–3,26]

With respect to the design of multicomponent hydrogels and aerogels from noble metal and semiconductor compounds, there have solely been very few reports so far: Hendel et al. reported on mixing of CdTe and noble metal nanoparticles resulting in arbitrary distribution of the gold domains in the network.^[27] Similar applies for Rosebrock et al. who were able to form a CdS network with CdSe domains inside in combination with an arbitrary distribution of the noble metal particles to control the spatial extent of fluorescence quenching.^[28] Zámbo et al. observed an in situ gelation and noble metal domain formation upon addition of multivalent metal ions to similar semiconductor nanocrystal building blocks resulting in

A. Schlosser, J. Schlenkrich, D. Zámbo, M. Rosebrock, R. T. Graf, G. Escobar Cano, N. C. Bigall
Institute of Physical Chemistry and Electrochemistry
Leibniz Universität Hannover
Callinstr. 3A, 30167 Hannover, Germany
E-mail: daniel.zambo@pci.uni-hannover.de, daniel.zambo@ek-cer.hu; nadja.bigall@pci.uni-hannover.de

D. Zámbo
Centre for Energy Research
Institute of Technical Physics and Materials Science
Konkoly-Thege M. str. 29-33, Budapest 1121, Hungary
N. C. Bigall
Cluster of Excellence PhoenixD (Photonics, Optics
and Engineering – Innovation Across Disciplines)
Leibniz Universität Hannover
30167 Hannover, Germany

The ORCID identification number(s) for the author(s) of this article can be found under <https://doi.org/10.1002/admi.202200055>.

© 2022 The Authors. Advanced Materials Interfaces published by Wiley-VCH GmbH. This is an open access article under the terms of the Creative Commons Attribution-NonCommercial License, which permits use, distribution and reproduction in any medium, provided the original work is properly cited and is not used for commercial purposes.

DOI: 10.1002/admi.202200055

a continuous semiconductor network with more homogeneous domain distribution.^[11,29] Moreover, the use of hybrid nanostructures and alloys in photoelectrochemical applications has been shown for TiO₂/Pt,^[30] Zn_{1-x}Cd_xSe/Pt,^[31] and CdSe/CdS/Pt systems.^[32]

However, when looking at the powerful tool of colloid chemistry, establishing highly controlled metal/semiconductor contacts is also possible nowadays. This might open the possibility of a better control over both the distribution and the contact between the noble metal and the semiconductor in the aerogels. Numerous elaborated wet-chemical synthesis methods of hybrid semiconductor/metal nanocrystals (NCs) have been demonstrated recently. The epitaxial deposition of metal domains onto semiconductor nanoplatelets (NPLs)^[33–36] and nanorods (NRs)^[7,37–41] by colloidal methods involving heterogeneous nucleation facilitates the separation of the photoexcited electrons. Therefore, it essentially alters the optoelectronic properties compared to the pure semiconductor materials. Upon illumination of CdSe/CdS dot-in-rods, electrons can delocalize in the rod-shaped CdS shell, while the holes are being trapped in the CdSe core quantum dot.^[42] This can occur, due to the small conduction band offset in the CdSe/CdS heterojunction. Especially for core/crown NPLs, this intrinsic separation does not take place: the high exciton binding energy favors the recombination of the exciton in the CdSe core of the nanoplatelet.^[9] Nonetheless, applying bias potential on Cd-chalcogenide NPL networks can overcome the high exciton binding energy leading to effective charge carrier separation.^[43]

We have demonstrated recently that charge carrier separation in hybrid semiconductor–metal nanoparticle gels can take place as well. In our work, photoexcited electrons were extracted and consumed in electrochemical processes in CdSe/CdS/Au hybrid gel networks prepared via the oxidative or ionic gelation of the hybrid nanoparticles.^[44] By varying the number and location of the gold domains grown directly onto the semiconductor NR surface prior to gelation, the efficiency of the electron extraction from the semiconductor to the noble metal domain can be tuned. Mixing and co-gelating CdSe/CdS NRs and Au NPs via H₂O₂ led to the formation of hyperbranched solvocal and aerogel networks, where the extent of the photoluminescence quenching is highly dependent on the number and spatial distribution of the Au NPs within the gel network as well as the dielectric constant of the solvent in the gap between the nanorods and Au NPs.^[28] These gel structures, however, were produced by means of partial oxidation and removal of the surface ligands, therefore, direct interparticle contacts were able to be achieved facilitating the formation of a branched semiconductor backbone.

As an important finding in the present work, a crucial difference between gel structures consisting of hybrid CdSe/CdS/Au NRs or CdSe/CdS/Pt NPLs (meaning that the metal domains are directly grown onto the semiconductor component), and co-gelated colloidal mixtures of the two components was found: the nature of the contact between the semiconductor and the metal domain/NP governs the charge carrier dynamics.

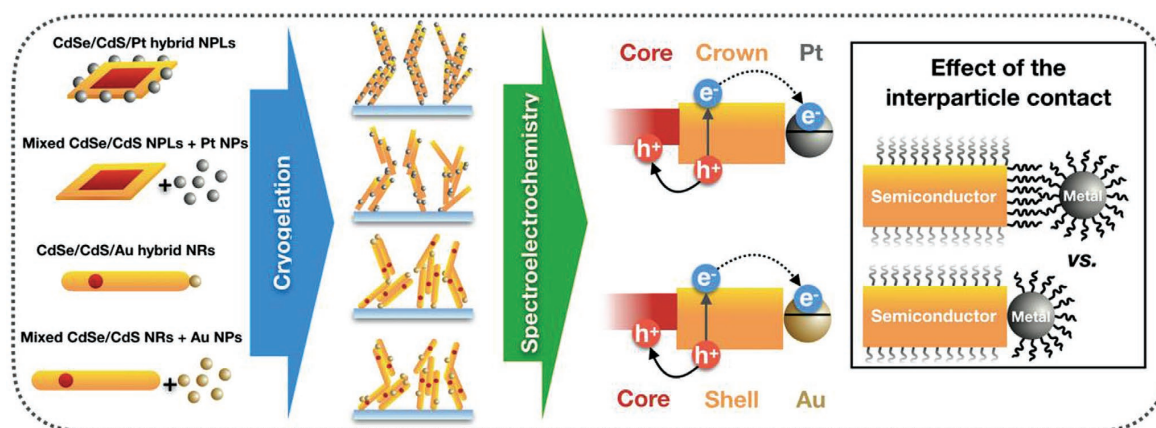
Beside the widely used chemical gelation methods, cryogelation is a novel physical gelation technique, which includes

the flash-freezing and the subsequent freeze drying of the aqueous NC solutions.^[18] Its versatility and ease (no oxidative ligand removal is required in the process) allowed us to fabricate various, highly porous nanoparticle gel structures from noble metal NPs,^[20,45–47] semiconductor NPLs,^[43] metal oxide NPs^[18] as well as mixed systems.^[19] These structures proved their potential in applications such as electrocatalysis and electrochemical sensing. In the present work, we use this method for combining semiconductor and noble metal components within the cryoaerogels leading to hybrid nanostructures, which display the advantages of both components. As we have a physical assembly method and not a chemical one, the surface chemistry of the assembled nanoparticles is of inferior importance and works regardless which route we choose: mixing semiconductor and noble metal nanoparticles or gelating semiconductor–metal hybrid nanoparticles. Thus, this method is beneficial for comparing different particle systems (in terms of the shape and ligands of the semiconductor and the type of the noble metal) without influencing the ligand coverage of the nanoparticles during the assembly. However, as we have experienced so far, in case of citrate-stabilized metal nanoparticle-based cryogels, the large-scale attractive forces during the freezing process are able to overcome the repulsive ligand-related interparticle forces, which leads to the welding of the metal nanoparticles.^[45,46] To suppress this effect, thiolated surface attached molecules were used in the present work.

The following key questions inspired this work:

- (i) Can a physically gelated hybrid gel network be effective in charge carrier separation?
- (ii) Has the wet-chemical growth of the noble metal on the semiconductor an influence on the charge carrier separation in comparison to mixed semiconductor and metal nanoparticles in cryoaerogel structures?
- (iii) Is it possible to control the distribution of noble metal NPs in mixed co-gelated structures as precisely as for the gel networks built up from originally hybrid semiconductor/metal nanoparticles?

To answer these questions, we prepare hybrid cryoaerogel coatings on conductive ITO-coated glass substrates and investigate these materials by means of structural and spectroelectrochemical methods. The highly porous hybrid cryoaerogels consist of either CdSe/CdS core/crown nanoplatelets or dot-in-rods and additionally a noble metal component Pt and Au, respectively. The different metals for the NPL and NR systems are used due to synthetic limitations regarding the growth and phase transfer of gold on CdSe/CdS NPLs and Pt on CdSe/CdS NRs. Nevertheless, the different metals, thus, show the general validity of the results. Beside the preparation of pristine semiconductor cryoaerogels, structures from semiconductor–metal nanoheteroparticles (in which the metal domains are directly grown onto the semiconductor NCs) as well as from mixed semiconductor and noble metal colloidal solutions are prepared (**Scheme 1**). We introduce here the following abbreviations to improve the readability: *h-NPLs* and *h-NRs* are used for the wet-chemically grown heterosystems (h), while *m-NPLs* and *m-NRs* refer to the mixed (m) gels. The used preparation methods represent two different approaches, which lead to essentially



Scheme 1. Schematics of the investigated model systems: nanoparticle building blocks (NPLs and NRs) are combined with noble metals at the nanoscale (via direct growth of the metal domains or mixing the semiconductor and noble metal colloidal solutions). The hybrid or mixed nanoparticle solutions are cryogelated to fabricate aerogel-coated ITO electrodes. The charge carrier dynamics is studied via spectroelectrochemical tools to shed light on the impact of the nanoscale design (i.e., interparticle contact) on the charge carrier dynamics.

different structures at the nanoscale. While the direct semiconductor–noble metal contact is ensured in a defined way for the hybrid NCs, it is of rather undefined nature for gelating the colloidal mixtures of the two counterparts. In other words, the presence of ligands between the semiconductor and the metal can hinder the direct crystal contact in the cryo-aerogel prepared from the colloidal mixture of the components. As we demonstrate, this structural difference at the nanoscale dramatically alters the charge carrier dynamics in the hybrid cryo-aerogels: direct growth of the noble metal domains facilitates an effective charge carrier separation upon illumination. However, the separation of photoexcited electrons is significantly suppressed in the mixed systems. Intensity modulated photocurrent spectroscopy (IMPS) sheds light on the effect of the nanoscale design on the spectroelectrochemical response of the cryo-aerogels. Notable amounts of negative photocurrent can solely evolve in the case of directly grown noble metals, which show their superior performance in the charge carrier separation process. Due to the versatility of the cryogelation method, these findings can further be adopted to other semiconductor–metal hybrid gel structures being active in photoelectrochemical sensing or photocatalysis.

2. Results and Discussion

2.1. Structure of Semiconductor–Metal Hybrid Cryo-aerogel Electrodes

To reveal the effect of nanoscale design on the assembled structures, three nanorod-based and three nanoplatelet-based model systems were established. Pristine semiconductor NRs and NPLs, metal decorated h-NRs and h-NPLs (via direct deposition of metal domains) as well as mixed colloidal solutions of semiconductor and metal NPs were prepared according to our previous studies or based on synthetic procedures adapted from the literature (see the Experimental Section for details).

These building blocks (see Figures S1–S5, Supporting Information, for their characterization) were assembled into cryo-aerogels. To enable the electrochemical characterization of these gel networks, coatings on functionalized ITO electrodes were fabricated (photographs of the cryo-aerogel electrodes can be seen in Figure S8, Supporting Information). After their synthesis in organic media, the nanoparticles were transferred to the aqueous phase (via using MPA or MUA as ligand) and were distributed in a preformed mold on the surface of MPTMS-coated ITO glass followed by flash-freezing with cooled liquid isopentane (corresponding to a freezing temperature of 113 K).^[43] This step was carried out by placing the electrode on the surface of the liquid isopentane until the liquid nanoparticle film was frozen. We have shown recently (for metal nanoparticles) that the freezing medium itself has a direct impact on the structure of the cryo-aerogel coatings due to the various freezing velocity and ice crystal nucleation rate in different media.^[46] Using liquid nitrogen, the dominating structures are lamellar sheets, however for isopentane, the high freezing velocity leads to cryo-aerogel coatings with dendritic sheet structures with open porosity. The latter also showed enhanced stability in electrochemical processes,^[45] which is of great importance in the practical use of cryo-aerogel coatings.^[47]

The microstructure and elemental composition of the cryo-aerogels were investigated with scanning electron microscopy (SEM) and energy dispersive X-ray spectroscopy (EDXS). **Figure 1** shows the typical dendritic structures consisting of interconnected sheets for the pure NPLs and NRs, the h-NPLs and h-NRs as well as for the co-gelated mixtures of semiconductor and metal nanoparticles. These sheets have dimensions of tens of micrometers which is three magnitudes larger than the size of the nanoparticles building blocks itself. The highly porous nature of the coatings endows the systems with high accessible surface areas for interfacial reactions, which is a significant advantage over their simply drop-cast nanoparticle film counterparts.^[43,46,47]

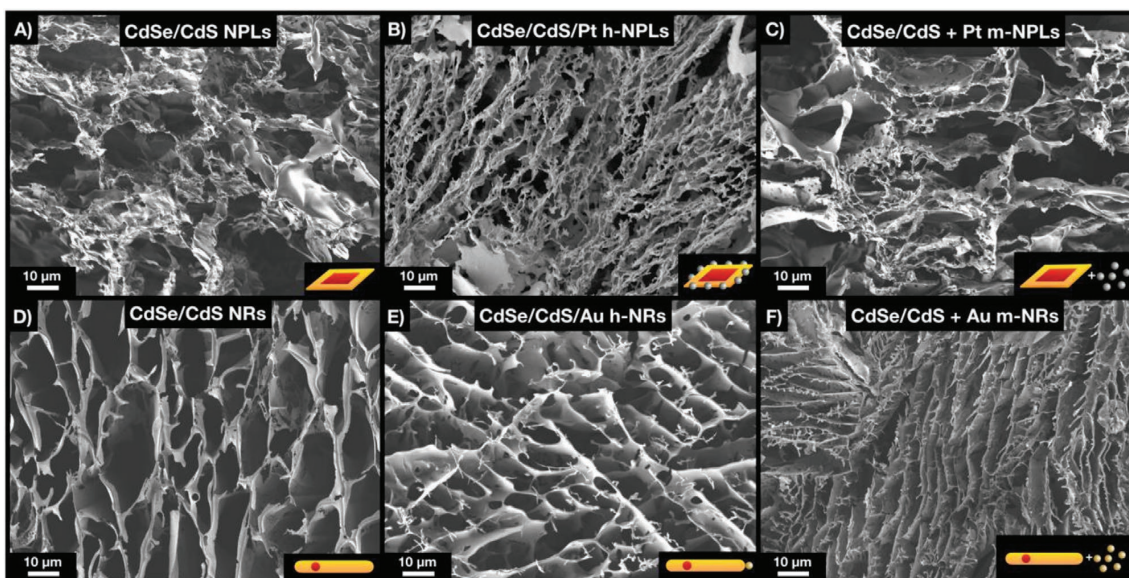


Figure 1. Microstructure of cryoaerogel coatings consisting of A) pure NPLs, B) h-NPLs, C) m-NPLs, D) pure NRs, E) h-NRs, and F) m-NRs.

As the particle concentrations were uniform for all the investigated systems, slight structural differences (e.g., distance of interconnected sheets, film thickness, sheet structure) can be attributed to the composition of the nanoparticle solutions, the differences in the shape of the NPs and the chain length of the NP ligands. The amount of free organic ligands in the solutions plays an important role in the structural properties of the coatings. Consequently, the nanoparticle solutions were purified to ensure the removal of excess ligands down to the limit of the colloidal stability. At the macro- and microscale, semiconductor-metal hybrid cryoaerogels show similar distribution of the metal nanoparticles (in the mixed systems) and the metal domains (for decorated NPs) in the elemental maps: the metals seem to be homogeneously distributed in all structures (see

Figure S9 Supporting Information). Nonetheless, investigation on the nanoscopic structure of the cryoaerogel sheets sheds light on the difference regarding the distribution of the metal NPs and domains in the hybrid structures (**Figure 2**). Nanoplatelets show different orientations on the transmission electron microscopy (TEM) images (**Figure 2A,B,E,F**) leading to low contrast plates or wire-like structures with higher contrast. This can be attributed to the 2D nature of the four-monolayer (ML) thick NPLs which can stand upright or lay on the grid. While the growth of Pt directly on the NPLs leads to a homogeneous distribution of the metal in the cryoaerogel, always a few Pt-NPs are in close vicinity in case of mixing and co-gelation of NPLs and Pt NPs (**Figure 2B,F**). This phenomenon can also be observed for the nanorod-based systems: Au nanoparticles

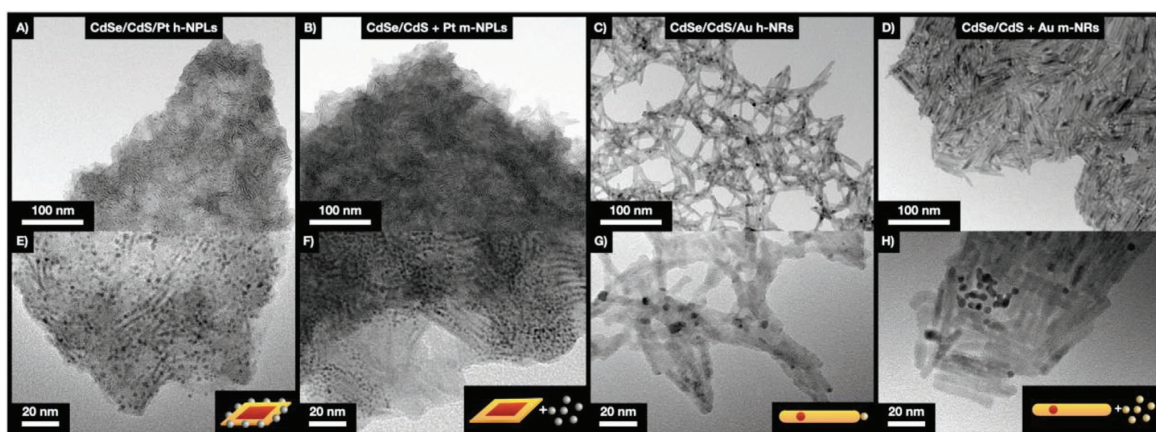


Figure 2. Nanostructure (lower and higher magnification TEM images) of cryoaerogel coatings consisting of A,E) h-NPLs, B,F) m-NPLs, C,G) h-NRs, and D,H) m-NRs.

accumulate in distinct areas leading to an inhomogeneous gold distribution in case of mixing, however, cryogelation of h-NRs ensures the homogeneous distribution of gold. Based on our recent finding that the nature of interparticle connection between CdSe/CdS NRs and Au NPs essentially governs the optical properties (extent of fluorescence quenching) of the hybrid gel structures,^[28] the differences in the metal distributions observed in these hybrid cryoaerogels are expected to have a significant impact on the spectroelectrochemical properties.

2.2. Optical Properties

The optical properties of the hybrid cryoaerogel electrodes show the characteristics of both the semiconductor and the metal components, respectively. From metal point of view, gold shows a distinct surface plasmon resonance (LSPR) in the visible wavelength range, while platinum has a broad, decay-like extinction (spectra of the nanoparticles can be seen in Figure S4, Supporting Information). This broad extinction of the Pt domains and NPs manifests itself in an increased absorption above 560 nm for the NPL-based hybrid cryoaerogels (Figure 3A). The characteristic excitonic transitions of the CdSe/CdS NPLs remain visible in the spectra of hybrid cryoaerogels, and the nanoscale design of the preparation (namely, the gelation of h-NPLs or the mixing and co-gelation of NPLs and Pt NPs) has solely slight impact on the overall absorption of the gel structures. This is a consequence of the size of the Pt domains and Pt NPs kept quasi-constant for both model systems. Due to the metal growth on the nanoplatelets, a decrease in oscillator strength of the semiconductor can be observed.

As the LSPR of Au NPs is located at 519 nm, the metal content leads to an increased absorption of the NR-based hybrid cryoaerogel coatings above 500 nm (Figure 3B) similar to the Pt for NPLs. Nevertheless, due to the similar size of the gold domains (grown on the NRs) and the Au NPs (in the mixed system), h-NR and m-NR cryoaerogels show comparable optical response. In case of the semiconductor–metal hybrid nanoparticles, the location of the LSPR is bathochromically shifted and becomes broader compared to the colloiddally dispersed Au NP solution. This can be attributed to the refractive index change in the vicinity of the Au NPs^[48] as well as to the possible Au NP–Au NP connections in the gel structures. The absorption of the CdSe core at 600 nm and the contribution of the LSPR of the Au domains and particles dominate the spectra of the gels. The absorption of the CdS shell becomes prominent below 470 nm, which is in agreement with the band edge of the CdS and the characteristics of the typical CdSe/CdS gel structures due to the high particle concentrations.^[10,11]

To shed light on the changes of the radiative lifetime of the excited carriers in all cryoaerogel systems, photoluminescence lifetime measurements were performed. Figure S6 (Supporting Information, for NPLs) and Figure S7 (Supporting Information, for NRs) show significant differences in the radiative lifetimes of the cryoaerogels prepared by means of different strategies. Due to the high exciton binding energy, the pristine NPL cryoaerogel shows a shorter lifetime than the one consisting of pristine NRs. In all systems, while growing the metal domains directly on the semiconductor leads to a drastic shortening of

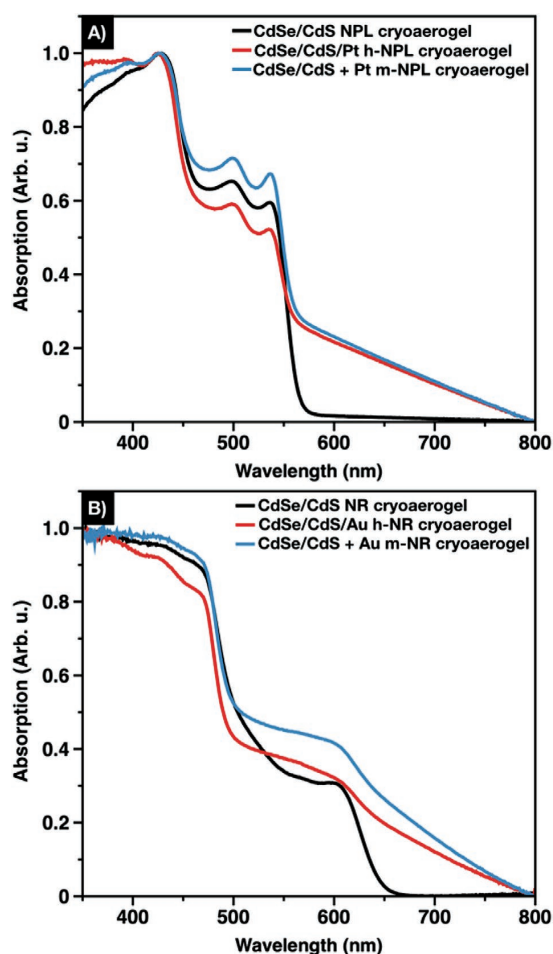


Figure 3. Optical properties of cryoaerogel coatings based on A) CdSe/CdS NPLs and B) CdSe/CdS NRs.

the measured lifetimes, mixing exerts a lower influence on the recombination kinetics. This implies a more efficient charge carrier separation in the h-NPLs and h-NR cryoaerogels, which was further investigated via spectroelectrochemical methods.

2.3. Photoelectrochemical Investigations

Although the macrostructural properties of the different investigated systems are similar, the semiconductor–noble metal interface as well as the distribution of the noble metal particles (i.e., the nanostructure of the co-cryogelated systems) essentially differ. As cryogelation is a physical method, the surface ligands play an important role in the nature of the connection between the building blocks. The aforementioned points are of central importance in terms of the charge carrier dynamics in the hybrid cryoaerogels.

To reveal these differences, spectroelectrochemical measurements have been performed. Linear sweep voltammetry (LSV)

was applied to shed light on the photocurrent directions and the photocurrent intensities as a function of the applied bias potential. Moreover, as a deeper insight into shorter time scales of the electrochemical response upon irradiation, intensity modulated photocurrent spectroscopy (IMPS) was used to gain resolutions up to the microsecond range. IMPS is a frequency dependent measurement technique where the photocurrent is monitored via sinusoidally modulated light pulses.^[49] By varying the frequency of the light pulses, the evolution of the photocurrent from microseconds to seconds can be monitored. A detailed description of the measurement is given in the (Supporting Information). In the following, different cryoaerogel systems will be compared and discussed: cryoaerogels prepared from the pristine semiconductor NPLs or NRs, from semiconductor/metal NPLs or NRs as well as from the mixed semiconductor and metal nanoparticles.

2.4. Nanoplatelet-Based Hybrid Cryoaerogels

The results of the photoelectrochemical characterization of the NPL-Pt hybrid cryoaerogels are displayed in Figure 4. From the LSVs (Figure 4A–C), the total photocurrent amount and direction in the equilibrium state dependent on the applied bias potential can be derived. Pristine CdSe/CdS NPLs (Figure 4A) show solely positive photocurrents which increase with

increasing bias potential. Hence, hole scavenging from the valence band is expectedly favored over electron transfer from the conduction band especially at high bias potentials.^[43,50] In the low bias potential region, no net photocurrent is produced by the system, only a remarkable decrease of the dark current due to increased proton reduction is visible. These characteristics are related to the high exciton binding energy in the NPL system, which is a clear difference compared to the NRs (Section 2.5). For the Pt-decorated NPLs (Figure 4B) and the mixed system (Figure 4C), this feature becomes even more pronounced due to the presence of the noble metal particles. In addition, both platinum-containing systems are characterized by lower overall photocurrents compared to the pristine CdSe/CdS NPL system. This effect might have been caused by a comparably high light absorption of the Pt particles and/or electron back transfer processes from the metal to the semiconductor domain. However, the contribution of the latter processes is negligible due to the chosen irradiation wavelength and intensity. Remarkable amounts of negative net photocurrents are only generated by the cryoaerogel consisting of h-NPLs.

By means of IMPS, the time-dependent charge carrier dynamics was investigated more in depth. In case of the h-NPL system, a turnaround from negative to positive photocurrents can be noticed at low negative bias potentials (–150 to 0 mV). Hence, processes leading to negative photocurrents, namely, proton reduction and electron transfer from the electrode,

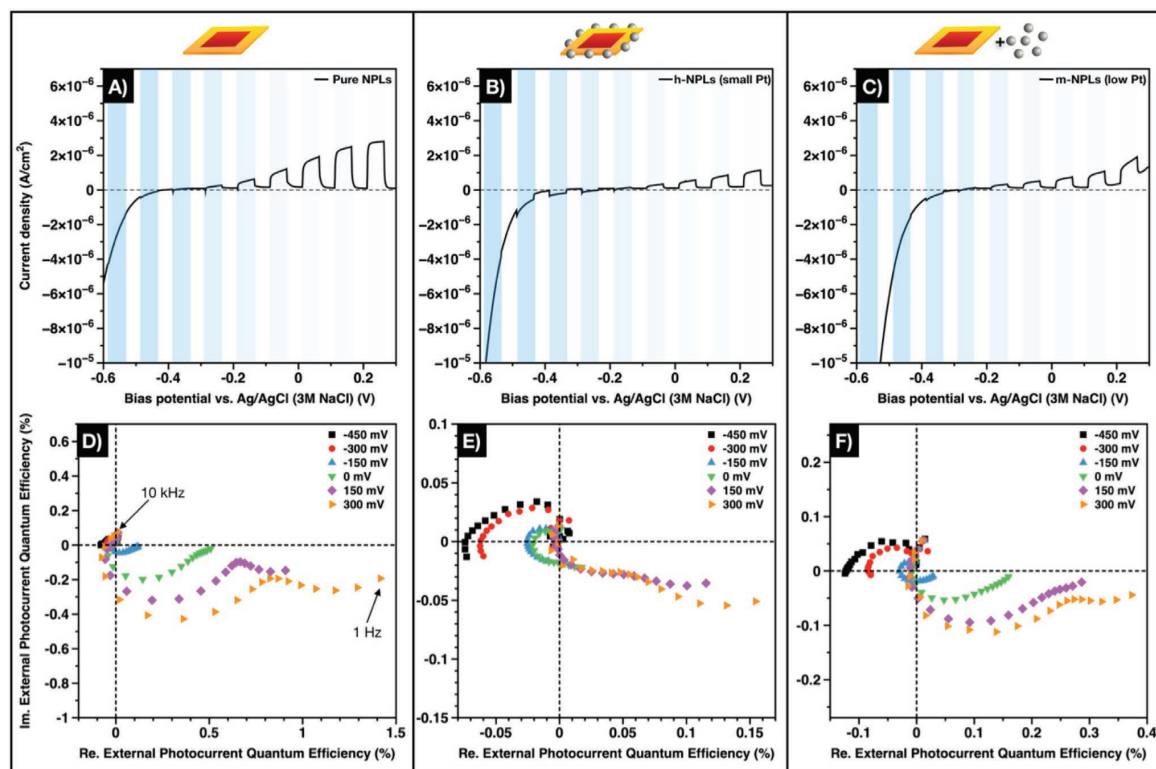


Figure 4. A–C) LSVs and D–F) IMPS Nyquist plots of cryoaerogel coatings prepared from pure CdSe/CdS NPLs (A,D), h-NPLs (B,E), and m-NPLs (C,F). Blue shaded areas represent the regimes where the sample was illuminated.

are faster than the corresponding processes leading to positive photocurrents. Upon further decreasing the bias potential, the IMPS does not cross the imaginary axis but remains close to the equilibrium (real axis) at low frequencies. A similar behavior cannot be observed for pure CdSe/CdS NPLs. In this system, the net photocurrent at high bias potentials is orders of magnitudes higher than the net photocurrent at low bias potentials. The described differences in the photoelectrochemical properties of both systems can be attributed to the metal particles grown directly onto the surface of the nanoplatelets. Due to the high electron affinity of Pt and the Fermi level of Pt being located within the bandgap of the CdS, efficient charge carrier separation takes place at the semiconductor–metal interface.^[50] Hence, in h-NPLs, holes will accumulate in the semiconductor domain, more specifically in the CdSe core, whereas electrons will preferably be located in the metal domain upon irradiation.^[33] This leads to enhanced charge carrier lifetimes and a strongly increased availability of the excited electrons for electrochemical reactions. However, in pristine NPLs, the band alignment facilitates the recombination of both charge carriers in the CdSe core due to the high exciton binding energy, unless an external driving force (e.g., a bias potential) is applied. It must be noted, that the m-NPL system also shows negative photocurrents, though only at low bias potentials (lower than -300 mV). Due to the high ionic strength of the electrolyte, electron transfer can take place between the semiconductor and the metal nanoparticles, however, the higher interparticle distances decrease the efficiency of this transfer significantly.^[28]

In a cryoaerogel, the single NPLs are in close proximity to each other forming stable sheets as can be seen in the TEM images (Figure 2A,B,E,F). This morphology allows the movement of charge carriers within the semiconductor backbone at certain bias potentials. In the IMPS, electron diffusion is reflected in the appearance of a second low-frequency semicircle especially at high bias potentials.^[11,12,43,51] For pristine NPLs, the high frequency semicircle has a larger diameter than the low frequency semicircle, implying that direct electron transfer at the electrode–particle interface contributes more effectively to the photocurrent than electron diffusion processes from electrode–far sites through the gel network to the electrode. A similar behavior can be observed for the m-NPL cryoaerogel, which indicates that Pt is likely not in direct contact with semiconductor platelets. This can be explained by the assumption that in this system both types of building blocks are separated by organic ligands and not in direct contact of the inorganic parts. Similar to other noble metals, Pt has a high sulfur affinity, hence MUA cannot be easily stripped from the surface. This assumption is further corroborated by the fact, that the m-NPL cryoaerogels are still strongly luminescent. In contrast, the luminescence is fully quenched in case of on-grown h-NPLs or their cryoaerogels. The IMPS response of the on-grown system is characterized by an inverted ratio of both semicircles compared to the other systems. To reveal the influence of the Pt load on the structural and spectroelectrochemical properties, cryoaerogels from hybrid NPLs with more Pt domains as well as from mixed solutions of NPLs and more Pt NPs were prepared (Figures S10 and S11, Supporting Information, show the structural properties). According to our expectations, the inverted semicircle ratio is even more pronounced for

NPLs with more on-grown Pt domains (Figure S12, Supporting Information). Thus, it can be attributed to the direct contact between CdS and the Pt domains in the epitaxially grown systems.

In summary, the photoelectrochemical response of all NPL systems shows important differences governed by the nanoscopic design of the corresponding systems. Notable amounts of negative photocurrents are only produced by h-NPLs, that is, nanoplatelets with directly on-grown Pt particles. This behavior was related to the highly effective charge carrier separation at the semiconductor/metal interface. In addition, the IMPS response of this system at high bias potential, more precisely the ratio of the two semicircles, was inverted if compared to the pristine CdSe/CdS NPLs and the mixed system. This result means that efficient charge carrier separation in cryoaerogels can be achieved by direct synthesis of Pt particles on the semiconductor surface and subsequent gelation but not by co-cryogelation of CdSe/CdS NPLs and Pt particles.

2.5. Nanorod-Based Hybrid Cryoaerogels

Model systems prepared from CdSe/CdS NRs and Au show similar spectroelectrochemical responses to the NPL-based cryoaerogels. Figure 5 shows the LSVs and the IMPS Nyquist plots of the nanorod-based samples. In the LSV measurements (Figure 5A–C), both hybrid cryoaerogels (h-NRs and m-NRs) as well as the pristine semiconductor cryoaerogels show a dominating positive photocurrent over the entire bias potential range, which is similar to the observations of Miethe et al. for semiconductor xerogels prepared by chemical destabilization.^[51]

Major differences in the photocurrent evolution can be observed in the negative bias potential range. In case of the pure NRs and the mixed m-NRs, transients with higher positive photocurrents can be observed at negative bias potentials directly after the beginning of the illumination. Importantly, these transients cannot be observed for the semiconductor–metal hybrid nanoparticle cryoaerogel. Furthermore, this course of the photocurrent is of a significant difference compared to the NPL systems. Due to the high exciton binding energy emerging in the NPLs, the charge mobility is less efficient and thus no transients in the LSV measurements occur. The high positive photocurrent and the following decrease to an equilibrium is correlated to an electron transfer toward the ITO electrode and a back electron transfer from the electrode to the nanoparticle gel network.^[52] This indicates that the electron transfer from the semiconductor to the ITO electrode outweighs the electron transfer from the semiconductor into the solution in case of pristine nanorods. For mixed semiconductor and metal nanoparticles, the same behavior can be observed. Meaning, the electron transfer from the semiconductor to the ITO electrode dominates over the transfer from the semiconductor to the metal particles and further the transfer into the solution. In the LSV of the semiconductor/metal hybrid nanoparticle gels (h-NRs) no transients are visible which contrasts with the other two systems. Consequently, the transfer from the semiconductor to the metal domains and from the metal domain into the solution is competing with the transfer of electrons from the semiconductor to the ITO electrode (Figure S13,

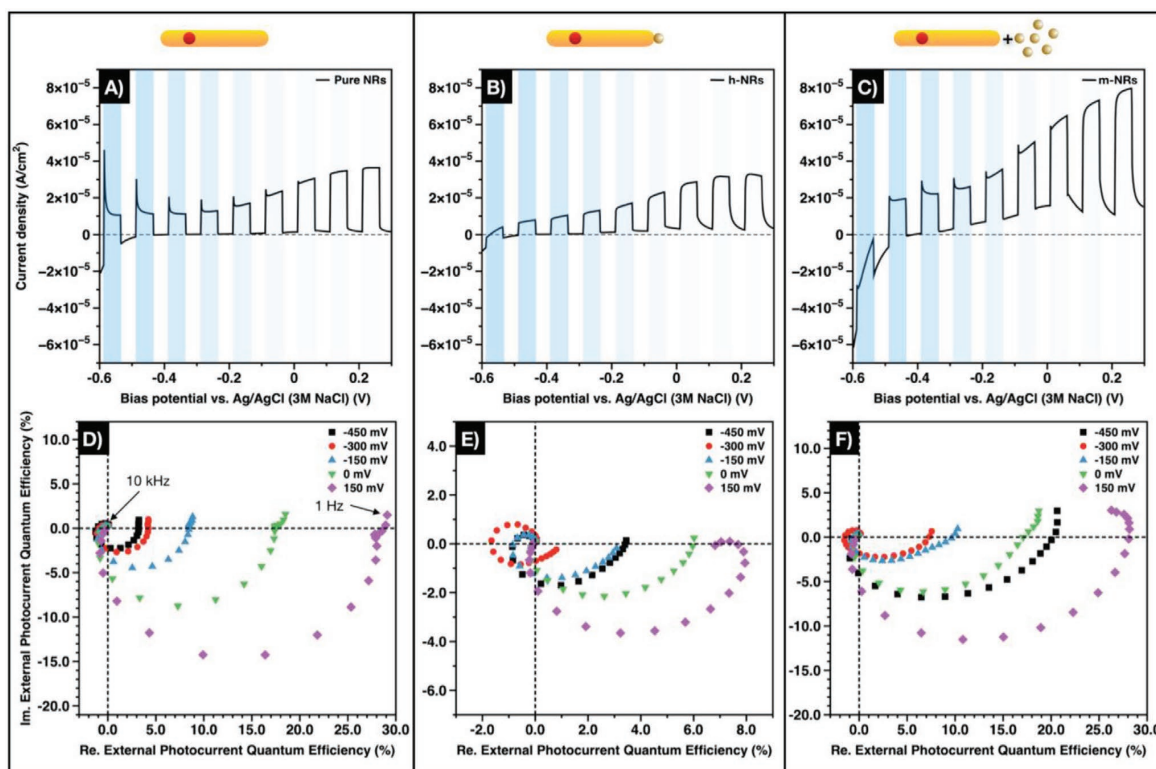


Figure 5. A–C) LSVs and D–F) IMPS Nyquist plots of cryoerogel coatings prepared from pure CdSe/CdS NRs (A,D), h-NRs (B,E), and m-NRs (C,F). Blue shaded areas represent the regimes where the sample was illuminated.

Supporting Information). The competing processes lead to a reduced electron transfer to the ITO electrode resulting in diminished photocurrent transients at high positive photocurrents. This firstly implies a significant difference between the mixed (m-NRs) and the grown semiconductor–metal hybrid cryoerogels (h-NRs) regarding the charge carrier dynamics. At more positive bias potentials, the LSV measurements of all three systems have the same course and no significant differences can be found. The back electron transfer is then less favored and the transfer of the electrons to the ITO electrode becomes more probable.^[52] Additionally, the bias potential is close to the Fermi level of the semiconductor–metal systems which leads to a less favorable transfer of the electrons to the metal domain or metal particles.^[53] Consequently, the semiconductor component dominates the photocurrent response at positive bias potentials.

The IMPS measurements support the results of the LSVs and give further insight into the charge carrier dynamics. Differences in the IMPS spectra can also be observed mainly for negative bias potentials. The mixed semiconductor and metal nanoparticle cryoerogel (m-NRs) shows similar spectra to the pure semiconductor nanorods. In this case, the measured photocurrent is positive for all measured bias potentials (from –450 to 150 mV). As discussed at the LSV measurements, the electron transfer from the semiconductor to the ITO electrode is dominant which leads to the formation of semicircles

with a positive photocurrent. Since the maximum timescale of illumination is one second (equals to 1 Hz) for the IMPS measurements, the back electron transfer is likely to occur at even longer illumination durations. Nevertheless, the signs of trapped charge carrier recombination appear in the low-frequency regime, which become more prominent for the pure NR and mixed cryoerogels (m-NRs). This manifests in the IMPS response in the first quadrant at very low frequencies, which is significantly suppressed for the h-NR structure indicating a mechanism with less loss in the charge carrier transport for the NRs with on-grown Au domains. Another characteristic which is known for connected semiconductor nanoparticle networks is that the IMPS spectra consist of more than one semicircle due to a photocurrent contribution of electrons which reach the electrode from particles locating further from the electrode.^[43] This implies that the electrons can travel through larger fragments of the network by applying a potential gradient.^[10,11,16] Consequently, even if in the cryoerogel system the NRs are partially separated via organic ligands, positive bias potentials can represent enough driving force to tunnel the electrons one rod to another, similarly to the NPL networks discussed above. This becomes prominent at lower frequencies resulting in not two distinct semicircles but in an elongation of the semicircles toward higher positive photocurrents. This elongation implies that the two semicircles overlap and manifest in a superposition of the two occurring processes: the direct

electron transfer from the semiconductor particles to the ITO (for the first several layers of particles) and electron transfer throughout the network to the ITO.

In contrast, the cryoaerogel which consists of semiconductor/metal hybrid nanoparticles (Figure 5B) has different characteristics at negative bias potentials. For high frequencies, remarkable negative photocurrents evolve and reach a maximum at a certain frequency followed by a turnaround toward positive currents. At low frequencies, all spectra end in the positive photocurrent region that is consistent with the photocurrents measured via LSV. The evolving negative photocurrents at high frequencies indicate that the electron transfer from the semiconductor to the metal domain and the transfer into the solution are dominating. The mechanism for the photocurrent evolution in semiconductor/metal hybrid nanoparticles is discussed more detailed in our recent study.^[44]

The results indicate that the NR-based and the NPL-based systems behave similarly and the nature of the interparticle connection between the semiconductor and metal components governs the charge carrier dynamics. Differences between the NR and NPL systems are attributed to the large exciton binding energy in the NPLs which leads to a lower charge carrier mobility. Pure semiconductor (NR and NPLs) cryoaerogels only provide positive photocurrent whilst the use of semiconductor–metal hybrid nanoparticles enables a charge carrier separation within the different materials and the transfer of the electron into the solution, where it can be consumed by redox reactions. Mixing semiconductor and metal nanoparticles results in a decrease of the photocurrent and solely a low negative photocurrent in case of the NPL system. From photoelectrochemical point of view, properties of m-NR cryoaerogels differ significantly from the cryoaerogels of h-NRs. Importantly, these differences between the mixed and on-grown systems underline the importance of the semiconductor–metal crystal contact. While there is a direct contact between the two components for the h-NR and h-NPL networks (originating from the epitaxial contact of the metal to the semiconductor), the indirect contact dramatically affects the properties in mixed and co-gelated systems. This is likely a consequence of the presence of covalently bound ligands on both building blocks hindering the efficient electron transfer from the semiconductor toward the metal particles.^[28] Thus, the physical forces during the cryogelation do not overcome the repulsive forces of the ligands in contrast to the citrate-stabilized metal nanoparticle-based cryogels.^[45,46] Therefore, heterogeneous nucleation of the metal directly on the semiconductor and the resulting large crystal contact endows the cryoaerogels with advantageous properties in terms of charge carrier separation, which makes them a promising candidate for photoelectrochemical sensing purposes.

3. Conclusion

In summary, this work shows that the physicochemical properties are strongly dependent on the nanoscopic and microscopic structural architecture in multicomponent aerogels consisting of semiconductor and noble metal nanoparticles. The nanoscale design of the building blocks has a great influence on the photoelectrochemical properties in hybrid cryoaerogel structures. Pure

semiconductor, hybrid semiconductor/noble metal and mixed semiconductor–noble metal NCs were cryogelated into porous aerogels on conductive substrates to shed light on the efficiency of the charge carrier separation upon different approaches. While the cryoaerogel structures show similar macrostructural properties, the distribution of the noble metal and the semiconductor–metal interface are of essential difference at the nano- and microscale. Homogeneous distribution of noble metal domains can be ensured for cryoaerogels of NRs and NPLs with on-grown metal domains. However, the mixing and co-gelation led to an uncontrollable distribution of the network components. Additionally, the direct contact of the metal to the semiconductor compartments can be formed in case of on-grown metal domains (h-NRs and h-NPLs). Structural differences alter the charge carrier dynamics significantly: while charge carrier delocalization in the semiconductor backbone governs the spectroelectrochemical response in pure and mixed systems (m-NRs and m-NPLs), charge carriers can effectively be separated in cryoaerogels from semiconductor building blocks with on-grown noble metal domains. This underlines the limitation of simple mixing and co-cryogelation in terms of charge carrier separation due to the arbitrary distribution and presence of ligands hindering the effective electron accumulation in the metal domains upon photoexciting the semiconductor counterparts. These results further imply that the physical forces appearing during the cryogelation cannot overcome the ligand shell repulsion in the mixed systems. Therefore, in mixed cryoaerogels (m-NRs and m-NPLs), tailoring the nanoscopic and microscopic structure regarding the component distribution, contact points of the components as well as the organic ligand shell possibly residing between the nanoparticles, is of essential importance. These findings point toward the utilization of hybrid cryoaerogel coatings in photocatalysis and spectroelectrochemical sensing.

4. Experimental Section

Chemicals: Sodium myristate ($\geq 99\%$), methanol (MeOH, $\geq 99.8\%$), cadmium acetate (99.995%), 1-octadecene (ODE, 90%), ethanol (EtOH, $\geq 99.8\%$), sulfur (S, $\geq 99.98\%$), isopropanol (iPrOH, $\geq 99.8\%$), 11-mercaptoundecanoic acid (MUA, 95%), iron(0) pentacarbonyl (Fe(CO)₅, 99.99%), tri-*n*-octylphosphine oxide (TOPO, 99%), 1,2,3,4-tetrahydronaphthalene (tetraline, 99%), oleylamine (OAm, 70%), 3-mercaptopropionic acid (MPA, 99%), didodecyltrimethylammonium bromide (DDAB, 98%), dodecylamine (DDA, 98%), and toluene ($\geq 99.7\%$) were purchased from Sigma Aldrich. Tri-*n*-octylphosphine (TOP, 97%), platinum(II) acetylacetonate (Pt(acac)₂, 98%), gold(III) chloride (AuCl₃, 99%), and cadmium acetate dihydrate (98%) were obtained from ABCR. Oleic acid (OAc, 90%), cadmium nitrate tetrahydrate (99.999%), selenium (Se, 200 mesh, 99.999%), cadmium oxide (CdO), hydrogen tetrachloroaurate(III) trihydrate (HAuCl₄·3H₂O, 99.99%), and borane *tert*-butylamine complex (TBAB, 97%) were supplied by Alfa Aesar. *n*-hexane ($\geq 99\%$) was purchased from Merck. Oleylamine (OAm, 80%–90%) was supplied by Acros. Hexylphosphonic acid (HPA, 99%) and octadecylphosphonic acid (ODPA, 99%) were purchased from PCI Synthesis. All chemicals were used as received without further purification. ODE applied for the preparation of TOP-S was degassed in vacuum at 100 °C for at least 6 h and stored in an air-free glovebox.

Synthesis of Cadmium Myristate: Cadmium myristate was synthesized following a literature procedure^[9] without modifications.

Synthesis of CdSe Core Nanoplatelets (NPLs): Quasi-rectangular CdSe NPLs with a thickness of four MLs were synthesized according to literature procedures^[43,54] with slight modifications. Briefly, 1360 mg

(2.40 mmol) of cadmium myristate and 96 mg (1.22 mmol) of Se were dispersed in 120 mL of ODE in a 250 mL three-neck flask. The reaction solution was degassed in vacuum twice for 30 min at 70 °C and was afterward heated to 240 °C under an Ar atmosphere. At 205 °C, a mixture consisting of 160 mg (0.60 mmol) of solid cadmium acetate dihydrate and 138 mg (0.60 mmol) of solid cadmium acetate was added swiftly to the reaction solution. After 9.5 min at 240 °C, 4 mL of OIAC was injected and the reaction was continued for further 30 s. The heating mantle was removed and further 4 mL of OIAC were added at ≈160 °C. The reaction solution was purified by adding 40 mL of EtOH followed by centrifugation (4226 rcf, 10 min). The precipitates were redispersed in 60 mL of *n*-hexane and centrifuged again (4226 rcf, 10 min) to remove 3 mL NPLs. To the supernatant, 30 mL of ethanol was added. The four mL NPLs were collected by centrifugation (4226 rcf, 10 min) and were redispersed in 6 mL of *n*-hexane.

Synthesis of CdSe/CdS Core/Crown NPLs: To synthesize CdSe/CdS core/crown NPLs, a slightly modified literature procedure^[55] was applied. In a 100 mL three-neck flask, 288 mg (1.08 mmol) of cadmium acetate dihydrate, 540 μL (1.70 mmol) of OIAC, and 2660 μL [calculated OD at first excitonic maximum (507 nm): 120.00] of the CdSe NPLs in *n*-hexane were dispersed in 24 mL of ODE. Subsequently, the solution was degassed in vacuum for 45 min at 60 °C. Under an Ar atmosphere, the dispersion was heated to 240 °C. Starting at 215 °C, a solution of 1100 μL 1 M TOP:S (prepared by dissolving elemental sulfur in TOP under stirring overnight in a glovebox) in 7.9 mL of ODE was injected with a syringe pump at a constant rate of 18 mL h⁻¹. After completion of the injection, the solution was kept at 240 °C for another 40 min and afterward allowed to cool down to room temperature. The product was collected by addition of 10 mL of *n*-hexane and 20 mL of ethanol followed by centrifugation (4226 rcf, 10 min). The NPLs were redispersed in *n*-hexane (5 mL).

Platinum Growth on CdSe/CdS Nanoplatelets: For the platinum growth, a procedure by Naskar et al.^[56] with slight modifications was applied. At first, 89.7 mg (0.23 mmol) of Pt(acac)₂, 1 mL (3.03 mmol) of OIAC, 354 μL (Cd ion concentration: 131.18 mmol L⁻¹) of the CdSe/CdS NPLs in *n*-hexane, and 30 mL of ODE were combined in a 100 mL three-neck flask. The *n*-hexane was removed carefully in vacuum at room temperature and the dispersion was heated to 130 °C under an Ar atmosphere. Depending on the desired Pt size the solution was kept at this reaction temperature for 30 min (smaller domains, shown in the main text) and 60 min (larger domains, shown in the Supporting Information), respectively. To collect the Pt decorated NPLs, 45 mL of *i*PrOH and 60 mL of EtOH were added and the solution was centrifuged (4226 rcf, 10 min). Finally, the solids were redispersed in *n*-hexane (3 mL).

Synthesis of Spherical Pt NPs: Pt NPs were synthesized according to Naskar et al.^[14] with slight modifications. Briefly, 200 mg (0.51 mmol) Pt(acac)₂ and 1 mL (3.03 mmol) of OIAC were dispersed in 15 mL of ODE and degassed in vacuum at 40 °C for 45 min. Under an Ar atmosphere, the temperature was raised to 120 °C within 30 min. At this temperature, 120 μL of a previously prepared 1:10 (v:v) mixture of Fe(CO)₅:ODE was injected with a syringe. The reaction temperature was then increased by 5 °C min⁻¹ to 180 °C and the heating mantle was removed. At room temperature, 20 mL of *i*PrOH and 30 mL of EtOH were added and the solution was centrifuged (8000 rcf, 10 min). The Pt NPs were redispersed in 3 mL of *n*-hexane.

Phase Transfer of CdSe/CdS NPLs, CdSe/CdS/Pt h-NPLs, and Spherical Pt NPs: CdSe/CdS NPLs, CdSe/CdS/Pt h-NPLs, and Pt NPs were transferred to aqueous medium following a slightly modified literature protocol.^[57] For the phase transfer of CdSe/CdS NPLs, 500 μL of the organic NPL solution was mixed with 2.5 mL of *n*-hexane and 4.24 mL of the phase transfer solution. CdSe/CdS/Pt NPLs were transferred by adding 3 mL of *n*-hexane and 5.63 mL of the phase transfer solution to 2.25 mL of the NPL solution. In both cases, the phase transfer solution consists of 280 mg (1.28 mmol) of MUA and 165 mg (2.94 mmol) of KOH dissolved in 20 mL of MeOH. For the phase transfer of spherical Pt NPs, 0.5 mL of the NP solution and 5.5 mL of *n*-hexane were mixed with 4 mL of the phase transfer solution. In this case, the phase transfer

solution consists of 30 mg (0.14 mmol) of MUA, 50 mg (0.89 mmol) of KOH, and 4 mL of MeOH. After mixing the solutions, the nanoparticles were shaken overnight to ensure complete transfer to the aqueous medium.

Afterwards, the vials were left undisturbed to separate the phases. The organic phase was removed and the methanolic phase was centrifuged (4226 rcf, 10 min). The solids were dispersed in 15 mL of 0.01 M KOH each and washed with 60 mL of 0.01 M KOH by means of a centrifuge filter. The centrifugation time of the last step was adjusted so that final solution volumes between 250 μL (CdSe/CdS/Pt NPLs and Pt NPs) and 500 μL (CdSe/CdS NPLs) were reached.

Synthesis of CdSe Core Nanoparticles (Seeds): The CdSe seeds were synthesized according to Carbone et al.^[58] Typically, CdO (60 mg), ODPA (280 mg) and TOPO (3.0 g) were mixed in a 25 mL flask and were degassed in vacuum at 150 °C for 1 h. At 300 °C in an Ar atmosphere, the solution was stirred until CdO is dissolved to obtain a clear solution. At this point, TOP (1.8 mL) was added, and the mixture was heated to 380 °C. A solution of selenium (58 mg) in TOP (1.8 mL) was swiftly injected and the reaction was quenched after 4 min by the addition of 4 mL ODE. The heating mantle was removed, and the seed solution was allowed to cool down to 90 °C, where 5 mL of toluene was added (to prevent the solidification of TOPO). The as-synthesized particles were purified by alternating addition of methanol (precipitation), centrifugation (8000 rcf, 10 min) and redispersion in toluene. The particles were finally stored in hexane and kept for CdSe/CdS shell growth.

Synthesis of CdSe/CdS Core/Shell NRs: The as-synthesized CdSe seeds were coated with an elongated CdS shell using the procedure of Carbone et al.^[58] with slight modifications. First, CdO (60 mg), HPA (80 mg), ODPA (280 mg), and TOPO (9.0 g) were degassed under vacuum at 150 °C for 1 h. The solution was heated to 300 °C in an Ar atmosphere until CdO was completely dissolved. After the addition of TOP (1.8 mL), the solution was heated to 350 °C. At this point, the mixture of CdSe seeds (0.08 μmol), sulfur (130 mg), and TOP (1.8 mL) was quickly injected, and the reaction was stirred for 8 min before cooling down to room temperature. During the cooling, 5 mL of toluene was added at 90 °C. The CdSe/CdS NRs were purified by precipitation with methanol, centrifugation (3773 rcf, 10 min) and redispersion in toluene. This step is repeated three times before the CdSe/CdS NRs were finally stored in toluene (12 mL).

Gold Growth on CdSe/CdS NRs: According to the method published by Menagen et al.^[38] AuCl₃ (10 mg), DDA (161.76 mg), and DDAB (101.2 mg) were mixed with toluene (24.12 mL) in a glovebox. The mixture was ultrasonicated for 15 min. When the solution became light yellow, it was mixed with the CdSe/CdS NR solution in toluene (27.2 mL, c_{Cd} = 0.156 mg mL⁻¹) inside a glove box. The mixture was irradiated with an LED (Ledxon Alustar 9008098, λ = 470 nm, operated at 350 mA) for 45 min under stirring. Afterward, methanol (20 mL) was added to quench the reaction, and the solution was centrifuged. Furthermore, the particles were washed twice with methanol and redispersed finally in toluene (2 mL).

Synthesis of Spherical Au NPs: Spherical Au NPs were synthesized according to Peng et al.^[59] in organic medium. HAuCl₄·3H₂O (100 mg) was dissolved in a mixture of tetraline (10 mL) and OAm (10 mL) at room temperature and ambient conditions by 10 min of stirring. TBAB (34.5 mg), tetraline (1 mL), and OAm (1 mL) were sonicated to dissolve the TBAB. The TBAB solution was quickly injected into the Au containing solution and stirred for 2 h at room temperature. For the purification of the particles, the solution was divided into multiple parts and separately precipitated with ethanol (35 mL per 11 mL synthesis solution) in 50 mL Falcon tubes. After centrifugation (8500 rcf, 10 min), the Au NPs were redissolved in toluene (5 mL).

Phase Transfer of CdSe/CdS NRs: The phase transfer was carried out by ligand exchange from TOP/TOPO to MPA according to Kodanek et al.^[57] Colloidal CdSe/CdS solution in toluene (12 mL) was precipitated with methanol (12 mL) and redispersed in hexane (12 mL). A mixture of methanol (100 mL), MPA (2.6 mL), and KOH (1.14 g) was prepared and added to the 12 mL of NRs in hexane followed by shaking for 2 h at room

temperature. After phase separation, the NRs were centrifuged (10 min, 8500 rcf), redispersed in 0.01 M KOH (5 mL) solution and treated with 2 mL of chloroform to remove the excess of organics. After vortexing, the mixture was centrifuged (10 min, 8500 rcf) and the colloidal NR solution was carefully collected from the upper phase. Finally, the aqueous phase of CdSe/CdS was five times washed with centrifugation filters (30 k MWCO) and 0.01 M KOH (7 mL). The final concentration of NRs was determined by atomic absorption spectroscopy (AAS) measurements and set to $\approx 80 \times 10^{-6}$ M.

Phase Transfer of Spherical Au NPs: The phase transfer of spherical Au NPs according to Hiramatsu et al.^[60] was carried out by addition of MPA (4.5 mL) to a boiling solution of Au NPs in toluene (44 mg NPs in 90 mL toluene). The NPs were immediately precipitated as a black solid. After centrifugation (10 min, 8500 rcf) the particles were redispersed in 0.01 M KOH (1 mL) and purified by centrifugation filters (30 k MWCO) as for CdSe/CdS. Finally, Au NPs concentration was determined by AAS measurements and set to $\approx 80 \times 10^{-6}$ M.

Phase Transfer of Gold Tipped CdSe/CdS/Au h-NRs: The method of the phase transfer was adapted from the work of Kodanek et al.^[57] The gold decorated particles were precipitated with methanol, centrifuged and redispersed in hexane (10 mL). The cadmium concentration was ≈ 0.4 mg mL⁻¹. After the addition of methanol (10 mL) and MPA (0.125 mL) the mixture was shaken for 1 h. The methanolic phase including the particles was separated and centrifuged. After redispersion of the nanorods in 0.01 M aqueous KOH solution (2 mL), the particles were washed five times with acetone and finally redispersed in 0.01 M aqueous KOH solution (300 μ L).

Preparation of Cryo-aerogel-Coated ITO Electrodes: Before coating the electrodes with the particles, the ITO-coated glass substrates (VisionTek Ltd., 12Ω square⁻¹, size of $1.5 \text{ cm} \times 3 \text{ cm}$) were cleaned and activated. For cleaning, the substrates were subsequently sonicated for 5 min in acetone, 2-propanol, and Millipore water. Afterward, the surface was activated with a solution of NH₄OH and H₂O₂ (10 mL 25% NH₄OH, 10 mL 35% H₂O₂) in water (50 mL) for 2 h at 70 °C under stirring. Next, the ITO surface was functionalized with 1 vol% MPTMS in toluene for 2 h at 70 °C under stirring. A mold ($0.75 \text{ cm} \times 0.75 \text{ cm}$ for all nanorod samples and $1.0 \text{ cm} \times 1.0 \text{ cm}$ for nanoplatelet samples, respectively) was fabricated from adhesive tape and $20 \mu\text{L cm}^{-2}$ of the nanoparticle solution ($c(\text{Cd}^{2+}) = 70 \times 10^{-3}$ M, in case of mixed systems with the addition of 2 μL Au NP $c(\text{Au}^{3+}) = 31 \times 10^{-3}$ M) were distributed inside the rectangular mold (see more details in Table S1, Supporting Information). To flash-freeze the aqueous nanoparticle solutions, the electrodes were placed on the surface of liquid 2-methylbutane (temperature: -160 °C) until the solution was frozen. Afterward, the electrodes were stored in liquid nitrogen overnight before drying the electrodes in the freeze dryer or in a freezer (at -20 °C), respectively.^[43,45-47]

Photoelectrochemical Measurements: Photoelectrochemical measurements were carried out in a lab-designed Teflon cell, in which the prepared cryo-aerogel coatings were carefully rehydrated by the supporting electrolyte (discussed below). For intensity modulated photocurrent spectroscopy, the current response of the electrochemical cell was measured while irradiating the cryo-aerogel sample with an LED light source operating at frequencies between 10 kHz and 1 Hz. Hereby, the value of the generated photocurrent and the phase shift between the sinusoidal light pulses and the sinusoidal current signal is measured. For this detection, a lock-in amplifier controls the sinusoidal light pulses with the specific frequency and links the outgoing signal to the incoming photocurrent detected by the potentiostat. A lock-in amplifier is necessary because a potentiostat in general is not able to adequately register the low and rapidly changing currents in the nA range, where the noise of the system is larger than the signal itself. These measurements were applied at different bias potentials between -450 and 150 mV (-450 , -300 , -150 , 0 , 150 , 300 mV). All given bias potentials are related to the applied Ag/AgCl reference electrode (3 M NaCl, purchased from BASi). As electrolyte, a 0.5 M solution of sodium sulfite in Millipore water was applied throughout all measurements. The pH of the electrolyte solution was adjusted to 7 by addition of sulfuric acid prior to use. A PE 1542 DC power supply from PHILIPS powers the LED (0.5 mW, $\lambda = 472$ nm)

and a Signal Recovery 7270 DSP lock-in amplifier from AMETEK gives the sinusoidal signal to the LED as well as detects the current signal from the measurement cell. A Solatron Modulab XM potentiostat from AMETEK was used to apply the bias potential and to measure the generated photocurrents.

Measuring the linear sweep voltammetry includes a scan of a predefined bias potential range over a fixed time range. In the experiments, the voltage was applied from -0.6 V up to 0.3 V with a slope of 4 mV s^{-1} . Before starting the measurement, a constant potential was applied for 30 s at the starting voltage of -0.6 V to reach the equilibrium state of the system. During the linear sweep voltammetry, the LED was turned on and off periodically with a frequency of 40 mHz. This corresponds to a time period of 12.5 s of irradiation and 12.5 s of darkness. To apply the voltage and to register the current, a potentiostat (Solatron Modulab XM from AMETEK) was used. The LED was controlled by an arbitrary generator HMF2550 from Rohde & Schwarz.

Optical Spectroscopy: For the optical characterization, the nanoparticle solutions were diluted with the respective solvent and measured in quartz cuvettes with a volume of 1 or 3 mL (optical path length of 1 cm). UV-vis extinction spectra of the samples were recorded by means of a Horiba Dual-FL, a Jasco V750, or an Agilent Cary 5000 UV-vis-NIR spectrophotometer. Emission measurements (PL emission spectra and photoluminescence quantum yields, PLQYs) were carried out on a Horiba Dual-FL (equipped with a Quanta-Phi integrating sphere for PLQY), a Horiba Fluoromax-4 or an Edinburgh Instruments FLS 1000 spectrofluorometer.

UV-vis absorption spectra of the cryo-aerogel coatings were measured by means of an Agilent Cary 5000 UV-vis-NIR spectrometer equipped with DRA-2500 integrating sphere. The measurements were carried out in center-mount position and the sample holder was tilted by 10° to ensure nearly perpendicular irradiation of the coating and to prevent direct back reflection to the optical illumination path.

Transmission Electron Microscopy: For TEM imaging, a FEI G2 F20 TMP equipped with a field emission gun operating at 200 kV was applied. Images were either taken by means of a bright-field detector or a high-angle annular dark field (HAADF) detector in scanning TEM (STEM) mode. Diluted nanoparticle solutions were drop-cast onto carbon coated copper grids (Quantifoil, 300 mesh). In case of the cryo-aerogels, the grid was gently pressed onto the cryo-aerogel coating to transfer gel fragments onto the grid.

Scanning Electron Microscopy: Scanning electron microscopy (SEM) images were taken using a JEOL JSM-6700F scanning electron microscope (operated at 2 kV). SEM samples were obtained by immobilizing the cryo-aerogel-coated ITO glasses on brass SEM holders using conductive paint (ACHESON 1415) to ensure the electrical contact between the ITO and the holder. SEM-EDX spectra were recorded in the energy range of 0–10 keV using an Oxford Instruments INCA 300 detector.

Atomic Absorption Spectroscopy: Cd and Au concentrations of the nanoparticle solutions were determined by AAS. Therefore, a certain amount of the solution was dried and mixed with 1 mL of aqua regia and left overnight for full metal dissolution. Afterward, the solution was diluted to 50 mL with MilliQ water. For all measurements, a Varian AA140 spectrometer equipped with hollow cathode lamps suitable to the different element absorption wavelengths was applied. The concentration of Pt was determined by SEM-EDX analysis.

Supporting Information

Supporting Information is available from the Wiley Online Library or from the author.

Acknowledgements

A.S. and J.S. contributed equally to this work. The authors would like to acknowledge the financial support from the European Research Council

(ERC) under the European Union's Horizon 2020 research and innovation program (Grant Agreement No. 714429). In addition, this work was funded by the German Research Foundation (Deutsche Forschungsgemeinschaft, DFG) under Germany's excellence strategy within the cluster of excellence PhoenixD (EXC 2122, project ID 390833453) and the grant BI 1708/4-1. D.Z. acknowledges the program financed by the National Research, Development and Innovation Office of the Ministry for Innovation and Technology, Hungary (TKP2021-NKTA-05). A.S. and R.T.G. are thankful for financial support from the Hannover School for Nanotechnology (hsn). The authors also thank Armin Feldhoff and Jürgen Caro for providing the SEM facility, and the LNQE for providing the TEM.

Open access funding enabled and organized by Projekt DEAL.

Conflict of Interest

The authors declare no conflict of interest.

Data Availability Statement

Research data are not shared.

Keywords

charge carrier separation, cryoaerogels, hybrid nanocrystal gels, semiconductor-metal hybrid gels, spectroelectrochemistry

Received: January 10, 2022

Published online: February 18, 2022

- [1] P. Rusch, D. Zámbo, N. C. Bigall, *Acc. Chem. Res.* **2020**, *53*, 2414.
- [2] B. Cai, V. Sayevich, N. Gaponik, A. Eychmüller, *Adv. Mater.* **2018**, *30*, 1707518.
- [3] C. Ziegler, A. Wolf, W. Liu, A.-K. Herrmann, N. Gaponik, A. Eychmüller, *Angew. Chem., Int. Ed.* **2017**, *56*, 13200.
- [4] D. Mongin, E. Shaviv, P. Maioli, A. Crut, U. Banin, N. Del Fatti, F. Vallée, *ACS Nano* **2012**, *6*, 7034.
- [5] E. Khon, A. Mereshchenko, A. N. Tarnovsky, K. Acharya, A. Klinkova, N. N. Hewa-Kasakarage, I. Nemitz, M. Zamkov, *Nano Lett.* **2011**, *11*, 1792.
- [6] M. Wächtler, P. Kalisman, L. Amirav, *J. Phys. Chem. C* **2016**, *120*, 24491.
- [7] Y. Nakibli, Y. Mazal, Y. Dubi, M. Wächtler, L. Amirav, *Nano Lett.* **2018**, *18*, 357.
- [8] F. T. Rabouw, P. Lunnemann, R. J. A. van Dijk-Moes, M. Frimmer, F. Pietra, A. F. Koenderink, D. Vanmaekelbergh, *Nano Lett.* **2013**, *13*, 4884.
- [9] M. D. Tessier, P. Spinicelli, D. Dupont, G. Patriarche, S. Ithurria, B. Dubertret, *Nano Lett.* **2014**, *14*, 207.
- [10] S. Sanchez-Paradinas, D. Dorfs, S. Friebe, A. Freytag, A. Wolf, N. C. Bigall, *Adv. Mater.* **2015**, *27*, 6152.
- [11] D. Zámbo, A. Schlosser, P. Rusch, F. Lübke, J. Koch, H. Pfnür, N. C. Bigall, *Small* **2020**, 1906934.
- [12] F. Lübke, J. F. Miethe, F. Steinbach, P. Rusch, A. Schlosser, D. Zámbo, T. Heinemeyer, D. Natke, D. Zok, D. Dorfs, N. C. Bigall, *Small* **2019**, *15*, 1902186.
- [13] F. Lübke, P. Rusch, S. Getschmann, B. Schremmer, M. Schäfer, M. Schulz, B. Hoppe, P. Behrens, N. C. Bigall, D. Dorfs, *Nanoscale* **2020**, *12*, 5038.
- [14] S. Naskar, A. Freytag, J. Deutsch, N. Wendt, P. Behrens, A. Köckritz, N. C. Bigall, *Chem. Mater.* **2017**, *29*, 9208.
- [15] S. Naskar, J. F. Miethe, S. Sánchez-Paradinas, N. Schmidt, K. Kanthasamy, P. Behrens, H. Pfnür, N. C. Bigall, *Chem. Mater.* **2016**, *28*, 2089.
- [16] P. Rusch, B. Schremmer, C. Strelow, A. Mews, D. Dorfs, N. C. Bigall, *J. Phys. Chem. Lett.* **2019**, *10*, 7804.
- [17] P. Rusch, F. Niemeier, D. Pluta, B. Schremmer, F. Lübke, M. Rosebrock, M. Schäfer, M. Jahns, P. Behrens, N. C. Bigall, *Nanoscale* **2019**, *11*, 15270.
- [18] A. Freytag, S. Sánchez-Paradinas, S. Naskar, N. Wendt, M. Colombo, G. Pugliese, J. Poppe, C. Demirci, I. Kretschmer, D. W. Bahnemann, P. Behrens, N. C. Bigall, *Angew. Chem., Int. Ed.* **2016**, *55*, 1200.
- [19] A. Freytag, C. Günemann, S. Naskar, S. Hamid, F. Lübke, D. Bahnemann, N. C. Bigall, *ACS Appl. Nano Mater.* **2018**, *1*, 6123.
- [20] A. Freytag, M. Colombo, N. C. Bigall, *Z. Phys. Chem.* **2017**, *231*, 63.
- [21] D. Wen, W. Liu, D. Haubold, C. Zhu, M. Oschatz, M. Holzschuh, A. Wolf, F. Simon, S. Kaskel, A. Eychmüller, *ACS Nano* **2016**, *10*, 2559.
- [22] D. Wen, A. Eychmüller, *Chem. Commun.* **2017**, *53*, 12608.
- [23] R. Deshmukh, E. Tervoort, J. Käch, F. Rechberger, M. Niederberger, *Dalton Trans.* **2016**, *45*, 11616.
- [24] F. J. Heiligtag, M. J. I. A. Leccardi, D. Erdem, M. J. Süess, M. Niederberger, *Nanoscale* **2014**, *6*, 13213.
- [25] F. Matter, A. L. Luna, M. Niederberger, *Nano Today* **2020**, *30*, 100827.
- [26] R. Du, J. Joswig, R. Hübner, L. Zhou, W. Wei, Y. Hu, A. Eychmüller, *Angew. Chem.* **2020**, *132*, 8370.
- [27] T. Hendel, V. Lesnyak, L. Kühn, A. K. Herrmann, N. C. Bigall, L. Borchardt, S. Kaskel, N. Gaponik, A. Eychmüller, *Adv. Funct. Mater.* **2013**, *23*, 1903.
- [28] M. Rosebrock, D. Zámbo, P. Rusch, D. Pluta, F. Steinbach, P. Bessel, A. Schlosser, A. Feldhoff, K. D. J. Hindricks, P. Behrens, D. Dorfs, N. C. Bigall, *Adv. Funct. Mater.* **2021**, *31*, 2101628.
- [29] D. Zámbo, A. Schlosser, R. T. Graf, P. Rusch, P. A. Kießling, A. Feldhoff, N. C. Bigall, *Adv. Opt. Mater.* **2021**, *9*, 2100291.
- [30] T. T. Guaraldo, J. F. de Brito, D. Wood, M. V. B. Zanoni, *Electrochim. Acta* **2015**, *185*, 117.
- [31] J. Y. Choi, K. M. Nam, H. Song, *J. Mater. Chem. A* **2018**, *6*, 16316.
- [32] K. D. Rasamani, Z. Li, Y. Sun, *Nanoscale* **2016**, *8*, 18621.
- [33] S. Naskar, F. Lübke, S. Hamid, A. Freytag, A. Wolf, J. Koch, I. Ivanova, H. Pfnür, D. Dorfs, D. W. Bahnemann, N. C. Bigall, *Adv. Funct. Mater.* **2017**, *27*, 1604685.
- [34] H. Chauhan, Y. Kumar, J. Dana, B. Satpati, H. N. Ghosh, S. Deka, *Nanoscale* **2016**, *8*, 15802.
- [35] B. Mahler, L. Guillemot, L. Bossard-Giannesini, S. Ithurria, D. Pierucci, A. Ouerghi, G. Patriarche, R. Benbalagh, E. Lacaze, F. Rochet, E. Lhuillier, *J. Phys. Chem. C* **2016**, *120*, 12351.
- [36] A. Dutta, A. Medda, A. Patra, *J. Phys. Chem. C* **2021**, *125*, 20.
- [37] G. Menagen, D. Mocatta, A. Salant, I. Popov, D. Dorfs, U. Banin, *Chem. Mater.* **2008**, *20*, 6900.
- [38] G. Menagen, J. E. Macdonald, Y. Shemesh, I. Popov, U. Banin, *J. Am. Chem. Soc.* **2009**, *131*, 17406.
- [39] P. Rukenstein, A. Teitelboim, M. Volokh, M. Diab, D. Oron, T. Mokari, *J. Phys. Chem. C* **2016**, *120*, 15453.
- [40] Y. Ben-Shahar, U. Banin, *Top. Curr. Chem.* **2016**, *374*, 54.
- [41] Y. Ben-Shahar, J. P. Philbin, F. Scotognella, L. Ganzer, G. Cerullo, E. Rabani, U. Banin, *Nano Lett.* **2018**, *18*, 5211.
- [42] D. V. Talapin, J. H. Nelson, E. V. Shevchenko, S. Aloni, B. Sadtler, A. P. Alivisatos, *Nano Lett.* **2007**, *7*, 2951.
- [43] A. Schlosser, L. C. Meyer, F. Lübke, J. F. Miethe, N. C. Bigall, *Phys. Chem. Phys.* **2019**, *21*, 9002.
- [44] J. Schlenkrich, D. Zámbo, A. Schlosser, P. Rusch, N. C. Bigall, *Adv. Opt. Mater.* **2021**, 2101712.
- [45] D. Müller, D. Zámbo, D. Dorfs, N. C. Bigall, *Small* **2021**, *17*, 2007908.

- [46] D. Müller, L. F. Klepzig, A. Schlosser, D. Dorfs, N. C. Bigall, *Langmuir* **2021**, *37*, 5109.
- [47] D. Zámbo, P. Rusch, F. Lübkeemann, N. C. Bigall, *ACS Appl. Mater. Interfaces* **2021**, acsami.1c16424.
- [48] U. Banin, Y. Ben-Shahar, K. Vinokurov, *Chem. Mater.* **2014**, *26*, 97.
- [49] E. A. Ponomarev, L. M. Peter, *J. Electroanal. Chem.* **1995**, *396*, 219.
- [50] J. F. Miethe, F. Lübkeemann, J. Poppe, F. Steinbach, D. Dorfs, N. C. Bigall, *ChemElectroChem* **2018**, *5*, 175.
- [51] J. F. Miethe, F. Luebkeemann, A. Schlosser, D. Dorfs, N. C. Bigall, *Langmuir* **2020**, *36*, 4757.
- [52] S. G. Hickey, D. J. Riley, *Electrochim. Acta* **2000**, *45*, 3277.
- [53] T. Kiyonaga, M. Fujii, T. Akita, H. Kobayashi, H. Tada, *Phys. Chem. Chem. Phys.* **2008**, *10*, 6553.
- [54] S. Pedetti, S. Ithurria, H. Heuclin, G. Patriarche, B. Dubertret, *J. Am. Chem. Soc.* **2014**, *136*, 16430.
- [55] A. Schlosser, R. T. Graf, N. C. Bigall, *Nanoscale Adv.* **2020**, *2*, 4604.
- [56] S. Naskar, A. Schlosser, J. F. Miethe, F. Steinbach, A. Feldhoff, N. C. Bigall, *Chem. Mater.* **2015**, *27*, 3159.
- [57] T. Kodanek, H. M. Banbela, S. Naskar, P. Adel, N. C. Bigall, D. Dorfs, *Nanoscale* **2015**, *7*, 19300.
- [58] L. Carbone, C. Nobile, M. De Giorgi, F. D. Sala, G. Morello, P. Pompa, M. Hytch, E. Snoeck, A. Fiore, I. R. Franchini, M. Nadasan, A. F. Silvestre, L. Chiodo, S. Kudera, R. Cingolani, R. Krahne, L. Manna, *Nano Lett.* **2007**, *7*, 2942.
- [59] S. Peng, Y. Lee, C. Wang, H. Yin, S. Dai, S. Sun, *Nano Res.* **2008**, *1*, 229.
- [60] H. Hiramatsu, F. E. Osterloh, *Chem. Mater.* **2004**, *16*, 2509.



Supporting Information

for *Adv. Mater. Interfaces*, DOI: 10.1002/admi.202200055

Interparticle Interaction Matters: Charge Carrier
Dynamics in Hybrid Semiconductor–Metal Cryoaerogels

Anja Schlosser, Jakob Schlenkrich, Dániel Zámbo,
Marina Rosebrock, Rebecca T. Graf, Giamper Escobar
Cano, and Nadja C. Bigall**

WILEY-VCH

Supporting Information

Interparticle Interaction Matters: Charge Carrier Dynamics in Hybrid Semiconductor-Metal Cryoaerogels

Anja Schlosser,[‡] Jakob Schlenkrich,[‡] Dániel Zámbo*, Marina Rosebrock, Rebecca T. Graf, Giamper Escobar Cano, Nadja C. Bigall*

*E-mail: nadja.bigall@pci.uni-hannover.de, daniel.zambo@pci.uni-hannover.de

[‡]*These authors contributed equally to this work*

Table of contents

1. Structural properties of the building blocks
2. Optical properties of the building blocks
3. Physical appearance of the prepared cryoaerogel electrodes
4. SEM-EDX Elemental mapping and HAADF-TEM images of the cryoaerogels
5. Structural characterization of hybrid cryoaerogels consisting of CdSe/CdS NPLs and Pt NPs (applying higher Pt loads)
6. LSVs and IMPS spectra of hybrid cryoaerogels consisting of CdSe/CdS NPLs and higher Pt load
7. Additional experimental details of the electrode preparation
8. Electron transfer mechanisms in NR-based hybrid cryoaerogels

1. Structural properties of the building blocks

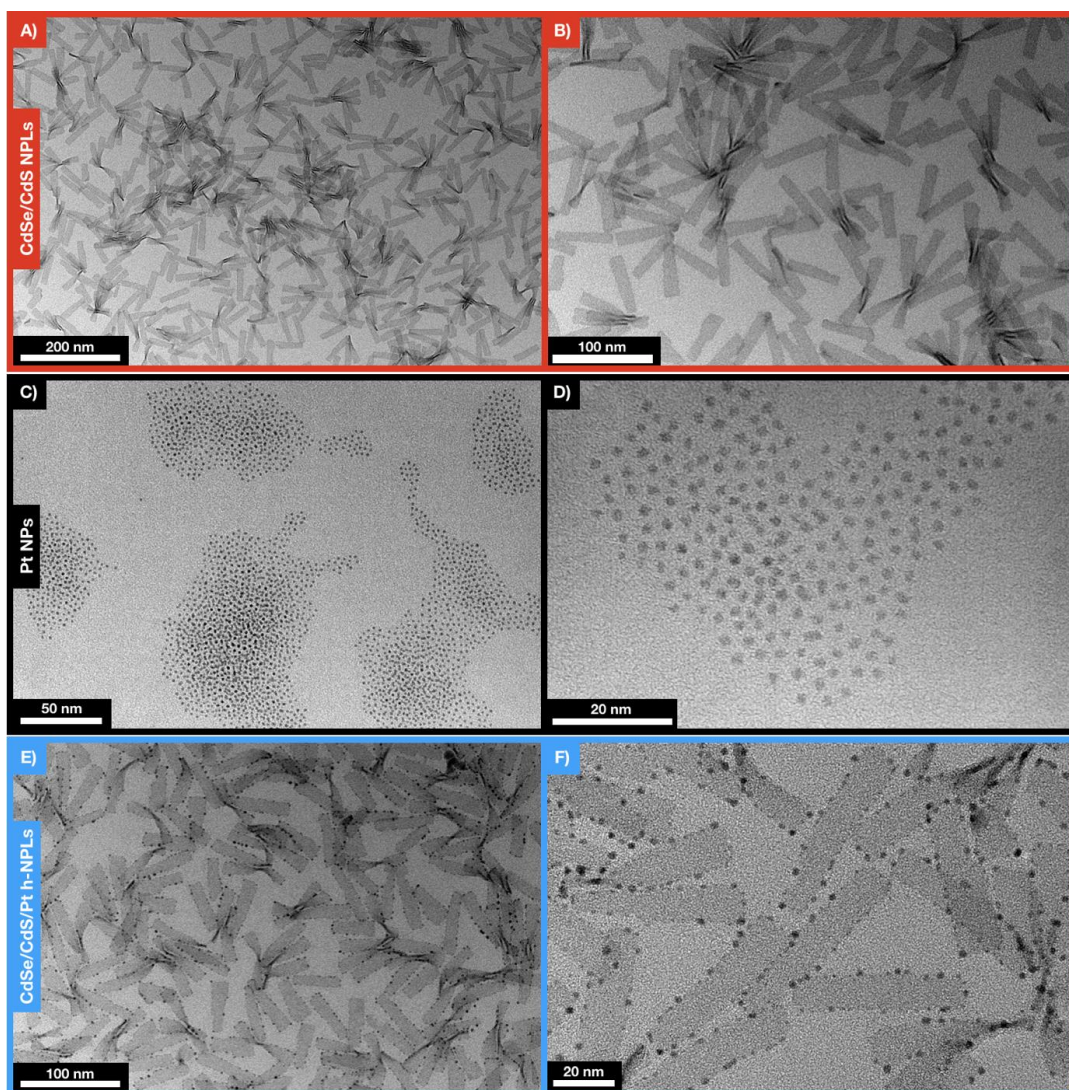


Figure S1. TEM images of CdSe/CdS core/crown nanoplatforms (A,B), Pt NPs (C,D) and CdSe/CdS/Pt hybrid nanoplatforms (E,F).

WILEY-VCH

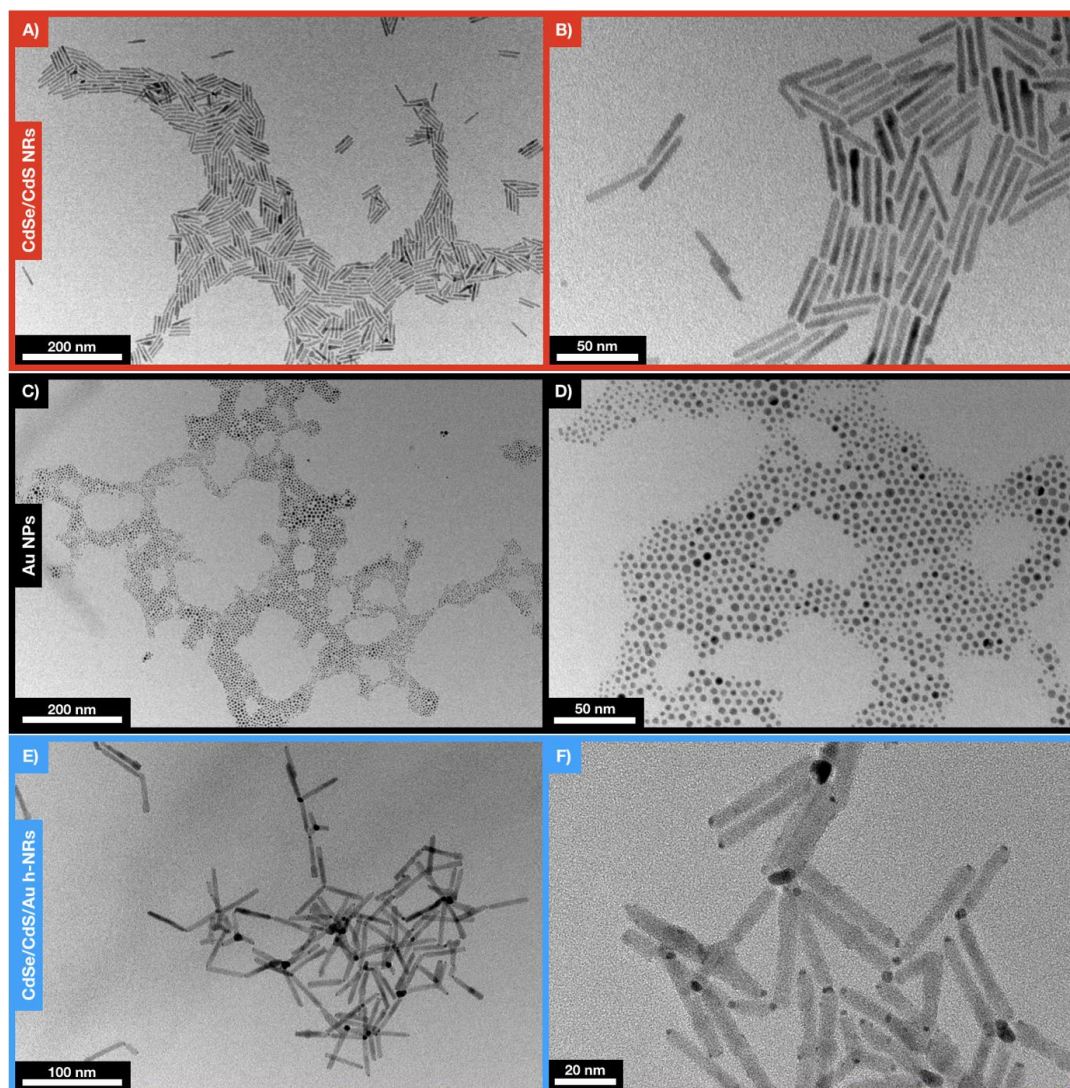


Figure S2. TEM images of CdSe/CdS nanorods (A,B), Au NPs (C,D) and CdSe/CdS/Au hybrid nanorods (E,F).

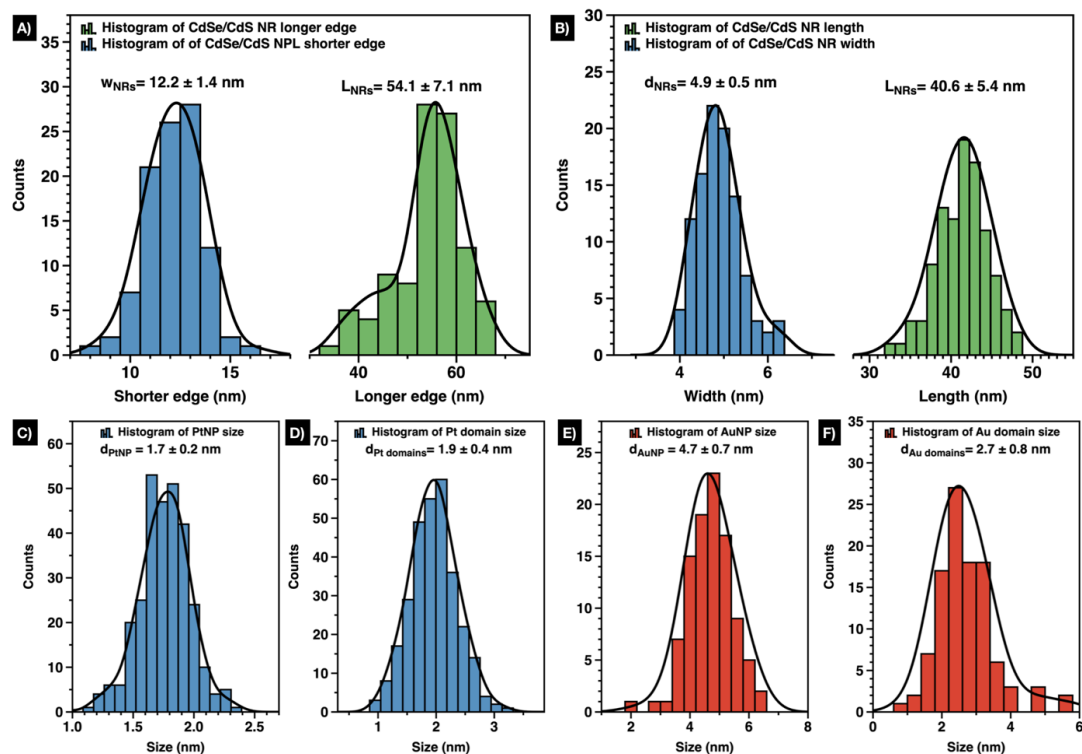


Figure S3. TEM size distribution analysis of CdSe/CdS NPLs (A), CdS/CdS NRs (B), Pt NPs (C), Pt domains on hybrid CdSe/CdS/Pt NPLs (D), Au NPs (E) and Au domains on hybrid CdSe/CdS/Au NRs (F).

2. Optical properties of the building blocks

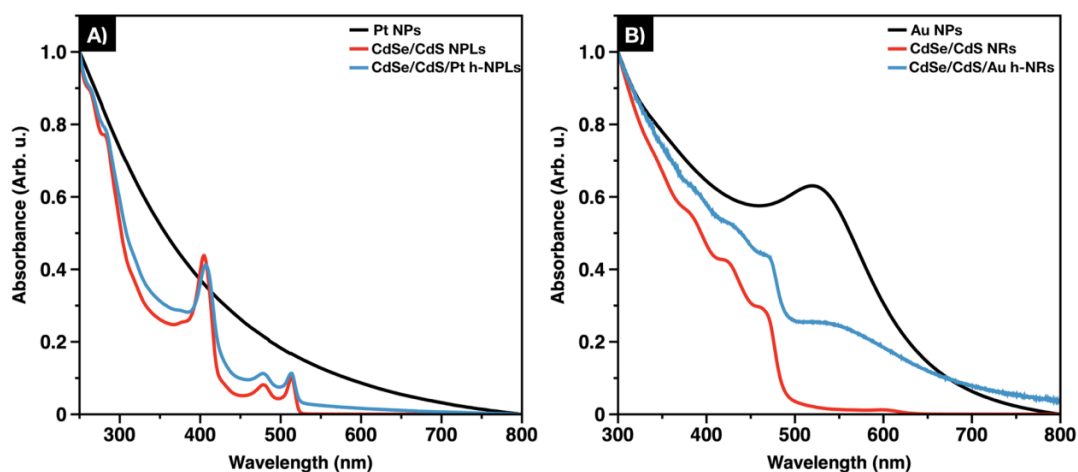


Figure S4. Absorbance spectra of pure NPLs, hybrid NPLs and Pt NPs (A), pure NRs, hybrid NRs and Au NPs (B).

WILEY-VCH

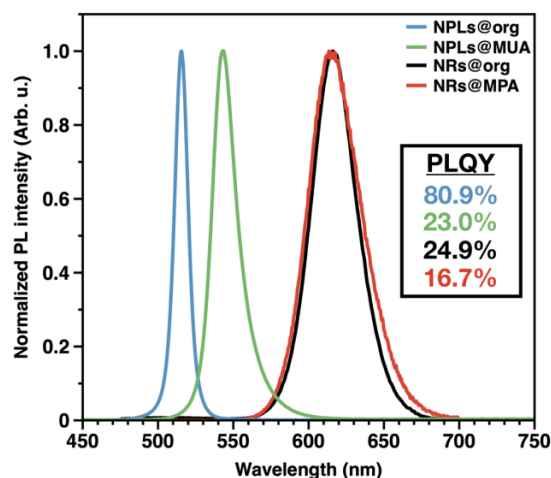


Figure S5. PL spectra and the corresponding PLQY values of pure NPLs and NRs in organic and aqueous media. For NPLs, MUA was used as phase transfer ligands, whilst for NRs, MPA was used.

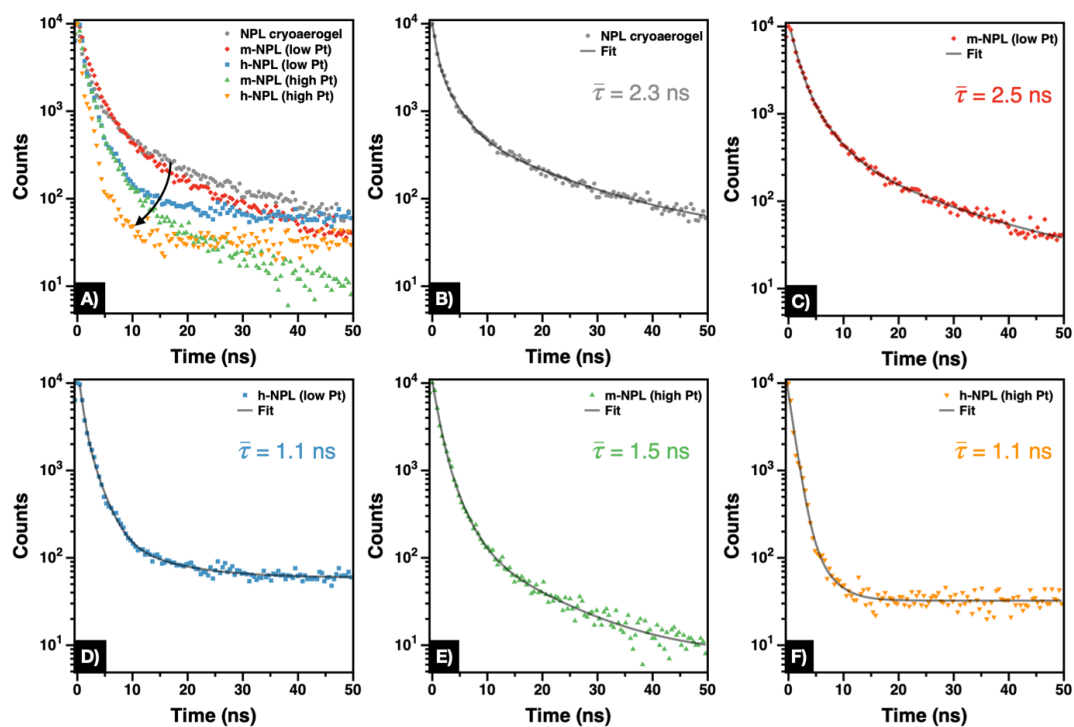


Figure S6. Photoluminescence lifetime decay curves of NPL-based cryoaerogels. Panel A gives an overview to see the trend (black arrow) of the lifetime shortening upon direct growth of the domains. Panel B-F represents the lifetime decay of each sample and the fitted biexponential curves. Average PL lifetimes ($\bar{\tau}$) are indicated with the respective color codes.

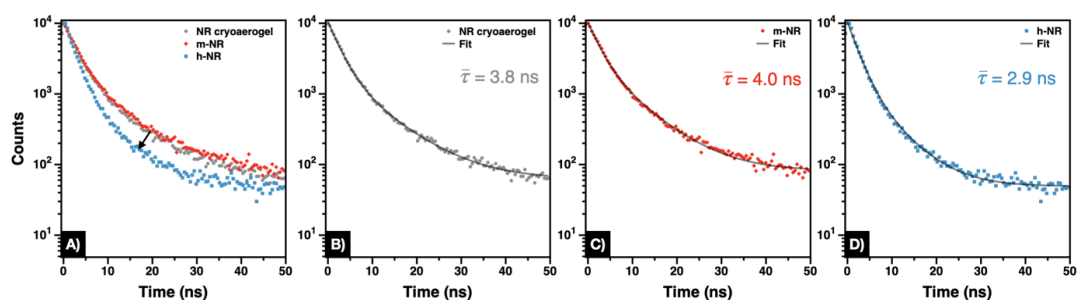


Figure S7. Photoluminescence lifetime decay curves of NR-based cryoaerogels. Panel A gives an overview to see the trend (black arrow) of the lifetime shortening upon direct growth of the domains. Panel B-D represents the lifetime decay of each sample and the fitted biexponential curves. Average PL lifetimes ($\bar{\tau}$) are indicated with the respective color codes.

3. Physical appearance of the prepared cryoaerogel electrodes

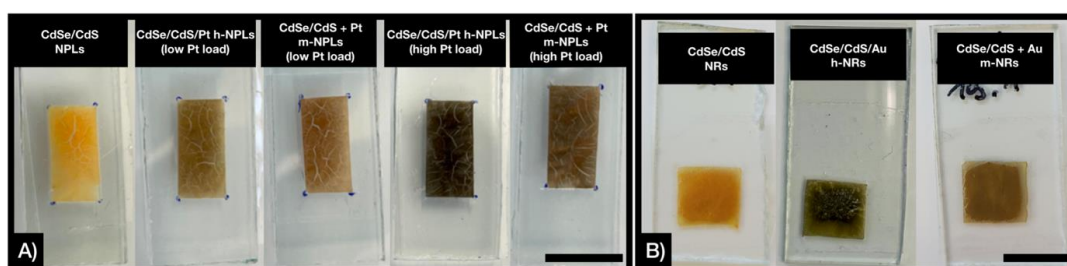


Figure S8. Photographs of the NPL-based (A) and NR-based (B) cryoaerogel electrodes. The scale bars are 1 cm.

WILEY-VCH

4. SEM-EDX Elemental mapping and HAADF-TEM images of the cryoaerogels

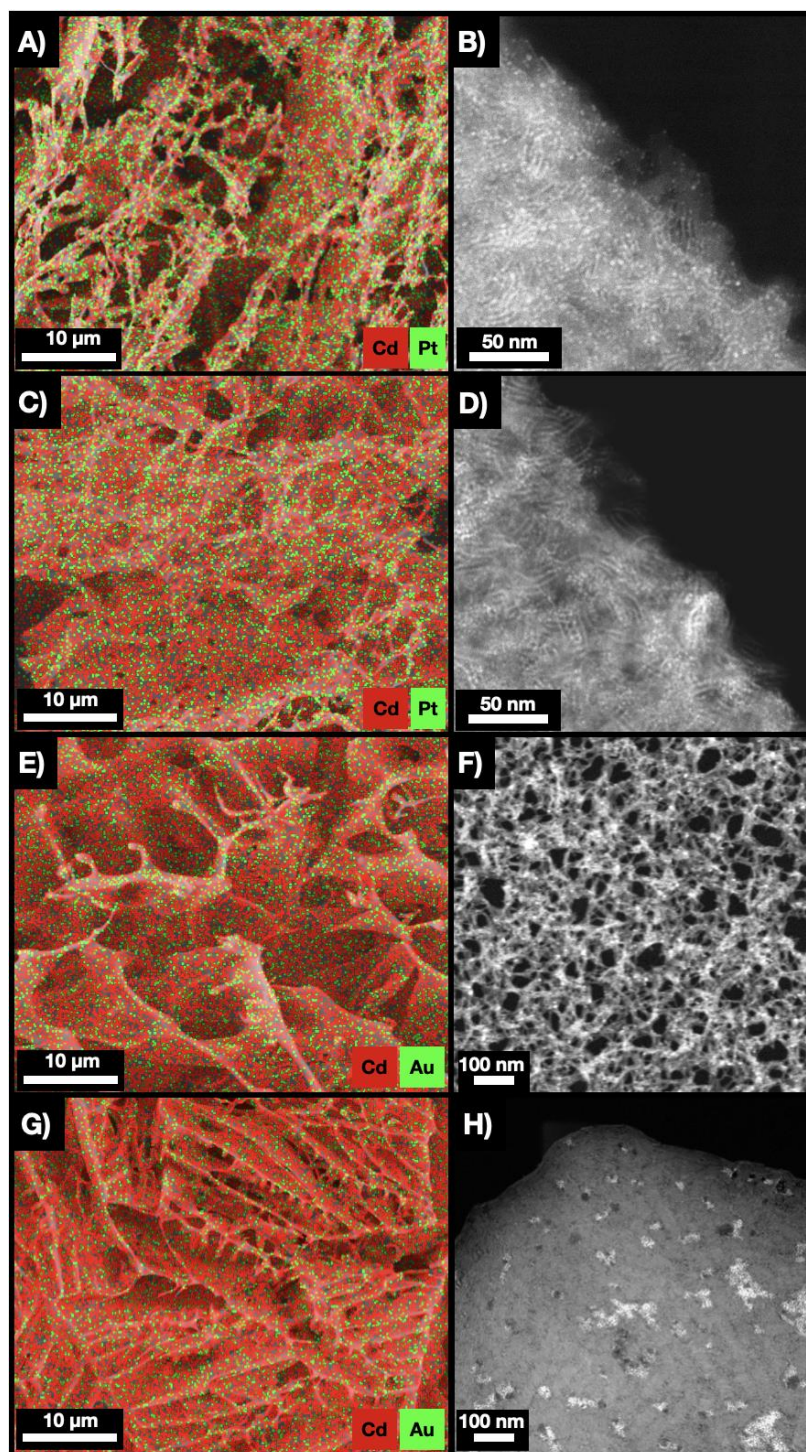


Figure S9. SEM-EDX elemental maps (A,C,E,G) and TEM-HAADF images of cryoaerogel structures consisting of CdSe/CdS/Pt h-NPLs (A,B), m-NPLs (mixed with Pt NPs) (C,D), CdSe/CdS/Au h-NRs (E,F) and m-NRs (mixed with Au NPs) (G,H).

5. Structural characterization of hybrid cryoaerogels consisting of CdSe/CdS NPLs and Pt NPs with higher Pt load

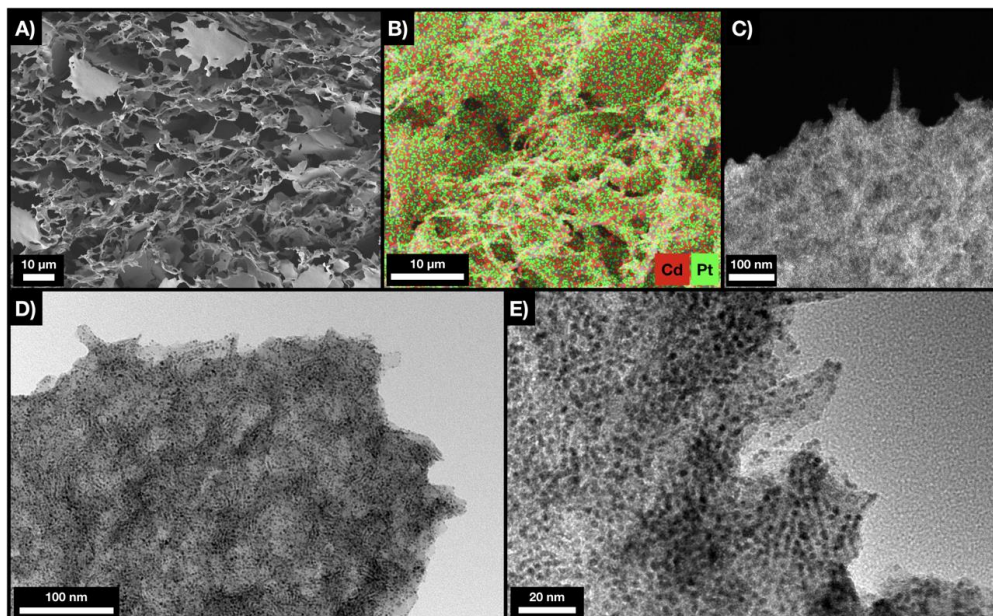


Figure S10. SEM (A), SEM-EDX elemental map (B), TEM-HAADF image (C) and TEM images (D,E) of cryoaerogels prepared from hybrid CdSe/CdS/Pt h-NPLs (higher Pt load)

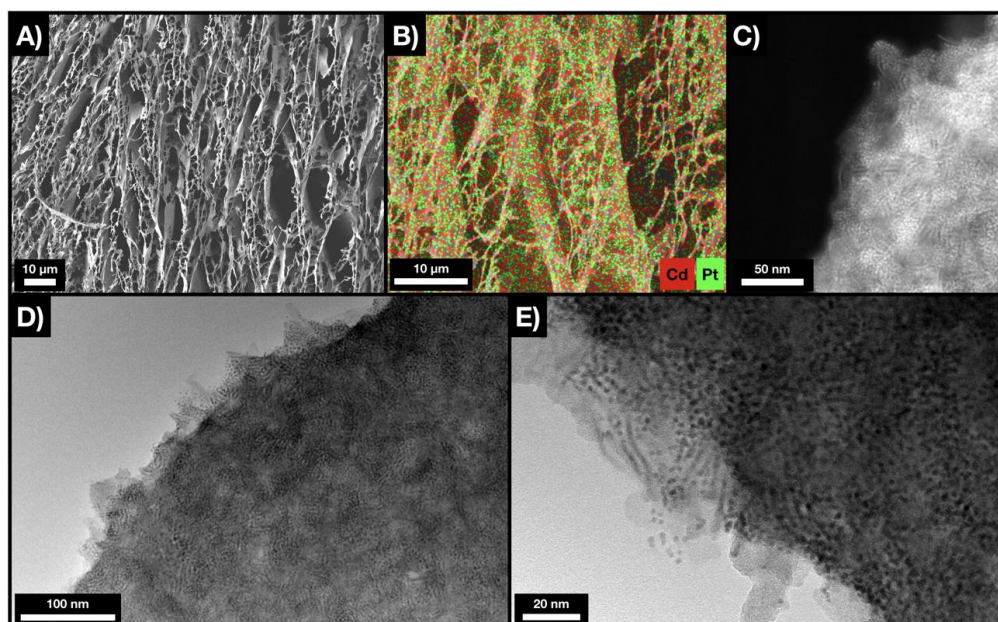


Figure S11. SEM (A), SEM-EDX elemental map (B), TEM-HAADF image (C) and TEM images (D,E) of mixed cryoaerogels prepared *via* mixing CdSe/CdS NPLs and Pt NPs (higher Pt load).

6. LSVs and IMPS spectra of hybrid cryoaerogels consisting of CdSe/CdS NPLs and higher Pt load

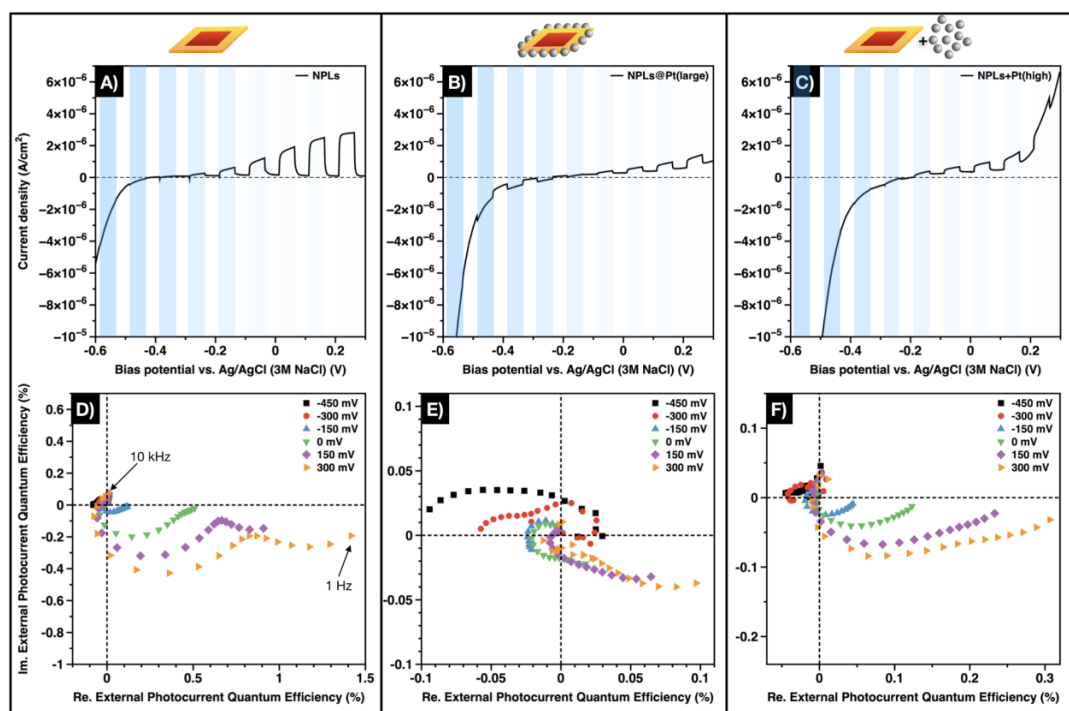


Figure S12. LSVs (A-C) and IMPS Nyquist plots (D-F) of cryoaerogel coatings prepared from pure CdSe/CdS NPLs (A,D), hybrid CdSe/CdS/Pt NPLs with more Pt domains (B,E) and mixed CdSe/CdS NPLs + higher load of Pt NPs (C,F). Blue shaded areas represent the regimes where the sample was illuminated.

7. Additional experimental details of the electrode preparation

Table S1. Molar ratios of cadmium and platinum/gold in the cryoaerogels. Determined by SEM-EDXS.

Sample	Molar ratios (Cd:Pt and Cd:Au)
<u>Lower load</u>	
CdSe/CdS/Pt NPLs	6.3:1
CdSe/CdS NPLs + Pt NPs	11:1
<u>Higher load</u>	
CdSe/CdS/Pt NPLs	2:1
CdSe/CdS NPLs + Pt NPs	3.5:1
CdSe/CdS/Au NRs	14:1
CdSe/CdS NRs + AuNPs	20:1

8. Electron transfer mechanisms in NR-based hybrid cryoaerogels

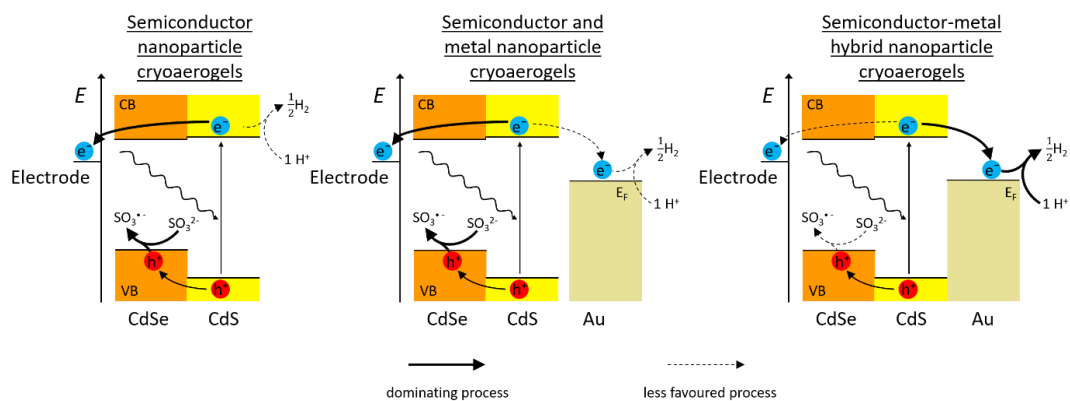


Figure S13. Schematic illustration of the dominating electron transfer in CdSe/CdS NR, CdSe/CdS + Au m-NR and CdSe/CdS/Au h-NR cryoaerogels.

2.3 Revealing the Effect of Nanoscopic Design on the Charge Carrier Separation Processes in Semiconductor-Metal Nanoparticle Gel Networks

Jakob Schlenkrich, Dániel Zámbo, Anja Schlosser, Pascal Rusch, and Nadja C. Bigall

Published in *Advanced Optical Materials* 2022, 10, 2101712

<https://doi.org/10.1002/adom.202101712>

RESEARCH ARTICLE

Revealing the Effect of Nanoscopic Design on the Charge Carrier Separation Processes in Semiconductor-Metal Nanoparticle Gel Networks

Jakob Schlenkrich, Dániel Zámbo, Anja Schlosser, Pascal Rusch, and Nadja C. Bigall*

In this paper, it is shown that the nanoscopic design of combining semiconductors and noble metals has a direct impact on the macroscopic (electrochemical) properties of their assembled, hyperbranched, macroscopic gel networks. Controlled and arbitrary deposition of gold domains on CdSe/CdS nanorods leads to tipped and randomly decorated heteroparticles, respectively. Structural and optical properties of the gel networks depend upon assembling the hybrid particles by means of oxidative or ionic routes. Additionally, the impact of different building block designs on the charge carrier separation processes is investigated from spectroelectrochemical point of view. A more efficient charge carrier separation is revealed in the tipped design manifesting in higher negative photocurrent efficiencies compared to the arbitrary decoration, where the charge recombination processes are more remarkable. This work sheds light on the importance of the nanostructuring on the spectroelectrochemical properties at the macroscale paving the way towards their use in photochemical reactions.

approach towards novel hybrid functional materials with unique properties, which differ from those of colloidal mixtures of the two materials.^[1–3] The synthesis of these hybrid nanomaterials is often challenging due to different lattice dimensions, thermal stability, or chemical reactivity.^[4] Nevertheless, various combinations of different materials have already been synthesized and their promising properties have been demonstrated.^[4,5] Combining a semiconductor and a (noble) metal at the nanoscale results in hybrid nanostructures with advantageous properties for potential applications in photocatalysis, photoelectrochemical sensing, and photovoltaic applications.^[6–10] To date, the importance of the design at the nanoscale (i.e., engineering the components towards different hybrid-particles) has mainly been demonstrated at the single particle

level and in solution-based ensembles.^[11–13] In semiconductor-metal hybrid nanoparticles, the photoelectrochemical performance relies on the efficient charge carrier separation and the utilization of the photogenerated electrons and holes in further reactions which is the major requirement for the above-mentioned applications.^[14] CdSe/CdS nanorods (NRs) alone offer some extent of charge carrier separation due to a negligible energy difference between the conduction band of CdSe and CdS and the resulting delocalization of the photoexcited electrons through the heterojunction and thus over the entire NR. Due to this special band alignment, this material combination behaves as a quasi-type II heterojunction.^[15] However, growing, e.g., gold on the semiconductor NRs leads to hybrid nanoparticles exhibiting further enhanced separation of the excited electrons and the holes within the different materials which enables the usage of these charge carriers in redox reactions.^[16] Nanostructural properties have remarkable impact on the overall optical or electrochemical response of the built-up macrostructures. We have shown recently that the number of gold nanoparticles relative to CdSe/CdS nanorods essentially governs the optical properties of macroscopic gel structures prepared by the cogelation of the two components.^[17] However, prior to the assembly, design of hybrid building blocks at the nanoscale (that is in terms of spatial distribution of the noble metal domains) is of great importance as well. These hybrid nanomaterials as ligand stabilized NPs in solution are usually restricted to solution-based applications, or the active


1. Introduction

Combining different material classes at the nanoscale (such as metals with magnetic materials, semiconductors with magnetic materials or semiconductors with metals) is a promising

J. Schlenkrich, D. Zámbo, A. Schlosser, P. Rusch, N. C. Bigall
Institute of Physical Chemistry and Electrochemistry
Leibniz Universität Hannover
Callinstraße 3A, 30167 Hannover, Germany
E-mail: nadja.bigall@pci.uni-hannover.de

A. Schlosser, P. Rusch, N. C. Bigall
Laboratory for Nano and Quantum Engineering
Leibniz Universität Hannover
Schneiderberg 39, 30167 Hannover, Germany

N. C. Bigall
Cluster of Excellence PhoenixD (Photonics, Optics and Engineering –
Innovation Across Disciplines)
Leibniz Universität Hannover
30167 Hannover, Germany

 The ORCID identification number(s) for the author(s) of this article can be found under <https://doi.org/10.1002/adom.202101712>.

© 2021 The Authors. Advanced Optical Materials published by Wiley-VCH GmbH. This is an open access article under the terms of the Creative Commons Attribution-NonCommercial License, which permits use, distribution and reproduction in any medium, provided the original work is properly cited and is not used for commercial purposes.

DOI: 10.1002/adom.202101712

materials are prepared via the conventional drying of the hybrid nanocrystals. However, assembling the nanoscopic building blocks into macroscopic, porous, 3D gel-like structures could significantly broaden their applicability.^[18] In nanocrystal gels, the nanoscopic characteristics of the nanoparticle building blocks can be retained and novel properties can emerge simultaneously, which underlines the advantages of these assembled structures over their colloidal solutions.^[19] Upon partial removal of the stabilizing ligands from the nanocrystal surface under controlled conditions, the assembly of the nanoparticles can be initiated leading to an interconnected nanocrystal network.^[20,21] Although gel-like structures have been prepared from various materials to date, we have recently presented novel routes towards the formation of hybrid nanocrystal networks for spectroelectrochemical applications, where the preparation route (i.e., via simple mixing of different building blocks or preparing the hybrid semiconductor-noble metal nanoparticles prior to their assembly) has been found to be of central importance.^[22–26] While simple mixing and co-gelation has not led to efficient charge carrier separation, growth of the metal domains directly on the nanorods or nanoplatelets enabled to fabricate hybrid gel structures with enhanced photoelectrochemical performance. This sheds light on the impact of proper nanostructuring on the emerging properties at the macroscale.

Consequently, in the present work, our objective is to synthesize and assemble different gold decorated CdSe/CdS NRs and form macroscopic porous gel-like structures with effective charge carrier separation (schematically shown in **Figure 1**) in order to investigate the impact of particle design on the spectroelectrochemical properties of the gel networks (at the macroscale). To deposit gold domains in controlled and arbitrary manner, different synthetic approaches were applied to prepare gold tipped and randomly decorated CdSe/CdS NRs (referred to as tipped-NR and random-NR, respectively). These NRs were employed as building blocks to fabricate different semiconductor-metal hybrid aero- and xerogels to investigate the macrostructural properties upon different nanoscale design. The key difference between these gels is the significantly diverse spatial distance between the neighboring gold domains in the hybrid nanostructures. The characterization with electron microscopy, UV-vis spectroscopy and electrochemical measurements like intensity modulated photocurrent spectroscopy (IMPS) give insights into the nanoscopic structure and its influence on the

optical and spectroelectrochemical properties of the assembled networks. Here, both an oxidative method using H_2O_2 and a nonoxidative method using Y^{3+} cations were applied to destabilize the aqueous nanoparticle solutions and trigger their assembly.^[20,21]

2. Results and Discussion

2.1. Characterization of the Nanoparticle Building Blocks

The spatial control over the growth of gold domains on CdSe/CdS NRs can be achieved by adjusting the reaction parameters. This can lead to differently designed hybrid NRs: the selective growth on the tips of the NRs as well as the growth of gold on defect sites along the NRs.^[5,27] In this work, a slightly modified method following Menagen et al. has been applied to synthesize the above-mentioned gold tipped-NR and the random-NRs.^[5] This offers two nanostructuring routes: (i) the light-induced growth procedure leads to the selective growth of gold on the preferred sulfur rich facets which are located at the tip of the NR, with the size of the domains being controlled by the reaction time. Gold is reduced directly by the photoexcited electrons supporting the growth on the preferred facets forming tipped NRs. (ii) Using a thermal growth mechanism (namely without irradiation during the growth process), reduction of gold is induced on several defect sites along the semiconductor NRs via the amine being present in the solution. This manifests itself in a form of randomly decorated hybrid nanoparticles. The morphology and optical properties of the hybrid particles using the selective growth mechanisms are demonstrated in **Figure 2**, where the transmission electron microscopy (TEM) images and the extinction spectra are shown before and after the phase transfer from organic to aqueous solutions. In the extinction spectra, the spectroscopic features of the semiconductor as well as of the metal can be observed. The rise in the extinction at 600 nm is correlated to the CdSe core and at 450 nm to the CdS rod. Tipped-NR and random-NR systems show additionally the localized surface plasmon resonance (LSPR) of the gold with a maximum between 500 and 600 nm. Differences between the tipped-NR and random-NR systems in the wavelength range of 480–700 nm can be attributed to the difference in the size of the grown gold domains. The domains on the randomly decorated

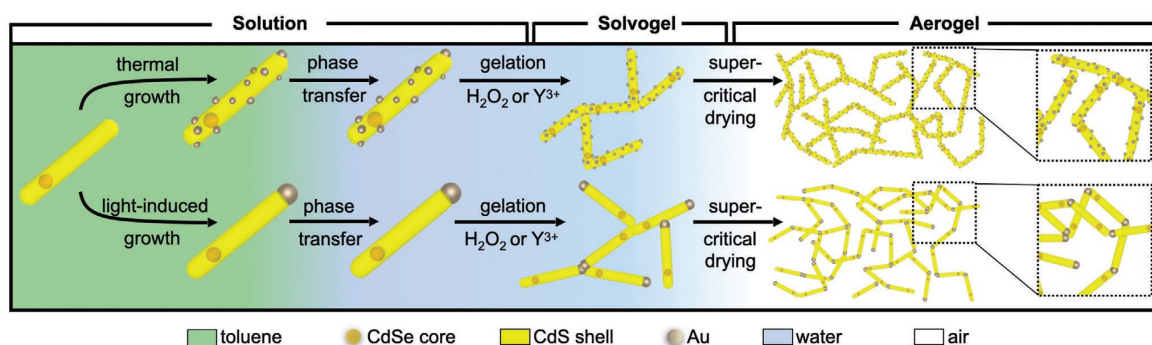


Figure 1. Schematic pathways from CdSe/CdS NRs to gold decorated gel networks using two different approaches.

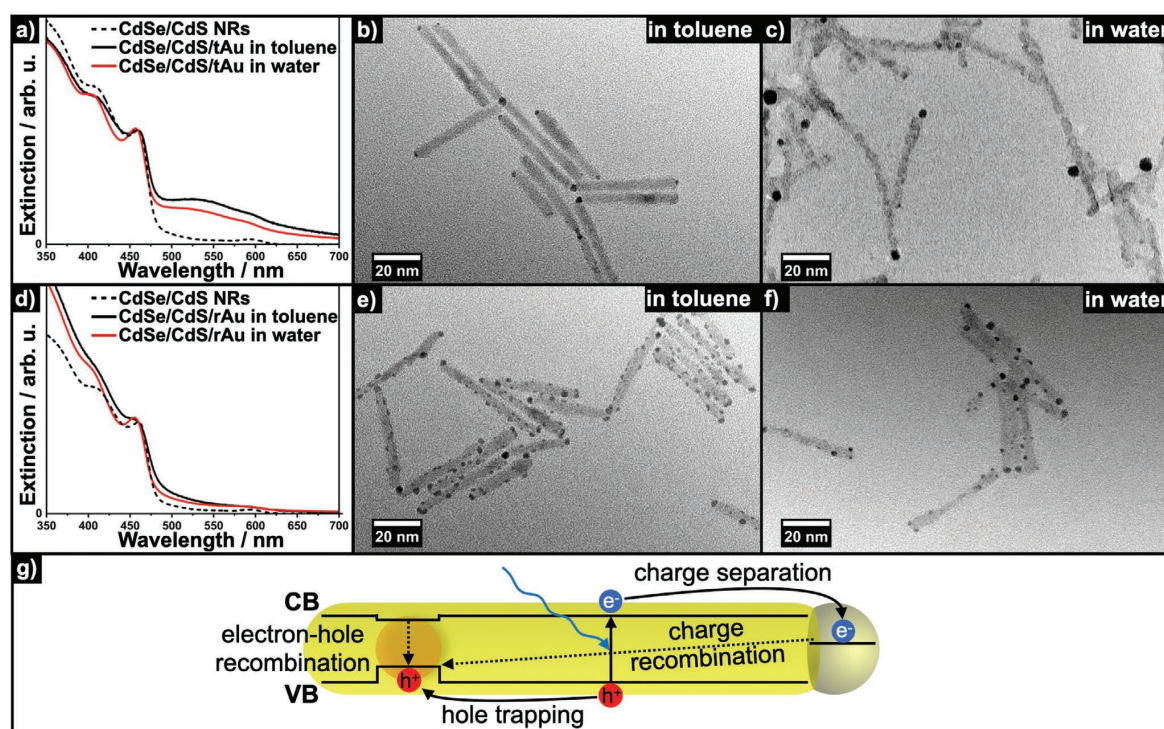


Figure 2. Extinction spectra in toluene and water (solid lines) compared to the spectrum of pure CdSe/CdS NRs in toluene (dashed line) and TEM images of a–c) tipped-NRs and d–f) random-NRs. g) Scheme of the electronic band structure of a gold decorated CdSe/CdS NR with the governing charge carrier processes upon illumination.

NRs are slightly smaller (2.0 ± 0.5 nm) compared to the gold tips (3.0 ± 1.4 nm), that alters their contribution to the extinction spectra due to different scattering and absorption cross sections of smaller and larger gold domains.^[28]

A phase transfer of the hybrid particles to aqueous solutions is required to trigger the assembly of the nanoparticle solution using H_2O_2 (to partially oxidize the surface ligands) or Y^{3+} cations (to partially remove and cross-link the ligands).^[20,21,29] By exchanging the TOP/TOPO ligands with the water soluble mercaptopropionic acid (MPA), the gold decorated particles were transferred to an aqueous solution by retaining the morphology of the gold decoration achieved in organic medium (Figure 2). To ensure the deprotonation of the carboxyl groups of MPA, alkaline pH is generally used during the phase transfer, that can be reached by the addition of tetramethylammonium hydroxide (TMAOH) or potassium hydroxide (KOH).^[30] In case of our hybrid particle systems, however, highly basic conditions led to the dissolution and detachment of the gold domains (Figure S3, Supporting Information). Therefore, the phase transfer was carried out without addition of extra base, hence the morphology of the gold decoration could be retained as shown in the comparative TEM images of Figure 2.

The electronic band structure of the synthesized semiconductor-metal hybrid NRs is shown in Figure 2c. Due to the quasi-type II band structure of the CdSe/CdS NR and the Fermi level of the gold which lies in between the valence- and the

conduction band of the semiconductors, spatial separation of the excited charge carriers can be achieved.^[14] Electrons are delocalized along the CdS shell are transferred to the metal domains within the picosecond range while holes become located in the CdSe core.^[14] The fast electron transfer to the metal domains and a long lifetime of the electrons in the gold (up to microseconds) enable the accumulation of electrons in the metal domain leading to a rise of the Fermi level upon irradiation.^[31] This efficient charge carrier separation and the electron accumulation accomplish promising properties for catalytic applications such as hydrogen evolution reaction (HER). Building up a connected network from the hybrid nanoparticles opens up new routes towards the utilization of the above-mentioned charge carrier separation. The delocalization of the electrons upon illumination can be observed throughout connected CdSe/CdS NRs which can enable the enhanced electron transfer to the metal domains.^[20,21]

2.2. Structural Characterization of the Semiconductor-Metal Nanoparticle Gel Networks

The formation of a macroscopic network structure from the differently designed hybrid NRs has been achieved by destabilizing the nanoparticle solutions with two different methods. Using H_2O_2 as destabilizing agent leads to the oxidation of the surface-attached MPA followed by a slow assembly of the

NRs into a network of connected particles.^[32] H_2O_2 at slightly elevated temperatures (80°C) oxidizes the thiolated ligands (RS^-) to a radical ($\text{RS}\cdot$) opening available active sites for the assembly.^[29] The slow oxidation due to low concentrations of the H_2O_2 enables the controlled formation of the network consisting of mainly tip-to-tip, crystal-to-crystal connected NRs.

As we have shown recently, trivalent cations in contrast destabilize the nanoparticle solution in a nonoxidative way without thermal activation.^[21] Cations like Y^{3+} have a high affinity to the surface of the metal and the semiconductor and thus are able to remove the ligands from the surface. Using this method, active sites for the assembly are formed which leads to the connection of the nanorods. Eventually a nanoparticle gel network is formed in a controlled manner. Additionally, the cations interact via Coulomb forces with the anionic carboxylic groups of the MPA which as well supports the assembly of the nanoparticles. Although the TEM analysis of the connections between CdSe/CdS NRs formed with both H_2O_2 and Y^{3+} showed crystal contact between the building blocks, Y^{3+} cations resulted in a somewhat larger contact area and thus a stronger contact between the nanorods (Figure 3).^[21]

At this stage, nanostructuring meets macrostructuring: the assembly of the semiconductor-metal hybrid nanoparticles leads to 3D, porous structures with the retained morphology of the gold decorated building blocks. The oxidative as well as the nonoxidative destabilization procedures results in gold

decorated semiconductor solvogels, from which monolithic aerogels can be prepared upon drying the structures in a critical point dryer (using supercritical CO_2). Scanning electron microscopy (SEM) images show the voluminous, porous 3D structure and the macroscopic character of the gel networks whereas the TEM images give an insight of the nanoscopic morphology and the position of the gold domains in the formed interconnected NR network (Figure 3).

Arbitrary and controlled spatial deposition of noble metal domains have impact on the structural properties of the gel materials. Assembling the random-NRs, a network with gold on the sides of the nanorods and additionally in many cases as the (partial) connection between the NRs is formed. A network from the tipped-NRs results in gold only in the connection points between the NRs. Mostly, the gold domains are located in-between the NRs, however, some direct rod-to-rod connections without gold can also be observed due to the single-tipped nature of the building blocks (i.e., one tip is non-decorated). In comparison to the random-NR network, the distance between two gold domains (<10 nm in case of tipped and ≈ 40 nm for random-NRs) and the size of the domains are larger (3.2 ± 1.2 nm in case of tipped and 2.0 ± 0.6 nm for random-NRs). Due to the larger distance between them, an extended mobility (enhanced spatial delocalization) of the electrons in the tipped-NR network is expected, which was expected to alter their spectroelectrochemical properties.

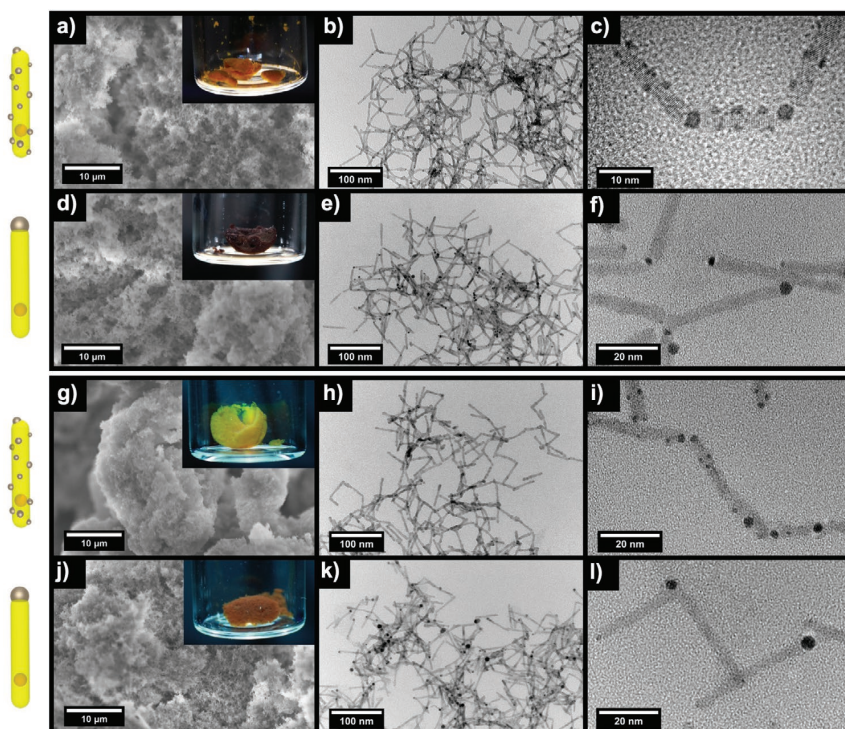


Figure 3. Comparative morphological overview of different hybrid aerogel networks assembled via a–f) H_2O_2 (upper panel) and g–l) Y^{3+} (lower panel). SEM images (a,d,g,i) and TEM images of random-NR aerogels assembled via H_2O_2 (b,c) and Y^{3+} (h,i) as well as tipped-NR aerogels assembled via H_2O_2 (e,f) and Y^{3+} (k,l). Insets of the SEM images show the photographs of the macroscopic aerogel monoliths.

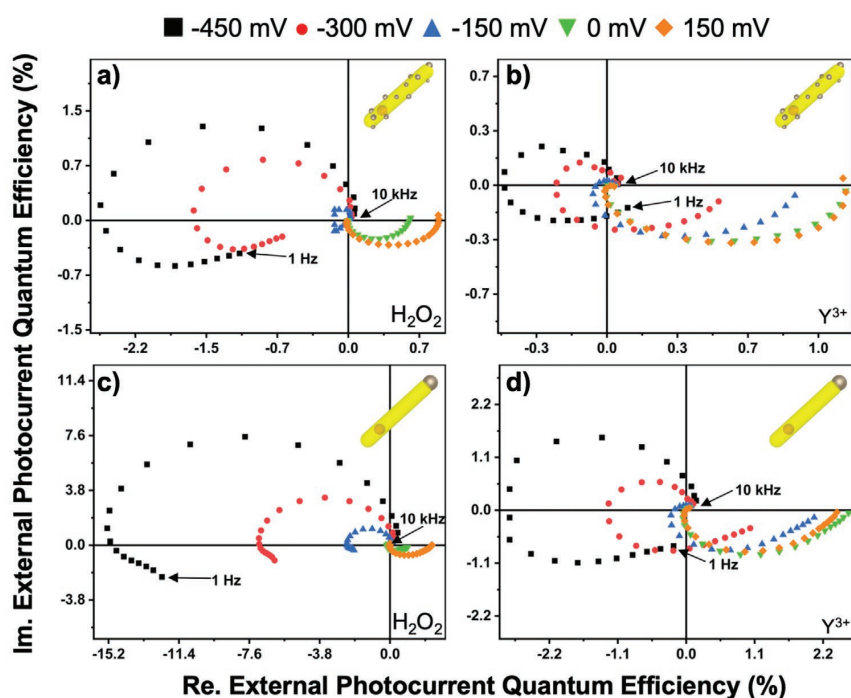


Figure 4. Nyquist plots of the IMPS response of random-NR xerogel networks formed with a) H_2O_2 and b) Y^{3+} and of tipped-NR xerogel networks formed with c) H_2O_2 and d) Y^{3+} .

2.3. Spectroelectrochemical Investigation of the Semiconductor-Metal Nanoparticle Gel Networks

To investigate the effect of the nanostructuring on the spectroelectrochemical properties (charge carrier dynamics) of the hybrid macrostructures, intensity modulated photocurrent spectroscopy (IMPS) was applied on xerogel samples (see Figure S7 in the Supporting Information for the experimental setup).^[33] IMPS is a frequency-resolved spectroscopic technique, where a frequency-modulated light source excites a photoelectrochemically active electrode which is under potentiostatic control. In the applied measurements, the working electrode consists of the nanoparticle network deposited on a conductive substrate. As a response to the frequency-modulated light (in the range of 1 Hz to 10 kHz), a photocurrent with a certain intensity and phase shift compared to the intensity and phase of the incoming light can be detected. In a Nyquist plot, the real and imaginary IMPS datapoints result in semicircles and can be interpreted with the knowledge of the charge carrier transfer processes in the investigated system. In **Figure 4**, the photoelectrochemical response of indium tin oxide (ITO) electrodes coated with the different xerogel networks (measured in an aqueous 0.5 M Na_2SO_3 solution at pH = 9 which acts as a hole scavenger) are shown. While pure ITO electrodes (without gel structures) do not show active electrochemical processes (see Figure S10 in the Supporting Information), positive and negative photocurrents can be observed in the xerogel electrodes under illumination which represent two major photoelectrochemical processes. The transfer of electrons from the

network to the electrode and the scavenging of the hole by sulfite ions from the electrolyte lead to positive photocurrent, whereas the electron transfer from the network to solution by reducing protons to hydrogen results in negative photocurrent (the main photoinduced electrochemical processes are detailed in Figure S8 in the Supporting Information). For the discussion of the results and the proposed mechanism only the course of the photocurrent and not the absolute values have been used. Although all samples have been prepared in the same way, the exact amount of the electrode material cannot be entirely unified, thus, the absolute values of the photocurrent might slightly differ. Consequently, the photocurrent response and its characteristics as a function of the bias potential and the frequency of the light pulses are used for the interpretation.

In the IMPS spectra, a different behavior of the networks upon applying positive and negative bias potentials can be observed. Positive photocurrent dominates at bias potentials of 0 and +150 mV, while negative photocurrent with a turnaround towards the positive photocurrent direction can be observed for 150, 300, and 450 mV, respectively (Figure 4). This turnaround indicates the competition between processes leading to positive and negative photocurrents. The negative photocurrent becomes more remarkable at high frequencies. In contrast, the positive photocurrent becomes more pronounced at lower frequencies. These observations are also supported by linear sweep voltammetry measurements, which show the evolution of the positive and negative photocurrents at different bias potentials in time as well (Figure S9, Supporting Information). Comparing the networks of random and tipped-NRs indicates

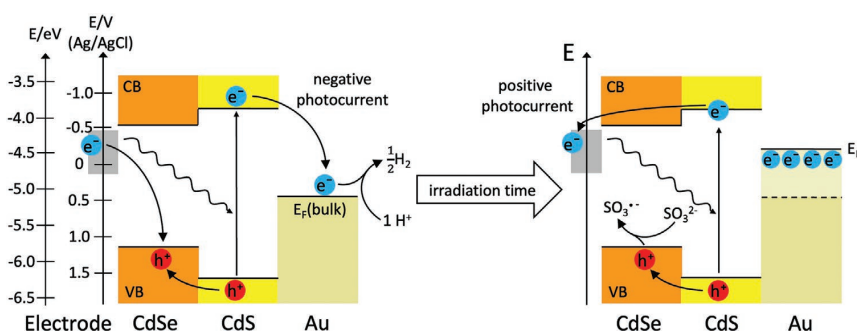


Figure 5. Schematic illustration of the energy landscape of the heteronanoparticle, the electron accumulation, and the rise of the Fermi level in the metal domain upon longer irradiation time and the subsequent change of the photocurrent direction. The conduction band offset at the CdSe/CdS heterojunction is around 0.23 eV, which leads to the formation of a quasi-type II alignment.^[15] For the positioning of the Au Fermi level, the bulk value was used (−5.1 eV), which can rise upon being contacted with a semiconductor surface^[36] but still remains within the band gap of the CdS shell.

that the tipped network reaches higher photocurrent quantum efficiencies regarding the negative as well as the positive photocurrent. Furthermore, the semicircles show an elongated shape at lower frequencies, which is less pronounced at negative bias potentials and not observed at positive bias potentials for the random-NR networks. The different destabilization methods show minor differences in the high frequency range. A less extensive turnaround at negative bias potentials in case of H_2O_2 destabilized networks and the elongation at positive bias potentials for the tipped network is slightly more pronounced in case of the Y^{3+} destabilized network.

2.4. Mechanism of the Charge Carrier Dynamics

Based on the above-discussed observations, a model for the charge carrier dynamics can be derived. **Figure 5** depicts the estimated energy landscape of the heteronanoparticles and illustrates the evolution of negative and positive photocurrents. Upon irradiation of the semiconductor-metal hybrid gel networks, the excited electrons are accumulated in the metal domains regardless of the location of the gold on the NRs. This is supported by the intrinsically small conduction band energy difference (≈ 0.23 eV) between the CdSe core and the CdS shell that makes the electron delocalization possible over the NR.^[15,19,34,35] Nevertheless, the main driving force of the electron extraction from the semiconductor into the noble metal domain is the Fermi level of the gold located in the band gap of the CdS.^[36] Electrons from the gold domains favorably reduce protons and form hydrogen, due to their longer lifetime in the metal domains and the catalytic activity of the metal. This leads to an increasing negative photocurrent with decreasing frequency of the light pulses (Figure S8, Supporting Information). In semiconductor-metal hybrid nanoparticles, not only the contact between the metal and the semiconductor,^[36] but the electron accumulation inside the Au upon irradiation might also be able to raise the Fermi level of the gold domain.^[31,37] On the one hand, with further decreasing frequency (i.e., increasing irradiation times), the Fermi level of the gold domains raises and the electron transfer from the conduction band of the semiconductor to the gold domains becomes less favorable while

the electron transfer to the electrode becomes more favorable (Figure 5). Furthermore, with the accumulation of the electrons and the holes, the possibility of charge carrier recombination increases due to the increasing Coulomb forces between the electrons and the holes. Additionally, for the random-NR network, tunneling processes between the gold domains can also occur which was shown by Lavieville et al. where shorter distances between metal domains led to an increased conductivity.^[38] The higher tunneling probability and thus shorter distances to the holes in random-NR networks leads to a larger recombination rate.^[39–41] Although in Figure 5, solely the vicinity of the electrode is depicted, these effects can also take place further from the electrode surface due to the NR–NR connections throughout the network.

The turnaround to more positive photocurrent with decreasing frequency can be explained with the raise of the Fermi level and the increasing recombination rate due to the accumulation of the electrons in the metal domains. Higher photocurrent quantum efficiencies for the tipped-NR network indicate a more efficient charge carrier separation and thus a more efficient electron transfer towards the electrolyte. Another feature which is observed for the tipped-NR network is the elongation of the semicircles at low frequencies having a positive bias potential. The elongation results when electrons from further distances reach the electrode, which is observed at lower frequencies due to the larger timescale of the electron transport through the network.^[21,42,43] Thus, the elongation suggests electron mobility within the semiconductor network, and consequently indicates larger metal-to-metal domain distances in the interconnected tipped structure. These tipped structures possess only one Au domain on each semiconductor NR which leads as well to semiconductor–semiconductor contacts that enable the electron delocalization and transport within larger parts of the network. This cannot be observed in the randomly decorated particle network, where the structural properties clearly showed remarkably smaller spatial distances (less than 10 nm) between the gold domains hindering the free electron movement across the connected NRs. Due to the better connection between the rods in case of the Y^{3+} destabilized networks, the electron seems to be more free to travel in these architectures compared to the H_2O_2 destabilized ones. That agrees well

with the findings regarding the larger contact areas between the NRs in such cases.^[21]

In comparison to the particle networks, we have shown earlier the spectroelectrochemical properties of random-NR particles as submonolayers.^[41] In case of individual particles on ITO, no turnaround to more positive photocurrents can be observed which is correlated to the connection of the particles to the ITO electrode and the missing contact between the NRs. Electrons in the gold domains can easily tunnel to the ITO electrode which hinders the accumulation of the electrons in the metal domains and thus the rise of the Fermi level. With this the photocurrent direction does not change with increasing frequency. Instead, for hybrid gel structures as investigated in the present work, the NR–NR connections have a higher impact on the charge carrier dynamics compared to submonolayers, where the contribution of the NR-ITO interface to the IMPS response is significantly overrepresented.

As it has recently been demonstrated by Banin et al., the catalytic activity of gold in hybrid nanostructures shows size dependency.^[11,44] The overall catalytic efficiency depends on the efficiency of electron transfer from the semiconductor to the metal domain and on the catalytic activity of the metal domain itself. Both show opposite dependencies regarding the size of the metal domains, and thus, an optimal metal domain size can be found to maximize the activity. Importantly, this size-effect of the gold domains in our networks cannot be simply correlated with the observed photoelectrochemical differences, since the optimal gold domain size is around 2 nm.^[11] According to this, a higher negative photocurrent for the random-NR network would be expected, which however, cannot be observed due to another important effect: the increased recombination rate in the random-NR network (due to the much smaller spatial distances between the Au domains) overweighs the auspicious gold domain size resulting in a lower observed photocurrent efficiency.

3. Conclusion

To conclude, 3D networks of interconnected CdSe/CdS/Au semiconductor–metal hybrid nanoparticles have been prepared. Different spatial distribution of the gold domains can be achieved by assembling randomly decorated and tipped CdSe/CdS/Au hybrid nanoparticles into 3D, hyperbranched networks. Using two different gelation routes for both types of building blocks, highly porous, voluminous, and branched aerogels have been obtained in all cases. In form of xerogels deposited on conductive substrates, all these gold-decorated networks show an effective charge carrier separation, which leads to the accumulation of the electrons in the metal domains upon irradiation. Intensity modulated photocurrent spectroscopy has revealed the effect of the spatial distance between the metal domains on the charge carrier separation efficiency. More efficient charge carrier separation has been found in the tipped-NR networks resulting in higher negative photocurrent efficiencies compared to the random-NR networks where the charge recombination is more pronounced. Our results imply that the design of the hybrid nanoparticles plays central role in the electrochemical properties of the assembled macrostructures, i.e.,

nanostructuring has a vast impact on the properties of macroscopic gel networks. Control over the location of metal domains on the building blocks—compared to the arbitrary decoration—facilitates a more effective charge carrier separation. Beside the nanoscale particle design, the linking procedure (gelation route) is of central importance in the tailoring of the interparticle interactions and, thus, the macrostructuring of different semiconductor-metal hybrid NPs with high application potential in photoelectrocatalysis and energy harvesting.

Supporting Information

Supporting Information is available from the Wiley Online Library or from the author.

Acknowledgements

J.S. and D.Z. contributed equally to this work. The authors would like to acknowledge the financial support of the European Research Council (ERC) under the European Union's Horizon 2020 research and innovation program (grant agreement 714429). Additionally, this work was funded by the German Research Foundation (Deutsche Forschungsgemeinschaft, DFG) under Germany's excellence strategy within the cluster of excellence PhoenixD (EXC 2122, project ID 390833453) and the grant BI 1708/4-1. A.S. is thankful for financial support from the Hannover School for Nanotechnology (hsn). Moreover, the authors thank Armin Feldhoff and Jürgen Caro for providing the SEM facility. Furthermore, the used TEM for the shown images was provided by the Laboratory of Nano and Quantum Engineering.

Open access funding enabled and organized by Projekt DEAL.

Conflict of Interest

The authors declare no conflict of interest.

Data Availability Statement

Research data are not shared.

Keywords

aerogels, charge carrier separation, hybrid-nanoparticle network, photoelectrochemistry, self-assembly

Received: August 17, 2021

Revised: September 23, 2021

Published online: October 29, 2021

- [1] Y. Hu, S. Mignani, J. P. Majoral, M. Shen, X. Shi, *Chem. Soc. Rev.* **2018**, *47*, 1874.
- [2] I. Balti, A. Barrère, V. Gueguen, L. Poussard, G. Pavon-Djavid, A. Meddahi-Pellé, P. Rabu, L. S. Smiri, N. Jouini, F. Chaubet, *J. Nanopart. Res.* **2012**, *14*, 1266.
- [3] S. Kundu, A. Patra, *Chemical Reviews* **2017**, *117*, 712.
- [4] R. Costi, A. E. Saunders, U. Banin, *Angew. Chem., Int. Ed.* **2010**, *49*, 4878.

- [5] G. Menagen, J. E. Macdonald, Y. Shemesh, I. Popov, U. Banin, *J. Am. Chem. Soc.* **2009**, *131*, 17406.
- [6] A. Freytag, C. Günemann, S. Naskar, S. Hamid, F. Lübckemann, D. Bahnemann, N. C. Bigall, *ACS Appl. Nano Mater* **2018**, *1*, 6123.
- [7] S. Naskar, A. Freytag, J. Deutsch, N. Wendt, P. Behrens, A. Köckritz, N. C. Bigall, *Chem. Mater.* **2017**, *29*, 9208.
- [8] P. Kalisman, L. Houben, E. Aronovitch, Y. Kauffmann, M. Bar-Sadan, L. Amirav, *J. Mater. Chem. A* **2015**, *3*, 19679.
- [9] P. Costi, A. E. Saunders, E. Elmalem, A. Salant, U. Banin, *Nano Lett.* **2008**, *8*, 637.
- [10] P. V. Kamat, *J. Phys. Chem. C* **2008**, *112*, 18737.
- [11] Y. Ben-Shahar, F. Scotognella, I. Kriegel, L. Moretti, G. Cerullo, E. Rabani, U. Banin, *Nat. Commun.* **2016**, *7*, 10413.
- [12] Y. Ben-Shahar, J. P. Philbin, F. Scotognella, L. Ganzer, G. Cerullo, E. Rabani, U. Banin, *Nano Lett.* **2018**, *18*, 5211.
- [13] N. Waiskopf, Y. Ben-Shahar, M. Galchenko, I. Carmel, G. Moshitzky, H. Soreq, U. Banin, *Nano Lett.* **2016**, *16*, 4266.
- [14] M. Waechtler, P. Kalisman, L. Amirav, *J. Phys. Chem. C* **2016**, *120*, 9.
- [15] H. Eshet, M. Grünwald, E. Rabani, *Nano Lett.* **2013**, *13*, 5880.
- [16] U. Banin, Y. Ben-Shahar, *Nat. Energy* **2018**, *3*, 824.
- [17] M. Rosebrock, D. Zámbo, P. Rusch, D. Pluta, F. Steinbach, P. Bessel, A. Schlosser, A. Feldhoff, K. D. J. Hindricks, P. Behrens, D. Dorfs, N. C. Bigall, *Adv. Funct. Mater.* **2021**, 2101628, <http://doi.org/10.1002/adfm.202101628>.
- [18] C. Ziegler, A. Wolf, W. Liu, A. K. Herrmann, N. Gaponik, A. Eychmüller, *Angew. Chem., Int. Ed.* **2017**, *56*, 13200.
- [19] P. Rusch, B. Schremmer, C. Strelow, A. Mews, D. Dorfs, N. C. Bigall, *J. Phys. Chem. Lett.* **2019**, *10*, 7804.
- [20] S. Sánchez-Paradinas, D. Dorfs, S. Friebe, A. Freytag, A. Wolf, N. C. Bigall, *Adv. Mater.* **2015**, *27*, 6152.
- [21] D. Zámbo, A. Schlosser, P. Rusch, F. Lübckemann, J. Koch, H. Pfnür, N. C. Bigall, *Small* **2020**, *16*, 1906934.
- [22] D. Zámbo, A. Schlosser, R. T. Graf, P. Rusch, P. A. Kißling, A. Feldhoff, N. C. Bigall, *Adv. Opt. Mater.* **2021**, *9*, 2100291.
- [23] T. Kodanek, A. Freytag, A. Schlosser, S. Naskar, T. Härtling, D. Dorfs, N. C. Bigall, *Z. für Phys. Chem.* **2018**, *232*, 1675.
- [24] S. Naskar, J. F. Miethe, S. Sánchez-Paradinas, N. Schmidt, K. Kanthasamy, P. Behrens, H. Pfnür, N. C. Bigall, *Chem. Mater.* **2016**, *28*, 2089.
- [25] W. Liu, A. K. Herrmann, N. C. Bigall, P. Rodriguez, D. Wen, M. Oezaslan, T. J. Schmidt, N. Gaponik, A. Eychmüller, *Acc. Chem. Res.* **2015**, *48*, 154.
- [26] A. Schlosser, J. Schlenkrich, D. Zámbo, M. Rosebrock, R. T. Graf, N. C. Bigall **2021**.
- [27] Y. Khalavka, S. Harms, A. Henkel, M. Strozzyk, R. Ahijado-Guzmán, C. Sönnichsen, *Langmuir* **2018**, *34*, 187.
- [28] V. R. Stull, G. N. Plass, *J. Opt. Soc. Am.* **1960**, *50*, 121.
- [29] J. L. Mohanan, I. U. Arachchige, S. L. Brock, *Science* **2005**, *307*, 397.
- [30] T. Kodanek, H. M. Banbela, S. Naskar, P. Adel, N. C. Bigall, D. Dorfs, *Nanoscale* **2015**, *7*, 19300.
- [31] V. Subramanian, E. E. Wolf, P. V. Kamat, *J. Am. Chem. Soc.* **2004**, *126*, 4943.
- [32] I. U. Arachchige, S. L. Brock, *Acc. Chem. Res.* **2007**, *40*, 801.
- [33] E. A. Ponomarev, L. M. Peter, *J. Electroanal. Chem.* **1995**, *396*, 219.
- [34] G. Rainò, T. Stöferle, I. Moreels, R. Gomes, J. S. Kamal, Z. Hens, R. F. Mahrt, *ACS Nano* **2011**, *5*, 4031.
- [35] E. R. Smith, J. M. Luther, J. C. Johnson, *Nano Lett.* **2011**, *11*, 4923.
- [36] Y. Zhang, O. Pluchery, L. Caillard, A.-F. Lamic-Humblot, S. Casale, Y. J. Chabal, M. Salmeron, *Nano Lett.* **2014**, *15*, 51.
- [37] M. Jakob, H. Levanon, P. V. Kamat, *Nano Lett.* **2003**, *3*, 353.
- [38] R. Lavieville, Y. Zhang, A. Casu, A. Genovese, L. Manna, E. Di Fabrizio, R. Krahn, *ACS Nano* **2012**, *6*, 2940.
- [39] T. Simon, M. T. Carlson, J. K. Stolarczyk, J. Feldmann, *ACS Energy Lett.* **2016**, *1*, 1137.
- [40] W. Choi, J. Y. Choi, H. Song, *APL Mater.* **2019**, *7*, 100702.
- [41] J. F. Miethe, F. Lübckemann, J. Poppe, F. Steinbach, D. Dorfs, N. C. Bigall, *ChemElectroChem* **2018**, *5*, 175.
- [42] A. Schlosser, L. C. Meyer, F. Lübckemann, J. F. Miethe, N. C. Bigall, *Phys. Chem. Chem. Phys.* **2019**, *21*, 9002.
- [43] J. F. Miethe, F. Luebckemann, A. Schlosser, D. Dorfs, N. C. Bigall, *Langmuir* **2020**, *36*, 4757.
- [44] Y. Nakibli, Y. Mazal, Y. Dubi, M. Wächtler, L. Amirav, *Nano Lett.* **2018**, *18*, 357.

**ADVANCED
OPTICAL
MATERIALS**

Supporting Information

for *Adv. Optical Mater.*, DOI: 10.1002/adom.202101712

**Revealing the Effect of Nanoscopic Design on the
Charge Carrier Separation Processes in Semiconductor-
Metal Nanoparticle Gel Networks**

*Jakob Schlenkrich, Dániel Zámbo, Anja Schlosser,
Pascal Rusch, and Nadja C. Bigall**

Supporting Information

Revealing the Effect of Nanoscopic Design on the Charge Carrier Separation Processes in Semiconductor-Metal Nanoparticle Gel Networks

Jakob Schlenkrich[†], Dániel Zámbo[†], Anja Schlosser, Pascal Rusch, Nadja C. Bigall*

Leibniz Universität Hannover, Callinstraße 3A, 30167 Hanover, Germany
E-mail: nadja.bigall@pci.uni-hannover.de

[†] These authors contributed equally to this work.

Chemicals: All chemicals used for the syntheses were used as purchased without any further purification. Cadmium oxide (CdO, 99.998%) and elemental selenium (200 mesh, 99.999%) were supplied by Alfa Aesar. Tri-*n*-octylphosphine oxide (TOPO, 99%), elemental sulfur (99.98%), 1-octadecene (ODE, 90%), didodecyl dimethyl ammonium bromide (DDAB, 98%), Dodecylamine (DDA, 98%), 3 - mercaptopropionic acid (MPA, $\geq 99\%$), ammonium hydroxide (NH₄OH, 28–30 wt%), (3 - mercaptopropyl)trimethoxy silane (MPTMS, 95%), 2-propanol ($\geq 99.8\%$), chloroform ($\geq 99.5\%$), yttrium chloride hexahydrate (YCl₃·6H₂O, 99.99%), were purchased from Sigma - Aldrich. Potassium hydroxide (KOH, $>85\%$), n-hexane ($\geq 99\%$), acetone (99.5%), hydrogen peroxide (H₂O₂, 35 w/w%), toluene ($\geq 99.7\%$), and methanol (MeOH, $\geq 99.8\%$) were purchased from Honeywell. Octadecylphosphonic acid (ODPA, 99.0%) and gold(III) chloride (AuCl₃, 99%) were purchased from ABCR. Tri-*n*-octylphosphine (TOP, 97%), elemental tellurium (60 mesh, 99.999%), and hexylphosphonic acid (HPA, 99%) were obtained from Roth, Fisher Scientific and PCI, respectively. Ultrapure water with a resistivity of 18.2 M Ω ·cm was used for aqueous solutions.

Experimental Section

Synthesis of CdSe Quantum Dots: The synthesis of the CdSe QDs was adapted by the method of Carbone *et al.*^[1] In a three-neck flask CdO (0.12 g), TOPO (6.0 g) and ODPA (0.56 g) were degassed under vacuum at 150 °C for 50 min. Under an argon atmosphere, the flask was heated

WILEY-VCH

to 300 °C until all CdO was dissolved completely. TOP (3.6 mL) was added, and the temperature was raised to 380 °C. The growth of the CdSe QDs was initiated with the addition of elemental selenium (0.116 g) dissolved in TOP (3.6 mL). After 4 minutes, the growth was stopped by addition of ODE (6 mL) and the flask was cooled down quickly using an air flow. Twice, the QDs were precipitated with methanol, centrifuged, and redispersed in toluene. The size of the nanocrystals and the concentration of the QD solution was determined with the position and the optical density (OD) of the first excitation maximum in an extinction spectrum.^[2]

Synthesis of CdSe/CdS Nanorods: In a modified synthesis of Carbone *et al.*, CdO (0.18 g), TOPO (9.0 g), ODE (0.84 g) and HPA (0.24 g) were mixed and degassed under vacuum at 150 °C for 1 h.^[1] After dissolving the CdO completely at 300 °C under argon atmosphere, TOP (5.6 mL) was added and the temperature was increased to 380 °C. Once the temperature was reached, the growth of the NRs was initiated by quick injection of sulfur (0.39 g) dissolved in TOP (5.4 mL) mixed with 144.8 µL of the previously synthesized CdSe NPs. After 8 minutes of reaction, the solution was cooled down by an air flow. At 70 °C, toluene (7 mL) was added and after further cooling (down to ca. 30 °C) the particles were washed twice with methanol and redispersed in toluene (2 mL).

Synthesis of random-NRs: The synthesis was performed following the method of Miethe *et al.*^{[3][4]} AuCl₃ (7.5 mg), DDA (40.44 mg) and DDAB (25.3 mg) were dissolved in toluene (6.03 mL) under ambient conditions and placed in an ultrasonication bath until the color became light yellow. While heating this solution to 40 °C under argon atmosphere, CdSe/CdS NR solution in toluene (6.8 mL; $c_{Cd} = 0.156$ mg/mL) was also heated to 40 °C under Ar for 30 minutes. The gold solution then was injected into the rod solution with a syringe. After 30 minutes of reaction time at 40 °C, the reaction was quenched with methanol and washed twice with methanol and finally, redispersed in toluene (2 mL).

WILEY-VCH

Synthesis of tipped-NRs: According to the method published by Menagen *et al.*,^[4] AuCl₃ (2.5 mg), DDA (40.44 mg) and DDAB (25.3 mg) were mixed with toluene (6.03 mL) in a glovebox. The mixture was shaken with a vortex until the gold was dissolved. When the solution became light yellow, it was mixed with the CdSe/CdS NR solution in toluene (6.8 mL; $c_{Cd} = 0.156$ mg/mL). The mixture was irradiated with an LED (Ledxon Alustar 9008098, $\lambda = 470$ nm, operated at 350 mA) for 45 minutes. Afterwards, methanol (5 mL) was added to quench the reaction, and the solution was centrifuged. Furthermore, the particles were washed twice with methanol and redispersed in toluene (2 mL).

Phase transfer: The method of the phase transfer was adapted from the work of Kodanek *et al.*^{[5][6]} The gold decorated particles were precipitated with methanol, centrifuged and redispersed in hexane (10 mL). The cadmium concentration was approximately 0.4 mg/mL. After the addition of methanol (10 mL) and MPA (0.25 mL) the mixture was shaken overnight. The methanolic phase with the particles was separated and centrifuged. After redispersion in 0.01M aqueous KOH solution (2 mL) the particles were washed with acetone and finally redispersed in Millipore water (0.5 mL).

Assembly to Hydrogels and Transfer to Aerogels: (i) To destabilize the particles with H₂O₂, the aqueous nanoparticle solution (400 μ L) was mixed with H₂O₂ solution (0.35 wt%, 37.5 μ L) in an Eppendorf tube followed by vortexing and placing it in an oven at 80 °C for one minute.^[7] Afterwards, the solution was stored in a dark place overnight. (ii) To assemble the particles with Y³⁺ cations, an aqueous YCl₃ · 6 H₂O solution (45 mM, 50 μ L) was injected into the particle solution (400 μ L).^[8] After vortexing, the solution was stored in a dark place overnight. After hydrogelation of route (i) and route (ii), subsequently, several washing steps with Millipore water were applied to remove the destabilizing agent and other by-products. Furthermore, to exchange water with dry acetone the gel was washed with mixtures of water and acetone and afterwards with pure acetone and anhydrous acetone. To obtain the aerogel,

WILEY-VCH

the acetogels were dried in a critical point dryer (Quorum Technologies, E3100) using supercritical CO₂. The procedure can be found in our previous paper.^[7]

Preparation of Xerogel ITO Electrodes: Before coating the electrodes with the particles, the ITO coated glass substrates (VisionTek Ltd., 12 ohms/square, size of 1.5 cm × 3 cm) were cleaned and activated. For cleaning, the substrates were subsequently sonicated for 5 minutes in acetone, 2-propanol and Millipore water. Afterwards, the surface was activated with a solution of NH₄OH and H₂O₂ (10 mL 25 % NH₄OH, 10 mL 35 % H₂O₂) in water (60 mL) for 2 h at 70 °C. Next, the ITO surface was functionalized with 1 vol% MPTMS in toluene for 2 h at 70 °C. A mold was prepared using a plastic cuvette glued on the ITO substrate with a silicone sealing paste. The aqueous nanoparticle solution (300 μL) was filled into the glued cuvette and the H₂O₂ or Y³⁺ solutions were added as described above. After mixing the solutions with the pipette, the gel formed overnight, and was afterwards washed with Millipore water by removing the solution above the gel network and adding 2 mL of water carefully. The washing step has been repeated 10 times and the gel networks were stored for a few days. The xerogel was formed by drying the hydrogel under ambient conditions.

Optical characterization: Extinction spectra of diluted nanoparticle solutions were performed with a Jasco V-750 spectrometer. Absorption spectra of xerogel coated ITO electrodes were measured in central position with an Agilent CARY 5000, which was equipped with a Diffuse Reflectance Accessory. Solid aerogel samples were measured with a Quanta-φ integrating sphere coupled to a Horiba Dual-FL spectrofluorometer. Measurements of nanoparticle solutions were performed in quartz cuvettes (1 cm path length) and solid samples in a Teflon holder, which was covered with a quartz glass plate.

Structural characterization: TEM images were taken with a FEI Tecnai G2 F20 TMP (operated at 200 kV). Samples were prepared by drop casting the nanoparticle solution on copper grids, covered with a carbon layer (Quantifoil). For measuring aerogel samples fragments of the aerogel were placed on the copper grid by scratching the grid along the aerogel.

WILEY-VCH

A JEOL JSM-6700F (operated at 2 kV) was used to obtain SEM images of the aerogel and xerogel samples. For the sample preparation parts of the aerogel were placed on a conductive carbon tape and ITO electrodes were contacted with a conductive silver lacquer.

Photoelectrochemical measurements: The photoelectrochemical measurements were performed in a self-build electrochemical cell which is further described by Miethe *et al.* and in figure S7.^[3] In the intensity modulated photocurrent spectroscopy the current response of the electrochemical cell was measured while applying light pulses with frequencies between 10 kHz and 1 Hz. Hereby, the value of the photocurrent and the phase shift between the sinusoidal light pulses and the sinusoidal current signal is measured. For this detection a lock-in amplifier controls the sinusoidal light pulses with the specific frequency and detects the incoming photocurrent. A lock-in amplifier is necessary because a potentiostat in general is not able to measure the appearing small currents in the range of μA where the noise of the system is larger than the signal itself. These measurements were also applied at different bias potentials between -450 mV and 150 mV (-450 mV , -300 mV , -150 mV , 0 mV , 150 mV), which were measured against Ag/AgCl reference electrode (3 M NaCl, purchased from BASi). A PE 1542 DC power supply from PHILIPS powers the LED (0.5 mW, $\lambda = 472\text{ nm}$) and a 7270 DSP lock-in amplifier from AMETEK gives the sinusoidal signal to the LED as well as detects the current signal from the measurement cell. The bias potential was controlled by the Modulab XM from AMETEK. Measuring the linear sweep voltammetry includes a scan from low to higher bias potentials over a fixed time range. In the experiments the voltage was applied from -0.6 V up to 0.3 V with a slope of 0.2 V/min . Before starting the measurement, a constant potential was applied for 30 s at the starting voltage of -0.6 V to reach an equilibrium state for the whole system. During the linear sweep voltammetry, the LED was turned on and off periodically with a frequency of 40 mHz. This corresponds to a time period of 12.5 s of irradiation and 12.5 s of darkness. To apply the voltage the potentiostat Modulab XM from AMETEK was used and the control system for the LED was the arbitrary generator HMF2550 from Rohde & Schwarz.

WILEY-VCH

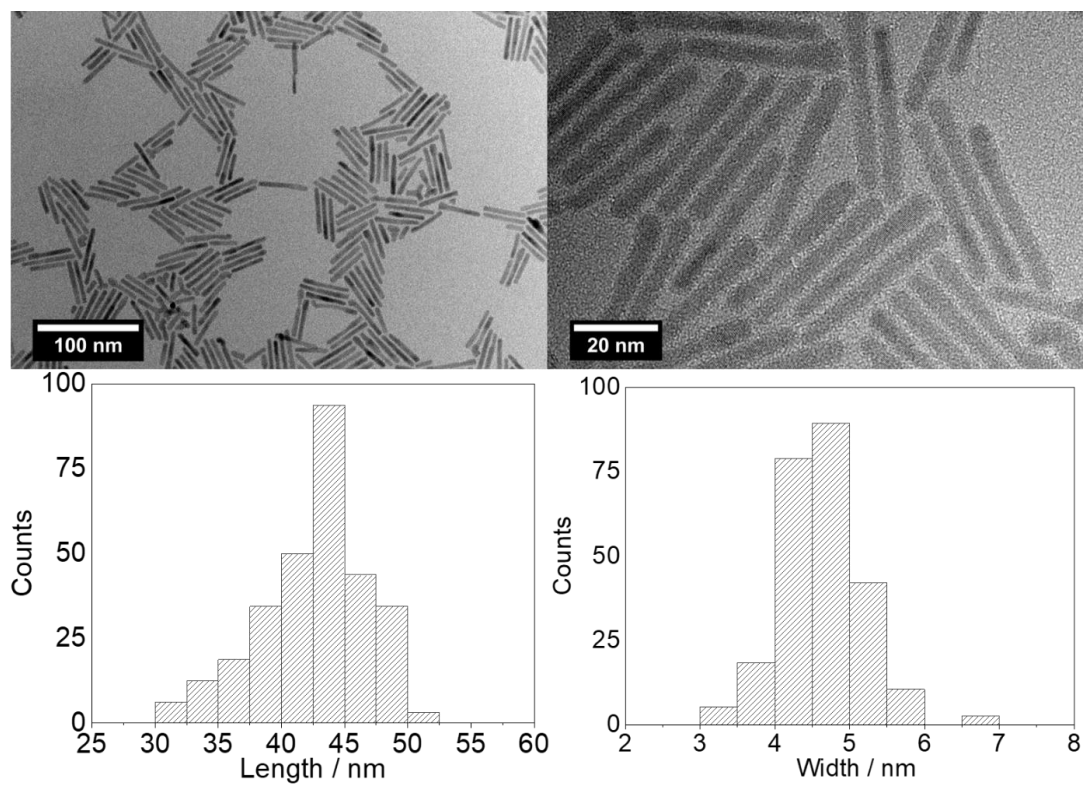


Figure S1. TEM images of the synthesized CdSe/CdS NRs (top) with the measured length and width (bottom).

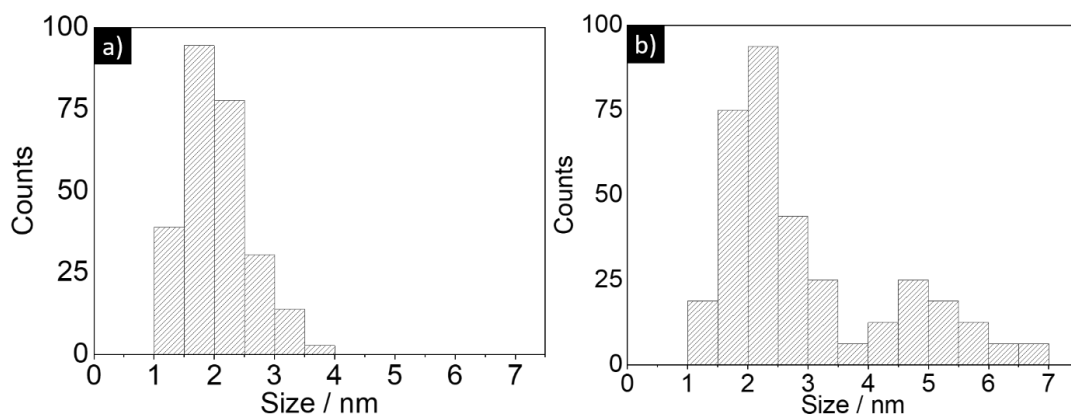


Figure S2. Size distribution of the gold domains on the random-NRs (a) and tipped-NRs (b).

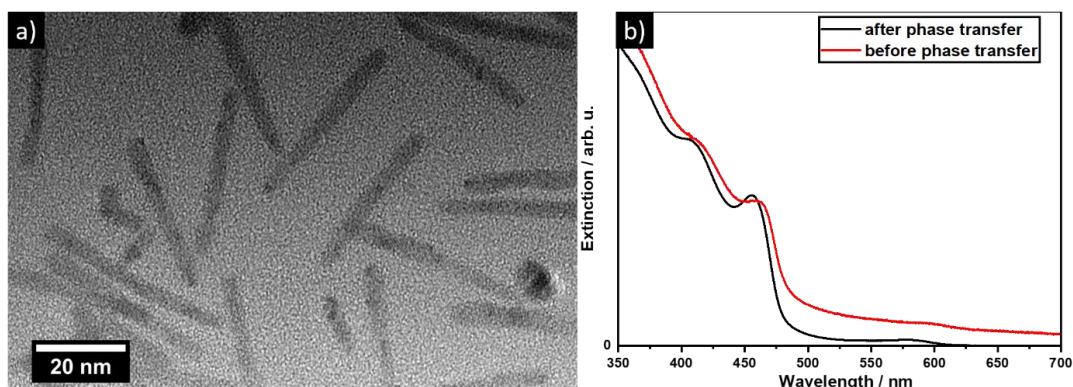


Figure S3. TEM image (a) and extinction spectra (b) of random-NRs after phase transfer using KOH in the transfer solution.

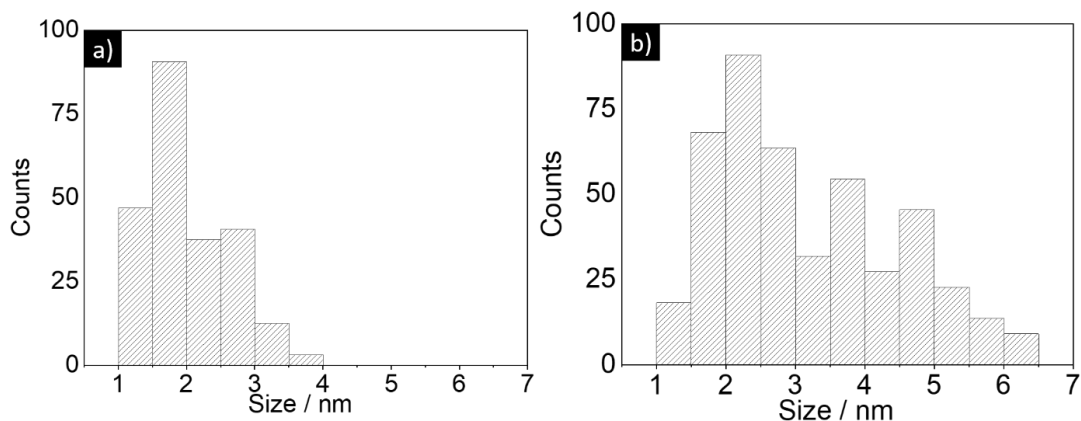


Figure S4. Size distributions of the gold domains in random-NR (a) and tipped-NR (b) aerogels.

Discussion of optical properties

Absorption spectra of the aerogels show the retained nanoscopic properties in the macroscopic gel structures. The characteristic band edges of the CdSe and the CdS can also be observed in the absorption spectra of the gold decorated aerogel networks (**Figure S5**). The prepared aerogels show the characteristic optical response of the building blocks measured in ensemble conditions. However, the broader spectral response over the whole measurement range can be attributed to the highly increased amount of material due to the aerogel nature of the sample and has been observed in semiconductor gels previously.^[7,8] In addition, the LSPR of the gold domains also increases the absorption cross-section of the NRs. Size distribution and plasmon coupling effects between the gold domains might further broaden the plasmon band.^[9] As for the particle measurements, it is observed that the absorption of larger gold domains is more

WILEY-VCH

prominent compared to the smaller gold domains which results in different physical appearance (e.g. color, shade) of the aerogel structures.

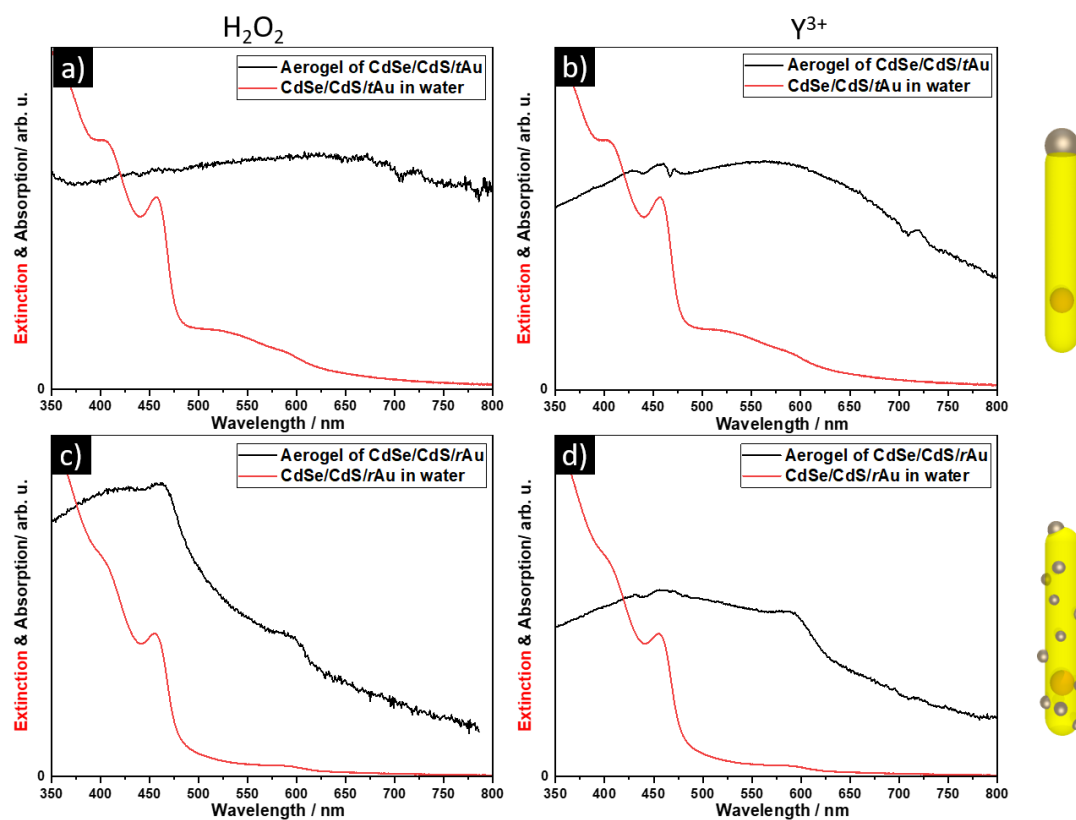


Figure S5. Absorption (black curves) of random-NR (c,d) and tipped-NR (a,b) aerogels destabilized with Y^{3+} cations (b,d) and H_2O_2 (a,c). Extinction (red curves) of random (c,d) and tipped (a,b) NRs (building blocks for gelation) in aqueous solution.

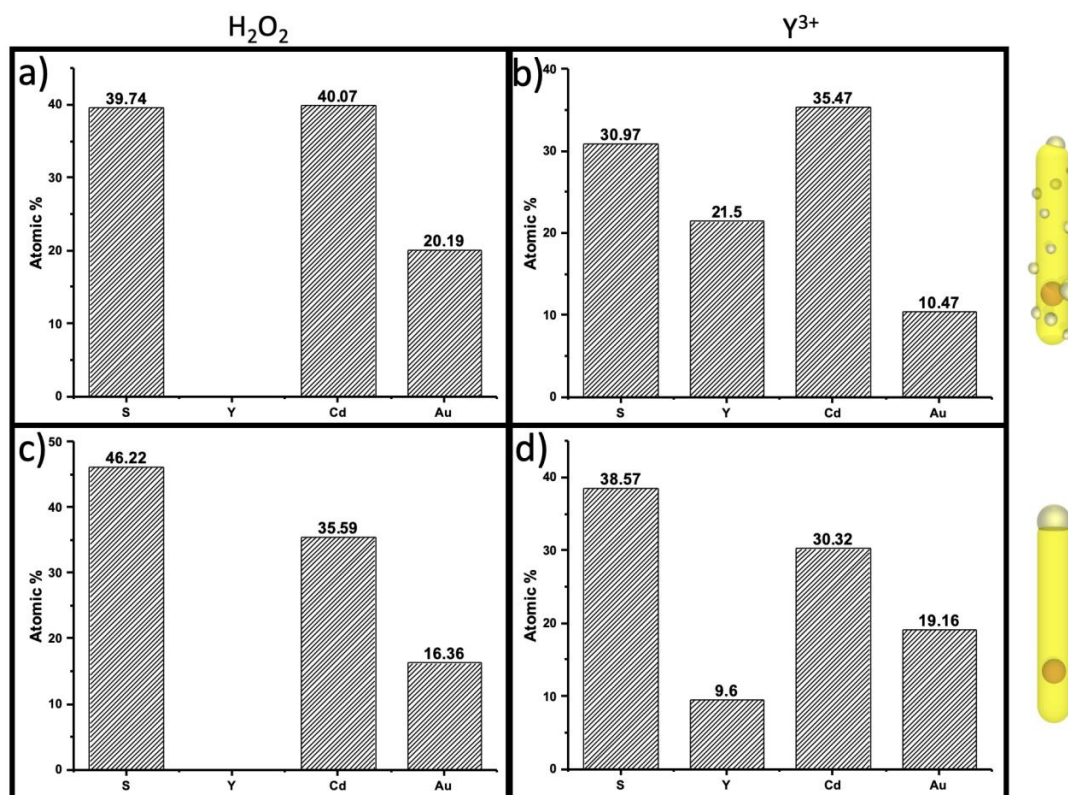


Figure S6. EDXS quantitative elemental analysis of aerogel samples: (a) random-NRs destabilized with H_2O_2 ; (b) random-NRs destabilized with Y^{3+} cations; (c) tipped-NRs destabilized with H_2O_2 ; (d) tipped-NRs destabilized with Y^{3+} cations.

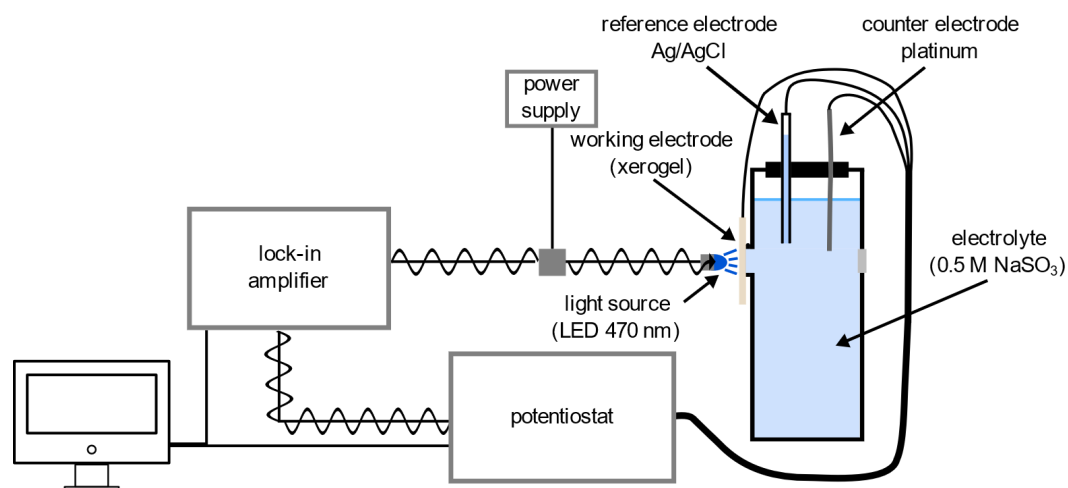


Figure S7. Schematic illustration of the intensity modulated photocurrent spectroscopy setup.

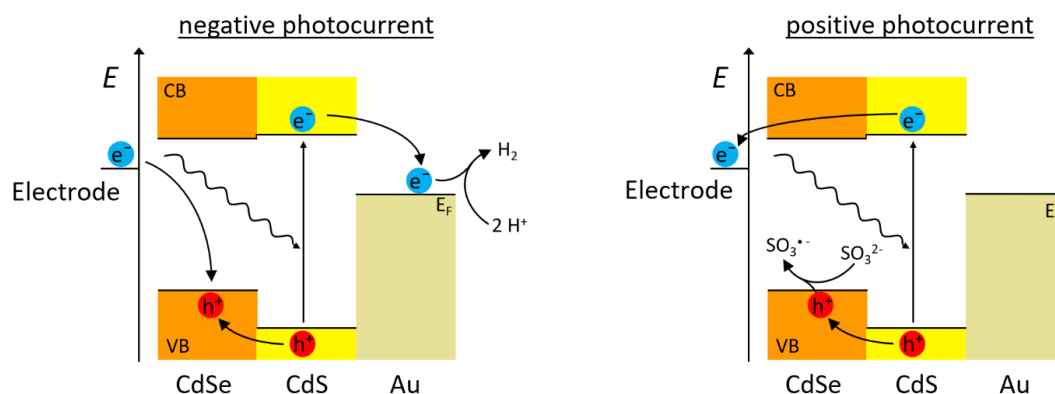


Figure S8. Schematic charge carrier reactions leading to negative and positive photocurrent.

Discussion of linear sweep voltammetry (LSV) measurements

The LSV measurements confirm the observed results of the IMPS spectra. For all samples, transients occur when turning on the light source at lower bias potentials. These transients indicate the formation of an equilibrium state for longer irradiation times. The formation of the equilibrium can be attributed to the observed turnarounds in the IMPS measurements, due to the competitive formation of positive and negative photocurrents. For the tipped-NR xerogel networks these transients are more intense which is as well shown in the turnaround at higher photocurrent quantum efficiencies in the IMPS responses. In general, the photocurrents are higher in the tipped-NR xerogel networks compared to the random-NR xerogel networks regardless the destabilization method.

In case of the tipped-NR network destabilized with H_2O_2 the photoelectrochemical photocurrent switching point (PEPS) is observed at higher bias potentials compared to the other xerogel networks. This can be correlated to a suppressed positive photocurrent due to the gold tipped morphology and the less crystal contact area compared to the network destabilized with Y^{3+} cations as discussed in the main text.

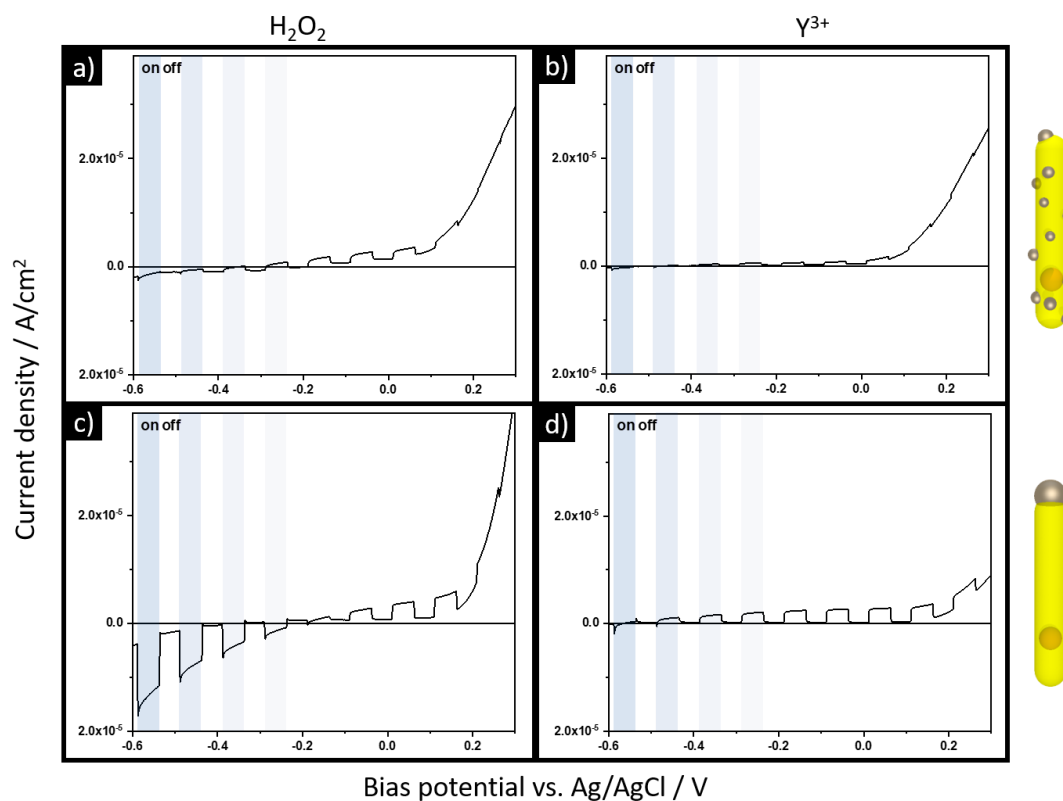


Figure S9. Linear sweep voltammetry measurements of xerogel coated electrodes: (a) random-NR destabilized with H_2O_2 ; (b) random-NR destabilized with Y^{3+} cations; (c) tipped-NR destabilized with H_2O_2 ; (d) tipped-NR destabilized with Y^{3+} cations.

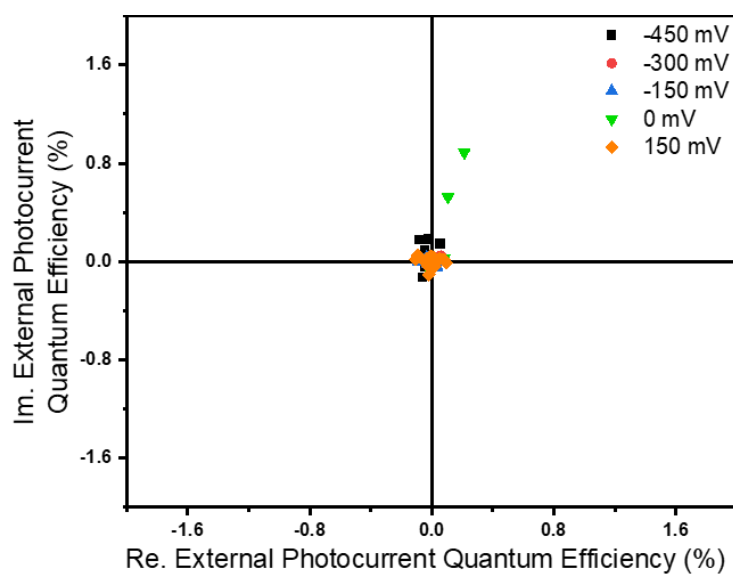


Figure S10. Linear sweep voltammetry measurements of MPTMS coated ITO glass sheets.

WILEY-VCH

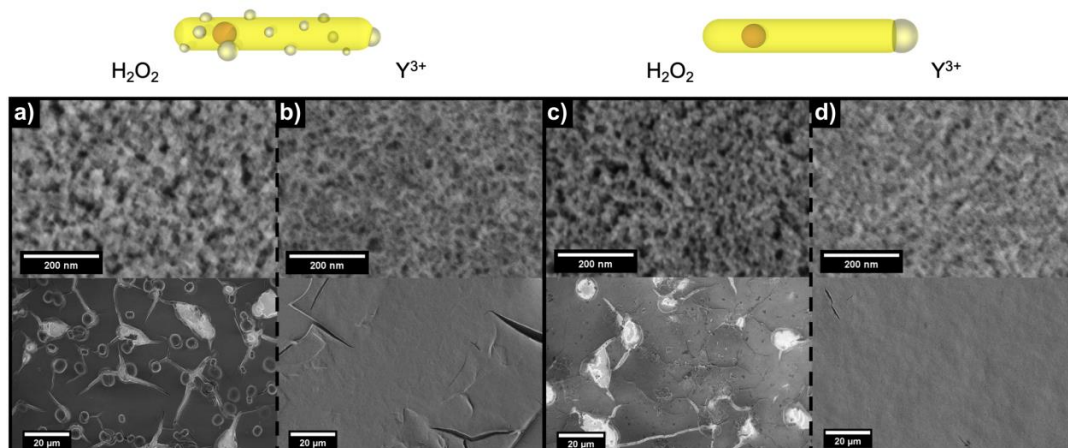


Figure S11. SEM images in different magnifications and photographs of xerogel coated ITO glass electrodes: (a) random-NR destabilized with H_2O_2 ; (b) random-NR destabilized with Y^{3+} cations; (c) tipped-NR destabilized with H_2O_2 ; (d) tipped-NR destabilized with Y^{3+} cations.

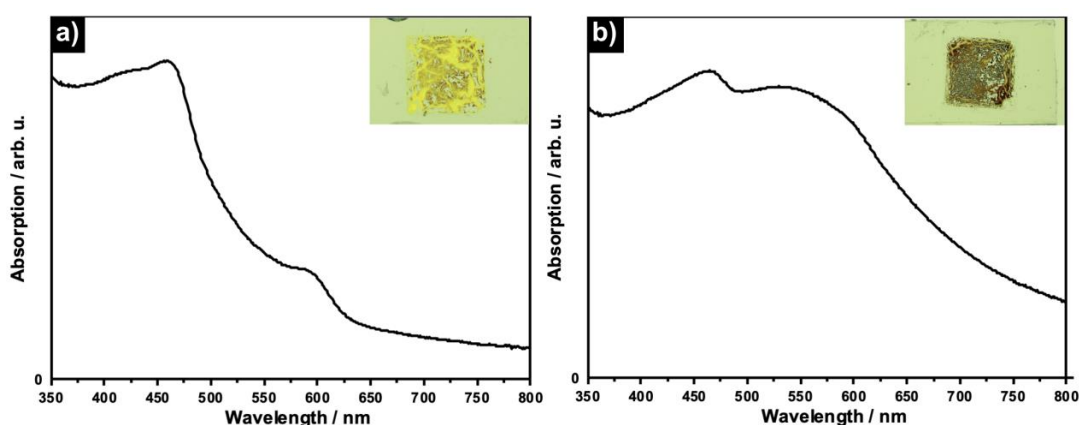


Figure S12. Absorption of random-NR (a) and tipped-NR (b) aerogels on ITO glass electrodes destabilized with Y^{3+} cations. Insets show the photographs of the xerogel-coated ITO electrodes (the coated area is 1×1 cm).

Reference

- [1] L. Carbone, C. Nobile, M. De Giorgi, F. Della Sala, G. Morello, P. Pompa, M. Hytch, E. Snoeck, A. Fiore, I. R. Franchini, M. Nadasan, A. F. Silvestre, L. Chiodo, S. Kudera, R. Cingolani, R. Krahn, L. Manna, *Nano Lett.* 2007, 7, 10, 2942-2950 **2007**, DOI 10.1021/NL0717661.
- [2] W. William Yu, Lianhua Qu, and Wenzhuo Guo, X. Peng*, **2004**, DOI 10.1021/CM033007Z.
- [3] J. F. Miethe, F. Lübke, J. Poppe, F. Steinbach, D. Dorfs, N. C. Bigall,

WILEY-VCH

ChemElectroChem **2018**, *5*, 175.

- [4] G. Menagen, J. E. Macdonald, Y. Shemesh, I. Popov, U. Banin, *J. Am. Chem. Soc.* **2009**, *131*, 17406.
- [5] T. Kodanek, H. M. Banbela, S. Naskar, P. Adel, N. C. Bigall, D. Dorfs, *Nanoscale* **2015**, *7*, 19300.
- [6] H. G. Bagaria, E. T. Ada, M. Shamsuzzoha, D. E. Nikles, D. T. Johnson, *Langmuir* **2006**, *22*, 7732.
- [7] S. Sánchez-Paradinas, D. Dorfs, S. Friebe, A. Freytag, A. Wolf, N. C. Bigall, *Adv. Mater.* **2015**, *27*, 6152.
- [8] D. Zámbo, A. Schlosser, P. Rusch, F. Lübke, J. Koch, H. Pfnür, N. C. Bigall, *Small* **2020**, 1906934.
- [9] N. J. Halas, S. Lal, W. S. Chang, S. Link, P. Nordlander, *Chem. Rev.* **2011**, *111*, 3913.

Chapter 3

Hydrogen Evolution Reaction on Nanoparticle-Based Hydrogels

3.1 Summary

Chapter 3 investigates the use of semiconductor and semiconductor-metal hybrid gel structures in photocatalytic applications. In Section 3.2, the advances of using semiconductor gels as hydrogels for photocatalysis has been investigated by comparing hydrogels with their respective nanoparticle dispersions. As semiconductor nanoparticles, CdSe, CdS, and CdSe/CdS were used to build up hydrogels for the photocatalytic hydrogen production. Section 3.3 furthermore shows, the efficiency of a hydrogel based photocatalyst was improved by platinum growth on the tips of the CdSe/CdS nanorod based hydrogels.

Hydrogels made of CdSe quantum dots, CdS nanorods and CdSe/CdS nanorods showed up to five times higher photocatalytic hydrogen production rates compared to their nanoparticle dispersions. CdSe/CdS hydrogels showed the best photocatalytic properties and were further investigated. The gelation mechanism and the network formation alter the charge carrier properties. Using hydrogen peroxide as destabilizing agent oxidizes the thiol ligands and triggers the assembly. Removing thiol ligands reduces hole trap states on the surface leading to a better hole transfer into the CdSe core. Furthermore, removing ligands from the surface makes the catalytically active surface better accessible. In case of nanoparticle dispersions, the ligand shell has to be overcome to reach the surface. Additionally, in the hydrogels, the network structure and crystal contact between nanoparticle building blocks enables the electrons to be delocalized beyond one nanoparticle building block. This further improves charge carrier separation and thus charge carrier lifetimes which is beneficial for use of these charge carriers for catalytic reactions.

In section 3.3, hydrogels with CdSe/CdS/Pt hybrid nanorods as nanoparticle building blocks showed high hydrogen production rates. To use hydrogen peroxide as destabilizing agent, the nanoparticles were dispersed in an acidic solution due to the catalytic degradation of hydrogen peroxide on the platinum surface. The acidic conditions used here lead to hydroxy radicals as intermediates in the degradation. These radicals themselves can oxidize the thiol ligands which made the destabilization of the colloidal solution possible.

Metal growth on the semiconductor and the formation of a CdSe/CdS/Pt hydrogel increases the non-radiative recombination rates due to the efficient electron transfer from the semiconductor to the metal. Interestingly, in this work the hydrogen production rate was further increased by mixing hybrid CdSe/CdS/Pt nanorods with pure CdSe/CdS semiconductor nanorods. Through reducing the amount of platinum domains increasing hydrogen production rates could be measured. The electron transfer thus seemed not to be the bottle neck of the catalytic reaction. Instead, diffusion limits in the gels structure or the need of two electrons for the hydrogen production might be the rate limiting steps.

3.2 Investigation of the Photocatalytic Hydrogen Production of Semiconductor Nanocrystal-Based Hydrogels

Jakob Schlenkrich, Franziska Lübkekmann-Warwas, Rebecca T. Graf, Christoph Wesemann, Larissa Schoske, Marina Rosebrock, Karen D. J. Hindricks, Peter Behrens, Detlef W. Bahnemann, Dirk Dorfs, and Nadja C. Bigall

Published in *Small* 2023, 19, 2208108
<https://doi.org/10.1002/sml.202208108>



Investigation of the Photocatalytic Hydrogen Production of Semiconductor Nanocrystal-Based Hydrogels

Jakob Schlenkrich, Franziska Lübke-Warwas, Rebecca T. Graf, Christoph Wesemann, Larissa Schoske, Marina Rosebrock, Karen D. J. Hindricks, Peter Behrens, Detlef W. Bahnemann, Dirk Dorfs, and Nadja C. Bigall*

Destabilization of a ligand-stabilized semiconductor nanocrystal solution with an oxidizing agent can lead to a macroscopic highly porous self-supporting nanocrystal network entitled hydrogel, with good accessibility to the surface. The previously reported charge carrier delocalization beyond a single nanocrystal building block in such gels can extend the charge carrier mobility and make a photocatalytic reaction more probable. The synthesis of ligand-stabilized nanocrystals with specific physicochemical properties is possible, thanks to the advances in colloid chemistry made in the last decades. Combining the properties of these nanocrystals with the advantages of nanocrystal-based hydrogels will lead to novel materials with optimized photocatalytic properties. This work demonstrates that CdSe quantum dots, CdS nanorods, and CdSe/CdS dot-in-rod-shaped nanorods as nanocrystal-based hydrogels can exhibit a much higher hydrogen production rate compared to their ligand-stabilized nanocrystal solutions. The gel synthesis through controlled destabilization by ligand oxidation preserves the high surface-to-volume ratio, ensures the accessible surface area even in hole-trapping solutions and facilitates photocatalytic hydrogen production without a co-catalyst. Especially with such self-supporting networks of nanocrystals, the problem of colloidal (in)stability in photocatalysis is circumvented. X-ray photoelectron spectroscopy and photoelectrochemical measurements reveal the advantageous properties of the 3D networks for application in photocatalytic hydrogen production.

1. Introduction

One of the main challenges in recent decades is the transformation toward a sustainable energy system.^[1] Hydrogen is a widely discussed alternative to fossil fuels and besides the yet industrially applied electrolysis, photocatalytic hydrogen production could be a method to supply hydrogen. A variety of materials, for example, TiO₂, MoS₂, CdS, SiC, or g-C₃N₄, has been investigated to find a suitable candidate to use sunlight efficiently for photocatalytic hydrogen production.^[2–4] In addition to the type of material, the structure or morphology plays a crucial role in the design of the catalyst.^[5] Nanomaterials in general provide a large surface-to-volume ratio leading to a high amount of catalytically active surface in an overall low amount of material. The expertise in the field of solution-based nanocrystal (NC) synthesis acquired over the past decades enables the production of a large number of different NC with a variety of shapes.^[6–10] Especially, CdSe, CdS, and CdSe/CdS

J. Schlenkrich, F. Lübke-Warwas, R. T. Graf, C. Wesemann, L. Schoske, M. Rosebrock
Leibniz University Hannover
Institute of Physical Chemistry and Electrochemistry
Callinstraße 3A, 30167 Hannover, Germany
F. Lübke-Warwas, L. Schoske, M. Rosebrock, K. D. J. Hindricks, P. Behrens, D. Dorfs, N. C. Bigall
Cluster of Excellence PhoenixD (Photonics
Optics and Engineering -Innovation Across Disciplines)
Leibniz University Hannover
30167 Hannover, Germany
E-mail: nadja.bigall@pci.uni-hannover.de

R. T. Graf, P. Behrens, D. Dorfs, N. C. Bigall
Laboratory of Nano- and Quantum Engineering
Leibniz University Hannover
30167 Hannover, Germany
K. D. J. Hindricks, P. Behrens
Leibniz University Hannover
Institute of Inorganic Chemistry
Callinstraße 9, 30167 Hannover, Germany
D. W. Bahnemann
Leibniz University Hannover
Institute of Technical Chemistry
Callinstraße 5, 30167 Hannover, Germany

D. W. Bahnemann
Laboratory "Photoactive Nanocomposite Materials"
Saint-Petersburg State University
Ulyanovskaya str. 1, Saint-Petersburg, 198504 Peterhof, Russia

The ORCID identification number(s) for the author(s) of this article can be found under <https://doi.org/10.1002/sml.202208108>.

© 2023 The Authors. Small published by Wiley-VCH GmbH. This is an open access article under the terms of the Creative Commons Attribution-NonCommercial License, which permits use, distribution and reproduction in any medium, provided the original work is properly cited and is not used for commercial purposes.

DOI: 10.1002/sml.202208108

heterostructured NCs have been intensively studied and the synthetic control of these materials allows specific design for the targeted application.^[10–14] Therefore, of particular interest is the design of the NC heterostructure, which allows targeted influence on the charge carrier mobility, its residence probability as well as band structure. Compared to the band structure of the pure CdSe quantum dots (QD) and CdS nanorods (NRs), with band gap energies of 1.7 and 2.4 eV, respectively, the CdSe/CdS dot-in-rod NR exhibits a quasi-type-II electronic structure. Here, the band offset of the conduction bands is small enough to allow the electron to delocalize over the entire NRs, whereas the hole is localized in the core (Figure 1). For photocatalytic applications, the choice of band structure in the semiconductor material is the first important step, but it has already been shown that pure semiconductor NCs are not as efficient as they are estimated to be.^[15–17] Therefore, a metal-based co-catalyst is usually added to capture the sunlight in the semiconductor and transfer the excited electrons from the semiconductor to the co-catalyst where the catalytic hydrogen production takes place. Metal complex^[18] can be used as co-catalysts or a metal-based co-catalyst domain, for example, Pt, Au, Au–Pt, Ni, and many more,^[15,19–21] can be grown on the semiconductor to obtain an efficient photocatalyst. When using ligand-stabilized NCs as photocatalysts the ligand surface has a major impact on the overall efficiency.^[22–24] Some ligands, for example, mercaptopropionic acid (MPA), can lead to trap states which have an influence on the charge carrier dynamics and lifetimes.^[22] Others are sterically large in size and therefore

have an influence on the catalytic behavior. Generally, the accessibility of the catalytic surface, the lifetime of the charge carrier, and the stability of the NCs play a key role in the efficiency of the photocatalytic reaction. The accessibility of the surface can be influenced on the one hand by the stabilizing ligand shell (too much prevent access to the surface) and on the other hand by the stability of the NCs in solution. If the NCs agglomerate in a way that the accessible surface area is reduced, the photocatalytic efficiency decreases.

In addition to the properties already discussed, the morphology of the photocatalyst may also influence the resulting efficiency and make the material interesting for future applications. A novel class of materials with an interesting morphology are nanocrystal-based gel structures, which exhibit high porosity and combine physicochemical properties of the NCs with the size of bulk material.^[25–28] Nanocrystal-based gel structures undergo a controlled destabilization of the ligand-stabilized nanocrystal solution to form a 3D, highly porous network which retains the properties of the NC building blocks. As has already been shown, semiconductor NC-based networks, for example, CdSe,^[29] CdS,^[30] and CdSe/CdS,^[31–33] can even exhibit improved and novel properties compared to the NCs in solution. A prominent feature of semiconductor NC-based gel structure is their electron and hole wavefunction beyond one single NC, which results from the crystal-to-crystal bond of the individual NC building blocks (Figure 1). In gel structures consisting of only one semiconductor material, for example, CdSe or CdS, this can lead to a delocalization of the charge carriers

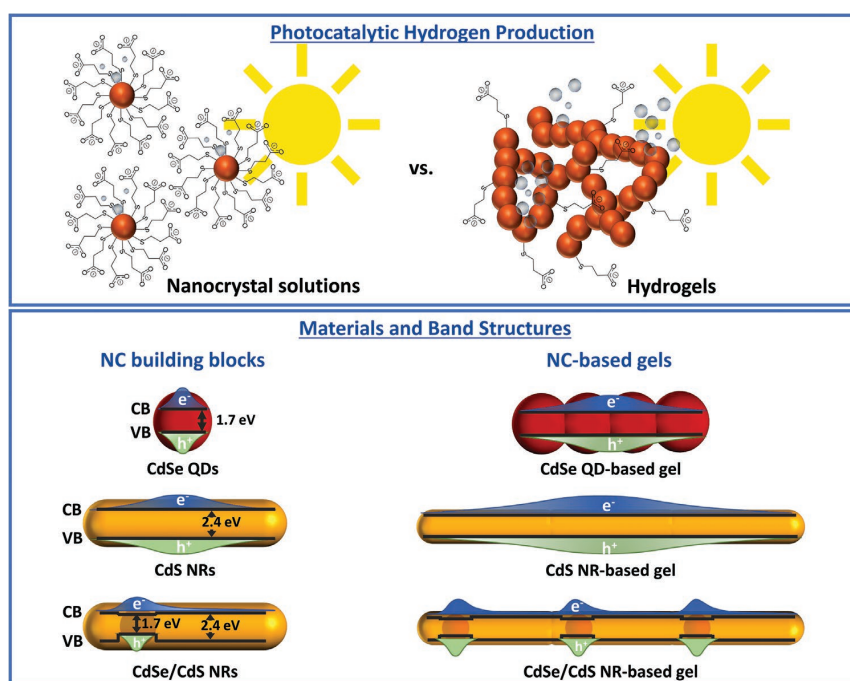


Figure 1. Schematic illustration of the photocatalytic hydrogen production combined with the materials and band structures of the NC building blocks and NC-based gels used (symbolized as a chain of three and four nanocrystals in direct contact). After a phase transfer from organic to an aqueous solution, the ligand-stabilized nanocrystals are destabilized by ligand oxidation with H_2O_2 . Nanocrystals in aqueous solution and hydrogels can be used for photocatalytic hydrogen production.

beyond one NC which would have a minor effect on the charge carrier separation in these network structures. However, the charge carrier separation in gel structures consisting of a semiconductor heterostructure, for example, CdSe/CdS, is significantly increased by the quasi-type-II electronic structure. In previous work, optical and photoelectrochemical investigations of CdSe/CdS NR-based gel structures have shown that crystal-to-crystal contact leads to a significant increase in charge carrier lifetime as well as charge carrier mobility and charge carrier separation. The long-lived charge carrier separation improves reactions of the respective charge carriers on the surface of the gel network.^[31–34] Semiconductor NC-based gel networks combine the advantages of pure NC, such as high control of electronic properties through synthesis, as well as high surface-to-volume ratio, and the advantages of a gel structure, for example, a high porosity, easily accessible surface, increased probability of charge carrier separation through crystal-to-crystal contact, in one material. Thus, all advantages make the gel structures to a promising class of materials for application in photocatalysis.^[35]

In this work, we present the influence of gel network formation of different semiconductor NC building blocks, here CdSe QDs, CdS NRs, and CdSe/CdS dot-in-rod-shaped NRs, on photocatalytic hydrogen production in aqueous solutions in comparison to their non-gelated NC building block counterparts (Figure 1). To destabilize the ligand-stabilized NC solutions, an oxidative method using H₂O₂ was used. Removal of the ligands from the surface leads to the formation of a hydrogel with more freely accessible surface and different surface properties, such as the formation of sulfate sites, compared to the ligand-stabilized NCs. In addition to the influence of gel network formation and band structure of the various NC building blocks, the influence of different hole scavengers, for example, methanol (MeOH), triethanolamine (TEOA), ascorbic acid (Ascorb.), and a mixture of sodium sulfide and sodium sulfite (Na₂S/Na₂SO₃), on the photocatalytic hydrogen production is shown. Furthermore, the CdSe/CdS system was investigated for its long-term stability due to its special quasi-type II band structure and high photocatalytic hydrogen production as a model system. X-ray photoelectron spectroscopy (XPS) and intensity-modulated photocurrent spectroscopy (IMPS) are used to obtain information on the mechanistic reactions and the differences between NC-based gel structure and non-gelated NCs. The assembly and immobilization of NCs into highly porous and voluminous NC-based gel networks significantly increase hydrogen production while enabling a better applicability of the functional NCs.

2. Results and Discussion

2.1. Structural and Optical Properties of Nanocrystal-Based Gel Structures

CdSe QD-, CdS NR-, and CdSe/CdS NR-based hydrogels have been synthesized by the addition of a 0.35 wt% H₂O₂ solution to a mercaptopropionic acid-stabilized NC solution. The oxidizing agent partially removes the thiolate ligands (RS⁻) by forming radicals (RS•), allowing controlled destabilization of the nanocrystal solution and the controlled assembly into a porous hydrogel.^[30] After the gel formation, the solvent must

be replaced to remove residual oxidation agent and oxidized and detached ligands. With this method partially transparent and slightly turbid hydrogels were obtained, which still possess the volume of the NC solutions (Figure 2).

Scanning electron microscope (SEM) images of supercritically dried hydrogels (aerogels) were obtained to further visualize the structure and porosity of the NC-based aerogels (Figure 2, center images). From the SEM images, a highly porous and voluminous network structure can be seen, which is comparable to that in hydrogels. However, it can be assumed that due to the supercritical drying process and the associated solvent exchange from water to acetone to liquid CO₂, there is a slight shrinkage of the aerogels, so that most likely a more filigree and slightly more porous structure is present in the hydrogel. To get a rough estimation of the specific surface area, Brunauer–Emmet–Teller nitrogen physisorption measurements (BET)^[36] of the aerogels were performed (Figure S3, Supporting Information). All three semiconductor aerogels have a specific surface area of 160–200 m² g⁻¹.

Further insights in the interconnection between the NC building blocks are shown in the transmission electron microscope (TEM) images (Figure 2, right images) prepared from hydrogels after several washing steps. For all three different types of semiconductor NCs, the TEM images show that the NC building blocks are interconnected by a direct crystal-to-crystal contact with grain boundaries in between two different nanocrystals (Figure S1, Supporting Information). In case of the CdS NRs and CdSe/CdS NRs, the building blocks are preferentially connected tip-to-tip or tip-to-side and only to a minor extend side-to-side. This behavior is typical for NR-based gel structures, as shown in previous work by our group.^[31,33,37,38]

The optical properties of the hydrogels are very similar to those of the NC solutions showing that the nanoscopic properties are retained in the macroscopic gel networks. However, differences can be observed in the photoluminescence (PL) properties (e.g., PL lifetimes, PL quantum yield (QY)). These properties have been studied intensively in previous works of our group and are discussed in detail in the Supporting Information (Figure S2, Supporting Information). Here we want to highlight the changes in the PL lifetimes from NCs in solution to hydrogels. In all types of hydrogels, a long lifetime component additionally to the short lifetime component of the NCs can be observed.^[31] Due to the interconnection of the individual NCs, the excited electrons can be delocalized beyond one NC building block. In the CdSe QD-based and CdS NR-based hydrogels, the excited hole can likely also be delocalized, while in CdSe/CdS NRs due to the quasi-type-II band structure the hole is preferably located in the CdSe core. The possible delocalization of excited electrons in the network and localization of the hole in the CdSe core effectively separate the charge carriers, which reduces the overlap of the electron and hole wave functions and increases the charge carrier lifetimes.^[39] The network formation thus has an impact on the charge carrier properties and is likely to be the reason why the photocatalytic properties are higher in these systems, as will be demonstrated below.

To further investigate the charge carrier dynamics transient absorption (TA) measurements would be very interesting. We ourselves have not yet been able to measure the hydrogels in a TA.

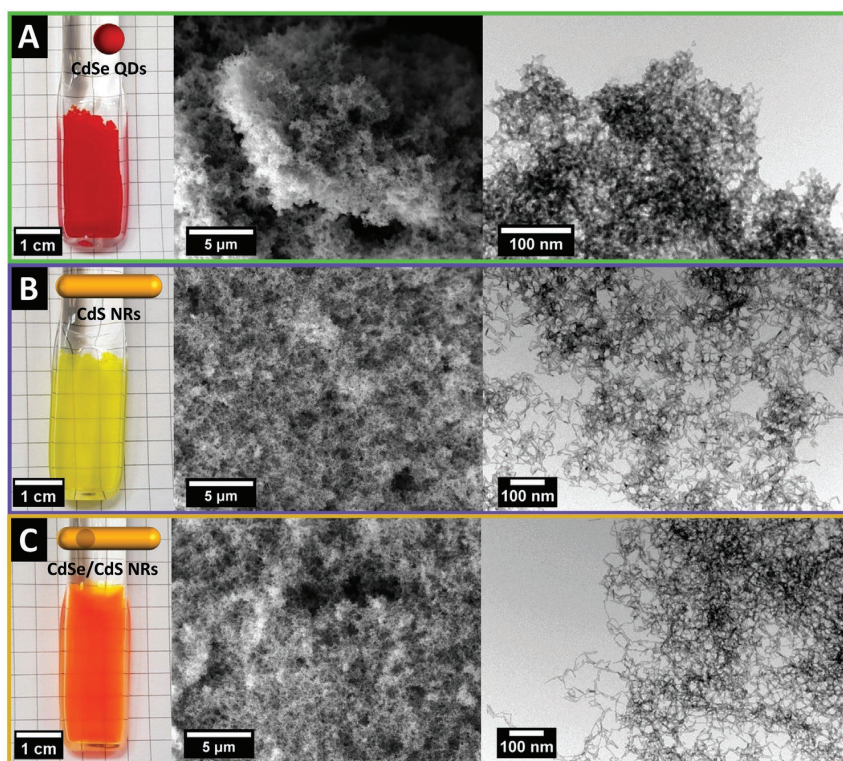


Figure 2. Structural visualization of the 3D networks of A) CdSe QD, B) CdS NR, and C) CdSe/CdS NR-based gel structures using (from left) a photograph of a hydrogel, a SEM image of a supercritically dried aerogel and a TEM image prepared from a hydrogel dried on the TEM grid.

Using TA studies from the literature to explain the mechanistic differences of NCs in solution and hydrogels would not be sufficient in our opinion. As Micheel et al.^[22] and Berr et al.^[40] showed in their studies, the hole and electron trap states have a major impact on the resulting TA measurements. Since we change the trap state situation in the hydrogels by removing the thiol ligands, we would expect a different TA signal compared to most ligand-stabilized nanoparticle systems. Additionally, most TA studies of CdS/CdS NR were performed without a hole scavenger. As well shown by Berr et al.^[40] this again affects the results from the TA measurements. To discuss the charge carrier dynamics in detail, TA measurements with the hydrogels and the hole scavenger should be performed.

2.2. Photocatalytic Properties of NC Solutions and NC-Based Hydrogels

NC-based hydrogels have a self-supporting 3D structure with water inside the pore system. By exchanging the water with an aqueous solution of a hole scavenger, these hydrogels can be used for photocatalytic experiments. Therefore, the hydrogels were washed five times with the aqueous hole scavenger solutions over 24 h to exchange the medium inside the hydrogel. Due to the self-supporting porous 3D structure, stirring during the experiments is not necessary to ensure a homogeneous

solution, as it is usually the case when NCs are used in photocatalytic reactions.^[41,42] This is not least due to the low colloidal stability of the ligand-stabilized NCs in the hole scavenger solution. Mercaptopropionic acid (MPA) stabilized NCs are stable only in the 10 vol % MeOH and TEOA solutions and not in ascorbic acid and $\text{Na}_2\text{S}/\text{Na}_2\text{SO}_3$ solutions as demonstrated in Figure S4, Supporting Information, by photographs and dynamic light scattering (DLS) measurements. To quantify the hydrogen production, we assume that the entire semiconductor hydrogel is excited and takes part in the photocatalytic hydrogen production. Due to the higher optical density compared to NC solutions and to ensure complete excitation of the hydrogels, the measurement cells are maximum 2 mm thick, so that the resulting hydrogels are also maximum 2 mm thick (Figure S6, Supporting Information).

All photocatalytic studies were performed for 24 h on the three semiconductor systems on both the pure NC solutions and the hydrogels with four different hole scavenger solutions. Using CdSe and CdS as catalyst materials necessarily leads to the use of a hole scavenger to enable the redox reaction,^[43] because the energy levels of the valence bands are not suitable to achieve the oxygen production and thus the full water splitting. It is already known for pure NC solutions that the hole scavenger can have an influence on the hydrogen production.^[44,45] So, in this work the four commonly known hole scavengers MeOH, TEOA, ascorbic acid, and sulfide/sulfite ($\text{Na}_2\text{S}/\text{Na}_2\text{SO}_3$)

were applied to the systems. Prior to the photocatalytic experiments, the hydrogels had a monolithic structure that had the volume of the NC solutions used. During the hydrogen production, the monolithic structure slightly broke due to the evolution of gas bubbles which had to rise through the gel network. Thus, corridors were formed where the gas could rise through the gel network (Figure S5, Supporting Information). Interestingly, the photocatalytic experiments in all three semiconductor systems with $\text{Na}_2\text{S}/\text{Na}_2\text{SO}_3$ as hole scavenger show that the hydrogels exhibit a hydrogen production rate several times higher than the corresponding ligand-stabilized NC solutions (Figure 3). More specifically, CdSe hydrogels had a 5.75 ± 0.05 -fold, CdS hydrogels a 4.72 ± 0.29 -fold, and CdSe/CdS hydrogels a 4.61 ± 0.3 -fold higher hydrogen production rate than the corresponding non-gelated, ligand-stabilized NC solutions. The use of methanol or triethanol amine as hole scavengers leads to negligible hydrogen production in case of CdSe QDs and CdSe/CdS NRs, whereas the CdS NRs show non-negligible hydrogen production in these hole scavenger solutions. Moreover, it can be observed in the CdS NR system that the pure NC solutions show higher hydrogen production than the hydrogel in case of MeOH, TEOA, and ascorbic acid, while the hydrogen production is generally low for both the colloid and the gels. The use of ascorbic acid as hole scavenger shows nearly similar hydrogen production rate as the $\text{Na}_2\text{S}/\text{Na}_2\text{SO}_3$ system only in the CdSe QD-based system. The various observations for the different semiconductors in the different hole scavenger solutions could be due to a variety of reasons. As discussed by Schneider et al. the mechanisms of the hole scavenger reactions are complex and it is not trivial to name the reactions that take place.^[44] An important key role has the energy level of the electron in the hole scavengers as shown by Berr et al. who observed that the higher the hydrogen production efficiency in CdS/Pt nanoparticle solutions, the stronger the reduction power of the hole scavenger is.^[45] The results shown here are not completely in line with the reduction power of the hole scavengers but the general tendency is in good agreement with the results reported by Berr et al. This might be explained by the facts that Berr et al. used pure CdS NR with a Pt domain and all of the hole scavenger molecules form highly reducing free radical intermediates following their one-electron oxidation. These free radicals usually are much more powerful reductants than the original hole scavengers and are known to even inject electrons into the semiconductor's conduction band.^[44] This so-called current-doubling phenomenon will in turn explain the increased H_2 formation rates. Beside the current-doubling phenomenon the stability of the intermediate radical can have an influence on the resulting hole scavenging efficiency. Depending on the pH, the free electron in the ascorbic acid radical, for example, can be partially delocalized within the molecule. The back reaction to the ascorbic acid is occurring with a second oxidation step toward a stable product. Thus, the faster the second oxidation step occurs, the less probable the back reaction takes place and the more stable the radical is, the more probable the second oxidation step becomes.

As another argument which does not directly relate to the two oxidation steps, the adsorption ability of the hole scavengers on the semiconductor surface should have an influence. Since the electron transfer from the hole scavenger to the

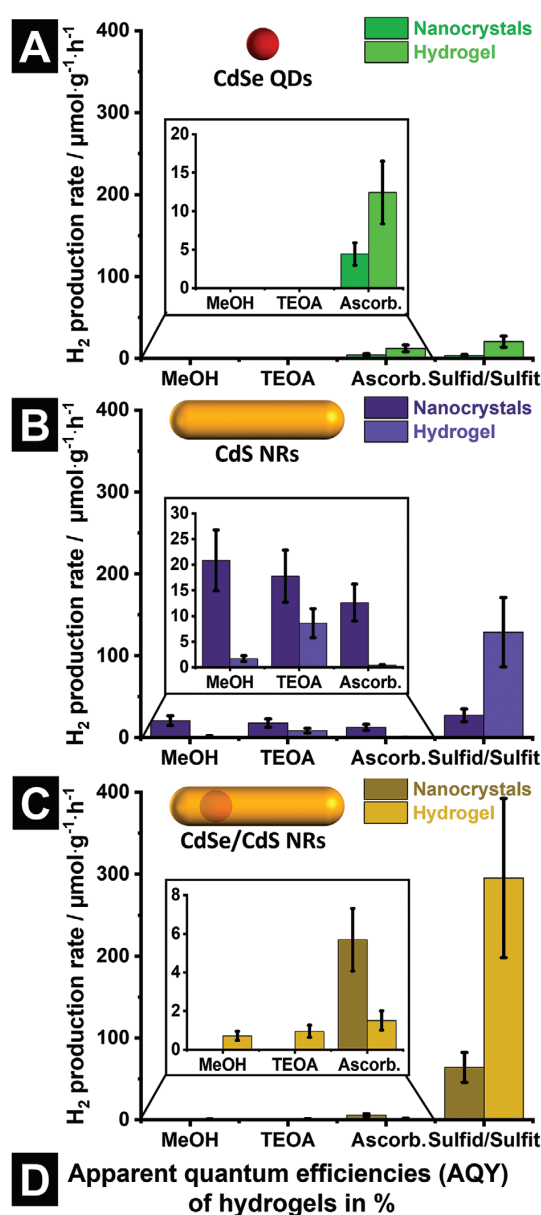


Figure 3. Photocatalytic hydrogen production of pure NC solutions (dark color) and hydrogels (light color) of A) CdSe QDs, B) CdS NRs, and C) CdSe/CdS NRs with methanol (MeOH), triethanol amine (TEOA), ascorbic acid, and sulfide/sulfite ($\text{Na}_2\text{S}/\text{Na}_2\text{SO}_3$) solutions as hole scavengers measured after 24 h. D) Calculated apparent quantum efficiencies (AQY) of the hydrogels in the different hole scavenger solutions.

semiconductor is more efficient when the molecule or ion is in direct contact with the surface of the semiconductor. A higher adsorption ability would support the opposite to the above discussed two oxidation steps in the case of ascorbic acid. However, it might be very different for the different hole scavengers. For the 0.1 M $\text{Na}_2\text{S}/\text{Na}_2\text{SO}_3$ solution, the stabilization of the radical for the two oxidation steps would not be crucial but here the absorption ability on the surface might play a major role. For ascorbic acid, this could be the opposite.

In particular, for the pure NCs in solution, steric hindrance by the ligand shell has an impact on the surface accessibility of the organic hole scavengers. Furthermore, charge carrier localization and thus surface trap states and especially hole trap states could play a key role in the hole scavenging process, which is discussed in the following for CdS hydrogels.^[22] Trap state emission was observed in the emission spectrum of the CdS NCs in solution, which exhibits higher intensity compared to the band gap emission (Figure S2, Supporting Information). This indicates that holes are trapped very efficiently, which could favor the hole scavenging process with the organic hole scavengers MeOH, TEOA, and ascorbic acid. The trapped hole has a longer lifetime and since it is located on the surface it can be extracted from the semiconductor more easily.

The other general observation that a mixture of a 0.1 M $\text{Na}_2\text{S}/\text{Na}_2\text{SO}_3$ solution is the most efficient hole scavenger for the CdSe, CdS, and CdSe/CdS systems is consistent with the findings in literature for different CdS-based NC solutions.^[15,45] It has to be emphasized that for all semiconductor systems investigated, a five times higher photocatalytic efficiency of the hydrogels compared to the respective nanocrystal solutions was demonstrated when using a mixture of $\text{Na}_2\text{S}/\text{Na}_2\text{SO}_3$ as hole scavengers. The apparent quantum efficiency (AQY) under illumination with a solar simulator has been determined for all hydrogel samples and is shown in the table Figure 3D. The highest AQY of 0.16% was calculated for the CdSe/CdS NR-based hydrogel with a 0.1 M $\text{Na}_2\text{S}/\text{Na}_2\text{SO}_3$ solution, followed by CdS NR-based hydrogel with 0.11% with a 0.1 M $\text{Na}_2\text{S}/\text{Na}_2\text{SO}_3$ solution. Since photocatalytic studies on NC solutions are often performed in the literature under stirring and excitation with

a 455 nm LED,^[47] the AQY was also determined here for comparison in addition to the xenon lamp with an AM1.5G filter under stirring using a 455 nm LED for excitation on the CdSe/CdS gel structure (Table S1, Supporting Information). Stirring only slightly increases the AQY by 0.01% for the CdSe/CdS NR-based hydrogels, whereas an increase of 0.09% is seen using excitation with the LED. The higher AQY when using an LED could be due to the excitation with higher energies above the band gap of the CdS shell. Using the full solar spectrum also excitation only in the CdSe core can be observed which would lead to a less efficient hydrogen production with this wavelength.

The 24 h measurements on the different systems we observed that the CdSe/CdS NR-based hydrogel in combination with the $\text{Na}_2\text{S}/\text{Na}_2\text{SO}_3$ hole scavenger is the most effective system for photocatalytic hydrogen evolution. Therefore, this system was used to investigate the longevity of the gel network as well as the hole scavenger and their effect on the photocatalytic activity in long-term measurements (5 days, Figure 4). These measurements were performed in two different variants: I) The hole scavenger in the hydrogel is exchanged every 24 h and the reaction vessel is flushed with nitrogen. II) The hole scavenger is not exchanged and only the reaction vessel is flushed with nitrogen every 24 h. The measurement of the photocatalytic activity over days (Figure 4A) shows that the hydrogels have a constant hydrogen production after 2 days when the hole scavenger solution is exchanged frequently. Without exchange of the hole scavenger solution, the hydrogen production decreases constantly, which is attributed to the consumption of the hole scavenger. Furthermore, it is needed to ensure that the difference between the CdSe/CdS NC solutions and the CdSe/CdS NC-based hydrogels is not only due to the uncontrolled aggregation of the NCs in the $\text{Na}_2\text{S}/\text{Na}_2\text{SO}_3$ hole scavenger solution. Therefore, control experiments under stirring with both a NC solution and a hydrogel have been performed. Stirring can increase the hydrogen production rate for both the NC solution and the hydrogel. However, the stirred NCs still showed a lower hydrogen production rate than the hydrogel without stirring.

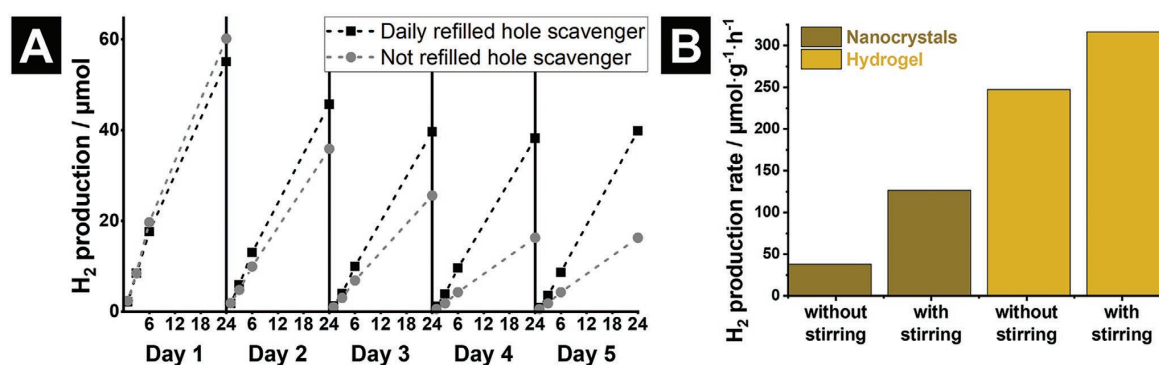


Figure 4. A) Long-term measurements (5 days) on CdSe/CdS NR-based hydrogels show the stability of the photocatalyst and the $\text{Na}_2\text{S}/\text{Na}_2\text{SO}_3$ hole scavenger. After 24 h in one sample (black squares) the hole scavenger solution has been exchanged and the measurement cell has been flushed with nitrogen. The other sample (grey circles) has been flushed with nitrogen without exchanging the hole scavenger solution. The dashed line is used to better visualize the course of the hydrogen production. B) Hydrogen production of NCs in solution and hydrogels with and without stirring, respectively. As hole scavenger solution a mixture of sulfide/sulfite ($\text{Na}_2\text{S}/\text{Na}_2\text{SO}_3$) has been used.

In summary, hydrogen production measurements on CdSe QD, CdS NR, and CdSe/CdS NR-based NC solutions as well as their hydrogels showed up to five times higher hydrogen production rate when using the hydrogel instead of nanocrystal in solution. As hole scavenger a 0.1 M solution of Na₂S/Na₂SO₃ has been the most efficient for all three semiconductor systems. In the following, the differences between the nanocrystals in solution and the hydrogel will be discussed and described using the CdSe/CdS NR-based system as an example, which led to the increased photocatalytic activity.

2.3. Photocatalysis Differences between Ligand-Stabilized Nanocrystals and Hydrogels

Possible reasons for the significantly higher hydrogen production rate of the hydrogels compared to the ligand-stabilized NCs in solution when using sulfite/sulfide as hole scavenger are discussed using CdSe/CdS NRs and their corresponding hydrogel as an example. The proposed mechanism is visualized in Figure 5, respectively.

In general, to obtain colloiddally stable nanocrystals in solution, their surface is covered with stabilizing ligands, here mercaptopropionic acid (MPA), that can lead to more difficult surface accessibility for the photocatalysis reaction. The MPA ligands used here ensure the colloidal stability and additionally induce hole trap states which influence the charge carrier dynamics.^[22] In order to synthesize gels from these nanoparticles, by using a 0.35 wt% H₂O₂ solution to destabilize a

ligand-stabilized NC solution, the thiol ligands are oxidized and removed from the NC surface.^[30,31] Controlled removal of the ligands, that is, very low concentration of the oxidizing agent, leads to the formation of the porous hydrogel structures shown. In this way, a high surface-to-volume ratio in the hydrogels is retained (Figure S3, Supporting Information), which would, for example, not be the case in compact NC agglomerates. Furthermore, without the ligand shell around the semiconductor NCs, the catalytically active surface is directly accessible for the hydrogen production without steric hindrance from the ligands. Additionally, removal of the thiol ligands leads to free Cd surface atoms, which could enable better interaction of the hole scavenger with excited charge carriers, especially in the 0.1 M Na₂S/Na₂SO₃ solution.

To investigate the differences on the surface of the ligand-stabilized NCs and their hydrogels, XPS measurements were performed (Figure 5B,E). Especially, the S 2p orbital gives a deep insight into the situation at the surface of the semiconductor materials. Figure 5B shows the XPS spectrum of the CdSe/CdS NRs of the S 2p orbital region with the fitted components of the ligand-stabilized NCs dropped on the silicon wafer. The spectrum had to be fitted with five components to achieve a standard deviation close to one. Two components (dark and light orange) can be attributed to the S 2p_{1/2} and S 2p_{3/2} of sulfur bound in CdS. Two additional components (dark and light blue) are needed to describe the sulfur in the MPA ligand which leads to a shift compared to the sulfur bound in CdS. The fifth component (green) is due to the Se 2p of the CdSe core. The Se 2p binding energy is in

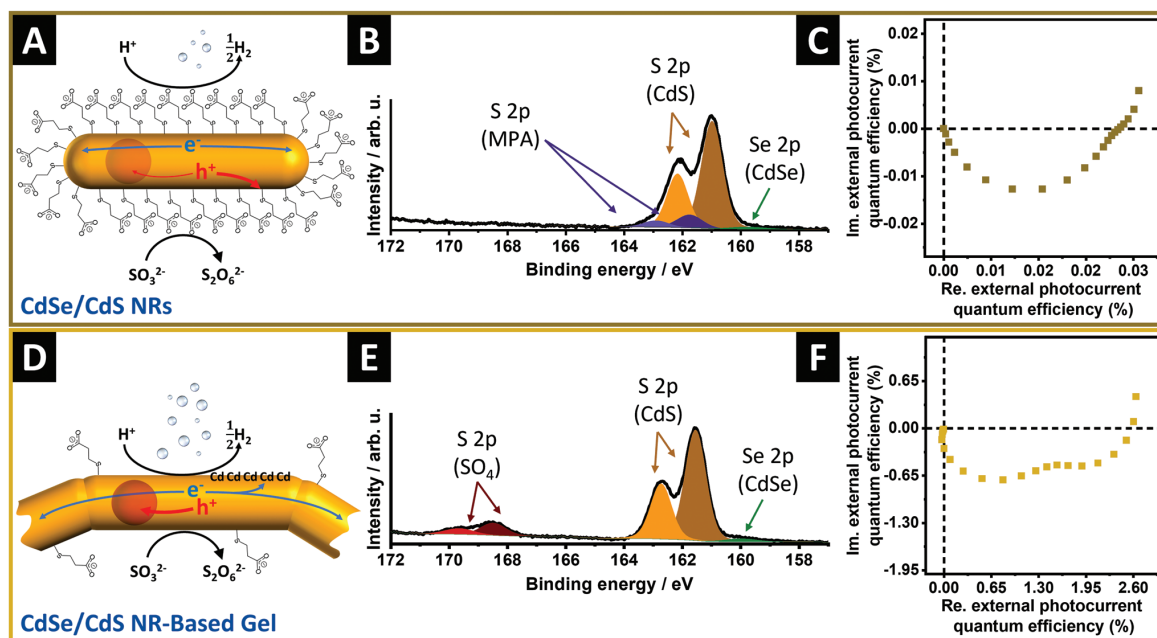


Figure 5. Schematic illustration of the surface and the charge carrier movements in A) CdSe/CdS ligand-stabilized NRs and D) CdSe/CdS NR-based hydrogels. CdCdCdCdCd represents unsaturated Cd surface atoms due to removed thiol ligands. XPS spectra of the S 2p region showing the differences between B) CdSe/CdS ligand-stabilized NRs and E) CdSe/CdS NR-based hydrogels. Nyquist plots of IMPS measurements of C) CdSe/CdS ligand-stabilized NRs showing one semicircle and Nyquist plots of a F) CdSe/CdS NR-based rehydrated xerogel showing two semicircles.

the same region. Due to the low intensity in the XPS spectrum, only one component is shown for the Se $2p_{3/2}$ state.

A difference can be observed in the XPS spectrum of the S $2p$ region of the CdSe/CdS NR-based hydrogel which is shown in Figure 5E. Here, the main peaks can be fitted with only three components to achieve a standard deviation close to one, compared to five components required in the ligand-stabilized NC samples. Two components (dark and light orange) can again be attributed to the S $2p_{1/2}$ and S $2p_{3/2}$ of sulfur bound in CdS. The third component (green) with a very low intensity is due to the Se $2p_{3/2}$ bound in the CdSe core. Compared to the pure NC solutions, the components for the sulfur bound in MPA are not needed here, indicating significantly less ligands on the surface of the hydrogels than on the colloidal nanoparticles. In the hydrogel sample there is also a signal with two components (dark and light red) which is shifted to higher binding energies. By comparing the signal position with literature values, this signal can be assigned to the S $2p_{1/2}$ and S $2p_{3/2}$ of sulfur bound in sulfate.^[48] During the oxidation of the ligands by the oxidizing agent H_2O_2 , the CdS surface is also partially oxidized to sulfate. The presence of sulfate groups on the surface of CdS after treatment with H_2O_2 was previously described by Zhang et al.^[48] They also showed that the sulfate ions on the surface can have a positive effect on the catalytic activity due to the preferential bonding of hydrogen atoms on the surface sulfate ions. Furthermore, the Cd3d XPS region gives more evidence for the results discussed with the S $2p$ and Se $2p$ regions. The spectra are shown in Figure S8, Supporting Information, and are discussed more deeply in the Supporting Information.

In addition to the changes in surface accessibility and surface modification of the hydrogel, which lead to an increase of the catalytic activity, the charge carrier properties also change. As described earlier, the CdSe/CdS NRs exhibit a quasi-type-II band structure in which the electron can be delocalized over the entire NR while the hole is localized in the CdSe core region. Due to the gelation, the individual NC building blocks are crystalline bound, which results in an extension of the band structure beyond a NC.^[31,32,34] The changes in charge carrier properties due to the gelation and the change in the band structure can be described using the optical properties (see Supporting Information). As known from literature, ligands with thiol end groups generate hole trap states at the NC surface. During the gelation process, the removal of the thiol ligands from the surface leads to a reduction of hole trap states on the surface of the semiconductors. Thus, the excited holes are located more probably in the CdSe core, which improves the charge carrier separation and extends the lifetime of the excited charge carriers. Micheel et al. discussed this using the PLQY differences when exciting in the CdSe core and the CdS nanorod, respectively. The PLQY measurements of the semiconductor nanocrystals in solution and their respective hydrogels indicate an improved hole localization in the CdSe core in case of hydrogels.^[22,24] Thus, a more pronounced charge carrier separation in the hydrogel compared to the nanocrystals in solution occurs. Since more than one hole in the CdSe core leads to sub-picosecond auger-mediated hole trapping,^[48,49] there is a higher probability to have two accessible holes very close to each other in the gel network due to close CdSe cores within the network. This would be beneficial for the whole two

step oxidation of the hole scavenger. In the NC solution in contrast two holes have to be more probable from two different NCs which possibly lead to a less efficient hole scavenging process. The excited electron in the interconnected hydrogel can have two different pathways, which both would lead to an extension of the lifetime of the excited charge carriers. First, the electron delocalization in the hydrogel is not limited to the nanocrystal building blocks due to the interconnection of the individual building blocks, so that the charge carrier separation is superior compared to the nanocrystals in solution.^[31,32,50] On the other hand, removal of the thiol ligands might lead to free cadmium atoms on the surface of the semiconductor, which are known to act as electron trap states.^[22] Both processes would lead to an extension of the lifetime of the excited charge carriers, which is beneficial for the use of the charge carriers for further catalytic reactions. To demonstrate the differences in charge carrier mobility between ligand-stabilized NCs and NC-based gel structures, and to show the ability of the electrons to be located beyond one NC building block, IMPS measurements (Figure 5C,F) were performed. During the IMPS experiments, the on-off frequency of the LED is varied (here from 10 kHz to 1 Hz) and the photocurrent response of the system is recorded.^[51] Thus, it is possible to distinguish between charge transfer processes that occur on different time scales, provided their rate constant differ by at least one order of magnitude.^[52] A sub-monolayer of CdSe/CdS NRs results in only one semicircle in the Nyquist plots of the IMPS measurements (Figure 5C), which is related to the fast diffusion from electrons from the NRs to the electrode. However, when using CdSe/CdS NR-based xerogels, a second semicircle in the spectrum appears in addition to the first semicircle in the frequency range of 100 to 1 Hz. The second semicircle results from charge carriers which are transported through the gel network and contribute to the measured photocurrent at a longer time scale.^[32,34,53,54] The appearance of the second semicircle illustrates the charge carrier mobility in the CdSe/CdS NR-based gel structure compared to non-gelated NCs.

In summary, the higher photocatalytic activity of the NC-based hydrogels compared to the NCs in solution could be explained by optical, XPS, and electrochemical measurements shown above. Removal of the ligands during the oxidative destabilization with H_2O_2 leads to an accessible semiconductor surface without the obstacle of organic ligands. These ligands additionally form hole trap states that reduce the charge carrier separation, so that their absence possibly results in a better charge carrier separation and longer charge carrier lifetimes. In addition to the influence of surface properties, the interconnection of the NCs in the hydrogels enables charge delocalization beyond one NC building block and thus also extends the charge carrier lifetimes. Longer charge carrier lifetimes make the photocatalytic reaction more probable leading to more efficient photocatalysts. Furthermore, the controlled destabilization and hydrogel formation ensures a high surface area which would not be the case by an uncontrolled agglomeration which can be observed using the nanocrystals in solution. As shown above the explanation of the interestingly higher hydrogen production rates using a hydrogel is off several factors. The differentiation of which factor has how many of an impact could not be determined.

3. Conclusion

In the present work, we demonstrate that nanocrystal-based gel networks are of interest for photocatalysis. The photocatalytic hydrogen production of NC-based hydrogels prepared from CdSe QDs, CdS NRs, and CdSe/CdS dot-in-rod NRs was investigated, and the results were compared to those of the pure NCs in solution. Among these semiconductor materials, the efficient charge carrier separation in the CdSe/CdS NRs favored the utilization of charge carriers for the photocatalytic reaction. NC-based hydrogels generally showed five times higher hydrogen production rates compared to their ligand-stabilized NC solutions. Controlled destabilization of the NC solution with a 0.35 wt% H₂O₂ solution as oxidation agent removes the ligands from the nanocrystal surface and leads to a highly porous, self-supporting 3D network. This enables an accessible catalytic surface without a ligand shell, resulting in reduced hole trapping and an extended charge carrier lifetime. In addition to the altered surface properties, the electronic properties in hydrogels differ from those of the NCs in solution. Network formation efficiently separates charge carriers by delocalizing electrons beyond one NC building block, also leading to a longer charge carrier lifetime and a more probable catalytic reaction. It has been shown, that advances in the NC synthesis and controlled destabilization of these ligand-stabilized NC solutions into highly porous gel structures create photocatalytic materials with enhanced photocatalytic activity and a better applicability. The gained knowledge about the photocatalytic behavior of nanocrystal-based hydrogels can further be used to investigate more efficient materials for the photocatalytic hydrogen production.

4. Experimental Section

Chemicals: All chemicals used for the syntheses were used as purchased without any further purification. Cadmium oxide (CdO, 99.998%) and elemental selenium (200 mesh, 99.999%) were supplied by Alfa Aesar. Tri-*n*-octylphosphine oxide (TOPO, 99%), elemental sulfur (99.98%), 1-octadecene (ODE, 90%), 3-mercaptopropionic acid (MPA, ≥99%), 2-propanol (≥99.8%), and chloroform (≥99.5%), were purchased from Sigma-Aldrich. Potassium hydroxide (KOH, >85%), *n*-hexane (≥99%), acetone (99.5%), hydrogen peroxide (H₂O₂, 35 w/w%), toluene (≥99.7%), and MeOH (≥99.8%) were purchased from Honeywell. Tri-*n*-octylphosphine (TOP, 97%) was purchased from ABCR. Elemental tellurium (60 mesh, 99.999%), octadecylphosphonic acid (ODPA, 99.0%), and hexylphosphonic acid (HPA, 99%) were obtained from Roth, Fisher Scientific and PCI, respectively. Ultrapure water with a resistivity of 18.2 MΩ cm was used for aqueous solutions.

Synthesis of CdSe Quantum Dots: The synthesis of the CdSe QDs was adapted from the method of Carbone et al. with certain modifications.^[11] In a three-neck flask CdO (0.12 g, 0.93 mmol), TOPO (6.0 g, 15.52 mmol), and ODPA (0.56 g, 1.67 mmol) were degassed under vacuum at 150 °C for 50 min. Under an argon atmosphere, the flask was heated to 300 °C until all CdO was dissolved completely. TOP (3.6 mL) was added, and the temperature was raised to 380 °C. The growth of the CdSe QDs was initiated with the addition of elemental selenium (0.116 g, 1.47 mmol) dissolved in TOP (3.6 mL). After 4 min, the growth was stopped by the addition of ODE (6 mL) and the flask was cooled down quickly using an airflow. Twice, the QDs were precipitated with methanol (5 mL), centrifuged (3775 RCF, 10 min), and redispersed in toluene (5 mL). The size of the nanocrystals and the concentration of the QD solution were determined by the position and the optical density (OD) of the first excitation maximum in an extinction spectrum.^[56]

Synthesis of CdS Seeds: CdS seeds were synthesized according to the method of Carbone et al. with certain modifications.^[11] For a fourfold scaled synthesis mixture CdO (0.3 g, 2.34 mmol), TOPO (9.9 g, 25.60 mmol), and ODPA (1.81 g, 5.41 mmol) were mixed in a 50 mL three-neck flask, heated up to 150 °C under vacuum, and degassed for 1 h. Subsequently, the solution was heated up to 320 °C under an argon atmosphere followed by the injection of TBP (9.12 mL) consisting (TMS)₂S (0.6 mL). The synthesis was held at 250 °C for 7 min, followed by cooling down to room temperature. At 70 °C 5 mL toluene was added, and the seeds were precipitated by the addition of 10 mL methanol and centrifuged (3775 RCF, 10 min). The CdS seeds were purified twice with a mixture of methanol/toluene (5 mL each) and stored in 1.5 mL toluene.

Synthesis of CdS Nanorods and CdSe/CdS Nanorods: In a modified synthesis of Carbone et al., CdO (0.18 g, 1.4 mmol), TOPO (9.0 g, 23.28 mmol), ODPA (0.84 g, 2.51 mmol), and HPA (0.24 g, 2.07 mmol) were mixed and degassed under vacuum at 150 °C for 1 h.^[11] After dissolving the CdO completely at 300 °C under an argon atmosphere, TOP (5.6 mL) was added and the temperature was increased to 380 °C. Once the temperature was reached, the growth of the NRs was initiated by a quick injection of sulfur (0.39 g) dissolved in TOP (5.4 mL) mixed with the previously synthesized CdSe or CdS QDs (concentration of quantum dots in TOP was always 400 μM). After 8 min of reaction, the solution was cooled down by an airflow. At 70 °C, toluene (7 mL) was added and after further cooling (down to ≈30 °C) the particles were precipitated with 10 mL methanol centrifuged (3775 RCF, 10 min). Afterward, the particles have been washed twice with a mixture of methanol/toluene (5 mL each) and redispersed in toluene (2 mL).

Phase Transfer: The method of phase transfer of Kodanek et al. was adapted.^[57,58] The nanoparticle solutions were precipitated with methanol, centrifuged and redispersed in 10 mL hexane. The cadmium concentration in the hexane solution was ≈2 mg mL⁻¹. After the addition of a 0.1 M KOH solution in methanol (10 mL) and MPA (0.25 mL) the mixture was shaken for at least 5 h. The methanolic phase with the nanoparticles was separated and centrifuged (3775 RCF, 10 min). After redispersion in a 0.01 M KOH solution in water, the particles were washed with acetone, centrifuged, and finally redispersed in Millipore water.

Assembly to Hydrogels and Transfer to Aerogels: To destabilize the ligand-stabilized nanoparticles by oxidizing the ligands with H₂O₂, the aqueous nanoparticle solution (with a Cd concentration of 3.6 g L⁻¹ determined by AAS) was mixed with a H₂O₂ solution (0.35 wt%, 93.75 μL mL⁻¹ nanoparticle solution) in an Eppendorf tube or in the photocatalytic glass cells followed by shaking and placing it in an oven at 80 °C for 3 min. Afterward, the solution was stored in the dark overnight. After hydrogelation, ten washing steps over 1 day with Millipore water (2–5 mL for each step) were applied to remove the excess of the destabilizing agent and other by-products. Therefore, 3 mL of the supernatant above the hydrogel has been removed with a pipette and 3 mL fresh Millipore water was carefully added with a pipette. For the BET and SEM measurements, the water was exchanged to dry acetone by washing the gel with mixtures of water and acetone and afterward with pure acetone and anhydrous acetone. To obtain aerogels, the aerogels were dried in a critical point dryer (Quorum Technologies, E3100) using supercritical CO₂. The whole procedure is described in more detail in the previous paper.^[31]

Preparation of Xerogel ITO Electrodes: For the photoelectrochemical measurements ITO electrodes were coated with an ambiently dried hydrogel (xerogel). Before coating the electrodes with nanocrystals and nanocrystal-based gel structures, the ITO-coated glass substrates (VisionTek Ltd., 12 ohms⁻², size of 1.5 cm × 3 cm) were cleaned and activated. For cleaning the glass substrates were rinsed with acetone, 2-propanol, and Millipore water. The activation afterward was performed with a solution of NH₄OH and H₂O₂ (10 mL 25% NH₄OH, 10 mL 35% H₂O₂) in water (60 mL) for 2 h at 70 °C. After washing with water in the next step, the ITO surface was functionalized with 1 vol% MPTMS in toluene for 2 h at 70 °C and have been rinsed with toluene afterward. For NC and NC-based gel coating, a specific area of mold was prepared using a plastic cuvette glued on the ITO substrate with a silicone sealing

paste. The aqueous nanocrystal solution (300 μL) was filled into the glued cuvette and the destabilization was applied as described above using H_2O_2 . After the washing steps (ten times with 1 mL Millipore water as described above), the closed hydrogels were stored for 3–4 days. The xerogel was formed by drying the hydrogel under ambient conditions (2 days).

Photocatalysis Measurements: The photocatalysis measurements were performed in Duran glass cells which are shown in Figure S6, Supporting Information. The hydrogels were synthesized inside the cells according to the description above. Before the irradiation with a 300 W xenon lamp (QuantumDesign LSH302) equipped with an AM 1.5 G filter (QuantumDesign solar simulator LS0308), the hydrogels were washed five times with the used hole scavenger solution. To measure the hydrogen production, aliquots (100 μL) were taken with a gas syringe. The aliquots were measured using a GC (Agilent GC 8860) equipped with an Agilent HP-PLOT Molesieve 30 $\text{m} \times 0.320 \text{ mm} \times 25 \mu\text{m}$ Column and a thermal conductivity detector detector. To calculate the hydrogen production rate, the following equation was used

$$n_{\text{H}_2} = \frac{A_{\text{H}_2}}{A_{\text{N}_2}} \times \text{GC Factor} \times \frac{V_{\text{Gas}} P}{RT} \quad (1)$$

$$\text{H}_2 \text{ production rate} = \frac{n_{\text{H}_2}}{m_{\text{Cd}} t} \quad (2)$$

A is the area of the measured peak of hydrogen or nitrogen in the GC. The GC Factor is the ratio of the sensitivity of the thermal conductivity detector regarding hydrogen and nitrogen. The factor was determined with calibration measurements.

The AQY has been calculated using the following equations^[59]

$$\text{AQY} = \frac{\text{reacted electrons}}{\text{incident light}} = \frac{2 \times n(\text{H}_2)}{n(\text{photons})} = \frac{2 \times n(\text{H}_2)}{\frac{I_{\text{inc}}}{E_{\lambda} \times N_A}} = \frac{2 \times n(\text{H}_2)}{\frac{I_{\text{inc}} \times \lambda}{h \times c \times N_A}} \quad (3)$$

$$I_{\text{inc}} = I_0 \times F_A = I_0 \times \frac{\text{absorbed light}}{\text{incoming light}} = I_0 \times \frac{\int_{\lambda_1}^{\lambda_2} I \times (1 - 10^{-A}) \times d\lambda}{\int_{\lambda_1}^{\lambda_2} I \times d\lambda} \quad (4)$$

λ has been assumed to be the wavelength of the energy of the band gap when calculating the AQY with the xenon lamp and the AM1.5 G filter, and λ was set to the wavelength of the LED when calculating the AQY using the LED. The absorbed light and the incoming light were measured using a Thorlabs PM100D power meter with a S121C photodiode (400–1100 nm, 500 mW, $d = 9.5 \text{ mm}$). Absorbed light (measured in mW) was determined with the sample in front of the photodiode (absorbed light = incoming light – transmitted light) and incoming light without the sample.

Long-term measurements over days were performed with an Atlas Suntest CPS+ operated at 650 W m^{-2} . The photocatalysis cells were placed in the device with a tilt of 45°. The measurement cells were flushed every 24 h with nitrogen (10 min with two needles; one for the inlet and one for the outlet).

Optical Characterization: Extinction spectra of nanoparticle solutions were performed with a Jasco V-750 spectrometer. Absorption spectra of the nanoparticle solutions and hydrogels were measured in a central position with an Agilent CARY 5000, which was equipped with a Diffuse Reflectance Accessory. The photoluminescence quantum yields were measured with a Quanta- ϕ integrating sphere coupled to a Horiba Dual-FL spectrofluorometer. Photoluminescence emission and lifetime measurements were conducted in an Edinburgh Instruments FLS 1000 spectrofluorometer using an Edinburgh Instruments EPL 445 pulsed laser (445.1 nm) for excitation of time-resolved measurements.

Measurements of nanoparticle solutions, as well as hydrogels, were performed in Hellma Analytic quartz cuvettes.

Structural Characterization: TEM measurements were performed with an FEI Tecnai G2 F20 TWP (operated at 200 kV). Samples were prepared on copper grids which were covered with a carbon layer (Quantifoil). For preparation, hydrogels and colloidal nanocrystal solutions were dropped on the grid. After drying the grids were ready for the measurement in the TEM.

A JEOL JSM-6700F which was operated at 2 kV was used to measure the SEM of the aerogels. For the sample preparation, parts of the aerogel were placed on a conductive carbon.

XPS measurements were conducted using a VersaProbe III from Physical Electronics (ULVAC-PHI) with an AL $K\alpha$ source at pass energy of 27 eV. Every spectrum was calibrated to the highest intensity of the C 1s peak of each sample. XPS samples were prepared by drop casting 10 μL NC solution as well as hydrogel sample on a Si wafer.

Physisorption Measurements: Argon physisorption was measured with a Micromeritics 3Flex instrument at 87 K. Prior to physisorption measurements, the samples ($\approx 2 \text{ mg}$) were degassed under vacuum at 25 °C for 24 h. Surface areas were estimated by applying the BET equation.

Photoelectrochemical measurements: Measurements were performed in an electrochemical cell which was described by Miethe et al. and is shown in Figure S9, Supporting Information.^[52] In the intensity modulated photocurrent spectroscopy, the current response of the electrochemical cell was measured while applying light pulses with various frequencies between 10 kHz and 1 Hz. Hereby, the value of the photocurrent and the phase shift between the sinusoidal light pulses and the sinusoidal current signal were measured. To detect the signal a lock-in amplifier controlled the sinusoidal light pulses with a specific frequency and detects the incoming photocurrent. A lock-in amplifier was necessary because a potentiostat in general was not able to measure the appearing small currents in the range of μA where the noise of the system was larger than the signal itself. As electrolyte, a 0.5 M Na_2SO_3 solution at pH 9 was used. The applied bias potential was measured against a Ag/AgCl reference electrode (3 M NaCl, purchased from BASi). A PE 1542 DC power supply from PHILIPS powered the LED (0.5 mW, $\lambda = 472 \text{ nm}$) and a 7270 DSP lock-in amplifier from AMETEK gave the sinusoidal signal to the LED and detected the current signal from the measurement cell. The bias potential was controlled by the Modulab XM from AMETEK.

Measuring the linear sweep voltammetry includes a scan from low to higher bias potentials over a fixed time range. In the experiments, the voltage was applied from -0.6 V up to 0.3 V with a slope of 0.2 V min^{-1} . Before starting the measurement, a constant potential was applied for 30 s at the starting voltage of -0.6 V to reach an equilibrium state for the whole system. During the linear sweep voltammetry, the LED was turned on and off periodically with a frequency of 40 mHz. This corresponds to a time period of 12.5 s of irradiation and 12.5 s of darkness. To apply the voltage the potentiostat Modulab XM from AMETEK was used and the control system for the LED was the arbitrary generator HMF2550 from Rohde and Schwarz.

Supporting Information

Supporting Information is available from the Wiley Online Library or from the author.

Acknowledgements

J.S. and F.L.-W. contributed equally to this work. This work was funded by the German Research Foundation (Deutsche Forschungsgemeinschaft, DFG) with the grant agreement BI 1708/4-1 and under Germany's excellence strategy within the cluster of excellence PhoenixD (EXC 2122, project ID 390833453). The studies performed in the laboratory

"Photoactive nanocomposite materials" were supported by Saint-Petersburg State University (ID: 73032813). R.T.G. is thankful for financial support from the Hannover School for Nanotechnology (hsn). Moreover, the authors thank Armin Feldhoff and Jürgen Caro for providing the SEM and XRD facility, and thank the Laboratory of Nano and Quantum Engineering for access to TEM.

Open access funding enabled and organized by Projekt DEAL.

Conflict of Interest

The authors declare no conflict of interest.

Data Availability Statement

The data that support the findings of this study are available from the corresponding author upon reasonable request.

Keywords

charge carrier separation, nanocrystal-based hydrogels, photocatalysis, photocatalytic hydrogen production, self-assembly

Received: December 23, 2022

Revised: February 3, 2023

Published online: February 24, 2023

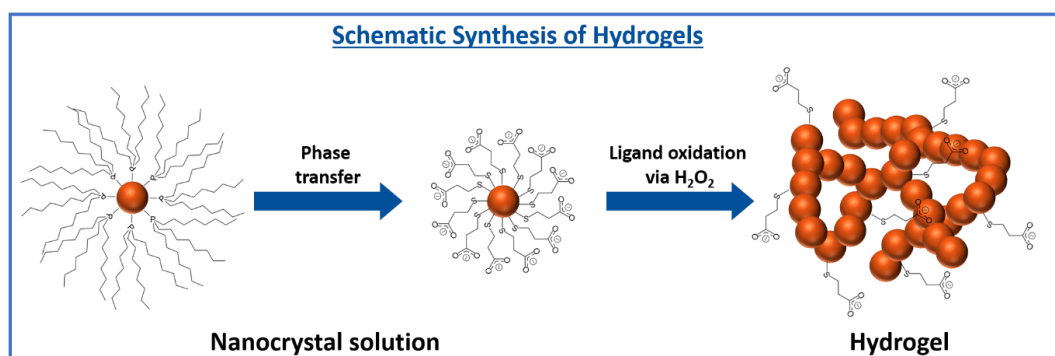
- [1] D. Gielen, F. Boshell, D. Saygin, M. D. Bazilian, N. Wagner, R. Gorini, *Energy Strategy Rev.* **2019**, *24*, 38.
- [2] K. C. Christoforidis, P. Fornasiero, *ChemCatChem* **2017**, *9*, 1523.
- [3] M. Tahir, S. Tasleem, B. Tahir, *Int. J. Hydrogen Energy* **2020**, *45*, 15985.
- [4] H. Zhao, H. Fu, X. Yang, S. Xiong, D. Han, X. An, *Int. J. Hydrogen Energy* **2022**, *47*, 8247.
- [5] W.-K. Jo, T. S. Natarajan, *Chem. Eng. J.* **2015**, *281*, 549.
- [6] R. Costi, A. E. Saunders, U. Banin, *Angew. Chem., Int. Ed.* **2010**, *49*, 4878.
- [7] M. Nasilowski, B. Mahler, E. Lhuillier, S. Ithurria, B. Dubertret, *Chem. Rev.* **2016**, *116*, 10934.
- [8] F. Montanarella, M. V. Kovalenko, *ACS Nano* **2022**, *16*, 5085.
- [9] A. L. Eφος, L. E. Brus, *ACS Nano* **2021**, *15*, 6192.
- [10] X. Peng, L. Manna, W. Yang, J. Wickham, E. Scher, A. Kadavanich, A. P. Alivisatos, *Nature* **2000**, *404*, 59.
- [11] L. Carbone, C. Nobile, M. de Giorgi, F. della Sala, G. Morello, P. Pompa, M. Hytch, E. Snoeck, A. Fiore, I. R. Franchini, M. Nadasan, A. F. Silvestre, L. Chiodo, S. Kudera, R. Cingolani, R. Krahn, L. Manna, *Nano Lett.* **2007**, *7*, 2942.
- [12] D. V. Talapin, R. Koeppel, S. Götzinger, A. Kornowski, J. M. Lupton, A. L. Rogach, O. Benson, J. Feldmann, H. Weller, *Nano Lett.* **2003**, *3*, 1677.
- [13] A. Schlosser, R. T. Graf, N. C. Bigall, *Nanoscale Adv.* **2020**, *2*, 4604.
- [14] S. Naskar, A. Schlosser, J. F. Miethe, F. Steinbach, A. Feldhoff, N. C. Bigall, *Chem. Mater.* **2015**, *27*, 3159.
- [15] M. Berr, A. Vaneski, A. S. Susha, J. Rodríguez-Fernández, M. Döblinger, F. Jäckel, A. L. Rogach, J. Feldmann, *Appl. Phys. Lett.* **2010**, *97*, 093108.
- [16] F. Qiu, Z. Han, J. J. Peterson, M. Y. Odoi, K. L. Sowers, T. D. Krauss, *Nano Lett.* **2016**, *16*, 5347.
- [17] V. L. Bridewell, R. Alam, C. J. Karwacki, P. V. Kamat, *Chem. Mater.* **2015**, *27*, 5064.
- [18] P. Zeng, W.-D. Zhang, *Mol. Catal.* **2021**, *515*, 111856.
- [19] L. Amirav, A. P. Alivisatos, *J. Phys. Chem. Lett.* **2010**, *1*, 1051.
- [20] P. Kalisman, L. Houben, E. Aronovitch, Y. Kauffmann, M. Bar-Sadan, L. Amirav, *J. Mater. Chem. A* **2015**, *3*, 19679.
- [21] Y. Nakibli, L. Amirav, *Chem. Mater.* **2016**, *28*, 4524.
- [22] M. Micheel, B. Liu, M. Wächtler, *Catalysts* **2020**, *10*, 1143.
- [23] R. Abargues, J. Navarro, P. J. Rodríguez-Cantó, A. Maulu, J. F. Sánchez-Royo, J. P. Martínez-Pastor, *Nanoscale* **2019**, *11*, 1978.
- [24] Y. Ben-Shahar, F. Scotognella, N. Waiskopf, I. Kriegl, S. Dal Conte, G. Cerullo, U. Banin, *Small* **2015**, *11*, 462.
- [25] A. Eychmüller, *J. Phys. Chem. C* **2022**, *126*, 19011.
- [26] C. Ziegler, A. Wolf, W. Liu, A.-K. Herrmann, N. Gaponik, A. Eychmüller, *Angew. Chem., Int. Ed.* **2017**, *56*, 13200.
- [27] P. Rusch, D. Zámbo, N. C. Bigall, *Acc. Chem. Res.* **2020**, *53*, 2414.
- [28] F. Rechberger, M. Niederberger, *Nanoscale Horiz.* **2017**, *2*, 6.
- [29] I. U. Arachchige, S. L. Brock, *J. Am. Chem. Soc.* **2006**, *128*, 7964.
- [30] J. L. Mohanan, I. U. Arachchige, S. L. Brock, *Science* **2005**, *307*, 397.
- [31] S. Sánchez-Paradinas, D. Dorfs, S. Friebe, A. Freytag, A. Wolf, N. C. Bigall, *Adv. Mater.* **2015**, *27*, 6152.
- [32] J. F. Miethe, F. Luebkmann, A. Schlosser, D. Dorfs, N. C. Bigall, *Langmuir* **2020**, *36*, 4757.
- [33] D. Zámbo, A. Schlosser, P. Rusch, F. Luebkmann, J. Koch, H. Pfnür, N. C. Bigall, *Small* **2020**, *16*, 1906934.
- [34] F. Luebkmann, J. F. Miethe, F. Steinbach, P. Rusch, A. Schlosser, D. Zámbo, T. Heinemeyer, D. Natke, D. Zok, D. Dorfs, N. C. Bigall, *Small* **2019**, *15*, 1902186.
- [35] L. Koral, J. R. Germain, E. Chen, I. R. Pala, D. Li, S. L. Brock, *Inorg. Chem. Front.* **2017**, *4*, 1451.
- [36] S. Brunauer, P. H. Emmett, E. Teller, *J. Am. Chem. Soc.* **1938**, *60*, 309.
- [37] P. Rusch, B. Schremmer, C. Strelow, A. Mews, D. Dorfs, N. C. Bigall, *J. Phys. Chem. Lett.* **2019**, *10*, 7804.
- [38] F. Luebkmann, P. Rusch, S. Getschmann, B. Schremmer, M. Schäfer, M. Schulz, B. Hoppe, P. Behrens, N. C. Bigall, D. Dorfs, *Nanoscale* **2020**, *12*, 5038.
- [39] P. Rusch, B. Schremmer, C. Strelow, A. Mews, D. Dorfs, N. C. Bigall, *J. Phys. Chem. Lett.* **2019**, *10*, 7804.
- [40] M. Berr, A. Vaneski, A. S. Susha, J. Rodríguez-Fernández, M. Döblinger, F. Jäckel, A. L. Rogach, J. Feldmann, *Appl. Phys. Lett.* **2010**, *97*, 093108.
- [41] Y. Nakibli, Y. Mazal, Y. Dubi, M. Wächtler, L. Amirav, *Nano Lett.* **2018**, *18*, 357.
- [42] K. Dong, C. Pezzetta, Q. C. Chen, A. Kaushansky, A. Agosti, G. Bergamini, R. Davidson, L. Amirav, *ChemCatChem* **2022**, *14*, 202200477.
- [43] D. Meissner, R. Memming, B. Kastening, D. Bahnemann, *Chem. Phys. Lett.* **1986**, *127*, 419.
- [44] J. Schneider, D. W. Bahnemann, *J. Phys. Chem. Lett.* **2013**, *4*, 3479.
- [45] M. J. Berr, P. Wagner, S. Fischbach, A. Vaneski, J. Schneider, A. S. Susha, A. L. Rogach, F. Jäckel, J. Feldmann, *Appl. Phys. Lett.* **2012**, *100*, 223903.
- [46] Y. J. Tu, D. Njus, H. B. Schlegel, *Org. Biomol. Chem.* **2017**, *15*, 4417.
- [47] P. Kalisman, Y. Nakibli, L. Amirav, *Nano Lett.* **2016**, *16*, 1776.
- [48] Z. Zhang, M. Wang, H. Zhou, F. Wang, *J. Am. Chem. Soc.* **2021**, *143*, 6533.
- [49] S. Dong, S. Pal, J. Lian, Y. Chan, O. V. Prezhdo, Z. H. Loh, *ACS Nano* **2016**, *10*, 9370.
- [50] A. Eφος, in *Semiconductor Nanocrystals: From Basic Principles to Applications*, (Eds: A. L. Eφος, D. J. Lockwood, L. Tsybeskov, Springer US, Boston, MA, **2003**, pp. 52–72.
- [51] P. Rusch, F. Luebkmann, H. Borg, J. G. Eckert, D. Dorfs, N. C. Bigall, *J. Chem. Phys.* **2022**, *156*, 234701.
- [52] L. M. Peter, J. Li, R. Peat, H. J. Lewerenz, J. Stumper, *Electrochim. Acta* **1990**, *35*, 1657.
- [53] J. F. Miethe, F. Luebkmann, J. Poppe, F. Steinbach, D. Dorfs, N. C. Bigall, *ChemElectroChem* **2018**, *5*, 175.
- [54] J. Schlenkrich, D. Zámbo, A. Schlosser, P. Rusch, N. C. Bigall, *Adv. Opt. Mater.* **2022**, *10*, 2101712.

- [55] A. Schlosser, L. C. Meyer, F. Lübke, J. F. Miethe, N. C. Bigall, *Phys. Chem. Chem. Phys.* **2019**, *21*, 9002.
- [56] W. W. Yu, L. Qu, W. Guo, X. Peng, *Chem. Mater.* **2004**, *16*, 560.
- [57] T. Kodanek, H. M. Banbela, S. Naskar, P. Adel, N. C. Bigall, D. Dorfs, *Nanoscale* **2015**, *7*, 19300.
- [58] H. G. Bagaria, E. T. Ada, M. Shamsuzzoha, D. E. Nikles, D. T. Johnson, *Langmuir* **2006**, *22*, 7732.
- [59] S. Naskar, F. Lübke, S. Hamid, A. Freytag, A. Wolf, J. Koch, I. Ivanova, H. Pfnür, D. Dorfs, D. W. Bahnemann, N. C. Bigall, *Adv. Funct. Mater.* **2017**, *27*, 1604685.

Supporting Information

Investigation of the photocatalytic hydrogen production of semiconductor nanocrystal-based hydrogels

*Jakob Schlenkrich[†], Franziska Lübke[†], Rebecca T. Graf, Christoph Wesemann, Larissa Schoske, Marina Rosebrock, Karen D. J. Hindricks, Peter Behrens, Detlef W. Bahnemann, Dirk Dorfs, Nadja C. Bigall**



Scheme S1: Schematic illustration of the hydrogel synthesis.

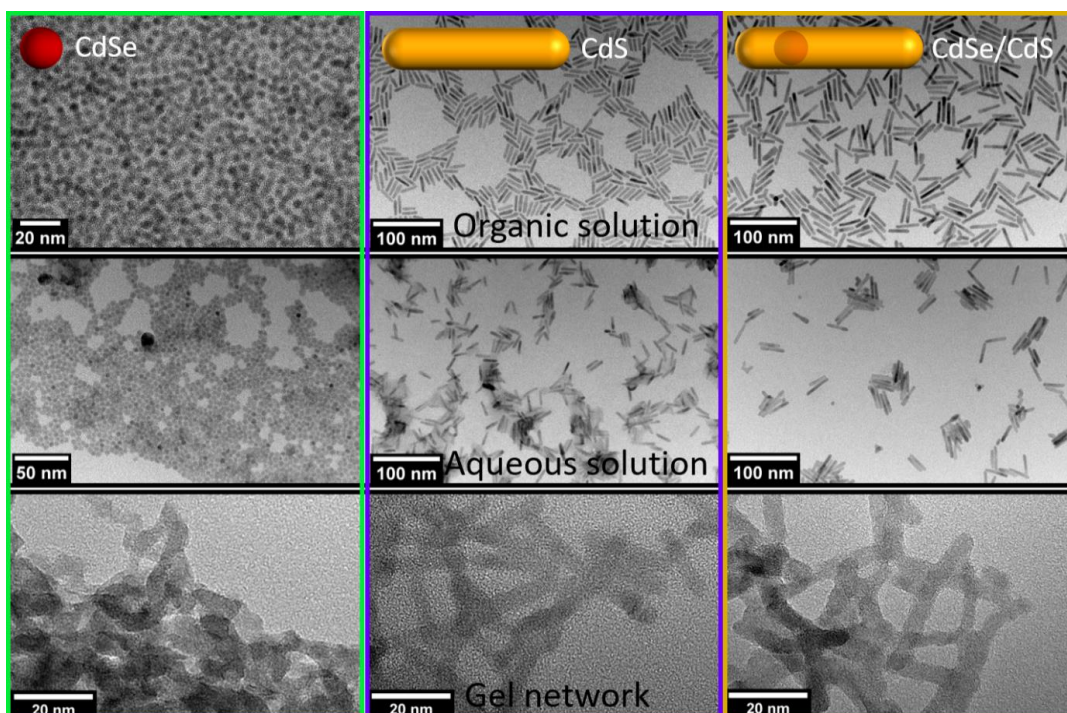


Figure S1: TEM images of (from left) CdSe, CdS, CdSe/CdS NCs in an organic solution, NCs in an aqueous solution and NCs in a gel network.

Optical properties

The CdS NR-based (**Figure S2**) and CdSe/CdS NR-based hydrogels show the same absorption properties as the nanocrystals in solution (**Figure S2**). Due to the high material content, the absorption maxima are less pronounced and have different intensities compared to the spectra of the pure nanocrystals. In case of CdSe QD-based hydrogels, a 27 meV decrease in the band gap is observed (**Figure S2**). Due to the connection of the CdSe nanocrystals, the exciton in the gel network is less confined, so that the confinement is less pronounced and the absorption shifts bathochromically (about 14 nm).

In the emission spectra of all three types of semiconductors, a bathochromic shift is observed in the hydrogel samples compared to the nanocrystals in solution (**Figure S2**). For CdSe, this is related to the reduction of the confinement due to gelation observed in the absorption properties. Additionally, there is a small difference in the Stokes shift of about 11 nm between the CdSe QD-based hydrogel and the nanocrystals in solution. In the CdSe/CdS NR and the pure CdS NR-based hydrogels, an even larger difference in the Stokes shift can be observed. As Talapin *et al.* reported an increasing Stokes Shift with increasing NR length in CdSe/CdS NRs, it can be assumed that the hydrogel behaves similarly to CdSe/CdS NRs with an increasing NR length due to gelation.^[1] According to Efros, the increase in Stokes shift is due to an anisotropic dependence of the effective-mass tensor in the A and B valence band in the CdSe core, which leads to an interchange of these valence bands.^[2] This effect can be observed in the pure CdS hydrogel and to a smaller extent in the pure CdSe hydrogel due to the introduced anisotropy.

All types of semiconductor gels show a difference in the PL lifetimes in the hydrogels compared to the nanocrystals in solution (**Figure S2**). In the PL lifetime spectra, a long lifetime component is observed beside a short component correlated with non-connected or not fully connected nanocrystals in the gel network. Due to the interconnection of the single nanocrystals, the excited electrons can be delocalized beyond one nanocrystal building block. In the CdSe QD-based and CdS NR-based hydrogels, the excited hole can also be delocalized, while in CdSe/CdS NRs it is preferably located in the CdSe core. The delocalization of the electron in the network and localization of the hole in the CdSe core effectively separate the charge carriers, which reduces the overlap of the electron and hole wave functions and increases the charge carrier lifetimes.^[3]

PL quantum yield (PLQY) was measured for CdSe/CdS NRs and provides further insight into the charge carriers and their localization. Due to the low emission intensity, it was not possible to measure the PLQY for the CdSe and CdS samples. **Table S2** shows the PLQY for the

CdSe/CdS nanocrystal solution in water and the hydrogel. Once excited at 400 nm, where CdS and CdSe are excited, and once at 500 nm, so that only the CdSe core is excited. The results show higher PLQY in the hydrogel and a smaller difference between excitation of both the CdS shell and CdSe core and excitation of CdSe core only. This indicates a reduction in hole trapping and a better localization of holes in the CdSe core after hydrogel formation. This could be caused by the removal of the thiol ligands from the surface during oxidative destabilization with H_2O_2 . Thiols are known to trap holes so that a transfer to the CdSe core is inhibited, reducing charge separation and charge carrier lifetime. These results fit with a study of Micheel et al. in which they investigated the influence of different ligands on the charge carrier properties.^[4] The discussion will be further extended in the interpretation of the photocatalytic experiments.

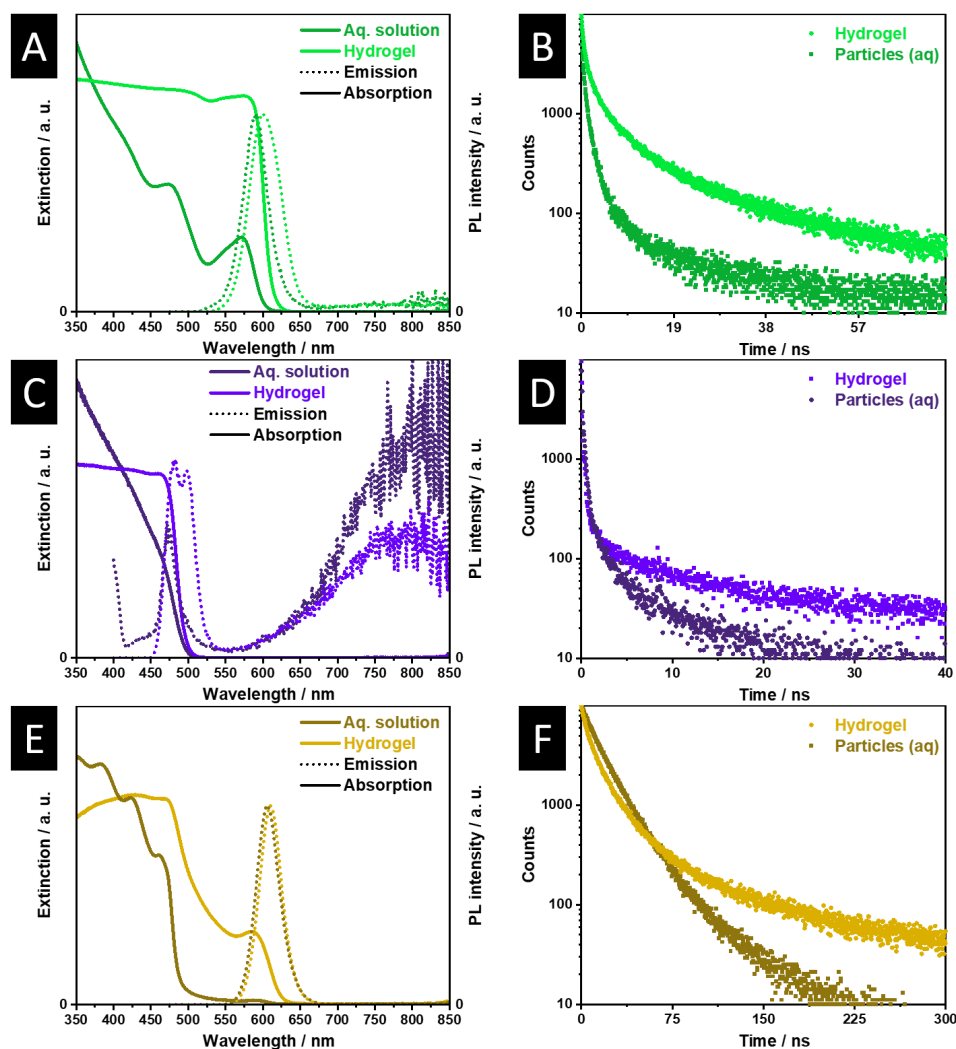


Figure S2: Absorption and emission spectra of (A) CdSe (C) CdS (E) CdSe/CdS NC in aqueous solution and as hydrogel. Photoluminescence lifetime measurements of the nanocrystals in aqueous solution and of the hydrogel of (B) CdSe (D) CdS (F) CdSe/CdS NCs.

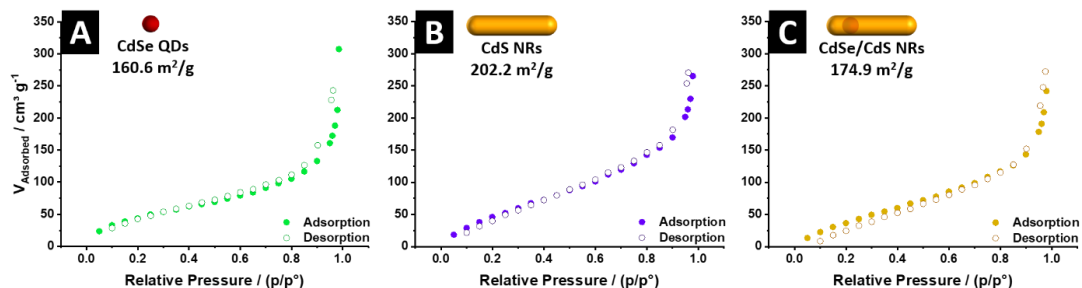


Figure S3: Argon adsorption and desorption curves of (A) CdSe (B) CdS (C) CdSe/CdS NC-based Aerogels showing the high porosity of the gel structures.

Table S1: Apparent quantum efficiencies of hydrogels in %.

	MeOH	TEOA	Ascorb.	S ²⁻ /SO ₃ ²⁻
CdSe	-	-	0.006	0.01
CdS	0.001	0.008	0.0003	0.11
CdSe/CdS	0.0004	0.0004	0.001	0.16
CdSe/CdS (stirring)				0.17
CdSe/CdS 455nm LED (stirring)				0.25

Table S2: Photoluminescence quantum yield of CdSe/CdS hydrogels and CdSe/CdS NR in aqueous solution measured with excitation at 450 nm and 500 nm. At 500 nm only the CdSe core is excited.

Excitation wavelength	PLQY CdSe/CdS hydrogel	PLQY CdSe/CdS aqueous solution
500 nm	46.22 %	58.34 %
450 nm	36.52 %	26.91 %

WILEY-VCH

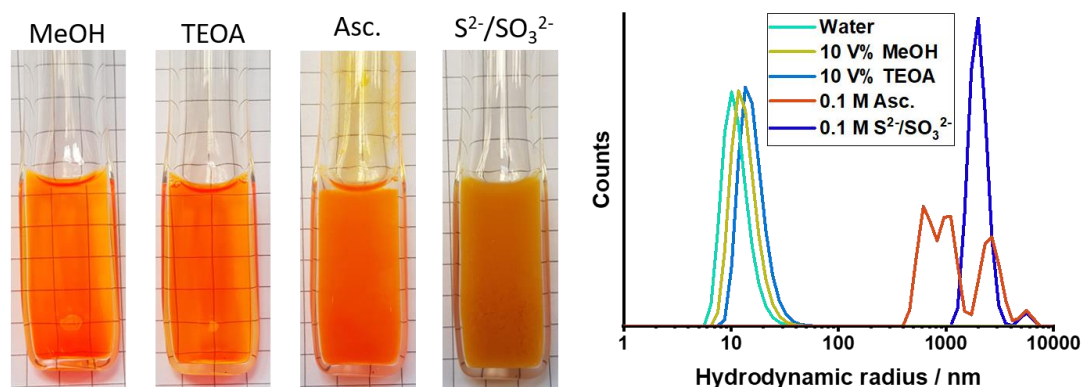


Figure S4: (left) Photographs of CdSe/CdS NC in different hole scavenger solutions showing the solubility of the ligand stabilized nanocrystals in the hole scavenger solutions. (Right) DLS measurements of ligand stabilized CdSe/CdS NC in different hole scavenger solutions showing the agglomerates when using 0.1M ascorbic acid or 0.1 M Na₂S/Na₂SO₃ solutions as hole scavengers.

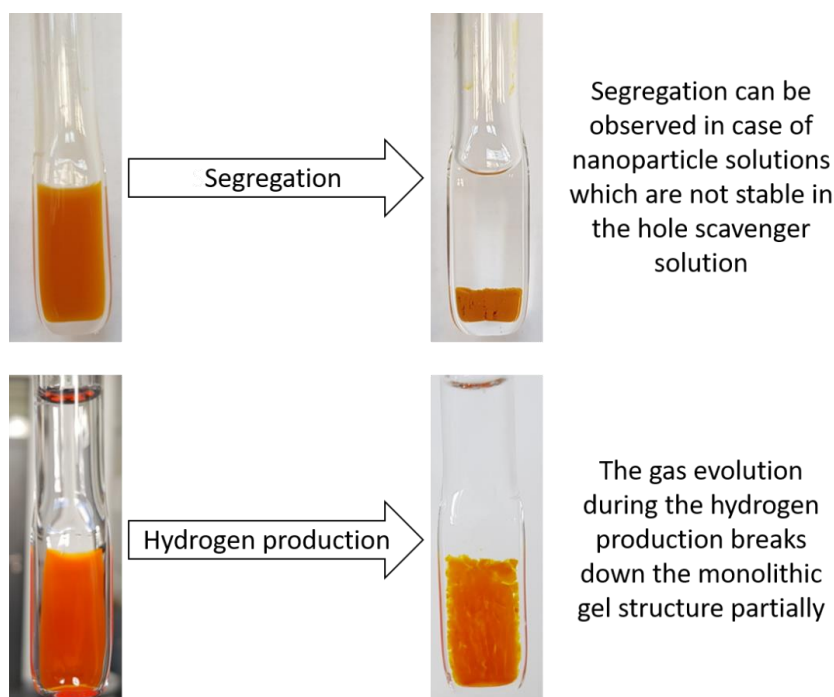


Figure S5: (Top) Photographs of CdSe/CdS NC in 0.1 M Na₂S/Na₂SO₃ solution demonstrating the segregation of the NCs by time. (Bottom) CdSe/CdS NC based hydrogel (left) before and (right) after the hydrogen production. The monolithic structure of the gel breaks apart but retains a voluminous structure.



Figure S6: Photographs of the measurement cell for the photocatalytic experiments. The glass vial is pressed to have a thickness of less than 2 mm to ensure the illumination of the whole hydrogel.

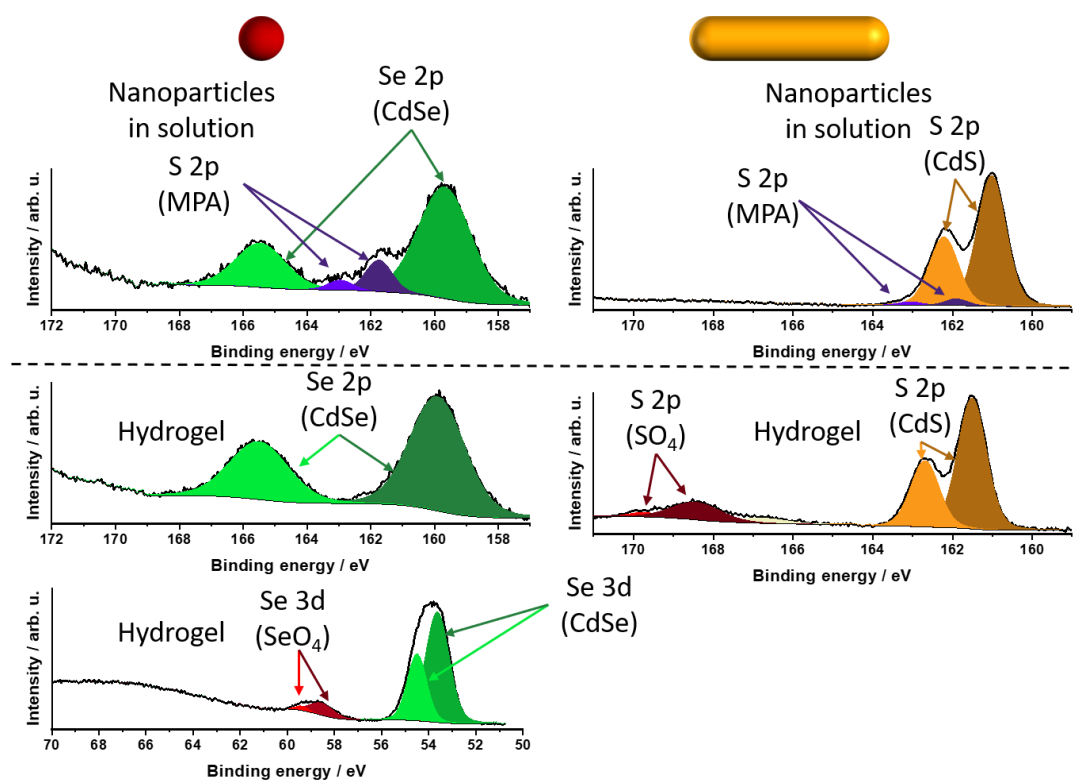


Figure S7: XPS spectra of S2p, Se2p and Se3d of CdSe and CdS NC solution (dropcasted) and as hydrogel. The spectra show the removal of the MPA ligands and the slight surface oxidation to SO_4 in case of CdS and the oxidation to SeO_4 in case of CdSe.

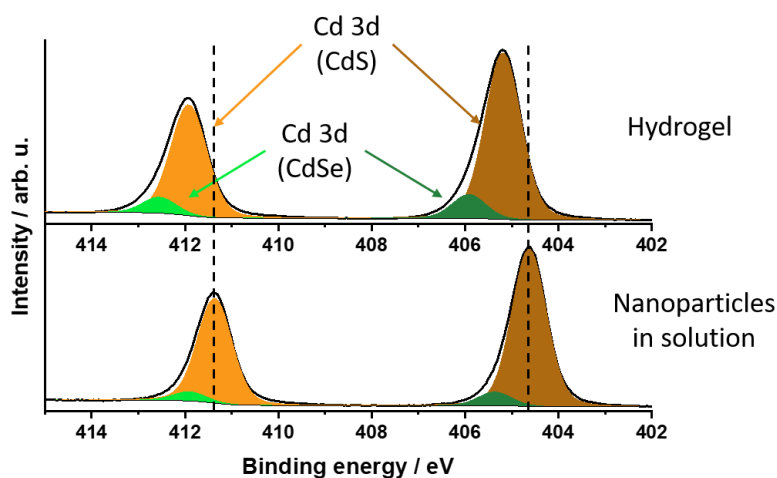


Figure S8: XPS spectra of Cd3d of CdSe/CdS NC solution (dropcasted) and as a hydrogel. The spectra show the peaks of the $3d_{5/2}$ and $3d_{3/2}$ orbitals of Cd related to CdSe (the core) and CdS (the NR shell). From NCs in solution to the hydrogel, a shift towards higher binding energies can be observed. This indicates a decreased electron density of the cadmium which leads to an increase in the binding energy in the XPS spectra. The electron density can be decreased due to unsaturated Cd atoms on the surface of the NCs due to the removal of the ligands. Furthermore, the XPS spectra of the S2p orbital sulfate groups can be found. Oxygen has a higher electron negativity and thus can as well reduce the electron density of the cadmium.

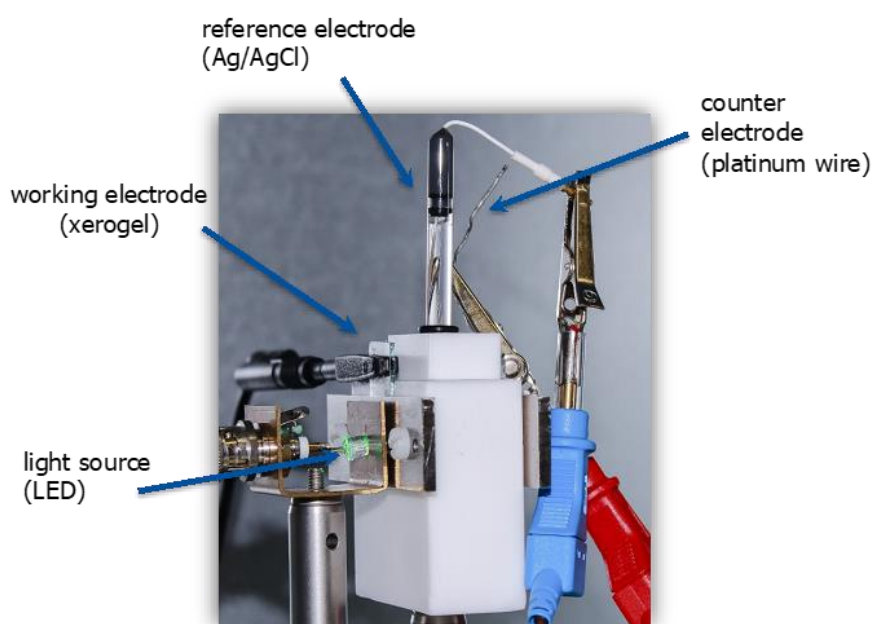


Figure S9: Measurement cell for the photoelectrochemical measurements.

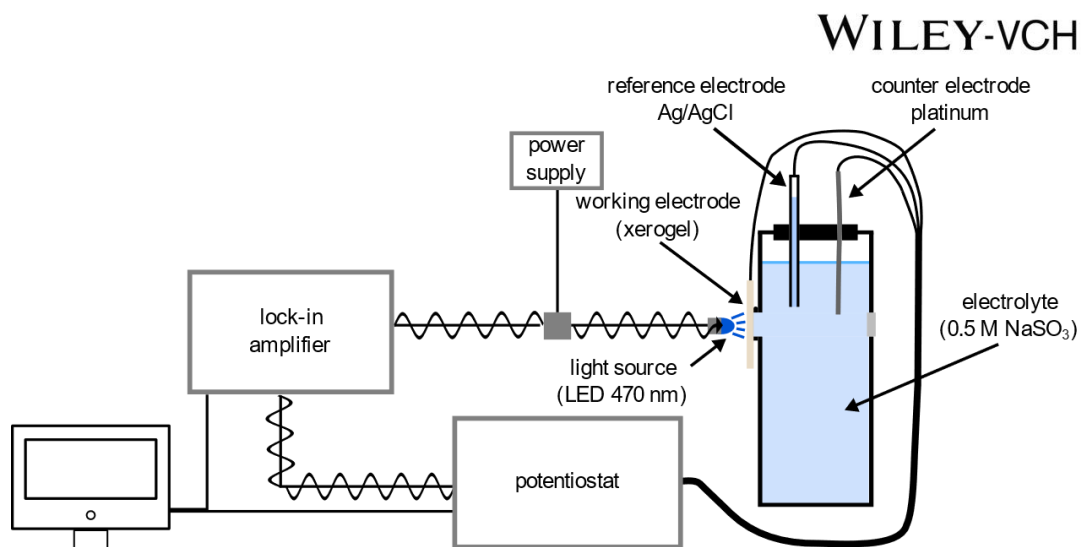


Figure S10: Measurement setup for intensity modulated photocurrent spectroscopy.

- [1] D. V. Talapin, R. Koeppel, S. Götzinger, A. Kornowski, J. M. Lupton, A. L. Rogach, O. Benson, J. Feldmann, H. Weller, *Nano Lett* **2003**, *3*, 1677.
- [2] A. L. Efros, *Luminescence Polarization of CdSe Microcrystals*, **1991**.
- [3] P. Rusch, B. Schremmer, C. Strelow, A. Mews, D. Dorfs, N. C. Bigall, *Journal of Physical Chemistry Letters* **2019**, *10*, 7804.
- [4] M. Micheel, B. Liu, M. Wächter, *Catalysts* **2020**, *10*, 1143.

3.3 Semiconductor-Metal Hybrid Nanoparticle-Based Hydrogels: Efficient Photocatalysts for Hydrogen Evolution Reaction

Jakob Schlenkrich, Denis Pluta, Rebecca T. Graf, Christoph Wesemann, Franziska Lübke-
mann-Warwas, Nadja C. Bigall

Submitted to a peer reviewed journal, 2023

Semiconductor-Metal Hybrid Nanoparticle-Based Hydrogels: Efficient Photocatalysts for Hydrogen Evolution Reaction

Jakob Schlenkrich, Denis Pluta, Rebecca T. Graf, Christoph Wesemann, Franziska Lübke-Warwas, Nadja C. Bigall*

In the semiconductor-metal hybrid nanoparticles excited charge carriers can be separated efficiently by transferring the electron to the metal, because the Fermi level is located within the band gap of the semiconductor. Besides the charge carrier separation, the catalytically active surface of the metal enables the use of these charge carriers for further reactions.

Due to limited colloidal stability the application of nanoparticles in solution is challenging. To circumvent these difficulties the destabilization can be used to build up monolithic gel-like structures with retained high surface area and an ensured diffusion within the network. The resulting nanoparticle-based hydrogels of semiconductor-metal hybrid nanoparticles show high photocatalytic hydrogen production rates. By simply mixing semiconductor and semiconductor-metal hybrid nanoparticles in one gel, the synthesis of the gels allows the reduction of the metal content to further tune the photocatalyst.

and platinum decorated CdSe/CdS nanoparticles showed high efficiencies in the hydrogen evolution reaction.^[8,10]

To optimize the applicability of such or other nanoparticles, colloidal stable dispersions can be destabilized to build up a self-supporting, highly porous three-dimensional network with good surface accessibility.^{[9][14–16]} With this limits in applications due to colloidal instability can be overcome by this approach. The self-supporting structure enables diffusion of various media like polar or less polar solvents inside the pore system making the gel structures highly versatile.

In a first study we could show that

the gelation by means of ligand oxidation improved the photocatalytic activity of CdSe/CdS-based hydrogels compared to the nanoparticle dispersion. Removing ligands makes the surface better accessible and the controlled destabilization maintains a high surface area. Furthermore, charge carrier properties were improved for photocatalytic applications with the ligand removal and network formation.^[17]

In this work, platinum has been grown on CdSe/CdS nanorods. Subsequently, the resulting hybrid nanoparticle dispersions were destabilized in a controlled way resulting in nanoparticle-based hydrogels. Here, the hydrogen evolution reaction was used to explore the photocatalytic advantages of this material. Not only hydrogels made of the hybrid nanoparticles were investigated but also mixtures of semiconductor and semiconductor-metal hybrid nanoparticles by which the amount of noble metal can be reduced. Figure 1 shows the pathway from CdSe/CdS semiconductor NRs to platinum decorated CdSe/CdS/Pt nanoparticle-based hydrogels schematically

1. Introduction

The combination of semiconductors and metals on the nanoscale can have superior properties for applications in catalysis.^{[1,2][3][4]} Especially in photocatalysis the semiconductor can efficiently absorb light. Excited charge carriers can be separated by transferring the electron to the metal so that the material can provide the charge carriers for further reactions.^{[5][6]}

CdSe/CdS nanorods (NRs) with CdSe as a spherical core in a rod shaped CdS shell are known to exhibit a high absorption coefficient and is able to separate photoexcited charges due to their quasi type II band structure.^{[7][8]} Adding a metal domain on the tip of the CdSe/CdS nanorod by means of epitaxial growth in solution can further separate the charges.^[5,6] Charge carrier lifetimes up to microseconds have been reported in these hybrid nanoparticles.^[9] Synthetically various metals like gold, nickel, silver, cobalt or platinum can be grown on the semiconductor.^{[10–12][13]} Especially, nickel

J. Schlenkrich, D. Pluta, R. T. Graf, C. Wesemann, F. Lübke-Warwas, N. C. Bigall
Institute of Physical Chemistry and Electrochemistry
Leibniz University Hannover
Callinstraße 3A, 30167 Hannover, Germany

J. Schlenkrich, R. T. Graf, F. Lübke-Warwas, N. C. Bigall
Cluster of Excellence PhoenixD (Photonics, Optics and
Engineering -Innovation Across Disciplines)
Leibniz University Hannover
30167 Hannover, Germany

D. Pluta, R. T. Graf, N. C. Bigall
Laboratory of Nano- and Quantum Engineering
Leibniz University Hannover
30167 Hannover, Germany

D. Pluta, R. T. Graf
Hannover School of Nanotechnology
Leibniz University Hannover
Schneiderberg 39, 30167 Hannover, Germany
E-mail: nadja.bigall@pci.uni-hannover.de

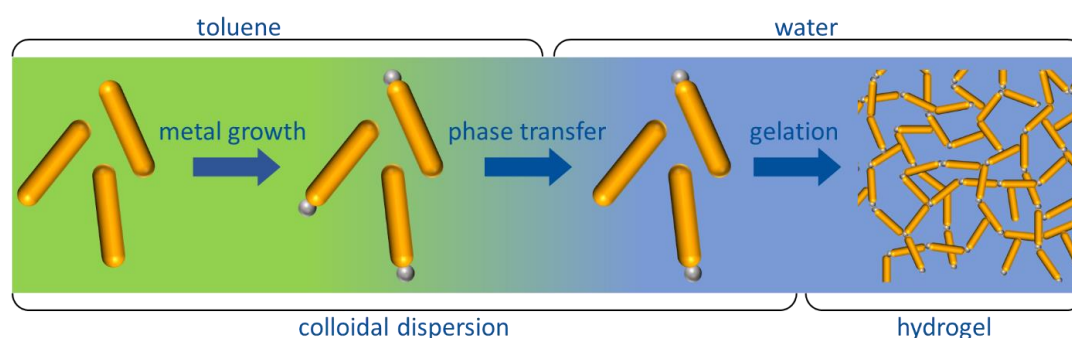


Figure 1: Schematic pathway from CdSe/CdS semiconductor nanorods to metal decorated CdSe/CdS/Pt nanoparticle-based hydrogels.

2. Results and discussion

The synthesis of CdSe/CdS nanorods is well established in nanocrystal research and is used in our group for years.^[9,14,17] Resulting particles have good optical properties and are colloidally stable for months. Thus, all following experiments have been performed with the same batch of NRs to ensure comparability. Still, metal growth on a semiconductor surface can be more challenging due to the larger lattice mismatches between CdS and platinum.^[18] An appropriate solvent, the right reaction temperature, precursor and surfactants can ensure the heterogeneous growth on the semiconductor instead of homogeneous nucleation of the metal itself. However, reaction conditions to completely inhibit the homogeneous nucleation have not been found in this study. Nevertheless, to obtain an almost pure hybrid nanoparticle solution selective precipitation needed to be used.

Since the colloidal synthesis is performed in organic media, the study of hydrogen production in water requires a phase transfer. In literature a ligand exchange using mercaptopropionic acid (MPA) is often applied to stabilize the particles in water.^[3,5] In our work there were some difficulties to stabilize the particles in water using MPA. Alternatively, using a longer aliphatic chain namely mercaptoundecanoic acid (MUA) was able to stabilize the particles in water in our experiments following the report of.^[19] Nevertheless, colloidal stability over days is challenging as the particles aggregated in aqueous solution within a few hours to days. Gelation of the nanoparticles can prevent dense agglomerates and form a material being stable for months and more.

In previous works we showed that low amounts of hydrogenperoxid can be used to destabilize an aqueous nanoparticle solution.^{[9][20]} By oxidizing thiol ligands, the controlled formation of a three-dimensional porous network can be triggered.^[21,22] We showed that removing ligands from the nanoparticle surface can even have positive effects on the photocatalytic properties.^[17]

In this work, destabilizing CdSe/CdS/Pt hybrid nanoparticles with MUA on the surface using H₂O₂ was not possible. To stabilize MUA capped particles in water a slightly basic pH is needed to deprotonate the acid group. However, in basic conditions platinum can catalyze the decomposition of H₂O₂ by forming oxygen and water. This prevents the thiol ligands from oxidation and thus inhibits the destabilization of the

colloidal solution. In contrast, in acidic conditions platinum catalyze the decomposition of H₂O₂ as well but forms hydroxy radicals as an intermediate.^[23] These radicals themselves can oxidize thiol ligands and destabilize the nanoparticle dispersion. To stabilize the CdSe/CdS/Pt hybrid NPs in acidic conditions a phase transfer and ligand exchange with 2-(dimethylammonium)ethanethiol (DMAET) has been applied.^[19] Having the hybrid NRs in acidic aqueous solution the controlled destabilization using H₂O₂ via the OH-radicals works as desired. However, from a certain size of platinum domains, the phase transfer using DMAET leads to partial detachment of platinum domains. These then separated platinum nanoparticles cannot be transferred to the aqueous solution using DMAET (Figure S1). For the interpretation of further results this has to be considered. Figure 2 shows TEM images of the hybrid nanoparticles in aqueous solution and nanoparticle-based gels made of this aqueous nanoparticle dispersion (more TEM images in Figure S2). Here, it can be seen that not every semiconductor nanorod has a metal tip in the aqueous dispersion. STEM images of the resulting hydrogels clearly show the metal domains in the network. The microscopic structure of these porous gels is always very similar as further demonstrated in several publications in our group.^[9,14] Thus, to visualize the structure and high porosity of the gel structures we refer to publications of our group with SEM images of gold decorated CdSe/CdS nanorod gels after supercritical drying.^[12]

From nanoparticles (NP) in organic solution to NP in aqueous solution to NP-based hydrogels the optical properties change. Adding a metal to the semiconductor a broad absorption of the metal is observed (Figure 2). The photoluminescence quantum yield (PLQY) decreases (Table S1) but the spectral position of the PL does not change (Figure 2 and S3). Major changes are found regarding PL lifetimes (table S1) and the radiative and non-radiative recombination rates which were calculated using the PLQYs and PL lifetimes according to equations (1-4) and are shown in Figure 2E.

$$\Phi_R = \frac{k_R}{k_R + k_{NR}} \quad (1)$$

$$\tau = \frac{1}{k_R + k_{NR}} \quad (2)$$

$$k_R = \frac{\Phi_R}{\tau} \quad (3)$$

$$k_{NR} = \frac{1}{\tau - k_R} \quad (4)$$

Both the phase transfer (investigated using pure semiconductor NRs) and the metal growth lead to an increase of the non-radiative recombination rates (k_{NR}) and a decrease in the radiative recombination (k_R) rates. The changes due to the phase transfer can be explained by an increased amount of hole trap states. Thiol ligands are known to efficiently trap holes on the surface. For radiative recombination, the hole has to be located in the CdSe core.^[5] Thus hole trapping increases the probability for non-radiative recombination while the probability for radiative recombination is decreased. The metal growth leads to electron transfer from the semiconductor (SC) to the metal domain which is competing with the radiative recombination and introducing an additional non-radiative recombination pathway. The phase transfer of NPs after metal growth combines the addition of hole trap states and the electron transfer to the metal. Colloidal destabilization and gel formation of pure semiconductor NRs leads to slightly reduced PLQY compared to the colloidal NP counterparts but the PL lifetime increases as it has been shown and explained in previous publications.^[9,17] Due to the crystal contact between the nanoparticles electrons can be delocalized beyond one nanoparticle building block. Additionally, oxidizing the thiol ligands minimizes the amount of hole trap states and thus improves hole transfer to the CdSe core. This leads to the decrease of radiative and non-radiative recombination rates. Platinum decorated NR-based hydrogels show lower PLQY and PL lifetime. In our case, this leads to increased non-radiative recombination rates and decreased radiative recombination rates compared to the platinum decorated NRs in aqueous solution. These changes indicated a more efficient electron transfer to the platinum domains in the nanoparticle network in the hydrogel

compared to the colloidal ensemble. As shown in the transmission electron microscopy (TEM) images not all SC nanorods have a contact to a platinum domain in the aqueous solution. Therefore, some SC NRs would show no changed optical properties. However, in the hydrogel electrons from SC NR without direct contact to platinum can reach a platinum domain by traveling through the SC network (Figure 4C). This was shown in a previous publication with gold nanoparticles.^[20]

To investigate the photocatalytic properties of CdSe/CdS/Pt NR-based hydrogels photocatalytic measurements have been performed in 1 mm thin glass cuvettes (Figure S4). This ensures the excitation of the whole material under illumination with a 300 W xenon lamp equipped with an AM 1.5G filter at an intensity of 1 sun (100 mW/cm²). Since the gel structures are self-supporting porous materials with high surface area, diffusion of the hole scavenger and the reactants through the catalytic measurement within the gels is possible. Therefore, all measurements were carried out without stirring.

The benefit of using NP-based gel structures is that the problem of uncontrolled aggregation of particle colloids in the hole scavenger solution during the photocatalytic measurement can be avoided (Figure S5). Photoexcited charge carriers cannot only be used for the catalytic reaction but also decompose the stabilizing ligands leading to agglomeration.

For the efficient hydrogen production reaction and to prevent material degradation a hole scavenger was utilized fulfilling a complete redox reaction.^[24] Full water splitting would be an ideal redox reaction but is not possible with CdSe/CdS/Pt NPs as photocatalysts. The hydrogen evolution reaction (HER) can be catalyzed efficiently by the

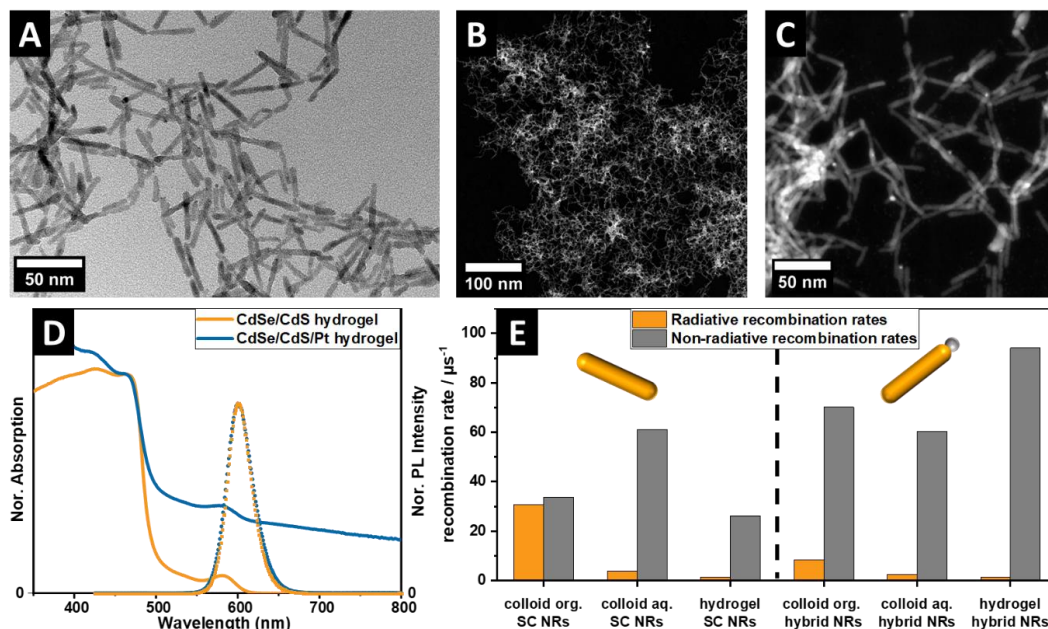


Figure 2: (A) TEM measurement of CdSe/CdS/Pt nanoparticles in aqueous solution. Spots with darker contrast shows platinum domains (B, C) STEM measurements of a CdSe/CdS/Pt hydrogel. Brighter spots show platinum domains. (D) Absorption and emission spectra of CdSe/CdS and CdSe/CdS/Pt hydrogels. (E) Radiative and non-radiative recombination rates of CdSe/CdS and CdSe/CdS/Pt colloids and hydrogels. Calculated using the PLQY and PL lifetimes using equation 1-4.

platinum^[3,25] whereas the oxygen evolution reaction (OER) cannot take place on the CdS surface.^[26] Therefore, the choice of the right hole scavenger is crucial for high efficiencies.^[27] Here, 0.1 M sodium sulfite/sodium sulfide ($\text{Na}_2\text{SO}_3/\text{Na}_2\text{S}$) solution, isopropanol (IPA) at pH 7 and isopropanol at pH 14 have been investigated. 0.1 M ($\text{Na}_2\text{SO}_3/\text{Na}_2\text{S}$) solution showed good hole scavenging properties in previous projects whereas isopropanol at pH 7 and 14 are known in literature to be efficient hole scavengers. The electrochemical potential of OH^- is pH dependent. At pH 14 OH^- can be oxidized by holes from CdSe forming hydroxy radicals. These highly reactive radicals can act as redox shuttles to oxidize the alcohol in the hole scavenging solution.^[28] First the influence of the different hole scavenger solutions on the hydrogen production rate has been investigated. The 10 V% IPA solution at pH 14 was the most efficient while the 0.1 M ($\text{Na}_2\text{SO}_3/\text{Na}_2\text{S}$) solution was the least efficient (Figure S6). Because of these results all further experiments were carried out using 10 V% IPA in water at pH 14 as hole scavenger solution.

To get insights into the influence of the reaction time of the platinum growth on the photocatalytic properties of the resulting hydrogels six different reaction times have been investigated. In general, the longer the reaction time of the platinum growth is, the larger become the platinum domains and the lower is the probability to find nanorods without a platinum domain. Performing the ligand exchange and phase transfer however leads to partial detachment or dissolution of the platinum domains as shortly discussed above. Hybrid NRs with small platinum domains can be phase transferred without any observed detachment while hybrid NRs with larger platinum domains showed detachment of the platinum domains (Figure S1). This being said, investigating the influence of the domain size was not feasible since the size and the amount of platinum could not be controlled to the anticipated degree during the phase transfer. Nevertheless, the results of the photocatalytic measurements of hydrogels with hybrid NRs from different reaction times showed interesting results (Figure 3A). From two to three minutes of reaction time a significant increase in the hydrogen production rate has been observed. For these small domain sizes (up to 3 min reaction time) no detachment during the phase transfer has been observed which makes the comparison of one, two and three minutes adequate. From four minutes on detachment during the phase transfer has been observed. Interestingly the detachment after five minutes of reaction time was

significantly more than after four minutes (Figure S1) effecting the hydrogen production rate negatively. Regardless the hydrogels synthesized from NRs, that underwent six minutes of platinum domain growth showed the highest hydrogen production rates so that further experiments have been performed using particles with six minutes reaction time of platinum growth. A benefit of nanoparticle-based gel structures is to combine different materials by simple mixing and cogelation.^{[20][29]} This way it is possible to achieve crystal contact between the different materials and circumventing highly complex chemical synthesis routes. Here, this can be used to reduce the noble metal amount by simply mixing hybrid NRs and pure semiconductor NRs before gelation. Using certain ratios of the two components, the influence of the platinum amount on the photocatalytic activity has been investigated. Reducing the amount of the noble metal without a drastic decrease in the catalytic activity would be desirable due cost and abundance of rear earth metals. Hydrogels with 0 % (pure semiconductor), 25 %, 50%, 75 % and 100 % of the hybrid NRs were synthesized. The TEM images show the reduced number of platinum domains when comparing 25 % and 100 % as expected (Figure S7). Optical properties also depend on the ration of the hybrid NRs. With increasing platinum amount within the hydrogel, mainly the PLQY decreases and the PL lifetime shortens (table S1). As discussed above combining the PLQY and PL lifetime can give information on the radiative and non-radiative recombination rates. For 0 %- to 100 %-hydrogels the non-radiative recombination rate increases with increasing platinum amount. In contrast the radiative recombination rates are very similar for all mixtures and the pure semiconducting gel, as illustrated in Figure 4. Furthermore, the amount of absorbed light increases with increasing platinum amount.

Measuring the photocatalytic hydrogen production using 10 V% isopropanol at pH 14 as the hole scavenger gave the following results: From 0 % to 75 % hybrid NRs the hydrogen production rate increases with increasing amount of platinum in the hydrogel. However, the hydrogen production rate then decreases slightly having a hydrogel based on 100 % hybrid NRs (Figure 3B, Figure S8). Combing these results with the trend of the non-radiative recombination rates indicates that the electron transfer to the metal is not the limiting process. More probable the bottle neck for the hydrogen production can be the diffusion within the gel

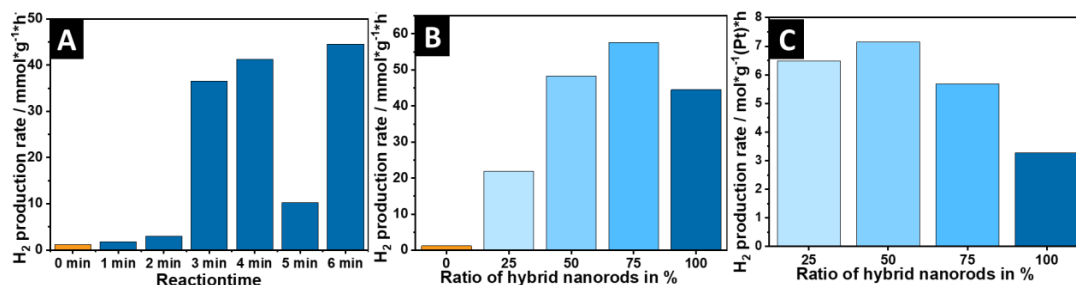


Figure 3: (A) Hydrogen production rates of hydrogels depending on the platinum domain growth reaction time. (B) Hydrogen production rates of hydrogels made of mixtures of CdSe/CdS nanorods and CdSe/CdS/Pt nanorods (6 min reaction time) with relative amount of 0 %, 25 %, 50 %, 75 %, 100 % hybrid nanorods. (C) Hydrogen production rates of hydrogels made of mixtures of CdSe/CdS nanorods and CdSe/CdS/Pt nanorods with relative amount of 25 %, 50 %, 75 %, 100 % calculated with regard to platinum amount.

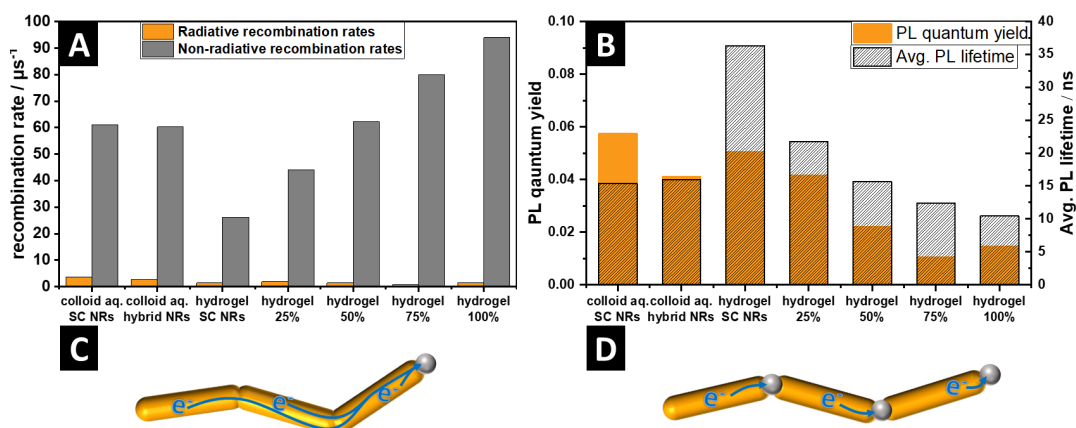


Figure 4: (A) Radiative and non-radiative recombination rates of colloids and hydrogels. Including mixtures of CdSe/CdS nanorods and CdSe/CdS/Pt nanorods with relative amounts of 0 %, 25 %, 50 %, 75 %, 100 % of hybrid nanorods. (B) PLQY and average PL lifetimes of colloids and hydrogels. Including mixtures of CdSe/CdS nanorods and CdSe/CdS/Pt nanorods with relative amounts of 0 %, 25 %, 50 %, 75 %, 100 % of hybrid nanorods. (C, D) Schematic illustration of electron transfer to a metal domain. (C) low amount of metal domains. (D) higher amount of metal domains.

structure or the catalytic reaction itself since it is a two-electron process. Diffusion in the network takes place but having these high hydrogen production rates without stirring it would be reasonable to reach diffusion limits. Reducing the amount of hybrid nanorods and still reach higher hydrogen production rates is a promising result. As we showed in previous works charge carriers can be transported through gel structures. In pure semiconducting CdSe/CdS gels the hole is transferred to the CdSe due to the quasi-type-II band structure and the electron can be delocalized beyond one nanoparticle building block.^[9,17] In semiconductor-metal hybrid gel structures electrons can travel over several NRs to one metal domain as shown by Rosebrock *et al.* for gold domains in CdSe/CdS NR based gels.^[20] Here mixing pure semiconductor NR with hybrid NR might show similar effects. Electrons from more than one semiconductor NR reach a platinum domain which could lead to slight electron accumulation in the platinum domain as it is known for the combination of semiconductors and metals on the nanoscale (Figure 4C, 4D).^{[30][31]} Having multiple electrons in the same platinum domain would be beneficial for the hydrogen production since it is a two electron process. Further reducing the platinum amount by 50 % and 25 % leads to similar or only slightly lower hydrogen production rates compared to 100 % hybrid NR based hydrogels, respectively. Considering that platinum is about 1000 time more expensive than cadmium the amount of platinum in the catalyst is crucial. To shed light on the hydrogen production rate per platinum, the amount of platinum has been measured using SEM EDX (table S2). Figure 3C shows the rates per gram platinum and shows that in this regard the most efficient mixture is 50 % of the hybrid NRs. Even with 25 % the hydrogen production rate is only slightly lower. This further indicates the benefits of the hydrogel formation of hybrid nanoparticles. In the hydrogels the amount of platinum can be controlled easily. Due to the network formation also with small amounts of platinum the electron transfer from the semiconductor NRs to the metal domains remains possible. This is the crucial difference to colloidal dispersions. When mixing semiconductor and hybrid

nanorods in a dispersion, an electron transfer from a semiconductor NR to a metal domain of a hybrid NR is not feasible.

3. Conclusion

Semiconductor-metal hybrid nanoparticle colloids with CdSe/CdS nanorods as semiconductor and platinum domains as metal can be phase transferred and destabilized in a controlled manner to build up nanoparticle-based hydrogels. The phase transfer of these hybrid nanoparticles from organic to aqueous media leads to partial detachment of metal domains. Metal growth and hydrogel formation increase non-radiative recombination rates and decrease radiative recombination rates. Photocatalytic hydrogen production rates increase significantly by adding platinum to the semiconductor. Furthermore, by mixing semiconductor nanorods with hybrid nanorods the platinum amount can be reduced easily while even increasing the hydrogen production rate by lowering the platinum amount.

4. Experimental Section

Chemicals: All chemicals used for the syntheses were used as purchased without any further purification. Sodium sulfite (97 %) and sodium sulfide (90 %) were purchased by ACROS. Cadmium oxide (CdO, 99.998 %) and elemental selenium (200 mesh, 99.999 %) were supplied by Alfa Aesar. Tri-*n*-octylphosphine oxide (TOPO, 99 %), elemental sulfur (99.98 %), 1-octadecene (ODE, 90 %), 3-mercaptopropionic acid (MPA, $\geq 99\%$), 2-propanol ($\geq 99.8\%$), chloroform ($\geq 99.5\%$), diphenyl ether (DPE, 99 %), oleylamin (OIAm 70 %), 2-(dimethylamino)ethanethiol hydrochloride (DMAET 95 %) were purchased from Sigma Aldrich. Potassium hydroxide (KOH, $>85\%$), *n*-hexane ($\geq 99\%$), acetone (99.5 %), hydrogen peroxide (H_2O_2 , 35 w/w %), toluene ($\geq 99.7\%$), and methanol (MeOH, $\geq 99.8\%$) were purchased from Honeywell. Tri-*n*-octylphosphine (TOP, 97 %) and platinum(II) acetylacetonate (Ptacac₂ 98 %) was purchased from ABCR., elemental

tellurium (60 mesh, 99.999%), octadecylphosphonic acid (ODPA, 99.0%) and hexylphosphonic acid (HPA, 99%) were obtained from Roth, Fisher Scientific and PCI, respectively. Ultrapure water with a resistivity of 18.2 M Ω ·cm was used for aqueous solutions.

Synthesis of CdSe Quantum Dots: The CdSe quantum dots (QDs) were synthesized following the procedure established by Carbone et al. with specific adaptations.^{[8][18]} In a three-neck flask, we introduced CdO (0.12 g, 0.93 mmol), TOPO (6.0 g, 15.52 mmol), and ODPA (0.56 g, 1.67 mmol), and subjected them to vacuum degassing at 150 °C for 50 minutes. Subsequently, under an argon atmosphere, the flask was heated until the complete dissolution of CdO occurred at 300 °C. At this point, TOP (3.6 mL) was introduced, and the temperature was further elevated to 380 °C. The growth of CdSe QDs was initiated by adding elemental selenium (0.116 g, 1.47 mmol) dissolved in TOP (3.6 mL). After 4 minutes, the growth process was terminated by adding ODE (6 mL), and rapid cooling was achieved using airflow. The QDs were then precipitated twice with methanol (5 mL), followed by centrifugation (3775 RCF, 10 min), and redispersion in toluene (5 mL). The size of the nanocrystals and the concentration of the QD solution were determined based on the position and optical density (OD) of the first excitation peak in an extinction spectrum.^[32]

Synthesis of CdSe/CdS Nanorods: In a modified version of Carbone et al.'s synthesis,^[8] CdO (0.18 g, 1.4 mmol), TOPO (9.0 g, 23.28 mmol), ODPA (0.84 g, 2.51 mmol), and HPA (0.24 g, 2.07 mmol) were vacuum-degassed at 150°C for 1 hour. CdO dissolved at 300°C under argon, followed by the addition of TOP (5.6 mL) at 380°C. Nanorod growth was initiated by injecting a solution of sulfur (0.39 g) in TOP (5.4 mL) containing CdSe QDs (400 μ M). After 8 minutes, the solution was cooled and toluene (7 mL) was added at 70°C and particles were precipitated in methanol, centrifuged (3775 RCF, 10 min), and redispersed in toluene (2 mL).^[17]

Synthesis of CdSe/CdS/Pt Nanorods: In a 50 mL flask, we vacuum-degassed a mixture of DPE (25.44 mL), HDD (100 mg) and OIAm (1.08 mL). After heating this under argon to 175°C, we introduced a suspension of dried CdSe/CdS NRs (198.11 μ L, Cd concentration: 38.069 g/L) and Pt(acac)₂ (30.8 mg) in DCB (1.27 mL) which was prepared in a glovebox and ultrasonicated outside a glovebox. We irradiated the reaction with a 470 nm LED for 1-6 minutes, then quenched it with pressurized air. Precipitation was achieved with 25 mL toluene and 25 mL MeOH, followed by centrifugation at 4000 rcf. This method was adapted from Hill et al.^[11]

Phase Transfer with MPA or MUA: Kodanek et al.'s phase transfer method was modified for our study.^[19] The nanoparticle solutions underwent precipitation using methanol, followed by centrifugation and subsequent redispersion in 10 mL of hexane. The hexane solution contained approximately 2 mg/mL of cadmium. Subsequently, a 0.1 M KOH solution in methanol (10 mL) and 0.25 mL of MPA were added to the mixture, which was then vigorously shaken for a minimum of 5 hours. The methanolic phase containing the nanoparticles was isolated and subjected to centrifugation at 3775 RCF for 10 minutes. After redispersion in a 0.01 M KOH solution in water, the particles underwent a series of washing steps with acetone and were redispersed in Millipore water.^[17]

Phase Transfer with DMAET: The method of phase transfer of Kodanek et al. was adapted.^[57,58] The nanoparticle solutions were precipitated with methanol, centrifuged and redispersed in 5 mL chloroform. The cadmium concentration in the chloroform solution was approximately 1.5 mg/mL. 4 mL of 0.5 M DMAET solution and 2 mL of water (pH 4.8 with HCl) were added. The mixture was shaken over night. The chloroform phase was removed using a pasteur pipette. The phase with the particles has been centrifuged for 3 min (~4000 rcf). Particles had been redispersed in 1 mL of water (pH 4.8 with HCl). Washing was possible with a centrifuge filter (100.000 MWCO).

Assembly to Hydrogels and Transfer to Aerogels: To induce the destabilization of ligand-stabilized nanoparticles through the oxidation of the ligands using hydrogen peroxide (H₂O₂), the aqueous nanoparticle solution, containing cadmium (Cd) at a concentration of 3.6 grams per liter as determined by Atomic Absorption Spectroscopy (AAS), was combined with an H₂O₂ solution (0.35 wt%, 93.75 microliters per milliliter of nanoparticle solution). This mixture was placed in either an Eppendorf tube or photocatalytic glass cells, followed by vigorous shaking. Subsequently, the solution was left undisturbed in darkness overnight.

After the formation of the hydrogel, a total of ten sequential washing steps were carried out over the course of three days using Millipore water. Each washing step involved the removal of 3 milliliters of the supernatant located above the hydrogel, accomplished using a pipette. Following the removal, 3 milliliters of fresh Millipore water were meticulously added using a pipette, with the aim of eliminating any residual destabilizing agent and other associated by-products. The procedure is described in more detail here.^[9]

Photocatalysis Measurements: The photocatalysis experiments were conducted within Duran glass cells, as illustrated in **Figure S4**. The hydrogels were synthesized inside these cells, following the previously described procedure. Prior to exposure to a 300 W xenon lamp (QuantumDesign LSH302) fitted with an AM 1.5 G filter (QuantumDesign solar simulator LS0308), the hydrogels underwent five washes with the designated hole scavenger solution. For the assessment of hydrogen production, 100 μ L aliquots were withdrawn using a gas syringe and subsequently analyzed using a GC (Agilent GC 8860) equipped with an Agilent HP-PLOT Mole sieve column measuring 30 m x 0.320 mm x 25 μ m, coupled with a thermal conductivity detector (TCD). The hydrogen production rate was computed using the following formula:

$$n_{\text{H}_2} = \frac{A_{\text{H}_2}}{A_{\text{N}_2}} \cdot \text{GC Factor} \cdot \frac{V_{\text{Gas}} p}{RT}$$

$$\text{H}_2 \text{ production rate} = \frac{n_{\text{H}_2}}{m_{\text{Cd}} t}$$

Here, A represents the area under the hydrogen or nitrogen peak in the GC chromatogram, and the GC Factor is the ratio of the thermal conductivity detector's sensitivity for hydrogen to that for nitrogen, which was determined through calibration experiments.^[17]

Optical Characterization: Absorption spectra of the nanoparticle solutions and hydrogels were measured in a central position using an Agilent CARY 5000, which was equipped with a Diffuse Reflectance Accessory. PLQY was measured with a Quanta- ϕ integrating sphere coupled to a Horiba Dual-FL spectrofluorometer. Photoluminescence emission and lifetime measurements were conducted in an

Edinburgh Instruments FLS 1000 spectrofluorometer with an Edinburgh Instruments EPL 445 pulsed laser (445.1 nm) for excitation of time-resolved measurements. Measurements of nanoparticle solutions, as well as hydrogels, were performed in Hellma Analytic quartz cuvettes.

Structural Characterization: TEM measurements were performed with an FEI Tecnai G2 F20 TMP (operated at 200 kV). Samples were prepared on copper grids which were covered with a carbon layer (Quantifoil). For preparation hydrogels and colloidal nanocrystal solutions were dropped on the grid. After drying the grids were ready for the measurement in the TEM.

Acknowledgements

This work was funded by the German Research Foundation (Deutsche Forschungsgemeinschaft, DFG) with the grant agreement BI 1708/4-3 and under Germany's excellence strategy within the cluster of excellence PhoenixD (EXC 2122, project ID 390833453). R. T. G. is thankful for financial support from the Hannover School for Nanotechnology (hsn). Furthermore, the used TEM for the shown images was provided by the Laboratory of Nano and Quantum Engineering. Moreover, the authors thank Armin Feldhoff and Jürgen Caro for providing the SEM facility.

Keywords

photocatalytic hydrogen production, NP-based hydrogels, semiconductor-metal hybrid, charge carrier separation, photocatalysis

- [1] S. K. Dutta, S. K. Mehetor, N. Pradhan, *J. Phys. Chem. Lett.* **2015**, *6*, 936.
- [2] O. Al-Madanat, M. Curti, C. Günemann, Y. AlSalka, R. Dillert, D. W. Bahnemann, *Catal. Today* **2021**, *380*, 3.
- [3] P. Kalisman, Y. Nakibli, L. Amirav, *Nano Lett.* **2016**, *16*, 1776.
- [4] Y. Ben-Shahar, D. Stone, U. Banin, *Chem. Rev.* **2023**, *123*, 3790.
- [5] M. Micheel, B. Liu, M. Wächter, *Catalysts* **2020**, *10*, 1143.
- [6] T. O'Connor, M. S. Panov, A. Mereshchenko, A. N. Tarnovsky, R. Lorek, D. Perera, G. Diederich, S. Lambright, P. Moroz, M. Zamkov, *ACS Nano* **2012**, *6*, 8156.
- [7] E. R. Smith, J. M. Luther, J. C. Johnson, *Nano Lett.* **2011**, *11*, 4923.
- [8] L. Carbone, C. Nobile, M. De Giorgi, F. Della Sala, G. Morello, P. Pompa, M. Hytch, E. Snoeck, A. Fiore, I. R. Franchini, M. Nadasan, A. F. Silvestre, L. Chiodo, S. Kudera, R. Cingolani, R. Krahn, L. Manna, *Nano Lett.* **2007**, *7*, 2942.
- [9] S. Sánchez-Paradinas, D. Dorfs, S. Friebe, A. Freytag, A. Wolf, N. C. Bigall, *Adv. Mater.* **2015**, *27*, 6152.
- [10] Y. Nakibli, L. Amirav, *Chem. Mater.* **2016**, *28*, 4524.
- [11] L. J. Hill, M. M. Bull, Y. Sung, A. G. Simmonds, P. T. Dirlam, N. E. Richey, S. E. DeRosa, I.-B. Shim, D. Guin, P. J. Costanzo, N. Pinna, M.-G. Willinger, W. Vogel, K. Char, J. Pyun, *ACS Nano* **2012**, *6*, 8632.
- [12] J. Schlenkrich, D. Zámbo, A. Schlosser, P. Rusch, N. C. Bigall, *Adv. Opt. Mater.* **2022**, *10*, DOI 10.1002/adom.202101712.
- [13] K. Dong, Q. C. Chen, Z. Xing, Y. Chen, Y. Qi, N. G. Pavlopoulos, L. Amirav, *Chem. Mater.* **2021**, *33*, 6394.
- [14] D. Zámbo, A. Schlosser, P. Rusch, F. Lübckemann, J. Koch, H. Pfnür, N. C. Bigall, *Small* **2020**, *16*, 1906934.
- [15] P. Rusch, D. Zámbo, N. C. Bigall, *Acc. Chem. Res.* **2020**, *53*, 2414.
- [16] F. Lübckemann, J. F. Miethe, F. Steinbach, P. Rusch, A. Schlosser, D. Zámbo, T. Heinemeyer, D. Natke, D. Zok, D. Dorfs, N. C. Bigall, *Small* **2019**, *15*, 1902186.
- [17] J. Schlenkrich, F. Lübckemann-Warwas, R. T. Graf, C. Wesemann, L. Schoske, M. Rosebrock, K. D. J. Hindricks, P. Behrens, D. W. Bahnemann, D. Dorfs, N. C. Bigall, *Small* **2023**, *19*, DOI 10.1002/sml.202208108.
- [18] R. Costi, A. E. Saunders, U. Banin, *Angew. Chemie - Int. Ed.* **2010**, *49*, 4878.
- [19] T. Kodanek, H. M. Banbela, S. Naskar, P. Adel, N. C. Bigall, D. Dorfs, *Nanoscale* **2015**, *7*, 19300.
- [20] M. Rosebrock, D. Zámbo, P. Rusch, D. Pluta, F. Steinbach, P. Bessel, A. Schlosser, A. Feldhoff, K. D. J. Hindricks, P. Behrens, D. Dorfs, N. C. Bigall, *Adv. Funct. Mater.* **2021**, *31*, DOI 10.1002/adfm.202101628.
- [21] J. L. Mohanan, I. U. Arachchige, S. L. Brock, *Science (80-)*. **2005**, *307*, 397.
- [22] I. U. Arachchige, S. L. Brock, *Acc. Chem. Res.* **2007**, *40*, 801.
- [23] R. Serra-Maia, M. Bellier, S. Chastka, K. Tranhuu, A. Subowo, J. D. Rimstidt, P. M. Usov, A. J. Morris, F. M. Michel, *ACS Appl. Mater. Interfaces* **2018**, *10*, 21224.
- [24] J. Schneider, D. W. Bahnemann, *J. Phys. Chem. Lett.* **2013**, *4*, 3479.
- [25] M. Berr, A. Vaneski, A. S. Susha, J. Rodríguez-Fernández, M. Döblinger, F. Jäckel, A. L. Rogach, J. Feldmann, *Appl. Phys. Lett.* **2010**, *97*, DOI 10.1063/1.3480613.
- [26] D. Meissner, R. Memming, B. Kastening, D. Bahnemann, *Chem. Phys. Lett.* **1986**, *127*, 419.
- [27] K. Wu, Z. Chen, H. Lv, H. Zhu, C. L. Hill, T. Lian, *J. Am. Chem. Soc.* **2014**, *136*, 7708.
- [28] T. Simon, N. Bouchonville, M. J. Berr, A. Vaneski, A. Adrovic, D. Volbers, R. Wyrwich, M. Döblinger, A. S. Susha, A. L. Rogach, F. Jäckel, J. K. Stolarczyk, J. Feldmann, *Nat. Mater.* **2014**, *13*, 1013.
- [29] J. L. Davis, K. L. Silva, S. L. Brock, *Chem. Commun.* **2020**, *56*, 458.
- [30] R. C. Jeff, M. Yun, B. Ramalingam, B. Lee, V. Misra, G. Triplett, S. Gangopadhyay, *Appl. Phys. Lett.* **2011**, *99*, 2012.
- [31] P. D. Cozzoli, M. L. Curri, A. Agostiano, *Chem. Commun.* **2005**, 3186.
- [32] W. W. Yu, L. Qu, W. Guo, X. Peng, *Chem. Mater.* **2004**, *16*, 560.

Supporting Information

Semiconductor-Metal hybrid Nanoparticle-Based Hydrogels for Hydrogen Evolution Reaction

*Jakob Schlenkrich, Denis Pluta, Rebecca T. Graf, Christoph Wesemann, Franziska Lübkekmann-Warwas, Nadja C. Bigall**

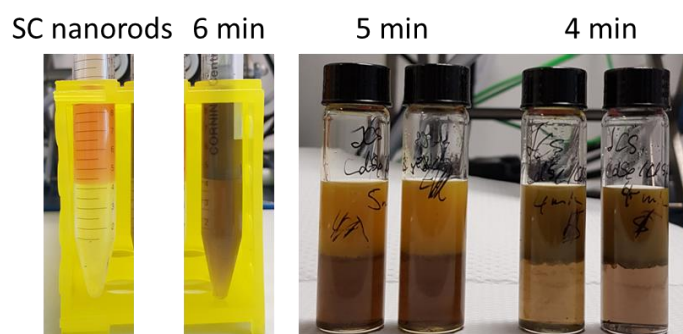


Figure S1: Photographs showing the phase transfer after shaking overnight. In the upper aqueous phase are the semiconductor nanorods or semiconductor-metal hybrid nanorods. In the lower chloroform phase are the detached platinum nanoparticles. According to the color of the NR after 5 min there is less platinum on the NRs than on the samples after 4 and 6 min.

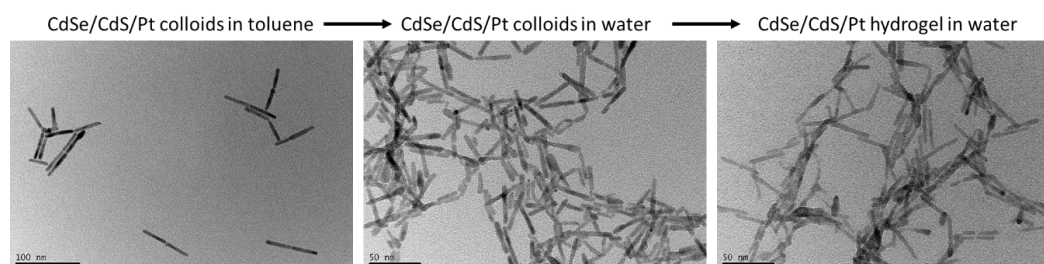


Figure S2: TEM images of CdSe/CdS/Pt colloids in toluene, water and as hydrogel in water

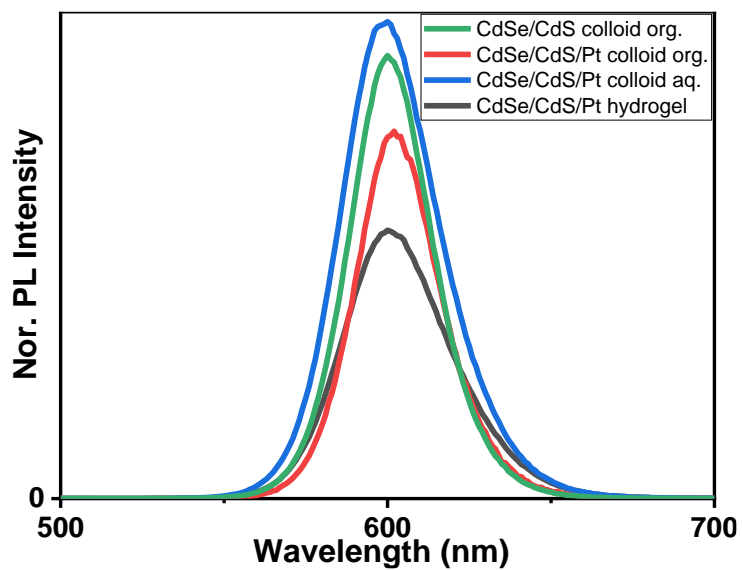


Figure S3: Normalized emission spectra of CdSe/CdS colloids in toluene, CdSe/CdS/Pt colloids in toluene, CdSe/CdS/Pt colloids in water and CdSe/CdS/Pt hydrogel in water.

Table S1: PLQYs and average PL lifetimes

hydrogels	PLQY	avg t / ns
0 % Pt	0.0505	36.3441465
25 % Pt	0.0415	21.7574761
50 % Pt	0.0221	15.7115218
75 % Pt	0.0104	12.3893555
100 % Pt	0.0146	10.478553
colloids		
CdSe/CdS colloids org.	0.4781	15.5163482
CdSe/CdS colloids aq.	0.0574	15.4162342
CdSe/CdS/Pt colloids org.	0.1065	12.7368472
CdSe/CdS/Pt colloids aq.	0.0412	15.9094115



Figure S4: Photographs of the measurement cell for the photocatalytic experiments. The glass vial is pressed to have an inner thickness of less than 2 mm to ensure the illumination of the whole hydrogel.

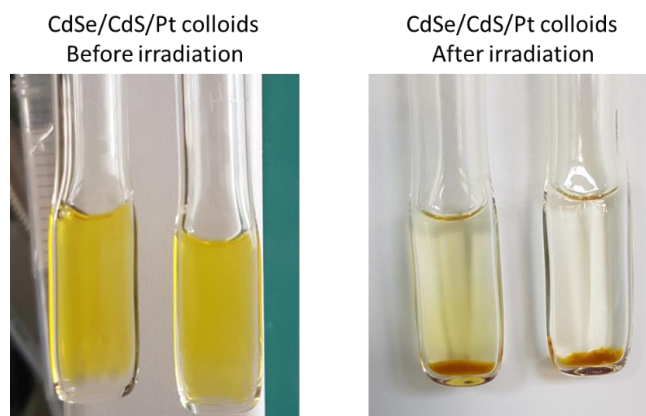


Figure S5: Photographs of a colloidal solution of CdSe/CdS/Pt nanorods before and after irradiation showing the light induced agglomeration.

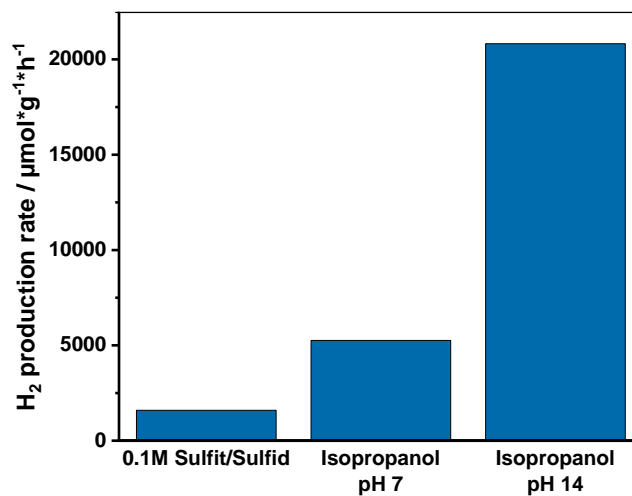


Figure S6: Hydrogen production rates of CdSe/CdS/Pt hydrogels in different hole scavenger showing the highest hydrogen production rates for isopropanol at pH 14.

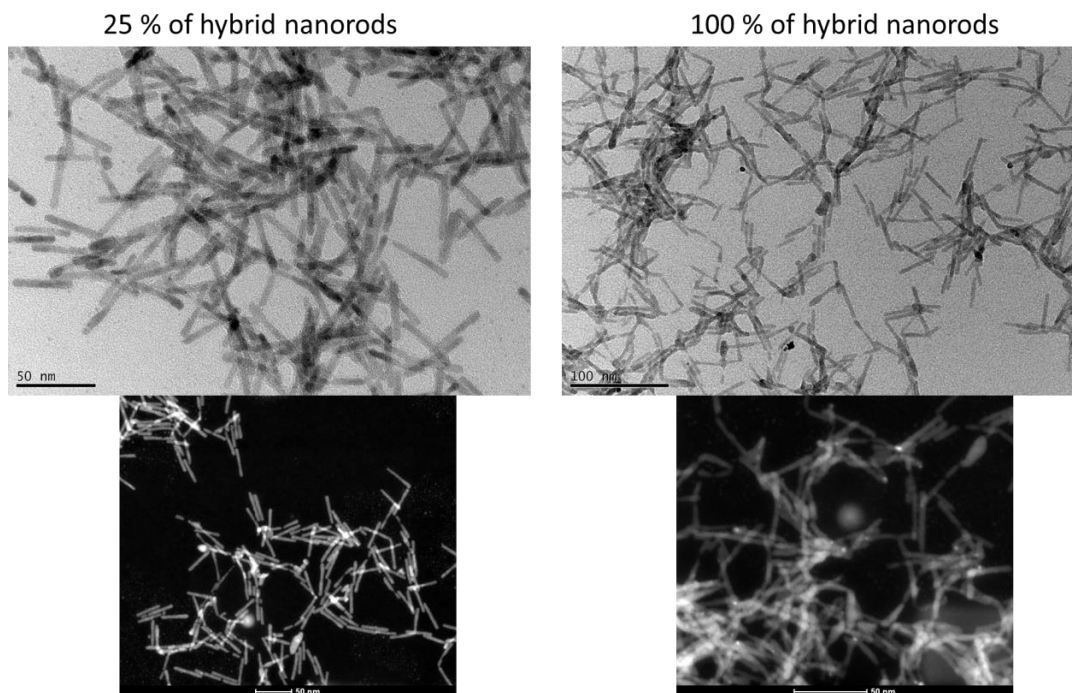


Figure S7: TEM images of CdSe/CdS/Pt hydrogels with 25 % and 100 % of hybrid nanorods. The difference is not clearly visible in the TEM images due to the small size of the platinum domains.

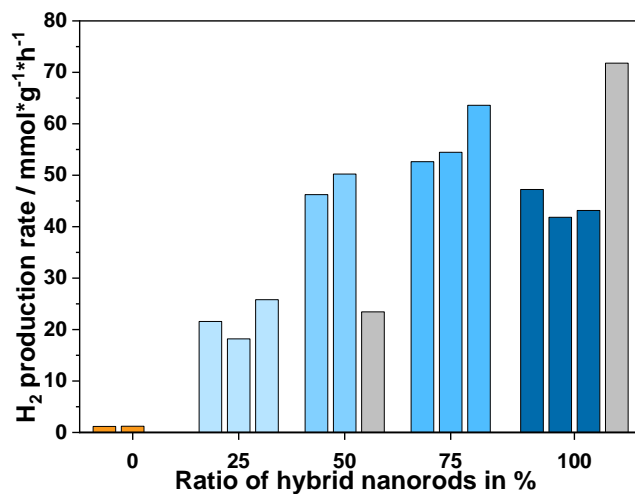


Figure S8: Hydrogen production rates of CdSe/CdS/Pt hydrogels with different ratios of hybrid nanorods. In figure 3B in the manuscript the average rate is shown. Here the single measurements are shown. The gray measurements deviate that much from the mean values that they have been handled as faulty measurements and were not used to calculate the average values.

Table S2: SEM EDX measurement data.

Element	Weight%	Atomic%
S (K)	19.24	45.56
Se (L)	1.55	1.49
Cd (L)	77.28000	52.2
Pt (M)	1.93000	0.75

Chapter 4

Summery and Outlook

In this thesis, photoelectrochemical and photocatalytic properties of semiconductor and semiconductor metal nanoparticle based gel structures were investigated. In hybrid gels structures the contact and the distribution of the metal in the semiconductor network is of importance. Ligands in between the metal and the semiconductor hinder the electron transfer from the semiconductor to the metal which has been seen when mixing semiconductor and metal nanoparticles in cryogels. In colloiddally destabilized nanoparticle based hybrid gels, the contact between the nanoparticle building blocks is crystalline. Here, less metal domains in the gel structure lead to a more efficient charge carrier separation. These investigations showed the high potential of semiconductor metal hybrid gel structures for photocatalytic applications. This has been underlined by comparing pure semiconductor nanoparticle based hydrogels with their respective nanoparticle dispersions. In the photocatalytic hydrogen production reaction, the hydrogels showed up to five times higher hydrogen production rates. From semiconductor hydrogels to semiconductor metal hybrid hydrogels, the hydrogen production rate has been increased by a factor of 50. Interestingly, the highest hydrogen production rates were achieved by reducing the platinum content which was attributed to a better electron accumulation in the metal domains.

In chapter 1, metal domains have been introduced into a cryogel structure by two different approaches. On the one hand, metal domains were grown epitaxially on CdSe/CdS semiconductor nanorods and nanoplatelets. On the other hand, metal nanoparticles were synthesized separately and mixed with the CdSe/CdS nanoparticles before the cryogelation. Cryogelation uses physikal forces of ice crystals to assemble the nanoparticles. With this, the stabilizing ligands are retained on the surface of the nanoparticles in the cryogels. The two different hybrid cryogel approaches lead to similar optical properties as well as comparable structures in SEM images. Metal domains were distributed equally in the network, visible trough SEM EDXS. For both, mixing and on-grown metal domains the observations in SEM EDXS were the same. However, in TEM images, smaller metal agglomerates were found in the mixed samples. When growing the metal on the semiconductor, the distribution is much more homogeneous due to the given crystal contact. Furthermore, the results emphasized that the crystal contact between the semiconductor and the metal has a significant influence on the photoelectrochemical properties of the cryogels. Having the contact in the on-grown samples leads to a more efficient electron transfer from the semiconductor to the metal compared to the mixed hybrid cryogels.

Gel formation by colloidal destabilization leads to even higher porosities and is as well applicable for semiconductor or semiconductor metal hybrid nanoparticles. Using this method, the influence of the metal domain distribution in the gel structures has been investigated. Gold was grown on the tip of CdSe/CdS nanorods or distributed over the nanorods by favoring the facet selective or defect growth, respectively. These different morphologies were transferred into the gel structures by gelation using hydrogen peroxide. Photoelectrochemical measurements revealed that the charge carrier separation in the tipped nanorod gel structures is more efficient. Having gold domains all over the nanorods enables electron tunneling from metal domain to metal domain. This increases the probability of electron hole recombination and thus reduces charge carrier separation. For photocatalytic applications, tipped nanorods should be preferred over several domains on the semiconductor.

Chapter 2 focused on the photocatalytic application of semiconductor and semiconductor metal hybrid hydrogels. The photocatalytic hydrogen production reaction on these material surfaces gave insight in the catalytic properties. Differences between the catalytic reaction on nanoparticles in dispersion and hydrogels has been investigated with pure semiconductor nanoparticles. CdSe, CdS and CdSe/CdS nanoparticles all confirmed that a hydrogel can be up to five times more efficient than their respective nanoparticles dispersion. Differences between hydrogels and nanoparticles were investigated through several techniques. The surface of hydrogels is better accessible due to the ligand oxidation and removal during the gelation with hydrogen peroxide. In nanoparticle dispersions, the surface is covered with a ligand shell, which might block the catalytic reaction to a certain extend. Changes on the surface of the nanoparticles also lead to changes of the trap state situation and thus charge carrier properties. A reduction of hole trap states in the hydrogels improves the charge carrier separation. In combination with the delocalization of electrons beyond one nanoparticle building block the charge carrier lifetimes in the hydrogels are increased making the catalytic reaction more probable.

Adding platinum as a co-catalyst to the semiconductor further improved the charge carrier separation and photocatalytic properties. The electron transfer from the semiconductor to the metal is very efficient resulting in the electron and hole being localized in different materials. Platinum growth on the tips of CdSe/CdS nanorods was possible in organic solution. A phase tranfer into an aqueous solution was needed to induce the gelation with hydrogen peroxide. Thereby, a ligand had to be used which can be stabilized in acidic media since in alkaline media the degradation of hydrogen peroxide is catalyzed on the platinum domains in a way that the gelation was not possible. Both, the growth of platinum on the nanorods and the gelation of the nanoparticles leads to an increase of the non-radiative recombination rates due to the fast transfer of electrons to the platinum. The more platinum is in the gel structure, the more the non-radiative recombination rate is increased. The photocatalytic hydrogen production rates of gels with platinum are about 50 times higher compared to the pure semiconducting materials. However, the highest hydrogen production rates have been achieved by reducing the platinum amount slightly. This indicates that the electron transfer from the semiconductor to the metal is not the bottle neck of the photocatalytic reaction.

Using the results and the experience of this thesis a goal would be to develop a ma-

terial which has similar photocatalytic properties but includes less toxic components. A prospect would be CuInS or CuInSe based materials. This semiconductor has suitable band positions for the hydrogen evolution reaction and absorbs light roughly from 700 nm - 800 nm on. With this, CuInS or CuInSe can use a higher fraction of the solar spectrum than common photocatalyst like TiO₂ or CdS. Using the knowledge of up-scaling approaches from TiO₂ and use CuInS as photocatalyst can be a step towards a large scale application of photocatalysts.

Not only the photocatalyst itself but also the sacrificial agent is of interest. The photocatalytic full water splitting is a challenging reaction as discussed previously. The use of earth abundant sacrificial agents like cellulose or not biologically degradable materials like polyethylene terephthalate (PET) is desirable. Investigating and optimizing the use of these sacrificial agents in combination with nanoparticle based gel structures would be beneficial.

To make the application of the nanoparticle based gels more versatile, the mixing of different nanoparticle solutions and cogelation should be further investigated. Combining two different materials by heterogeneous growth is challenging as it has been emphasized in chapter 1. In contrast, there are much more possibilities combining different materials with mixing and cogelation. The restrictions of heterogeneous growth reactions can be overcome like this. However, mixing and cogelation might be easy on the first glance but comes with some challenges. Both materials need to be compatible with regard of the colloidal stability but also with regard of the possible gelation methods. Even when this is ensured, the kinetics during the gelation process have to be similar to guarantee a homogeneous distribution of both materials. If not, this can have a significant impact on the photocatalytic properties as shown in chapter 2.

Curriculum Vitae

Personal data

Name **Jakob Cornelius Schlenkrich**
Date of birth **06.07.1996**
Place of birth **Hannover**
ORCID **<https://orcid.org/0000-0001-9854-1443>**

Education

- since 2020 **Doctoral student to gain the academic title Dr. rer. nat.**, Leibniz University of Hannover, Institute of Physical Chemistry and Electrochemistry
- Title: *Investigation of Semiconductor-Metal Heteronanostructured Assemblies and Their Photoelectrochemical Properties*
- 2017-2019 **Masters "Chemistry"**, Leibniz University of Hannover, Institute of Physical Chemistry and Electrochemistry
- Masters thesis: *Investigation of Semiconductor-Noble Metal Hybrid Nanoparticles and Their Self-Assembly*
 - Masters grade: 1.4
- 2014–2017 **Bachelors "Chemistry"**, Leibniz University of Hannover, Institut of Inorganic Chemistry
- Bachelor thesis: *Investigation of the Reaction of NO₂ with a Calix[4]aren based Zirconium Metal-Organic Framework*
 - Bachelors grade: 2.1
- 2007–2014 **Gymnasium Goetheschule Hannover**
- Abitur grade: 2.0

Publications and Conferences

Publications included in this thesis

- Revealing the Effect of Nanoscopic Design on the Charge Carrier Separation Processes in Semiconductor-Metal Nanoparticle Gel Networks
Jakob Schlenkrich, Dániel Zámbo, Anja Schlosser, Pascal Rusch, and Nadja C. Bigall
Published in Adv. Opt. Mater. 10 (2021) 2101712
- Interparticle Interaction Matters: Charge Carrier Dynamics in Hybrid Semiconductor-Metal Cryoaerogels
Anja Schlosser, Jakob Schlenkrich, Dániel Zámbo, Marina Rosebrock, Rebecca T. Graf, Giamper Escobar Cano, and Nadja C. Bigall
Published in Adv. Mater. Interfaces 2022, 9, 2200055
- Investigation of the Photocatalytic Hydrogen Production of Semiconductor Nanocrystal-Based Hydrogels
Jakob Schlenkrich, Franziska Lübkeermann-Warwas, Rebecca T. Graf, Christoph Wesemann, Larissa Schoske, Marina Rosebrock, Karen D. J. Hindricks, Peter Behrens, Detlef W. Bahnemann, Dirk Dorfs, and Nadja C. Bigall
Published in Small 19 (2023) e2208108

Submitted Manuscripts included in this thesis

- Semiconductor-Metal Hybrid Nanoparticle-Based Hydrogels: Efficient Photocatalysts for Hydrogen Evolution Reaction
Jakob Schlenkrich, Denis Pluta, Rebecca T. Graf, Christoph Wesemann, Franziska Lübkeermann-Warwas, Nadja C. Bigall
Submitted to a peer review journal, 2023

Publications not included in this thesis

- Interparticle Distance Variation in Semiconductor Nanoplatelet Stacks
Rebecca T. Graf, Anja Schlosser, Dániel Zámbo, Jakob Schlenkrich, Pascal Rusch, Atasi Chatterjee, Herbert Pfnür, Nadja C. Bigall
Adv. Funct. Mater. 2022, 32, 2112621

-
- Interpenetrating Self-Supporting Networks from Anisotropic Semiconductor Nanoparticles and Noble Metal Nanowires
Marina Rosebrock, Jakob Schlenkrich, Hannah Christmann, Rebecca Graf, Patrick Bessel, Dirk Dorfs, Dániel Zámbo, Nadja C. Bigall
Small Struct. 2023, 2300225
 - Self-Assembly of Semiconductor Nanoplatelets into Stacks Directly in Aqueous Solution
Rebecca T. Graf; Kevin Tran; Marina Rosebrock; Hadir Borg; Jakob Schlenkrich; Franziska Lübkekmann-Warwas; Franz Renz; Dirk Dorfs; Nadja C. Bigall
*Adv. Mater. Interfaces*2023, 2300408

Contributions to conferences

- Charge carrier dynamics in semiconductor-metal hybrid nanostructures
Jakob Schlenkrich, Dániel Zámbo, Anja Schlosser, Marina Rosebrock, Pascal Rusch, Nadja C. Bigall
Bunsen-Tagung 2021, Deutsche Bunsen-Gesellschaft, online (Oral Presentation)
- Charge carrier dynamics in semiconductor-metal hybrid nanostructures
Jakob Schlenkrich, Dániel Zámbo, Anja Schlosser, Marina Rosebrock, Pascal Rusch, Nadja C. Bigall
Summer School: Exciting Nanostructures 2021, German Physical Society, Bad Honnef (Poster and Pitch Presentation)
- Semiconductor-metal hybrid nanostructures with efficient charge carrier separation
Jakob Schlenkrich, Dániel Zámbo, Anja Schlosser, Marina Rosebrock, Rebecca T. Graf, Pascal Rusch, Franziska Lübkekmann-Warwas, Nadja C. Bigall
Bunsen-Tagung 2022, Deutsche Bunsen-Gesellschaft, Gießen (Poster Presentation)
- Nanoparticle-based gel structures with efficient charge carrier separation
Jakob Schlenkrich, Franziska Lübkekmann-Warwas, Dániel Zámbo, Anja Schlosser, Marina Rosebrock, Pascal Rusch, Rebecca T. Graf, Christoph Wesemann, Larissa Schoske, Nadja C. Bigall
Nanohybrid 2022, Graduiertenkolleg Nanohybrid, Hamburg (Oral Presentation)
- Semiconductor-metal hybrid nanostructures with efficient charge carrier separation
Jakob Schlenkrich, Dániel Zámbo, Anja Schlosser, Marina Rosebrock, Rebecca T. Graf, Pascal Rusch, Franziska Lübkekmann-Warwas, Nadja C. Bigall
Nanoday 2022, Laboratory of Nano- and Quantum Engineering, Hannover (Poster Presentation)
- Nanoparticle-based gel structures for photoelectrochemical applications
Jakob Schlenkrich, Franziska Lübkekmann-Warwas, Rebecca T. Graf, Christoph Wesemann, Larissa Schoske, Marina Rosebrock, Karen D. J. Hindricks, Peter Behrens, Detlef W. Bahnemann, Dirk Dorfs, and Nadja C. Bigall
NANAX10 2023, Wien (Poster Presentation)

-
- Nanoparticle-based gel structures for photoelectrochemical applications
Jakob Schlenkrich, Franziska Lübke mann-Warwas, Rebecca T. Graf, Christoph Wesemann, Larissa Schoske, Marina Rosebrock, Karen D. J. Hindricks, Peter Behrens, Detlef W. Bahnemann, Dirk Dorfs, and Nadja C. Bigall
ACS Fall 2023, American Chemical Society, San Francisco (Oral Presentation)
 - Nanoparticle-based gel structures for photoelectrochemical applications
Jakob Schlenkrich, Franziska Lübke mann-Warwas, Rebecca T. Graf, Christoph Wesemann, Larissa Schoske, Marina Rosebrock, Karen D. J. Hindricks, Peter Behrens, Detlef W. Bahnemann, Dirk Dorfs, and Nadja C. Bigall
Nanoday 2023, Laboratory of Nano- and Quantum Engineering, Hannover (Poster Presentation)
 - Photocatalytic Benefits of Semiconductor Nanoparticle-Based Gel Structures
Jakob Schlenkrich, Franziska Lübke mann-Warwas, Rebecca T. Graf, Christoph Wesemann, Larissa Schoske, Marina Rosebrock, Karen D. J. Hindricks, Peter Behrens, Detlef W. Bahnemann, Dirk Dorfs, and Nadja C. Bigall
Particle Based Materials 2023, TU Braunschweig, Braunschweig (Oral Presentation)